3D and 4D Characterisation of Lithium Ion Battery Electrode Microstructures using X-ray Tomography

Oluwadamilola Olaniyi Taiwo

Submitted in part fulfilment of the requirements for the degree of Doctor of Philosophy at University College London

2016

Declaration

I, Oluwadamilola Olaniyi Taiwo, confirm that the work presented in this thesis is my own. Where information has been derived from other sources, I confirm that this has been indicated in the thesis.

…….

Signature

October 2016.

Abstract

There is a direct link between electrode microstructure and their performance in lithium-ion batteries (LIBs); however, this relationship remains poorly understood. By utilising tomographic X-ray imaging techniques, it is possible to characterise LIB electrode microstructure in three dimensions. Moreover, extending these imaging techniques to explore changes in these materials gives rise to the notion of "four-dimensional" (4D) tomography to study microstructural evolution with time.

This work focused on characterising, both qualitatively and quantitatively, the three-dimensional (3D) microstructure of LIB electrode materials at multiple length and time scales with the aid of laboratory and synchrotron X-ray sources. The suitability and reliability of direct 3D microstructural analysis for quantifying LIB electrodes was demonstrated by comparing it with stereological methods, which are shown to introduce bias when applied to inhomogeneous 3D microstructures.

Silicon (Si) and metallic lithium (Li) are highly energy-dense electrode materials and promising candidates for use in LIBs; however, they experience significant microstructural degradation upon electrochemical cycling. Using a custom-built, X-ray transparent *in-situ* electrochemical cell, 4D characterisation of the microstructural evolution and degradation within the aforementioned electrode materials was performed both *in-situ* and *in-operando*. Phase transformation, fracture formation and propagation within individual Si particles was visualized and tracked in 3D during the course of a half-cell discharge. At a higher X-ray imaging resolution, microstructural evolution in Si microparticles as a result of repeated cycling was captured and quantified in 3D. Visualisation of formation and growth of pits and mossy lithium deposits along metallic Li electrode surfaces was also presented. Finally, an X-ray contrast-enhancement approach for imaging lowly attenuating electrode materials such as graphite was also demonstrated.

This work has demonstrated X-ray tomography as a diagnostic tool for providing valuable insight into electrode microstructure which can aid the efficient design of these electrode materials in future generation LIB systems.

Acknowledgements

First of all, I'm grateful to my supervisors, Dr. Paul Shearing and Prof. Dan Brett, for the opportunity to study for a PhD at the Electrochemical Innovation Lab at UCL. Throughout these last few years, your guidance and unwavering support have gone a long way to get me to where I am now. Thanks for providing me with great opportunities to work on interesting projects and with seasoned researchers. Thanks Paul, for being a great mentor and role model, and for always encouraging me to aim high.

To Folashade, thank you for being my biggest cheerleader, for being my sunshine and a pillar of support during this PhD adventure. Thanks for being patient with me and for always being there for me whenever I was feeling down and burdened. To my parents, thanks for your confidence, support and love; you both have been a constant source of happiness and encouragement and I am forever grateful for this. To my brothers, Gbenro, Tobi and Tomisin, thanks for the love and for being there for me.

I would also like to thank all my collaborators. Through these collaborations, I have been able to grow and gain experience working in a group and as an effective team player. Special thanks to Dr. David Eastwood and Prof. Peter Lee at the Manchester X-ray Imaging Facility at Harwell for the opportunity to work with their group, for their generous support during beamtime experiments at the Diamond Light Source, and for the many constructive and insightful discussions about my research. Thanks to Dr. Juan Manuel Paz García, Dr. Erika Tudisco and Dr. Stephen Hall at Lund University for the opportunity to work with them, for all their help during synchrotron beamtime experiments at the Swiss Light Source and for introducing me into the world of digital image correlation. Thanks to Dr. Shane Beattie and Dr. Melanie Loveridge at the Warwick Manufacturing Group for chance to work them on battery electrode laminate preparation in your laboratory. I would also like to thank the synchrotron beamline scientists for all their support: Dr. Andrew Bodey, Dr. Kaz Wanelik, Prof. Christoph Rau and Dr. Joan Vila-Comamala at the i13 Imaging Branchline of Diamond Light Source, and Dr. Julie Fife, Dr. Rajmund Mokso, Dr. David Haberthur, Dr. Pablo Villanueva-Perez and Dr. Alessandra Patera at the TOMCAT beamline of the Swiss Light Source. Thanks to Richard at the UCL Institute of Making for all his help in the

Makespace workshop. I would also like to thank the UK EPSRC, UCL BEAMS, and STFC Batteries for the funding and grant awards towards my PhD research.

I am fortunate to have been a member of the research group at the UCL Electrochemical Innovation Lab, and to be part of a great team to scientific researchers from different parts of the world. Thanks to all current and past members who made my time both in and out of the lab memorable. Thanks to Donal Finegan, Xuekun Lu, Josh Bailey, Tom Heenan, Erik Engebretsen, Vidal Bharath, Rhodri Jervis, James Robinson, Bernhard Tjaden, Sohrab Randjbar-Daemi, Chun Tan, Alvin Lim and Francesco Iacoviello for all their valuable input and discussions contributing to the progress of the work; Toby Neville, Jay Millichamp and Tom Mason for their generosity and help during the initial stage of this work; and Krisztian Ronaszegi for all your help with learning programming in MATLAB.

To the Awe family, thank you so much for your warmth and encouragement over the years. To all the guys at Elly House, thank you all for the warm company and friendship during my stay there.

Table of Contents

List of Figures

List of Tables

List of Symbols and Abbreviations

Symbol	Definition
A_A	Phase area fraction
D_{eff}	Effective diffusivity
L_A	Total 2D phase boundary perimeter per unit area
L_e	Effective curve length
S_v	Volume-specific surface area
σ_{2D}	Stereologically-predicted mean pore radius
τ^2	Tortuosity factor
Z	Atomic Number
Φ	Pore volume fraction
D	Intrinsic diffusivity
L	Euclidean distance between the end points of a curve
τ	Geometric tortuosity

Abbreviation	Definition
AC	Alternating Current
CC	Correlation Coefficient
CC-CV	Constant Current–Constant Voltage
CCD	Charged Coupled Device
CE	Coulombic Efficiency
CPSD	Continuous Pore Size Distribution
CT	Computed Tomography
DEC	Diethyl Carbonate
DOHT	Distance-Ordered Homotopic Thinning
DVC	Digital Volume Correlation
EC	Ethylene Carbonate
EDS	Energy Dispersive Spectroscopy
EMC	Ethyl Methyl Carbonate
FIB	Focused Ion Beam
LCO	Lithium Cobalt Oxide
LMO	Lithium Manganese Oxide
MA-FM	Medial Axis Fast Marching
NMC	Nickel Manganese Cobalt Oxide
NMP	N-methyl-2-pyrrolidone
PAA	Polyacrylic Acid
PFA	Perflouroralkoxy
ROI	Region of Interest
RVE	Representative Volume Element
SE	Structuring Element
SEI	Solid Electrolyte Interphase
SEM	Scanning Electron Microscopy
XANES	X-ray Absorption Near Edge Spectroscopy

Chapter 1

Introduction

1.1 Motivation

Lithium-ion batteries (LIBs) have achieved widespread application in portable electronic devices and have attracted a lot of interest in automotive and grid storage applications due to desirable properties, such as relatively high energy and power densities and long calendar life. Since their commercialization in the early 1990s, interest in LIB technology has considerably increased and numerous research efforts have been made to improve the performance of LIBs. However, there are still significant challenges associated with LIBs, such as capacity fade and unpredicted safety issues. Significant research effort has been put into developing novel electrode materials with improved properties [1,2] in order to address LIB performance issues.

In addition to the electrode material properties, the electrode microstructure also plays a vital role in determining the performance of a LIB [3]. Electrodes in LIBs are porous, consisting mainly of particles of active material mixed with a conductive additive and binder. These porous composites possess complex microstructures, and they support the electrochemical reactions that take place in LIBs. As with all functional materials, there is a direct link between the microstructure of the electrode and its performance; the electrode microstructure affects the response of the LIBs with respect to battery charging behaviour, capacity, durability and safety.

Moreover, the electrochemical and transport behaviour of these battery electrodes are generally modelled using the macro-homogeneous model [4,5] which requires particle radius, electrode thickness, and electrode porosity as input parameters; otherwise it assumes the electrodes are isotropic, homogeneous, 1-dimensional porous materials made from mono-disperse spherical particles [4,6]. Although this model has been utilized successfully in studying battery electrode design and optimisation [5], it has limited use in the studies involving electrode degradation, ageing and failure due to their restricted ability to account for microstructural

heterogeneity [7]. Modelling and simulation performed using actual 3D morphologies of LIB electrodes can provide additional understanding of battery electrode performance [8–10]. The availability of real life LIB electrode microstructural data will therefore aid in more accurately modelling of LIB systems and in establishing the validity of the assumptions made by simpler battery models.

Hence, there is a clear need to understand electrode microstructures, particularly the influence of electrode preparation, as well as changes during battery operation and failure. For instance, the insertion and removal of Li within the electrodes during battery operation causes the electrode microstructure to evolve and experience volume changes (expansion and contraction), e.g., during discharge, graphite electrodes have been observed to "swell" when intercalated with lithium ions, with about 10% change in volume [11]; alloy-type electrodes (e.g. Si, Sn), however, undergo larger volume changes of up to 400 % [12]. These microstructural evolution processes cause changes in electrode particle shape and arrangement, and also generate mechanical stresses that can induce microstructural degradation processes over extended operating times.

In the recent past, a number of investigations on LIB electrode microstructures and electrode microstructural evolution processes have been performed using a suite of microscopy tools such as optical microscopy [13,14], scanning electron microscopy [15], transmission electron microscopy [16], and atomic force microscopy [17,18], in combination with techniques such as nuclear magnetic resonance imaging [19] and time-of-flight secondary ion mass spectroscopy [20,21]. These tools, however, provide microstructural information in two-dimensions (2D), which is insufficient for accurate evaluation of the volumetric structural features of the porous electrodes.

Three-dimensional microstructural characterisation of an extended range of materials has been made possible by recent developments in 3D imaging tools, and this has been achieved with remarkable resolution. A range of 3D imaging methods with varying length scales are now available, some of which include atom probe tomography, electron tomography, X-ray computed tomography (CT), neutron tomography and focused ion beam (FIB) tomography. The most commonly applied of these imaging techniques for obtaining real configuration of LIB electrode microstructures are FIB-SEM tomography [8,22,23] and X-ray tomography [9,24–33].

Although destructive in operation, FIB-SEM tomography techniques provide sufficiently high resolution (typically <100 nm) and contrast suitable for understanding nano-scale properties within a porous electrode. X-ray tomography techniques are, however, particularly versatile, not only demonstrating multiple length scale capabilities [24] but also providing a non-destructive imaging platform to explore microstructural evolution processes over time.

Tomography techniques offer, for the first time, access to detailed microstructural information in three dimensions; however, extending these techniques to explore transient changes in LIB electrodes without the requirement for battery cell disassembly gives rise to the idea of "4-dimensional" tomography to study microstructural transformations at different stages of cell lifetime [34,35]. In addition, the wide range of physical phenomena that take place in LIBs makes it desirable to perform tomography at multiple length scales, and this includes studies at the particle, electrode, cell and even pack level.

1.2 Research aims and objectives

This main aim of this research is to use X-ray CT as a diagnostic tool to study the microstructure of LIB electrode materials, with a particular focus on microstructural degradation resulting from battery operation. This will involve the application of X-ray CT with the aid of both synchrotron and lab-based probes to reveal a variety of qualitative and quantitative microstructural features and changes in LIB electrodes such as deformation and degradation. By employing *in-situ* and *in-operando* imaging techniques, new insight into the microstructural evolution processes that occur within the electrodes during electrochemical testing can be provided. Specific objectives of this research are:

- To demonstrate the need for 3D quantification techniques, and the limitations of 2D techniques.
- To develop an *in-situ* electrochemical cell to facilitate X-ray CT imaging *in tandem* with electrochemical performance testing.
- To perform X-ray tomographic experiments on LIB electrodes using the developed *in-situ* cell to obtain microstructural evolution data on battery electrodes at different stages of battery operation and at multiple length scales.

- To characterise electrode microstructure using suitable 3D image analysis methods in order to extract information on key microstructural parameters from the X-ray CT data.
- To relate the 3D microstructural information obtained to the electrochemical performance measurements taken from the battery cells.

1.3 Thesis outline

The thesis is organized into the following chapters:

Chapter 2 reviews the basic principles and components for LIB operation, as well as the state-of the art of 3D microstructural characterisation of LIB electrodes. *Chapter 3* discusses the electrode and cell manufacture procedures, as well as electrochemical testing methods used in the work. 3D material characterisation with X-ray CT, 3D image processing and quantification methods used in the study are covered. The design and development of an *in-situ* electrochemical cell to facilitate 3D microstructural evolution studies with X-ray CT is also presented. *Chapter 4* demonstrates the suitability and reliability of direct 3D analysis for quantifying LIB electrode microstructures, in comparison to stereological prediction methods which utilise 2D image information to extrapolate 3D microstructural parameter information. *Chapter 5* examines the 3D morphological changes that occur at the surface of metallic Li electrodes as a result of electrochemical cycling, using both synchrotron and laboratory X-ray CT techniques. *Chapter 6* demonstrates the use of both laboratory and synchrotron X-ray imaging to investigate microstructural evolution within bulk Si electrodes during the early stage of electrochemical cycling at the electrode and particle levels, respectively. *Chapter 7* presents microstructural investigations on silicon and graphite electrode materials using nano-scale X-ray CT. Finally, *Chapter 8* provides a conclusive summary of the thesis and proposes suggestions for future investigations.

Chapter 2

Literature Review

Lithium-ion batteries (LIBs) are considered to be one the most promising energy storage devices due to their inherent advantages such as high energy and power density, high efficiency, no memory effect and long cycling life compared with other batteries. Since their commercialization in 1991 by Sony [36], LIBs have been widely used as power sources for numerous consumer electronic devices e.g. mobile phones, notebook computers, cordless power tools, laptops, etc. Moreover, in recent years, great advancements in LIB technology has made them attractive candidates in higher energy-demanding applications such as electric vehicle power sources, stationary energy systems for solar and wind energy, and smart grids. LIBs exhibit higher volumetric and gravimetric densities compared to other rechargeable battery systems (Figure 2.1) due to their higher operating cell voltages which can be achieved by using non-aqueous electrolytes.

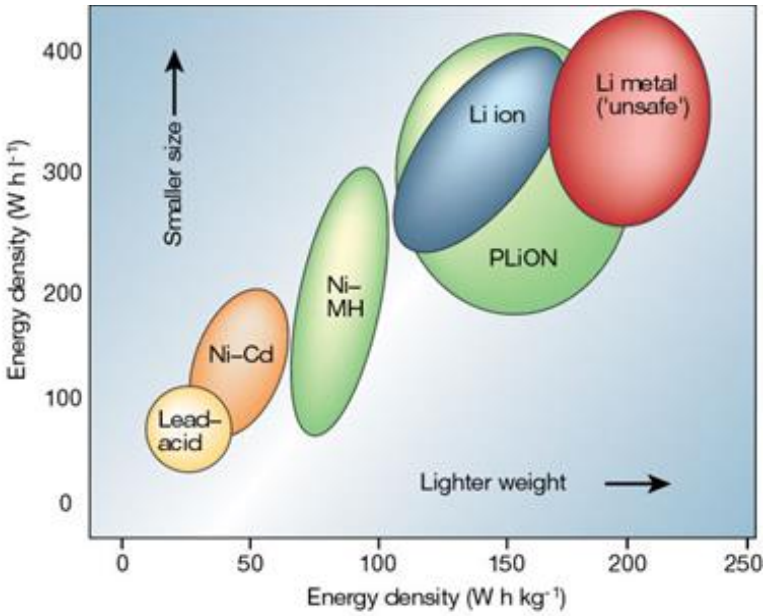

Figure 2.1. Comparison of volumetric and gravimetric energy density of different battery technologies. Reproduced from [37].

In this chapter, a brief introduction into the fundamental operating principles and the main components of LIBs is presented, followed by a review of the state-of-the-art of microstructural characterisation of LIB electrode materials in three dimensions.

2.1 Working principle of lithium-ion batteries

The lithium-ion battery consists of three functional components: a positive electrode (which is usually a lithium-rich compound or material), a negative electrode (usually a lithium-sink material), and the electrolyte serving as an ionic conductor. During operation of LIBs (as shown in the schematic in Figure 2.2), lithium ions (Li^+ ions) are exchanged between the positive and negative electrodes via an ion-conducting electrolyte in a series of oxidation and reduction reactions. Typically, lithium ions are extracted from their positive electrode host, move through the electrolyte, and are inserted into the negative electrode during charging; meanwhile, electrons flow to and from the electrodes via current collectors forming an electric circuit; the reverse is the case during discharging. During the first charge-discharge cycle of LIBs, a solid layer known as the "*solid-electrolyte-interphase*" (SEI) will be formed on the surface of the electrodes as a result of electrolyte decomposition at the extreme voltage range, typically < 1.2 V or > 4.6 V [38]. The principal concept of LIB operation is based on the intercalation/insertion reaction and is therefore different from conventional secondary batteries which are based on chemical reactions.

2.2 Lithium-ion battery components

Electrochemical reactions that take place within lithium-ion batteries are supported by the porous electrodes: typically, a lithium ion battery electrode is a composite material, also referred to as a laminate, comprising of the following components: (1) the active material, which is acts as the source and acceptor of the lithium-ions, (2) the conductive additive, which enhances the electronic conductivity within the electrode laminate and lowers the internal cell resistance but does not contribute to the cell's electrochemical process, and (3) the binder, which ensures cohesion between the active material and conductive additive particles and their adhesion to the current collector. In most commercially available LIB systems, intercalation materials (i.e. materials that allow the reversible insertion of guest

elements or molecules within their structure) have been commonly utilized as active materials for positive and negative electrodes. These materials possess relatively stable crystal lattice structures and their interstitial sites can be intercalated/de-intercalated with lithium ions without significantly altering the main crystal structure. Many of the intercalation materials used as positive electrodes in LIBs have relatively high potential vs. lithium metal and are quite stable mechanically and chemically.

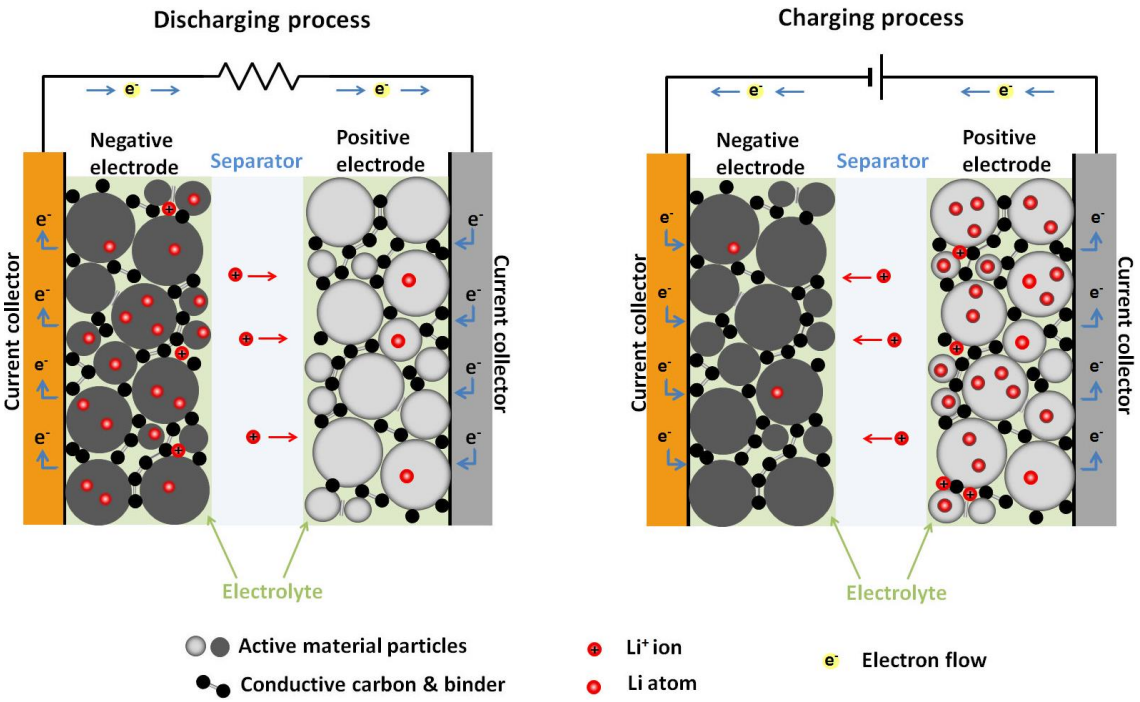

Figure 2.2. Schematic representation of a typical lithium-ion battery operation. During discharge, Li^+ ions migrate from the lithiated negative electrode (the anode) into a delithiated positive electrode (the cathode) with associated oxidation and reduction of both electrodes, respectively. The reverse process occurs during battery charging process.

2.2.1 Positive electrode

Positive electrode materials found in commercial LIB systems are mostly based on transition metal intercalation oxides. Typical positive materials can be classified according to structure as layered compounds $LiMO_2$, olivine compounds $LiMPO_4$ and spinel compounds LiM_2O_4, where M = transition metal e.g. Co, Mn, Fe, etc. Over the years, numerous developments and optimisation efforts have been made to the positive electrode materials in the different classifications mentioned above in order improve properties such as chemical stability, cycling performance, capacity retention and rate capabilities: for example, the use of cation-substituted materials in layered

compounds [39–50], the use of multiple dopants in spinel compounds [51–57], the development of carbon-coated particles, nano-sized crystalline particles and doping transition metal ion sites with supervalent cations with olivine compounds [58–66]. Such material optimisations are usually initiated from two important aspects: altering the intrinsic material's chemistry, and modifying the morphology (e.g. particle size, surface property, etc.) of the materials by understanding their microstructural behaviour [38].

2.2.2 Negative electrode

Negative electrode materials for LIBs can be grouped into two major types: carbon based negative electrode materials and alternative (or non-carbon based) negative electrode materials. Carbon based materials are the most widely utilized negative electrodes in state-of-the-art LIBs. These carbon materials possess favourable characteristics such as good cyclability and reliability; they are also abundant, relatively cheap, light weight, environmentally friendly and safe. Li^+ ions intercalate into and de-intercalate from the carbon during charge and discharge respectively, as described in Equation (2.1).

$$Li_xC_n \rightleftharpoons x \cdot Li^+ + x \cdot e^- + C_n \qquad (2.1)$$

Graphite and graphitized carbons have been desirable choices for negative electrode materials in LIB applications due to their high specific capacity (theoretically 372 mAh/g with LiC_6 stoichiometry), low operating potential vs. lithium metal, long plateau in voltage profiles, as well as their excellent cycling behaviour [67,68]. However, drawbacks such as significant irreversible capacity loss during the first charge process SEI formation [69] and electrolyte sensitivity [70] has spurred the search and development for alternative negative electrode materials to replace carbonaceous ones in LIBs.

In selecting alternative negative electrode materials, an important factor is that their electrochemical potential must be comparable with that of lithium metal or of lithiated carbon in order to achieve a high cell voltage. Layered transition metal compounds (e.g. $Li_4Ti_5O_{12}$ [71–76]), composite metal alloys and intermetallic compounds [77–79], and tin-based oxides [80–82] are examples of alternative systems that have been investigated. However, the higher potential of $Li_4Ti_5O_{12}$ at about 1.5 V versus metallic lithium [83], the significant irreversible capacity of SnO_2 [84], and the

huge volume change of alloy-type electrodes (e.g. Si, Sn) upon lithiation [85–87] are some major challenges with these types of negative electrode materials.

2.2.3 Electrolyte

Rechargeable lithium battery systems use organic electrolytes, which normally comprise of a lithium salt dissolved in either a mixture of aprotic organic solvents (liquid organic electrolytes) or a flexible, high molecular weight polymer host (solid and gel polymer electrolytes). Some key characteristics that electrolytes for LIBs should possess are: good ionic conductivity (> 1 $mScm^{-1}$), good thermal stability and compatibility with other cell components, wide electrochemical voltage window with significant thermodynamic or kinetic stability within that window, chemical inertness to the strong oxidizing/reducing surface of the electrode (especially after SEI formation on electrode surface), low cost, reliable safety and environmental compatibility [88,89]. A common electrolyte recipe used in lithium-ion battery systems is 1M $LiPF_6$ solution of ethylene carbonate (EC) : dimethyl carbonate (DMC) in a 1:1 weight ratio, which has a conductivity of 10.7 $mS.cm^{-1}$ [90] and is useable in the temperature range of -20 °C to 50 °C. Organic additives such as fluoroethylene chloride (FEC) and vinylene chloride (VC) can also be added to electrolyte mixtures in order to improve SEI formation and electrode cycling stability [91–95].

2.2.4 Separator

The separator is a critical component in rechargeable lithium-ion batteries – it is placed between the positive and negative electrodes in order to prevent direct electrical and physical contact of electrodes while allowing ion transport between them. Due to the relatively low ionic conductivity of organic electrolytes, separators in LIBs should satisfy a number of requirements e.g. micrometre-scale thickness, chemical and electrochemical stability against electrolyte, good mechanical strength after cell assembly, effective thermal stability over a range of operating temperatures. In addition, the separator can act as a safety device by densifying at certain temperatures and forestalling huge current flow in the event of an external short circuit, over-charging or over-discharging outside the operating potential window [96]. The separator must also possess sufficient porosity to retain liquid electrolyte and provide ionic mobility between the electrodes, as well as a uniform pore size (below

the size of the electrode particles) with high tortuosity in order to mitigate lithium dendrite growth. The most common separator type found in commercial LIB cells is the micro-porous polymeric membrane [97], which may consist of either polyethylene or polypropylene or a combination of both. In addition to polymer-type separators, glass fiber separators are commonly used in laboratory-made rechargeable Li cells for research purposes [98,99].

2.3 Microstructural evolution in LIB Electrodes

Both positive and negative electrode materials in LIB cells undergo structural changes in the form of ageing and degradation. However, the changes associated with the negative electrode / electrolyte interface is generally considered to be the most critical part of the cell [100] due to the high reactivity of the organic electrolyte with the electrode material and lithium ions.

During LIB operation, the reaction between lithium and the electro-active material in the porous electrodes drives morphological and microstructural changes within the electrodes. Li diffuses into and out of the active particles, causing them to expand and contract. These structural changes may generate diffusion-induced stresses and eventually lead to stress-induced degradation which can be demonstrated at several different length scales within the electrode structure.

2.3.1 Graphite

Graphite, which is a commonly used negative electrode material in commercial LIBs, undergoes microstructural changes upon intercalation with lithium ions. During battery charging, Li^+ ions intercalate between the interlayer spaces of the graphite in stages (as in Figure 2.3), forming a sequence of well-ordered, graphite-lithium intercalation compounds [101]:

$$LiC_{72}\ (dilute\ stage) \leftrightarrows\ LiC_{36}\ (stage\ 4) \quad \text{(I)}$$

$$LiC_{36}\ (stage\ 4) \leftrightarrows\ LiC_{27}\ (stage\ 3) \leftrightarrows\ LiC_{18}\ (stage\ 2L) \quad \text{(II)}$$

$$LiC_{18}\ (stage\ 2L) \leftrightarrows\ LiC_{12}\ (stage\ 2) \quad \text{(III)}$$

$$LiC_{12}\ (stage\ 2) \leftrightarrows\ LiC_{6}\ (stage\ 1) \quad \text{(IV)}$$

At slow C-rates, the voltage profile of lithiating graphite shows several well-defined plateaus which correspond to each graphite intercalation stage in Equations I – IV above [Figure 2.4(a)], and the staging behaviour become more apparent in the

dQ/dV plot obtained by differentiating capacity with respect to potential [Figure 2.4(b)].

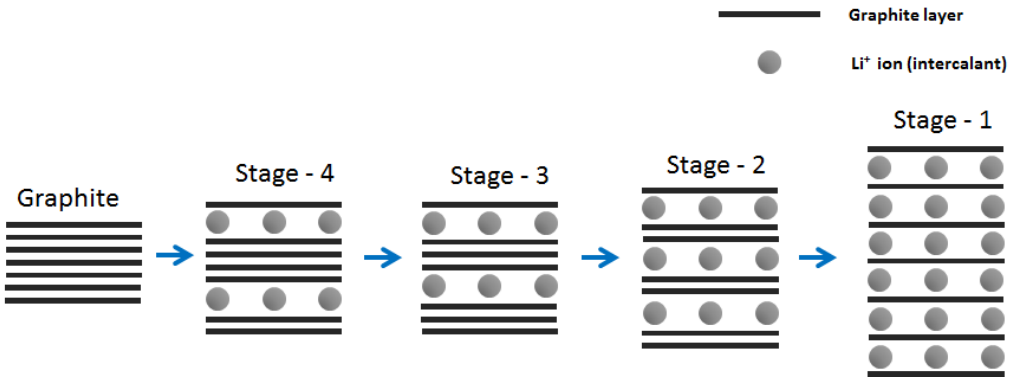

Figure 2.3. Schematic representation of the mechanism of Li intercalation into graphite. Adapted from [102].

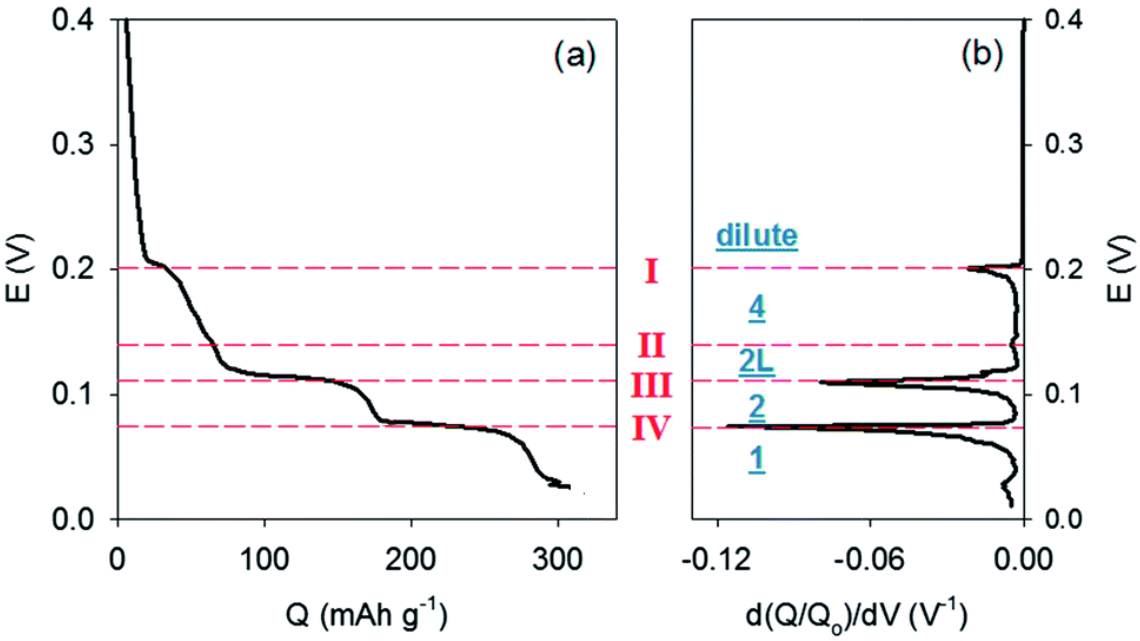

Figure 2.4. (a) Potential *versus* capacity profile of lithiation of graphite at 0.05C (Q = capacity; E = cell potential *versus* Li/Li^+). (b) Differential capacity with respect to potential. Dashed red lines indicate peak potentials associated with corresponding reactions, which are highlighted by the red Roman numerals. Graphite intercalation compound stages are indicated by the underlined blue numbers or characters. Reproduced with permission from [101]. Copyright (2014), Royal Society of Chemistry.

Each stage is identified by the formation of its own graphite intercalation compound [103] and is associated with a characteristic graphite layer spacing [104],

and changes in the layer spacing at the atomic scale are translated through to multiple length scales within the graphite electrode.

At the micrometre scale, fully intercalated graphite particles demonstrate volume expansion of up to 10 % [105,106]. Upon repeated battery operation, such microscale expansion (and contraction during deintercalation) causes stress development within the electrodes and can ultimately lead to particle fracturing and cause damage to electrode microstructure. Other degradation and ageing mechanisms such as graphite exfoliation and particle cracking resulting from solvent co-intercalation, electrolyte reduction and gas evolution inside graphite (Figure 2.5) also contribute to morphological evolution and degradation of graphite electrode within commercial batteries [107].

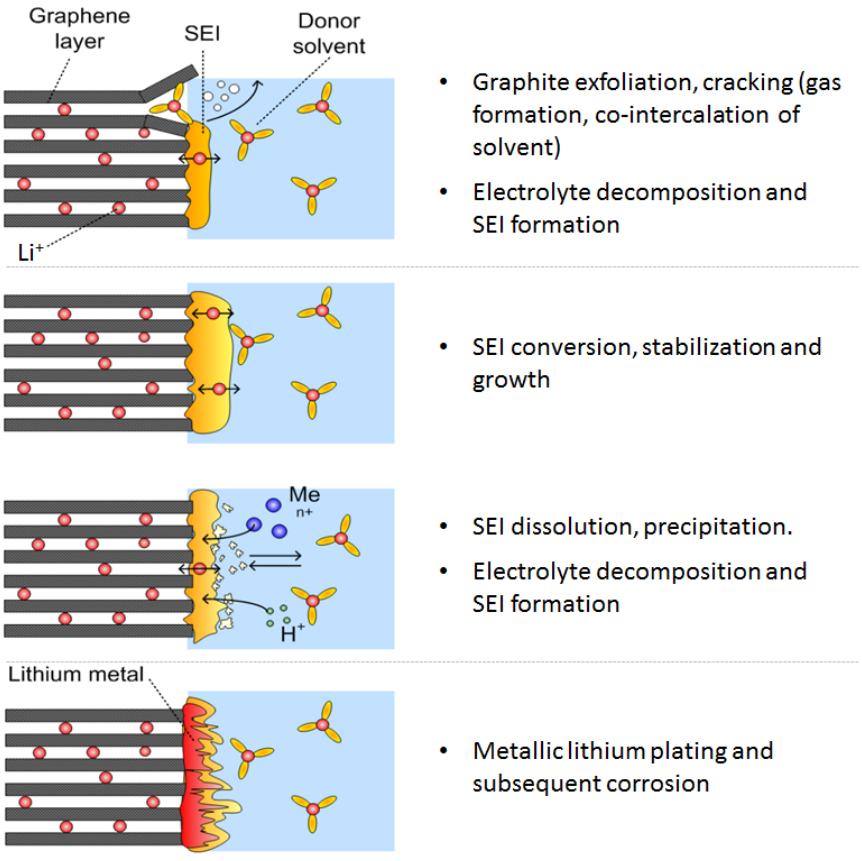

Figure 2.5. Structural changes at the graphite negative electrode / electrolyte interface. Reproduced with permission from [108]. Copyright (2005), Elsevier Science.

2.3.2 Silicon

In order to meet demanding applications such as in electric vehicles and in grid energy storage, the development of high-performance lithium-ion batteries is crucial and significant research effort has been devoted to achieve this. Carbonaceous

materials such as graphite are commonly used as negative electrodes in traditional lithium-ion batteries; these materials have high Coulombic efficiencies (> 95 %) but are limited by their rather low specific capacities (372 $mAhg^{-1}$). Materials that form alloys with lithium (e.g. Sn, Sb, Si, and Ge) [109] are being considered as replacements for graphite due to their much higher theoretical specific capacities.

Amongst alloy-type electrode materials, silicon (Si) is a particularly promising candidate studied for more demanding energy applications because its reaction with lithium occurs at low discharge potentials ($<$ 0.5 V vs. Li/Li^+) [110], and it possesses a large theoretical specific capacity (*ca.* 4200 $mAhg^{-1}$, [85]). However, a major challenge of the application of silicon in rechargeable lithium batteries is the huge volume expansion of silicon upon lithiation.

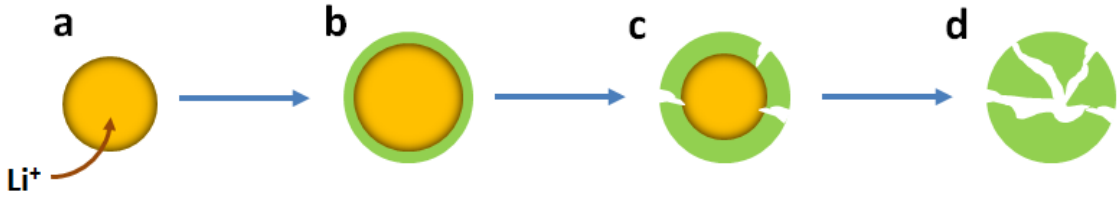

Figure 2.6. Schematic diagram showing the surface-to-center lithiation behaviour of bulk silicon particles.

Figure 2.6 shows a schematic illustration of how bulk crystalline Si particles react to lithiation. As Li diffuses faster in the surface of Si than within the particle, it reacts with crystalline silicon (yellow) form an amorphous lithiated silicon (a-Li_xSi, green) shell around the Si particle upon lithiation (Figure 2.6b), that is:

$$\mathrm{Si} + x\mathrm{Li} \rightleftharpoons \mathrm{Li}_x\mathrm{Si} \qquad (2.2)$$

The migration of Li^+ ions in the electrolyte is controlled by the diffusion of Li through the Li_xSi phase and the reaction of Li and Si at the interface between Li_xSi and Si. As this a-Li_xSi shell grows and thickens, cracks form at the surface of the particle (Figure 2.6c) due to large tensile hoop stress induced by volume expansion of newly lithiated silicon at the interface with the shrinking core. These cracks propagate and lead to the pulverisation of the Si particle (Figure 2.6d).

Although Li reacts with Si and transforms into several distinct Si-Li crystalline phases at high temperatures [111], the electrochemical lithiation of Si at room temperature results in an a-Li_xSi phase, where x is approximately 3.5 [112–115]. Moreover, studies have shown that below a potential of about 50 mV vs. Li/Li^+,

amorphous Li_xSi transforms to crystalline $Li_{3.75}Si$ [115]. However, the alloying or insertion of such amount of Li is accompanied by volume expansion of up to 300 % [114], which leads to the huge stress developments that can cause electrode material fracturing and pulverisation, which results in loss of electrical contact and rapid capacity fading within the battery (Figure 2.7).

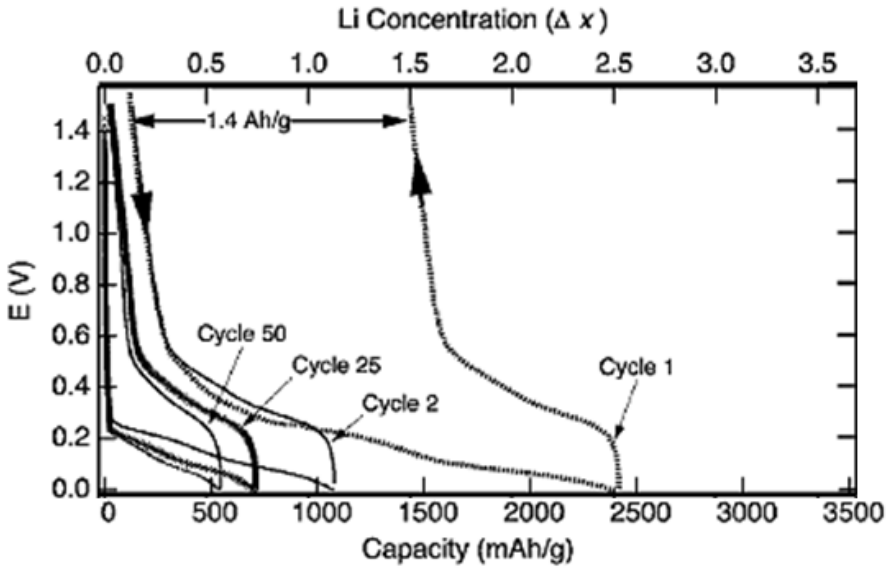

Figure 2.7. Voltage profiles from a silicon electrode showing a huge irreversible capacity losses after the 1st cycle and up until the 50th cycle. Reproduced with permission from [116]. Copyright (2003), The Electrochemical Society.

Numerous strategies have been proposed to mitigate these failure mechanisms in Si electrodes; for example: nanostructured Si materials, such as nanowires [117–120] and carbon-coated nanocomposites [121–124]; conductive and self-healing polymer binders [125,126]; modified cycling protocols [114]. Although nano-sized Si materials have been shown to mitigate the severe fracturing associated with lithiation-induced volume expansion, their high production cost, poor first- and later-cycle Coulombic efficiency, and significant solid electrolyte interphase (SEI) formation still remain major drawbacks to their use in commercial battery applications. Therefore, the use of low cost, more readily available Si microparticles as electrode materials appears promising. However, a clear understanding of the degradation and failure of Si microparticles during battery operation is crucial.

2.3.3 Lithium

Compared to graphite-based negative electrodes used in commercial rechargeable lithium (Li) batteries, metallic lithium offers several advantages: Li has an extremely high specific capacity of 3800 $mAhg^{-1}$ which is ten-fold higher than that of lithiated graphite (372 $mAhg^{-1}$), and it also has the lowest negative electrochemical potential (-3.04 V vs. the standard hydrogen electrode [127]). However, Li metal suffers severe safety and efficiency challenges that have prevented its use as a negative electrode in commercial rechargeable Li batteries. Many of these challenges are associated with morphological changes that occur on the lithium metal surface upon repeated charge-discharge cycling in non-aqueous electrolyte, which lead to the growth of dendritic deposits [Figure 2.8(a)] across the electrode surface that can result in battery short circuits [19,128,129], which are potential fire hazards.

Since the observation of the phenomenon in the 1960s [130], strong efforts have been dedicated to mitigate the growth of dendritic lithium. Various strategies, such as the use of solid polymer electrolytes, separators and ceramic coatings [131–134], liquid electrolyte additives [135,136] and Li metal surface passivation [137] have been developed to mitigate dendrite growth and moss formation. However, these approaches are currently not completely fail-safe, and therefore, a detailed understanding the mechanisms of how these dendritic microstructures form as well as the conditions under which they can occur in a working battery cell is imperative for developing a definite solution to the problem of dendritic growth.

There is, so far, only limited understanding of lithium dendrite growth behaviour but some key observations have been made from previous studies:

1. Electrodeposition of dendrites can result in the isolation of metallic lithium or formation of ‘dead’ lithium crystals [138,139], as described schematically in Figure 2.8(b).

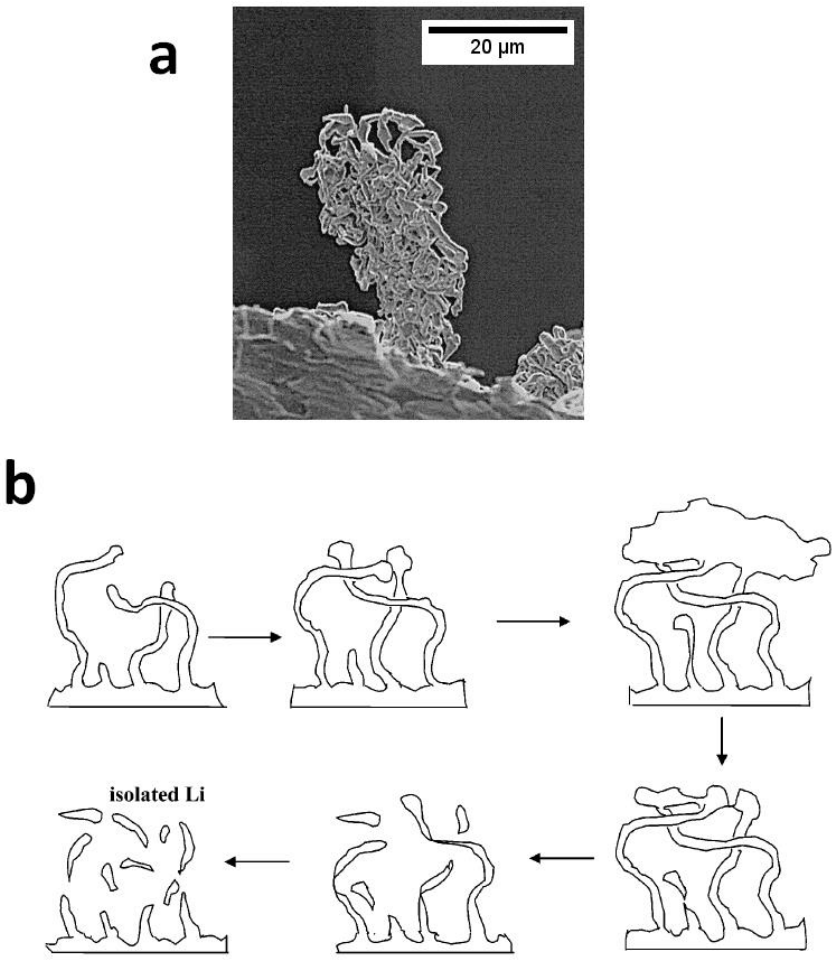

Figure 2.8 (a) SEM image of a lithium dendrite. Reproduced with permission from [140]. Copyright (1998) Elsevier Science. (b) Schematic description of isolated lithium of the formation of isolated lithium particles. The uneven dissolution of dendrites leaves lithium crystals detached from the lithium substrate. The isolated lithium crystals become electrochemically dead but chemically reactive due to their high surface area. Reproduced with permission from [90]. Copyright (2004) American Chemical Society.

2. The SEI layer on the lithium, particularly its homogeneity, plays an important role in dendrite growth [141,142]. It is argued that an intrinsically non-uniform nature of the SEI layer at the nanometre and micrometre length scales causes localised deposition and dissolution at parts of the SEI that have higher ion-conductivity due to their smaller thickness or greater ion-conductive composition, leading to stress development between the shape-shifting lithium layer and the SEI above it. Moreover, during lithium dissolution, the inhomogeneous distribution of current causes the formation of deep pits across the lithium surface, which can serve as active sites for dendritic growth.

3. Besides filamentous dendritic growth, bush-like or mossy lithium can also form at low currents and have been observed to grow from their roots rather than at the outermost tip [135,143], in contrast to existing growth models.

2.4 3D microstructural characterisation of LIB electrodes

There is a clear need to understand the relationship between electrode microstructure and macroscopic performance of LIBs; however, historically, this relationship has been poorly understood. This limited understanding is compounded by the fact that electrode microstructure is liable to physically evolve during operation, which could lead to degradation and failure of the electrode and ultimately the entire battery.

To this end, a variety of characterisation techniques have been employed to investigate the microstructures within LIB electrodes. Over the past two decades, numerous microstructural examinations have been performed on LIB electrode materials using various microscopy techniques such as optical microscopy (e.g. [13,14,144,145]), scanning electron microscopy (e.g. [146–149]), transmission electron microscopy (e.g. [16,150,151]) and atomic force microscopy (e.g. [87,152–154]) in order to reveal their morphology and study microstructural evolution and degradation mechanisms. With these high resolution surface techniques, it is possible to resolve electrode microstructural features which could range from tens of nanometres to tens of microns in size, thus providing a wealth of qualitative information on the electrode materials.

These tools, however, are limited in their ability to provide accurate quantitative information on inherently three-dimensional microstructural parameters that influence Li^+ ion transport behaviour, such as tortuosity and phase connectivity within the electrode pore network. Such geometrical properties directly influence the performance of the electrode in the cell, thus motivating material microstructural studies in three dimensions. Moreover, volume changes and degradation that occur as a result of electrochemical lithiation / delithiation within the electrodes during battery operation cannot be accurately visualized and quantified using two-dimensional imaging tools.

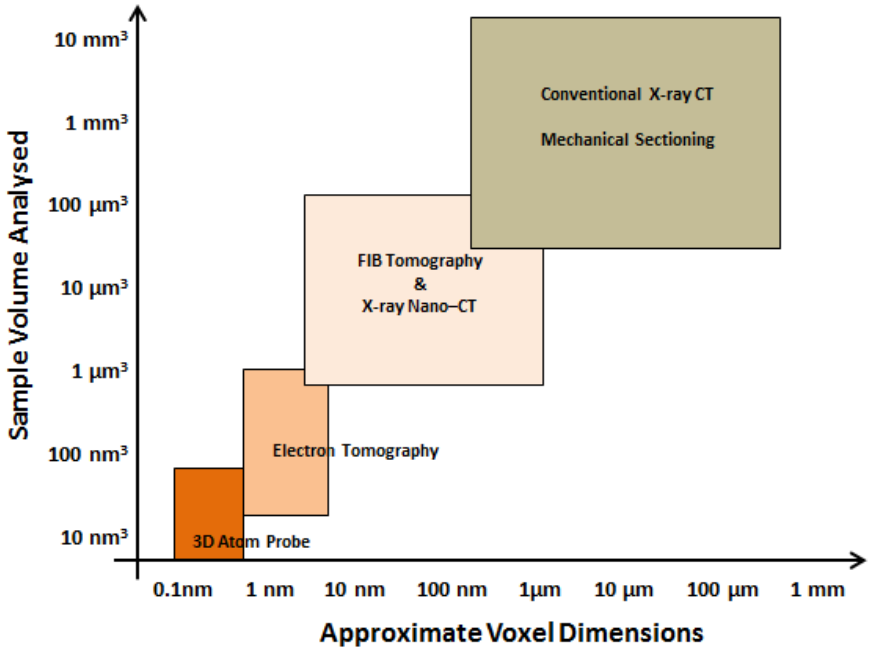

Figure 2.9. Graphical representation of the resolution and typical volume analysed per experiment for modern tomographic characterisation techniques. Adapted from [155].

The proliferation of tomographic imaging techniques has made it possible to characterise the microstructure of an extended range of materials in three dimensions with remarkable resolution. The term 'tomography' derives from the Greek word '*tomos*' which translates to slice or section, and 'graph' to image. In its general meaning, tomography is the technique used to obtain a 3D image of an object through acquisition of transmitted or reflected images by illuminating the object with a penetrating wave from multiple varying directions [156]. Figure 2.9 shows some tomography techniques, demonstrating their potential for application based on achievable spatial resolution.

The choice of any of these tomography techniques depends primarily on a balance of the sample volume to be characterised and the corresponding resolution necessary to resolve relevant features of interest; other factors to be considered include the sample properties such as such as its X-ray attenuation coefficient or the rate of ion beam milling, and the preservation of the analysed sample. Figure 2.10 classifies the various tomographic imaging tools by their spatial resolution capabilities and their invasive or destructive ability.

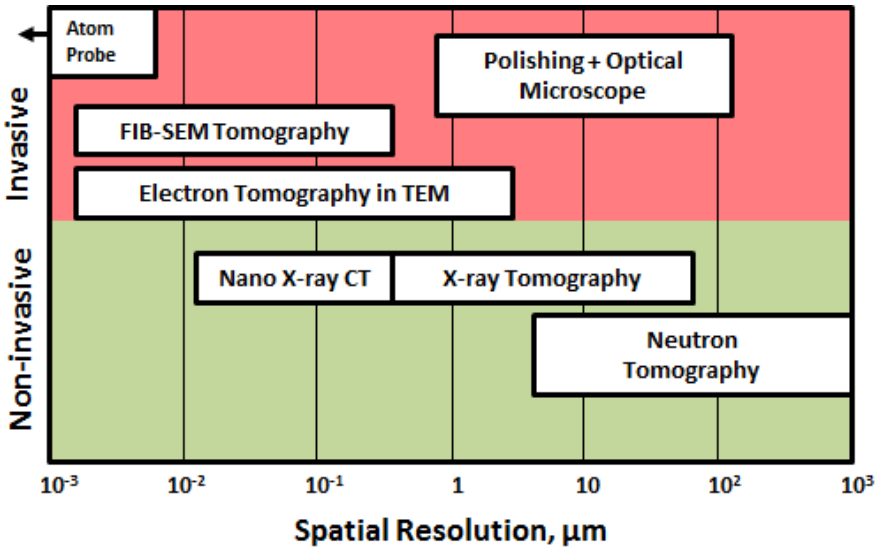

Figure 2.10. Comparison of tomographic imaging techniques for invasive and non-invasive analyses at various spatial resolutions.

The choice of tomography technique is therefore application specific, and employing more than one technique can provide complementary information and aid validation of results [33]. The most commonly applied of these 3D imaging techniques for obtaining real configuration of LIB electrode microstructures are FIB-SEM tomography (which combines focused ion beam (FIB) milling and SEM imaging) and X-ray computed tomography (X-ray CT).

2.4.1 FIB-SEM tomography

Detailed reviews of the theory, recent developments and applications of FIB-SEM tomography can be found in Uchic *et al* [157] and Zaefferer *et al* [158]. FIB-SEM tomography, also known as 'slice-and-view', is accomplished by the serial acquisition of two-dimensional images at different depths in a structure on the base of surface-SEM. The FIB instrumentation, schematically illustrated in Figure 2.11, incorporates the functions of a conventional SEM with a focused gallium ion beam. By positioning both electron and ion beams at eucentric coincidence, the specimen is repeatedly milled (ablated) with the focused Ga^+ ion beam and each newly produced block face is imaged with the SEM, followed by a digital reconstruction of the images. The acquired 2D images are then aligned and superimposed in order to generate a 3D volume. The FIB milling process can be repeated *ad libitum* allowing 3D analysis of relatively large sample volumes with an edge length of several micrometres [159]. The functionality of FIB systems is not limited to serial sectioning with standard ion/electron imaging –

they can be retrofitted to accommodate additional detection systems for combined or simultaneous analyses e.g. energy dispersive spectroscopy (EDS), electron back scatter diffraction (EBSD) and secondary ion mass spectroscopy (SIMS).

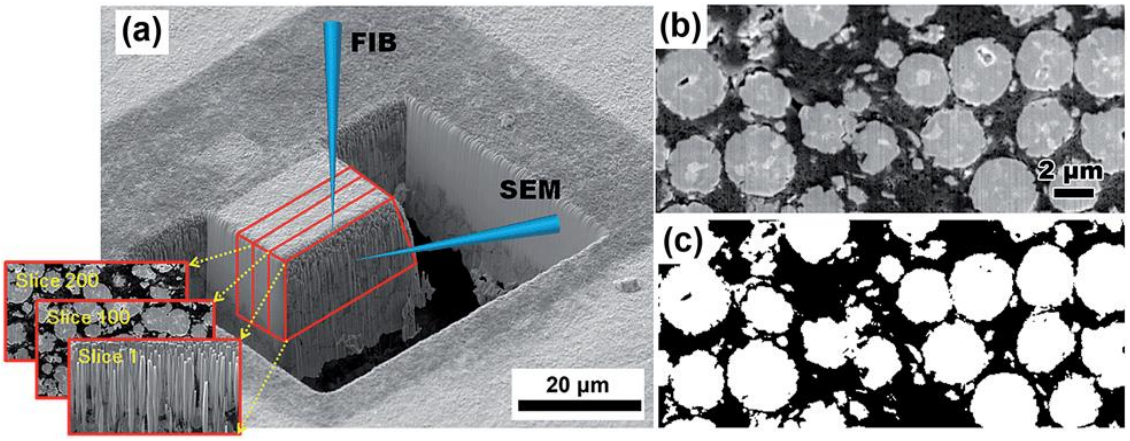

Figure 2.11. (a) SEM image showing a FIB-SEM configuration and a milled trench formed within a LIB electrode sample. (b) A cross-sectional SEM image of the electrode sample taken after FIB milling, and (c) the corresponding segmented image. Reproduced from [160], with permission from The Royal Society of Chemistry.

The use of FIB tomography is popular in the semi-conductor industry, as well as in the fields of biology and material science. Typical resolutions (i.e. voxel sizes) that can be achieved with the FIB tomography are in the range of tens of nanometres down to 5 nanometres, thus rivalling resolutions provided by X-ray tomography or by other serial sectioning techniques [161]; with such resolution, FIB techniques can be valuable for studying individual morphologies of particles within LIB electrodes.

FIB-SEM tomography has been used to study LIB microstructure: Wilson *et al*. used the FIB-SEM approach to provide the first quantitative 3D microstructural data of the $LiCoO_2$ active phase in a fresh commercial LIB positive electrode and were able to resolve in great detail, the irregular shapes and significant internal cracking of individual micrometre-sized $LiCoO_2$ particles [23]. With sufficient contrast, Hutzenlaub *et al*. however were able to identify three individual phases: active particles, pores, and the carbon black/binder mixture in a reconstructed fresh $LiCoO_2$ electrode [22]. Ender *et al.* also identified the particle, pore space and carbon black/binder phases but for a porous composite electrode containing nanometre-sized $LiFePO_4$ particles. [8].

There are, however, some limitations to the application of FIB tomography techniques. FIB-SEM is a destructive technique (Figure 2.11), as slices of the investigated material are physically milled away by the focused-ion beam, thus

restricting the use of FIB tomographic imaging in studies that require tracking temporal evolution of microstructural morphology in the same material sample. Moreover, the rate of ion beam milling of a material sample is a function of the stopping distance of the milling ions within the material; for instance, graphitic structures absorb the Ga^+ focused-ion beam energy resulting in slow milling thus hindering the acquisition of sufficiently large sample volumes within reasonable amounts of time. Shearing *et al.* recognised these limitations of FIB-SEM tomography to generate high resolution images of a graphite electrode material in a LIB and instead, used X-ray computed tomography (CT) to reconstruct the graphite structure [26].

2.4.2 X-ray computed tomography

Due to its penetrating nature, X-ray radiation has achieved extensive use in imaging applications, and this makes it well suited for 3D imaging by tomography [162]. Unlike X-ray radiography which generates 2D image information based on the measurement of the amount of X-ray transmission through an object, X-ray computed tomography (X-ray CT) is an imaging technique that employs digital geometry processing to generate or reconstruct a 3D image of the internal structure of an object from a series of 2D X-ray projection images (or radiographs), which are recorded as the object is rotated about a single axis perpendicular to the X-ray beam. A schematic illustration of the basic principle of X-ray CT is presented in Figure 2.12.

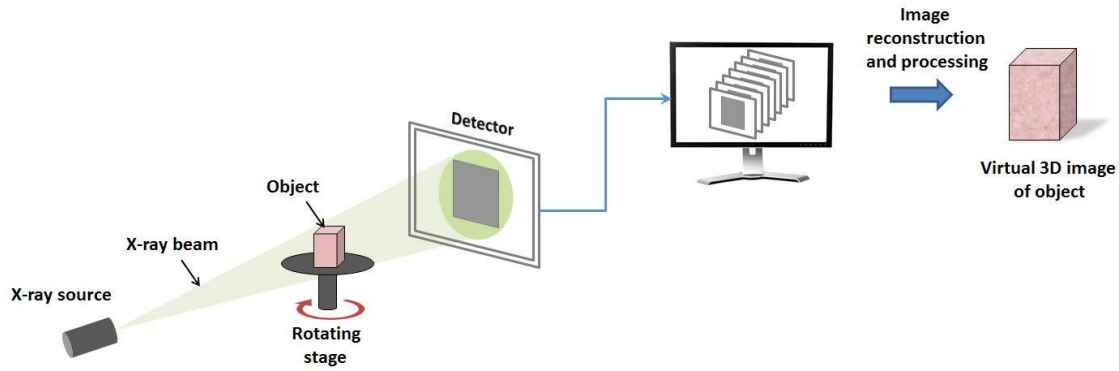

Figure 2.12. Schematic illustration of the principle of X-ray computed tomography.

When X-rays are incident upon an object, they are absorbed, transmitted or scattered. In standard X-ray CT, the 2D projection images (typically several hundred projections) are progressively obtained by passing a beam of X-rays from an X-ray source through the sample object as it is rotated at certain angular increments. The transmitted X-rays are then recorded by an X-ray detection system, in which it is

converted to visible light by a scintillator; the resulting visible image is then digitized and read out into a computer for further processing. A 3D virtual image of the object is then created by mathematically reconstructing the acquired series of 2D projection images where each *voxel* (volume element or 3D pixel) represents the X-ray absorption at that point.

Conventional X-ray CT (also referred to as *absorption-contrast* X-ray CT or *attenuation-contrast* X-ray CT) is a mode of CT imaging based on the detection of X-ray radiation attenuated by an object. Attenuation is the extent to which X-ray energy is lost in a material. The denser the object is, the more the X-rays incident on it are attenuated according to the Beer-Lambert's law which states that the attenuation is exponential:

$$I(x) = I_0 e^{-\mu x} \tag{2.3}$$

where I_0 is the intensity of the incident X-ray beam, and I is the beam's intensity after passing through a material of thickness x characterised by a linear attenuation coefficient μ (cm^{-1}). In this imaging mode, contrast[1] is dictated by the difference between the linear attenuation coefficient of materials / phases in an object; in other words, the larger the difference in attenuation coefficient, the better the image contrast and the easier subsequent image analysis will be. The linear attenuation coefficient closely relates to the atomic numbers of elements as well as the density and geometry of objects. Moreover, absorption contrast is achieved when the sample being imaged is placed close to the detector. A more extensive review of attenuation–based tomography can be found in References [163,164].

Phase–contrast X-ray CT is a CT imaging mode which is used to increase the contrast between objects with similar X-ray attenuation. In other words, objects with poor X-ray absorption contrast [165]. Phase contrast is achieved when the beam is (partially) coherent and when the sample-to-detector distance is increased in comparison to absorption-contrast imaging [166]. Phase-contrast imaging has been reviewed in detail elsewhere [164,165].

[1] Contrast is a measure of how well a feature can be distinguished from the neighbouring background [164]. Contrast levels are often quantified by either the 'signal-to-noise ratio' or the 'contrast-to-noise ratio', and although the ratios are mathematically different, they provide similar information.

X-ray CT, initially implemented in the field of medical imaging, today has also found application in geology and materials research. For many materials, this technique can, in a non-invasive manner, enable the three-dimensional visualization of their internal structure, and this can even now be achieved at higher spatial resolutions ranging from hundreds to tens of nanometres [167]. Maire *et al*. [165] provide a detailed review of the advances and capabilities of X-ray computed tomography as a diagnostic tool. Compared to FIB-SEM imaging, X-ray CT has several advantages such as sample preservation during imaging, the ability to reconstruct samples that are too delicate or costly to be sectioned, and the capacity to capture temporal changes in material structures through successive 3D image acquisition giving rise to the notion of "4-dimensional" tomography or "4D imaging".

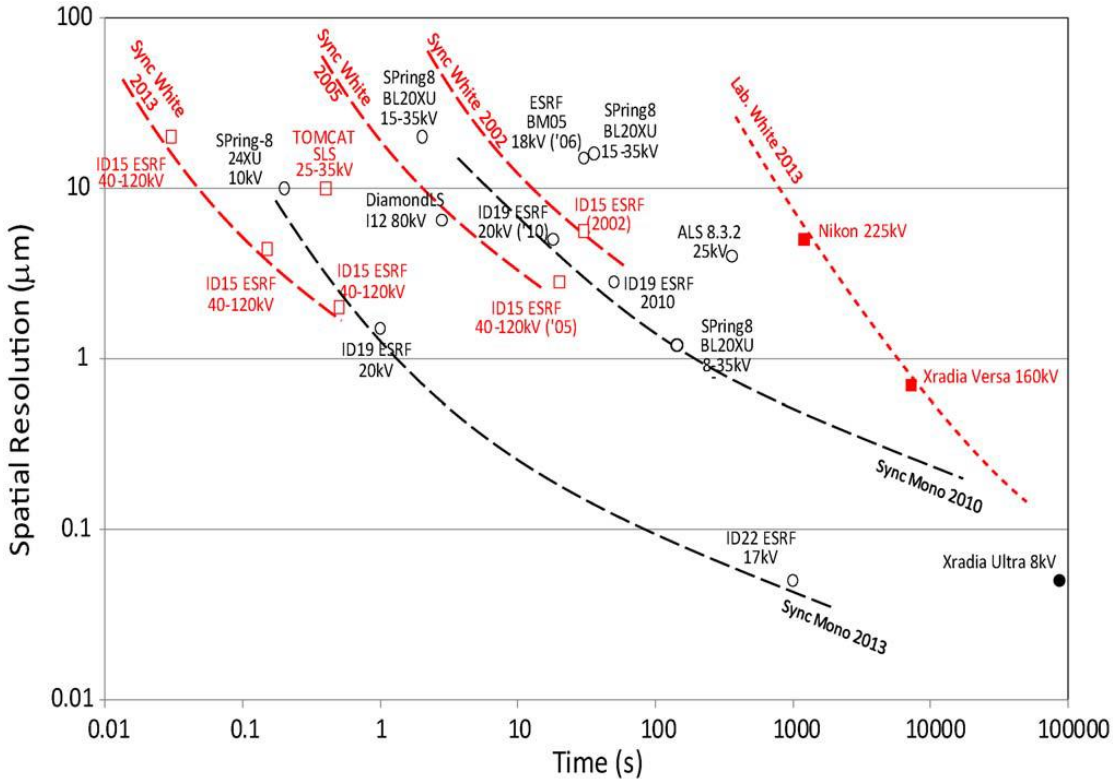

Figure 2.13. Plot of achievable spatial resolution versus scan-frequency of various X-ray CT facilities and equipment. Open symbols indicate synchrotron sources, filled symbols represent laboratory sources, red squares denote white beam and black circles denote monochromatic beam, scanners. Reproduced from [165].

The proliferation of laboratory-based and synchrotron X-ray CT systems has enabled spatial resolutions below 100 nm to be attainable with this imaging technique whilst achieving a high frequency of 3D images. Figure 2.13 compares the resolution and scan-frequency capabilities of various X-ray CT facilities and systems.

In recent years, X-ray CT has been demonstrated to be an invaluable tool for visualizing and understanding the microstructure of LIB electrode materials as well as the temporal behaviour of the microstructure during battery operation and failure. With this imaging platform, battery researchers can now study and even predict the role of electrode microstructure on battery performance. Two reviews by Shearing *et al*. [34,35] discuss the application of X-ray CT as a powerful diagnostic tool for microstructural examination of electrochemical devices including LIBs, highlighting the ability of the tomographic techniques to identify a wide range of physical phenomena.

Shearing *et al*. were the first to publish on the use of X-ray tomography to characterise the 3D microstructure of lithium ion battery electrodes [26]. This study reconstructed a graphite electrode harvested from a fresh commercial LIB using a laboratory X-ray source and demonstrated the potential to use X-ray tomography to study carbon based electrode materials at length scales sufficient to study their microstructures. A cross sectional image slice through the reconstructed graphite electrode is shown in Figure 2.14.

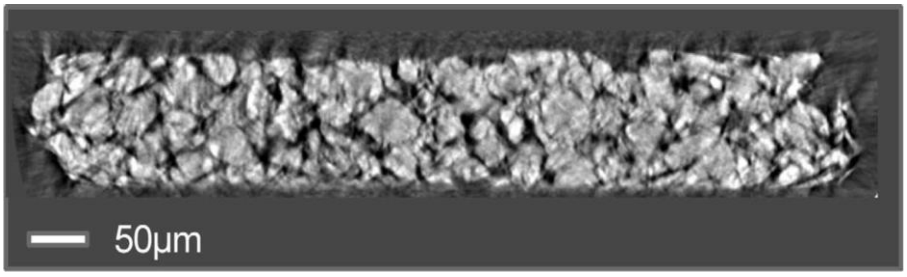

Figure 2.14. Vertical cross section through a graphite electrode obtained from tomographic reconstruction. Reproduced with permission from [26]. Copyright 2010 Elsevier.

Electrode materials with low atomic (*Z*) number can also be captured using X-ray imaging techniques. Using synchrotron nano-tomography, Tariq *et al*. were able to image the 3D micro/nano structure of mesocarbon–microbead (MCMB) based electrodes (having low *Z*-number) at sub-100 nm resolution and with the aid of enhanced contrast labelling, the authors were able to identify binder particles and binder coatings around the active particles [27].

Multiple length scale X-ray tomographic characterisation of LIB electrodes has also become desirable in order to reveal a wealth of microstructural information as it can help provide further insight into the wide range of phenomena occurring in LIBs. In a later study, Shearing *et al*. extracted a range of microstructural information by

examining a commercial LIB positive electrode at different length scales, demonstrating the need for different resolution depending in the physical parameters or properties under investigation [24].

Phase-contrast X-ray imaging has proved instrumental in helping to reveal further microstructural detail in lithium ion batteries, particularly in low atomic number (low *Z*) materials. The proliferation of phase-contrast X-ray imaging modalities [168–172] has helped enhance contrast in X-ray images of weakly absorbing materials by utilizing phase shifts across the incident X-ray beam.

Obtaining accurate and representative 3D information on electrode microstructure and constituent particle morphology can significantly influence understanding of how electrode materials behave during fabrication, during battery operation and even battery failure. Ebner *et al*. used synchrotron X-ray tomographic microscopy to obtain statistically relevant 3D reconstructions of NMC-based cathodes, studying variations in their microstructural properties and electrochemical performance with varying carbon-binder concentrations and different laminate calendaring pressures [29]. Their work also demonstrates the capability of high resolution X-ray imaging for use in the detection of fabrication–induced fracture in micron-sized electrode particles and in examining the inhomogeneous particle size distribution through the electrode. In another study, Ebner *et al*. showed using SXRM that particle shape and fabrication-induced alignment can cause tortuosity anisotropy within electrode materials, which may have an impact on battery performance [173].

X-ray tomographic techniques provide access to detailed microstructural data on the battery electrode materials in three dimensions; however, extending these imaging techniques to explore transient changes in electrode morphology and microstructure gives rise to the notion of '4-dimensional tomography' to study microstructural evolution and degradation processes in the time domain. X-ray tomographic characterisations have been carried out *ex-situ* to directly visualize morphological evolution in LIB electrode microstructure: Chen-Wiegart *et al*. performed an *ex-situ* investigation on the degradation mechanism of $LiVO_2$ electrode material by using synchrotron X-ray nano-tomography to visualize and quantify the 3D microstructure of a $LiVO_2$ composite electrode material before and after oxidation upon exposure to air, and observed crack growth in active material particles as well as

the formation of a low contrast oxidation layer after oxidation of the air-sensitive $LiVO_2$ particles [9]. In an attempt to quantitatively analyse three-dimensional electrode microstructural changes before and after electrochemical cycling, Liu *et al.* obtained multiple three-dimensional image volumes of LCO/NMC electrode materials harvested from different positions in fresh and cycled commercial LIB cells using both FIB-SEM tomography and synchrotron X-ray nano-tomography [33]. However, microstructural inhomogeneities present in the different analysed reconstructed volumes limited the comparison of any microstructural changes in their study. Moreover, the use of different sample volumes to measure microstructural changes *ex-situ* (particularly when using FIB-SEM) can introduce significant error into the analysis, as the statistical differences in material microstructure can often cloud the interpretation of microstructural change [34]. Furthermore, contamination may occur during sample preparation and handling between battery use and characterisation which interrupt *ex-situ* measurements.

Contrary to conventional *ex-situ* methods, *in-situ* and *operando* X-ray tomographic imaging techniques provide the opportunity to directly monitor various physical and chemical changes (e.g. volume changes, phase transitions, side reactions etc.) that electrode materials undergo during battery operation without the need to disassemble the battery, thus offering the ability to directly link these phenomena to the electrochemical behaviour of the battery.

'*In-situ*' in Latin translates to '*in position*' and in the context of battery research, this refers to measurements that are carried out on materials in their original position within a battery or in the relevant environment (for example, in an electrolyte and under bias), thus enabling material characterisation under more realistic and representative conditions. Some *in-situ* experiments do not necessitate battery operation; however, those that do may require interruption of battery operation prior to any characterisation – in this PhD thesis, such experiments will be referred to as 'time–lapse *in-situ*' investigations. *Operando* characterisation is a unique case of *in-situ* experiments where the material of interest is within a battery or electrochemical cell under typical operating conditions, i.e. the battery or electrochemical cell is being (dis)charged during characterisation.

To successfully perform *in-situ* experiments on LIBs, it is required that the batteries or cells must be accommodate any constraints imposed by the diagnostic / characterisation tool being used. A comprehensive overview of *in-situ* investigations on LIB materials using various characterisation techniques has been done by Harks *et al*. [174]. *In-situ* characterisation using X-rays has become a very useful way of examining structural changes in LIB electrode materials. However, one major challenge with this technique, especially for higher resolution studies on electrode microstructure, is that commercial batteries are often encased in materials having high X-ray attenuation such as steel, preventing adequate exposure of battery electrodes / innards to the X-rays.

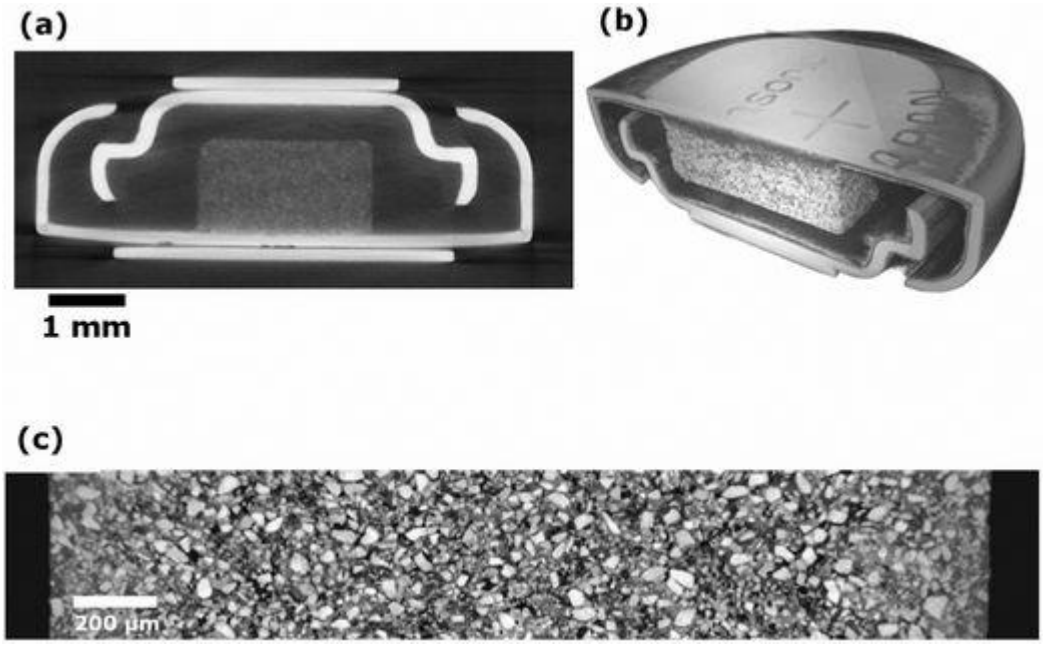

Figure 2.15. (a) A vertical cross-sectional slice through an X-ray tomogram of the commercial MnO_2/LiAl coin cell battery used by Eastwood *et al.* [175], showing the cell architecture. Although the steel casing is in strong contrast, the electrode geometry can also be clearly resolved. (b) A cut-away rendered image of the reconstructed cell, showing the MnO_2 cathode attached to the positive (uppermost) battery terminal. (c) At higher resolution, the virtual slice shows the MnO_2 electrode and particles. Reproduced with permission from [175]. Copyright (2013) John Wiley and Sons.

Eastwood *et al.* successfully conducted an *in-situ*, high resolution 3D X-ray microscopy study on a functionally complete rechargeable lithium battery cell before and after cell discharge [175]. Without the need for cell modification, the uniquely

small geometry of the commercial coin cell battery housing (*ca.* 4.8 mm wide, 1.45 mm thick) made it suitable for such high resolution imaging microstructural studies (see Figure 2.15), and enabled the authors to quantify and map lithiation-induced dilation of active particles in a composite manganese oxide cathode in three-dimensions. However, such level of microstructural detail achieved in this study will be much more challenging to achieve using much larger, ubiquitous commercial cell geometries such as the cylindrical 18650 and coin shaped 2325 designs without implementing modifications to the original battery cell design.

This challenge has spurred the design and fabrication of bespoke electrochemical cells / batteries with X-ray transparent packaging / windows which facilitate high X-ray penetration through the sample of interest whilst keeping the cell operational. With X-ray tomographic imaging, cells fabricated for *in-situ* experiments have, so far, been modifications of standard electrochemical cell types used in laboratory battery research; these cells are usually made from X-ray transparent material to minimize absorption of hard X-rays, and have been modified to minimally absorb hard X-rays whilst permitting an unobstructed view of the electrode material of interest through an entire 180° rotation, e.g. polymeric Swagelok cell [176] and capillary tube cell [177]. A conventional pouch cell design has also been used for *in-situ* X-ray tomographic imaging [178], but due to its flat design, measurable angular range for CT is limited to *ca.* 140°.

The development of ever brighter synchrotron facilities has led to faster 3D image acquisition rates thus providing the opportunity for applying *operando* X-ray CT characterisation to study transient processes during LIB operation, degradation and even failure. Ebner *et al*. [176] performed the first *operando* X-ray tomographic investigation on LIBs. In their study, the morphological and chemical composition changes within individual SnO particles during the first (de)lithiation were captured: this involved the acquisition of several sequential X-ray CT images during the course of the electrochemical lithiation and delithiation. The authors were able to track lithiation-induced volume expansion and crack formation within individual SnO particles and also quantitatively link the measured capacity loss within the bulk electrode to the observed electrically disconnected SnO particles.

At the cell level, Finegan *et al*. [179] were able high speed synchrotron X-ray CT (up to 2.5 Hz) and thermal imaging to track the progression of rapid structural deformation during thermal runaway and failure of commercial 18650 LIB cells. The approach has provided unprecedented insight into a number of crucial degradation modes (e.g. gas–induced electrode delamination, electrode layer collapse etc.) and enabled evaluation of the effect of current cell architecture and engineering design on battery safety and electrochemical performance.

With ongoing developments in the temporal and spatial resolution of X-ray techniques, coupled with phase contrast and XANES tools, the battery community is progressively becoming equipped to explore the microstructural effects on battery performance in real time.

2.5 Summary

The electrochemical performance of lithium-ion batteries is directly influenced by the microstructure of the electrode materials assembled within them. These microstructures evolve over time and with battery state of charge, thus closely linking microstructural degradation with device lifetime. Despite the clear importance of electrode microstructure in LIBs, there is currently only a limited understanding of these inherently three-dimensional structures and how they evolve upon manufacture, and during battery operation and failure.

The recent rapid development of X-ray CT techniques has enabled characterisation of the microstructure of a wide range of electrode materials in three dimensions with remarkable resolution. The non-invasive and non-destructive nature of X-rays makes this technique particularly suitable for studying the microstructural evolution that occurs in LIB electrodes, even at multiple length scales. However, there are only a few studies in the literature that have been reported to apply 3D X-ray characterisation techniques to investigate microstructural evolution during battery operation, especially at the micrometre and nanometre length scales. This is mainly because rechargeable lithium batteries are often encased in materials with high X-ray attenuation which prevent adequate exposure of battery electrodes/innards to the X-rays, and thus requiring the development of miniaturized version of LIB cells which, in itself is non-trivial.

This work aims to apply X-ray CT techniques at multiple time and length scales in provide insight into the microstructural evolution that occurs LIB electrodes during battery operation and ageing.

Chapter 3

Experimental Methods and *In-situ* Cell Development

As discussed in the previous chapter, electrodes in LIBs possess complex microstructures which play a critical role in determining battery performance, especially as these microstructures evolve during battery operation, degradation and even failure. This work aims to use X-ray CT techniques to characterise the 3D microstructure and morphology of LIB electrodes in order to gain insights into their microstructural degradation. This chapter presents the experimental methods and techniques used in sample preparation and characterisation in this research work. The general procedures for electrode preparation and electrochemical testing which are later applied in subsequent chapters are introduced. Techniques and tools used for electrode microstructural characterisation and image-based quantification are also described. In addition, the design and development of an *in-situ* electrochemical cell suitable for 3D microstructural evolution studies using X-ray CT is presented.

3.1 Electrode preparation

In the course of this research work, electrode laminates or coatings were either obtained as ready-made laminates from a commercial supplier or were prepared directly from mixing and drying electrode slurries in the laboratory.

Figure 3.1 shows a general workflow for the preparation procedure of the electrodes studied in this research. Electrode laminates used in the studies reported later in this chapter (for development of X-ray transparent *in-situ* cells) and in Chapter

4 were commercially sourced. Prior to any cell assembly, all commercially-made electrode laminates that were used in electrochemical tests were dried under vacuum at 80 °C for 24 h to remove any traces of moisture.

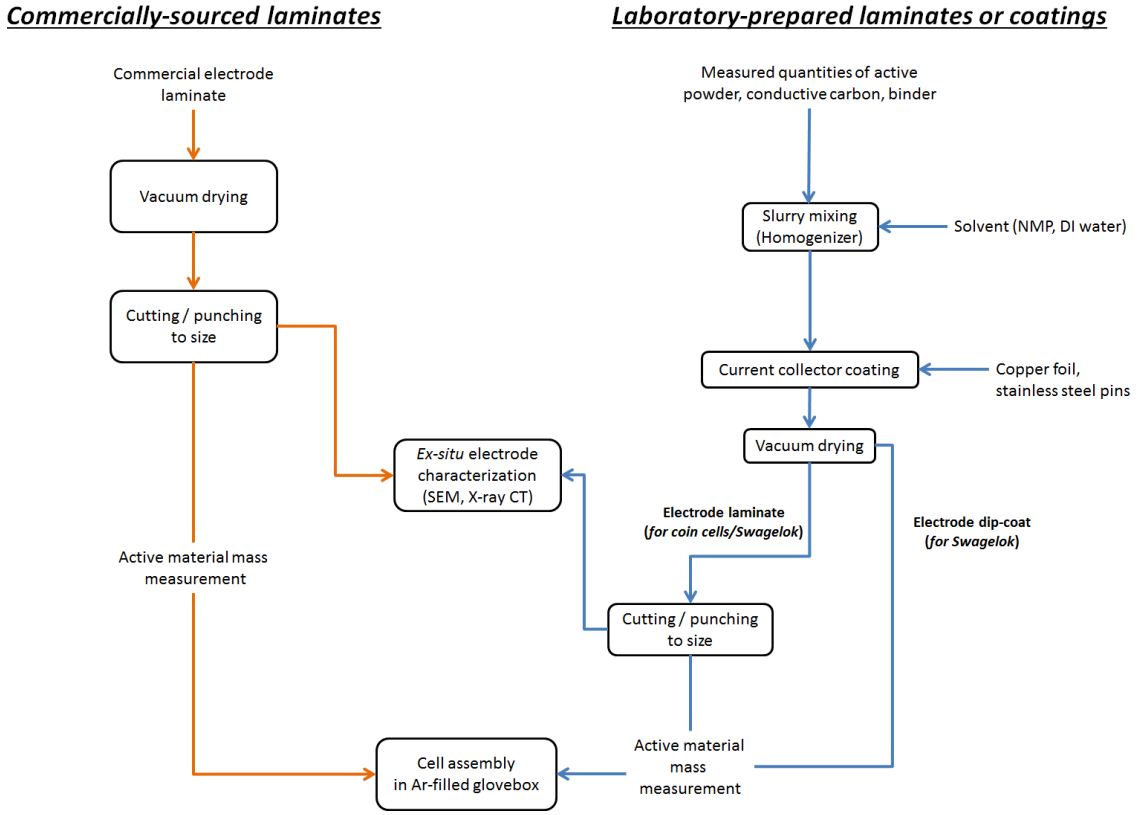

Figure 3.1. General workflow for the electrode preparation procedure.

Electrode laminates and coatings used in the studies reported in Chapters 5, 6 and 7 were prepared by mechanically mixing electro-active materials with conductive additives in powder form; the mixture was subsequently dissolved in a solution containing the binder material dissolved in a solvent to form slurry. In this research work, graphite and silicon-based electrodes are investigated and were prepared in the laboratory, and solvents that were used were N–methyl–2–pyrrolidone (NMP) or de-ionized water. Prepared electrode slurries were then coated onto a current collecting surface. Conducting foils or stainless steel rods were used as current collectors, depending on the cell design. Slurry coating onto current collecting foils was performed using a micrometre adjustable doctor blade and film coater (MTI Corp, USA), while dip-coating was used to apply slurry onto one end of the stainless steel rods.

Surfaces coated with slurry were dried under vacuum to remove any traces of solvent. Dried electrode laminates, separators and metallic lithium chips were cut in

disc shape using circular hole punches. The detailed electrode preparation procedures for each electrode material studied will be discussed in the relevant sections.

3.2 Cell fabrication

For all cell assembly, prepared electrodes and clean electrochemical cell parts were transferred into a glove box with high-purity argon atmosphere (MBraun LABstar, Germany). The O_2 and H_2O levels in the glove box were maintained below 0.5 parts per million (ppm) during use. Electrochemical cells used in the course of the work were either of coin cell type or Swagelok-type geometry, with a two-electrode configuration. Modified versions of these cell geometries were also designed to facilitate *in-situ* and *operando* X-ray tomographic investigations.

2032-type coin cell (CR2032, MTI Corp, USA) and Swagelok cell hardware (PFA-820-6 and PFA-220-6, Swagelok, USA) were cleaned in isopropanol ($\geq$ 99.5 % purity), followed by a 12 h drying at 60 °C under vacuum before use. All cells were assembled with a working electrode (an electrode laminate or coating), a separator soaked in $LiPF_6$-based electrolyte, and a metallic lithium counter electrode. In the two-electrode configuration, the counter electrode also serves as a pseudo-reference electrode, providing data for the working electrode potential versus lithium. Because all the cells in this work were assembled with a lithium counter electrode, they are also referred to as "*half-cells*" in the course of this thesis.

Coin cells were pressure-sealed during assembly using a manual hydraulic crimping machine (MSK–110, MTI Corp, USA) equipped with a 2032-type die at pressures of 1000 – 1200 psi. After cell assembly, the cells were left to sit for at least half an hour prior to any electrochemical testing to allow time for the electrode to be sufficiently soaked with electrode. Swagelok cells were sealed off after assembly by tightening the Swagelok nuts against the (front and back) ferrules in order to create a leak-tight seal on the stainless steel current collecting pins.

3.3 Electrochemical cycling

Electrochemical cycling, or charge–discharge cycling, is a widely used electrochemical technique in rechargeable battery research, in which electric current is controlled and potential is measured. This technique usually involves the application of a current between the positive and negative electrodes of a battery, and the direction

of the current determines whether the battery is being charged or discharged. This applied current is often expressed as a 'C-rate' in the battery industry in order to normalize against battery capacity, which usually varies with batteries.

A C-rate is a measure of the rate at which a battery is discharged relative to its maximum achievable capacity. For example, a 1C rate means that the galvanostatic discharge current applied will discharge the battery within 1 hour; hence, a 100 mAh battery discharged at a 1C rate should deliver a current of 100 mA for 1 hour, a 3C rate for the same battery would be 300 mA for one-third of an hour and a C/5 rate would be 20 mA for 5 hours.

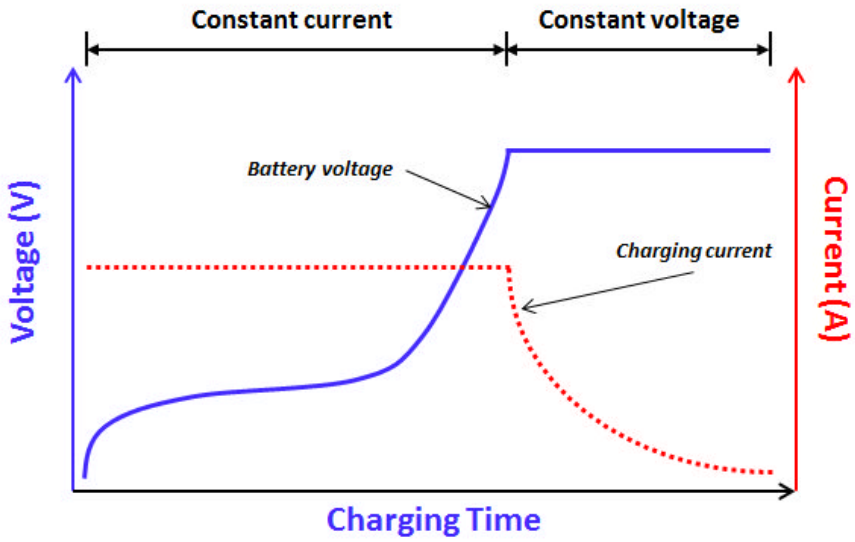

Figure 3.2. Constant current-constant voltage (CC-CV) charging with battery voltage and current response.

A number of charge–discharge cycling methods exist for rechargeable batteries: common cycling protocols in rechargeable lithium battery research include constant current cycling (sometimes referred to as galvanostatic cycling) and constant current-constant voltage (CC-CV) cycling. In lithium-ion battery charging, the CC-CV charging protocol (Figure 3.2) is one of the most often used – it is a two-step charging method in which a constant current is applied across the battery until the upper limit of the cycling voltage window is reached; the charger is then switched into constant voltage mode during which the voltage is maintained at the upper voltage limit while the current decreases exponentially with time. The charging is terminated when the current drops below a specified level, e.g. 3% of the initial current in the constant step. The constant voltage step in the CC-CV cycling protocol is a saturation charge which

boosts the cell/electrode capacity but can also add stress to the electrode material due to high voltage. Others battery charging protocols include: trickle charging, float charging, taper charging and pulsed charging.

In this thesis, electrochemical cycling measurements were performed on the assembled cells either by means of a computer controlled potentiostat (Ivium Technologies, UK) or battery cycler (Maccor 4300 series, Maccor UK). Cell cycling conditions such as charging current or C-rate and cycling potential window for each given study are detailed in the relevant sections. Throughout the research work, all potentials are reported with respect to the metallic lithium voltage (Li/Li^+).

3.4 Material Characterisation

3.4.1 Scanning electron microscopy

Scanning electron microscopy (SEM) is used to reveal surface morphology information on investigated material samples. In SEM, the surface of the sample is scanned in a raster pattern with a focused electron beam controlled by an accelerating voltage using an electron gun. Depending in the penetration depth, the electron beam interacts with atoms at various depths within the material sample, producing signals such as back-scattered electrons (by elastic scattering) and secondary electrons (by inelastic scattering) which can be detected by specialized detectors. These signals are then amplified and displayed as variations in brightness in a computer-generated image. Simultaneous sample analysis can be also done using energy dispersive X-ray spectroscopy (EDS) which uses the detection of characteristic X-rays from the excitation of inner-shell electrons to spatially resolve and perform elemental analysis of the sample.

In the course of this work, SEM imaging was performed using an EVO MA 10 microscope (ZEISS, UK). For SEM imaging experiments in this research work, electrode samples were cut into 0.5 cm wide disks and mounted onto stubs using adhesive carbon tape. Typical SEM parameters used were: working distance 8.5–9 mm, accelerating voltage 5–10 kV, and gun vacuum below 5×10^{-7} mbar.

3.4.2 X-ray CT Imaging

In the course of this research work, LIB electrode microstructural investigations were extensively performed using both laboratory and synchrotron based X-ray CT. Both types of X-ray CT instrumentation are described in the following subsections.

3.4.2.1 Laboratory X-ray CT

In a conventional laboratory X-ray CT setup, X-ray radiation is produced with the aid of an X-ray tube source in which electrons are emitted from a filament (cathode), are accelerated by an electric potential difference and then sharply decelerated upon collision with a heavy metal target (anode) producing Bremsstrahlung radiation (the target is a heavy metal such as Cu, Mo, Ag, or W). Figure 3.3 shows a conventional X-ray tube source. The X-rays produced have a broad ('polychromatic') spectrum and the X-ray flux is controlled by the target material as well as the applied current.

Laboratory X-ray CT instruments are categorized according to their achievable resolution and available field-of-view into *micro*– or *nano–CT* systems.

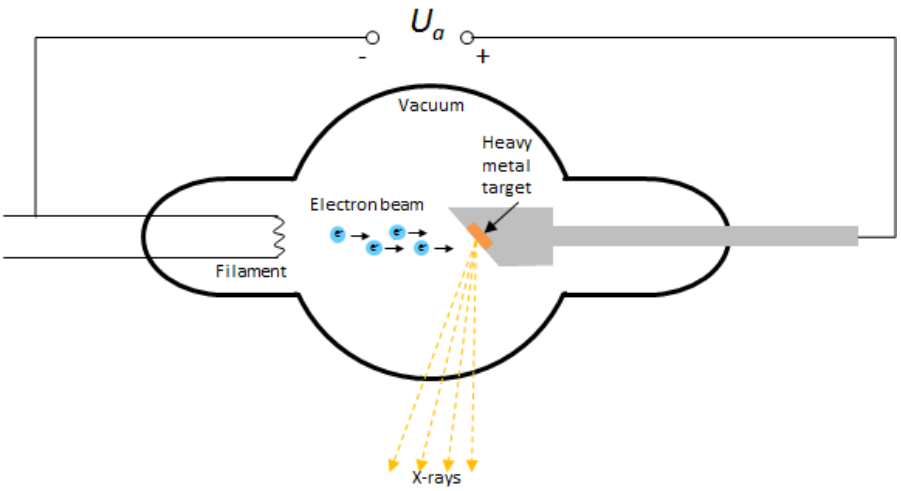

Figure 3.3. Schematic diagram of a conventional X-ray tube.

3.4.2.1.1 X-ray micro–CT systems

An example of an X-ray micro–CT setup is shown in Figure 3.4. Typical laboratory X-ray micro–CT systems employ cone-shaped X-ray beam geometry for which the imaging spatial resolution of the system is determined by the detector pixel size and the focal spot size of the X-ray source (i.e. the size of the region on the target anode material from which the X-rays are created). The X-ray source spot size limits

the resolution achievable for large geometrical magnification[2]. Spot sizes of *ca.* 1 µm are typically achieved in high resolution micro–CT systems which employ microfocus X-ray sources. Detector pixel size can be controlled by using the optical magnification between the scintillator and the CCD detector sensor, and the effective pixel size is a function of the optical and geometrical magnifications.

Phase contrast can be achieved in X-ray micro–CT systems through the use of the in-line (or 'propagation') method [164,165]. In this method, the detector is placed much farther away from the sample than is normal for (absorption) X-ray imaging, with the extent of phase contrast increasing with distance. As illustrated in Figure 3.5, X-rays that are refracted upon passing through an object diverge and interfere with other traversed X-rays at the detector plane, producing detectable fringes in the image at the external and internal boundaries between materials of different electron densities / refractive indices [164]. These fringes produce edge-enhancements at the appropriate sample-to-detector distance, and the amount of edge enhancement is a function of the X-ray source voltage, spot size, detector pixel size, as well as source-to-sample and sample-to-detector distances [180,181].

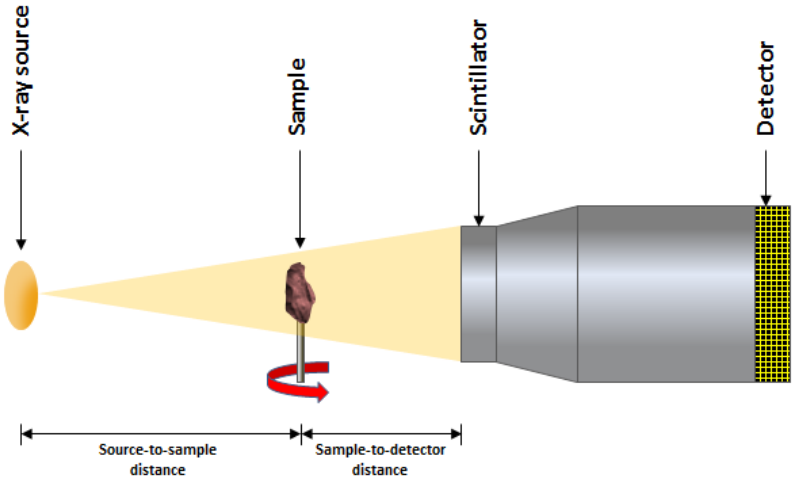

Figure 3.4. An X-ray micro–CT system setup, featuring cone beam geometry.

[2] Geometrical magnification is given by the ratio of the source-to-detector distance and the source-to-sample distance.

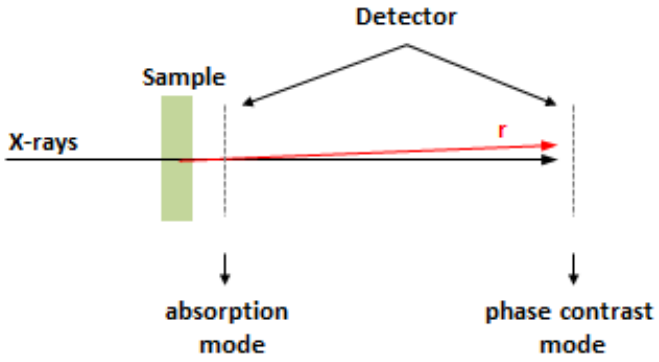

Figure 3.5. Schematic illustration of the in-line method of phase contrast X-ray CT imaging. Images acquired with the detector near the sample are dominated by absorption contrast, but moving the detector further away from the sample allows the interference of refracted X-rays 'r' with transmitted X-rays and edge contrast generation. Adapted from [164].

This type of X-ray imaging requires an X-ray beam with adequate spatial coherence[3]; for a given X-ray energy, high spatial coherence may be achieved by using a small X-ray source spot size (usually the case with laboratory X-ray CT) or by large source-to-sample distances (usually exploited in synchrotron X-ray CT).

In this research work, two laboratory-based X-ray micro-CT instruments were used, namely: ZEISS Xradia Versa 520 (Carl Zeiss Microscopy Inc., Pleasanton, USA) and Nikon XTH 225 ST (Nikon Metrology, Leuven, Belgium). Both micro-CT instruments are equipped with micrometre spot size laboratory X-ray sources with cone beam geometry. The ZEISS Xradia Versa 520 can achieve true spatial resolution to around 700 nm while, with the Nikon XTH 225 ST, resolutions down to 3 µm can be achieved for sample sizes of < 10 mm diameter. For each sample material examined, the accelerating voltage and tube current of the X-ray CT instrument were chosen based on the X-ray absorption coefficients of the samples.

3.4.2.1.2 X-ray nano–CT systems

Current laboratory based X-ray nano-CT systems can achieve resolutions down to 50 nm, using a Fresnel zone plate as the X-ray focusing optical element or objective lens, as shown in the schematic in Figure 3.6. Due to the wavelength dependence of the optical elements, microscope designs for nano-CT systems employ a narrow range of X-ray energies in order to obtain monochromatic, quasi-parallel X-ray illumination.

[3] Spatial coherence is a measure of how divergent is a wavefront is, and with respect to X-ray imaging, it is a function of the X-ray source-to-object distance, wavelength and X-ray focal spot size.

Phase contrast in laboratory based X-ray nano–CT systems is achieved using 'Zernike phase contrast', a method developed by Frits Zernike [182] with initial application in optical light microscopy. In this method, a phase ring (also referred to as 'Zernike' ring) is placed after the Fresnel zone plate (Figure 3.6) which introduces a phase shift between diffracted and undiffracted light from the sample.

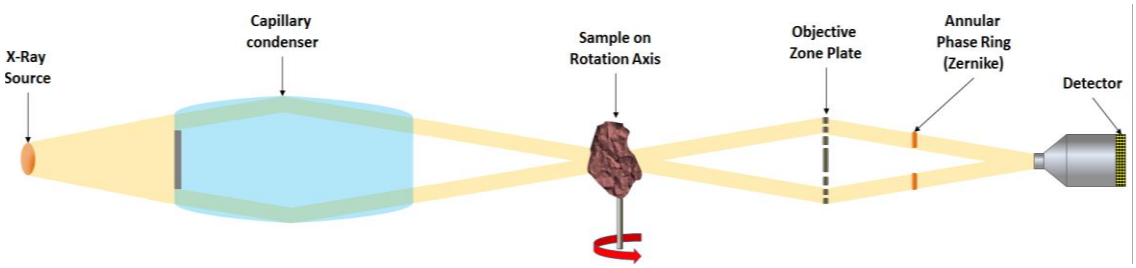

Figure 3.6. Schematic illustration of a X-ray nano–CT system setup.

In this research work, laboratory based X-ray nano-CT investigations were conducted using a ZEISS Xradia 810 Ultra (Carl Zeiss Microscopy Inc., Pleasanton, USA). This instrument can achieve considerably better resolution compared to conventional laboratory X-ray micro-CT, as fine as 50 nm. It also possesses both absorption and Zernike phase contrast CT imaging capabilities to enable non-invasive imaging of a variety of materials at the nanometre scale.

3.4.2.2 Synchrotron X-ray CT

The use of synchrotron radiation as an X-ray source can give enhancements to the quality of imaging that can be performed with X-rays. Synchrotron radiation is the result of bending or steering a high energy electron beam with bending magnets in a continuous circular or ring path. This is done within a series of particle accelerators in a synchrotron light source. A synchrotron light source can generate very high intensity beams of X-rays, infrared and ultraviolet light, called 'synchrotron light'.

The schematic illustration of the layout of a typical synchrotron light source is shown in Figure 3.7(a). Within the linac (linear accelerator), electrons are released in a heated electron gun and propelled using magnets into the booster synchrotron ring. In the booster ring, electrons are further accelerated before being injected into the storage ring; the booster often only works a few times a day to refill the storage ring. In the storage ring, the electrons circle around close to the speed of light, and are forced to release radiation and energy through the use of magnets. The high energy X-rays emitted by the electrons (due to their circular path movement) are then

tangentially projected from the storage ring to be captured and channelled to experimental stations called beamlines for various experimental investigations.

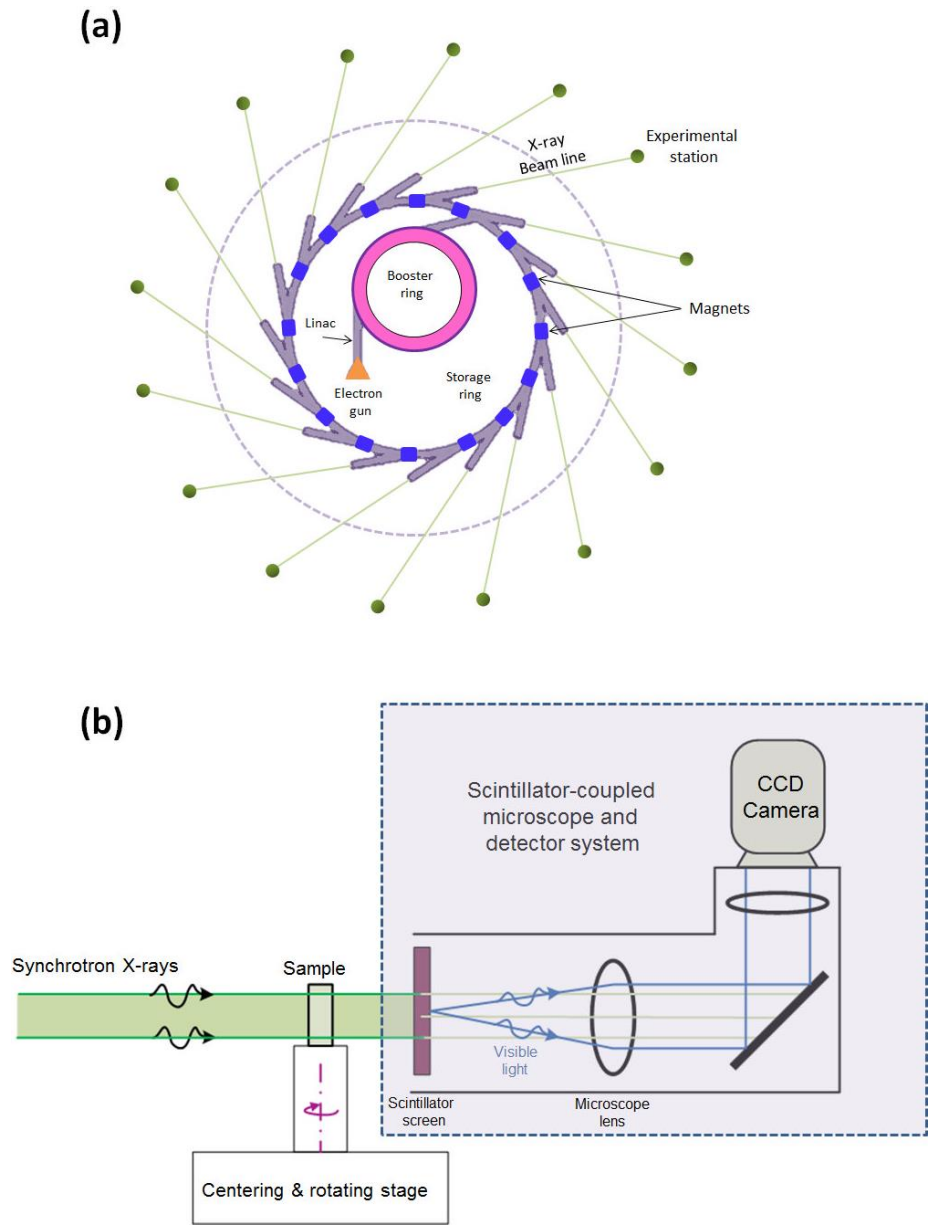

Figure 3.7. Schematic representation of (a) a typical synchrotron, adapted from [183] (b) synchrotron X-ray CT station setup featuring parallel beam geometry.

The use of synchrotron radiation as an X-ray source in place of the conventional X-ray tube has advantages such as:

- Higher X-ray flux (i.e. number of photons per second), which is three to four orders of magnitude higher than that from conventional X-ray generators [184], greatly

improves both image and contrast resolution and thus enabling rapid tomography data collection especially for dynamic experiments.

- High X-ray coherence, which significantly improves phase contrast compared to that obtained with laboratory sources.
- X-ray beam collimation (i.e. small angular divergence of the beam), which eases the tomographic reconstruction.
- The tune-ability of the X-ray energy to a narrow energy band (i.e. beam monochromatization), which offers the possibility of reducing sample radiation dose and beam hardening [185], as well as providing phase identification about material absorption edges (using XANES) [34,186].

Moreover, the parallel X-ray beam geometry employed at synchrotron sources [Figure 3.7(b)] facilitates the implementation of *in-situ* and *operando* experimental rigs since a large sample-to-detector distance can be maintained without loss of intensity in acquired images.

In this thesis, the CT imaging parameters and conditions for each study (both laboratory and synchrotron based) are reported in the relevant sections.

3.4.2.3 Sample preparation for X-ray CT experiments

Before each tomographic imaging experiment, the sample of interest needed to be prepared in a manner that would optimise the quality of the resulting 3D image or tomogram[4]. In this work, X-ray CT experiments were performed on LIB electrode materials under *ex-situ, in-situ* or *in-operando* conditions. *Ex-situ* studies involved imaging of bare electrode samples in their fresh (pristine) state, or after charge-discharge cycling where the cycled battery cell had to be taken apart to extract the electrode sample of interest. *In-situ* and *in-operando* studies involved imaging of the electrode sample within an assembled electrochemical cell.

For *ex-situ* CT imaging studies, electrode samples were carefully dissected with a scalpel into smaller sizes in order to meet the field of view requirements of the X-ray CT instrument being used. This helps produce better imaging results (i.e. higher signal-to-noise ratio and thus better spatial resolution) and reduce CT scan time. Figure 3.8 shows images of electrode samples mounted for X-ray CT experiments and the

[4] In this thesis, a tomogram is referred to a complete 3D image recorded during a tomography scan.

materials used in the sample mounting procedure. Dissected samples were then mounted onto a needle tip coated with two-part epoxy resin (Araldite, Germany) and allowed to set for at least 4 h prior to any CT imaging experiments. Samples prepared for nano-CT imaging were much smaller in size (*ca.* 0.5 - 1 mm tall), compared to those for micro-CT experiments (*ca.* 3 - 5 mm tall), and often required the use of an optical microscope to aid sample mounting. The needle-mounted samples were then placed into sample holders suited to the rotating sample stage of the X-ray instrument.

For *in-situ* and *in-operando* imaging studies, the electrode samples were assembled into bespoke *in-situ* electrochemical cells that enabled adequate exposure of the electrode material of interest to X-rays. After cell assembly, the *in-situ* cells were placed in a sample holder suited to the rotating sample stage of the X-ray instrument. Mounted functional cells were electrically isolated from the rotating stage with electrically insulating tape to prevent any interference that may come from the rotating stage electronics of the CT instrument. More detail on the preparation of each CT sample studied is reported in the relevant sections.

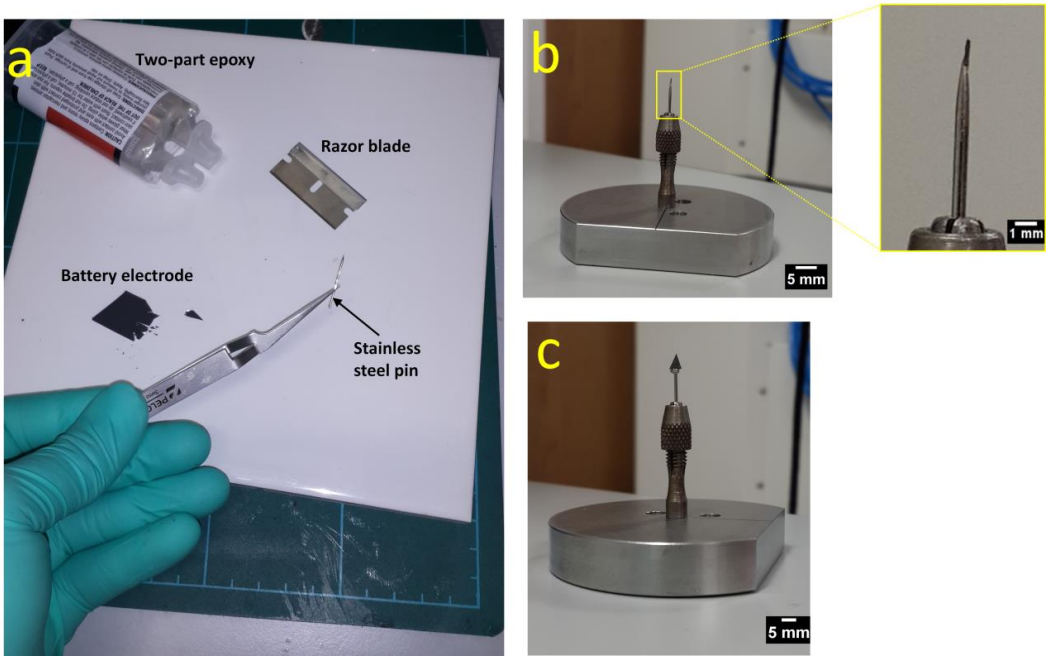

Figure 3.8. Materials used in the sample mounting procedure for *ex-situ* studies. Samples were mounted on the stainless steel pin tip. (b) Electrode sample for nano-CT imaging experiment. (c) Electrode sample mounted for micro-CT imaging experiment.

3.5 Image processing and segmentation

In this work, reconstructed image datasets resulting from the tomographic imaging scans were acquired as a stack of 2D greyscale images in TIFF format. In order to extract 3D image information from within these datasets, image processing and segmentation had to be performed. Here, image processing was used to enhance greyscale image quality and extract regions of interest within an entire 3D dataset, and image segmentation was used to extract features of interest based on the pixel greyscale intensity within the images, in order to generate a 3D model of the features of interest. Figure 3.9 shows an overview of the image data analysis workflow following tomographic image acquisition. All image processing and segmentation operations in this work were performed in Avizo (v9.0, FEI Visualization Sciences Group, Mérignac Cedex, France) and ImageJ image analysis software (http://rsbweb.nih.gov/ij/).

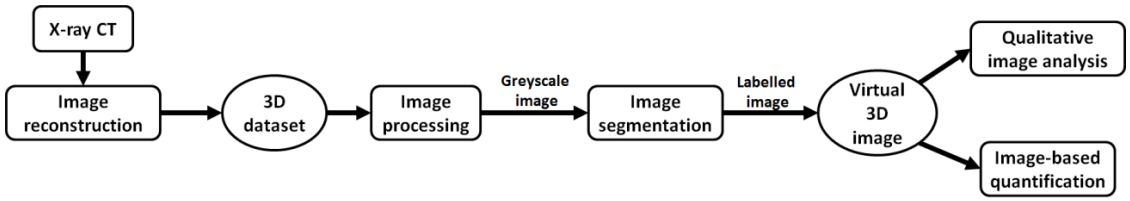

Figure 3.9. Schematic representation of the workflow for 3D image data analysis.

3.5.1 Image processing

Image processing of reconstructed tomographic images involves the enhancement of the image grey-levels and application of image filters [165]. Grey-level modifications could be in the form of greyscale histogram equalization, and adjustments to image brightness and contrast. Prior to image processing, it is common practice to extract the region of interest (a volume containing the features of interest) by image cropping; this is also done to reduce the amount of data to be processed. In some cases, down-sampling of greyscale images (e.g. conversion of images from 16-bit to 8-bit format) is performed to improve ease of data handling and processing of large image datasets.

To reduce background noise or remove unwanted artefacts in the greyscale image datasets collected in this work, digital image filters were applied to greyscale image stacks; this also eases the image segmentation process. However, care was

taken during filter application to ensure that the features of interest were not significantly distorted by the smoothing or de-noising operation of the image filters.

Digital image filters used in this work are the median filter [187] and non-local means filter [188], both of which are available in the Avizo software. Figure 3.10 is an example of the outcome obtained from applying image filters.

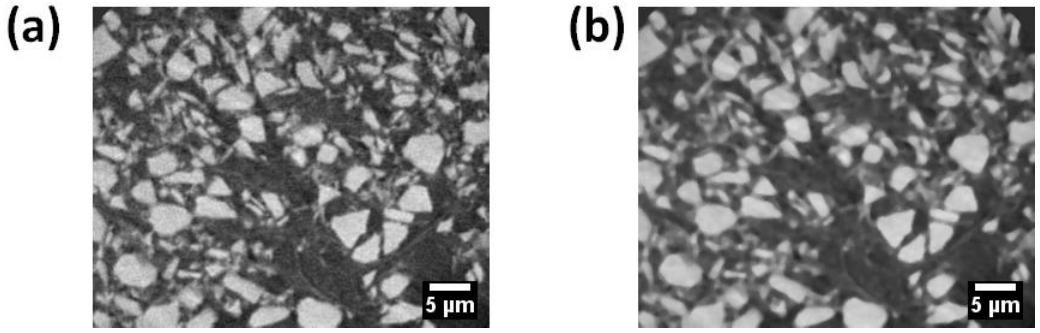

Figure 3.10. An example of filter application to a single reconstructed image slice of a LIB battery electrode to reduce image noise. (a) Original image. (b) Median-filtered image.

3.5.2 Image segmentation

Image segmentation is typically used to identify the objects and relevant boundaries within images. During segmentation, greyscale images are partitioned into homogeneous, non-intersecting regions (i.e. into different materials or phases) by assigning a label to every pixel (or voxels in 3D) in the image such that pixels with the same label share similar greyscale intensity information. For example, a greyscale image of a battery electrode could be separated into a solid phase consisting of electrode particles and a pore/electrolyte phase. For a 3D greyscale image, the output of the segmentation process is a stack of labelled images. Figure 3.11 shows an example of the segmentation process.

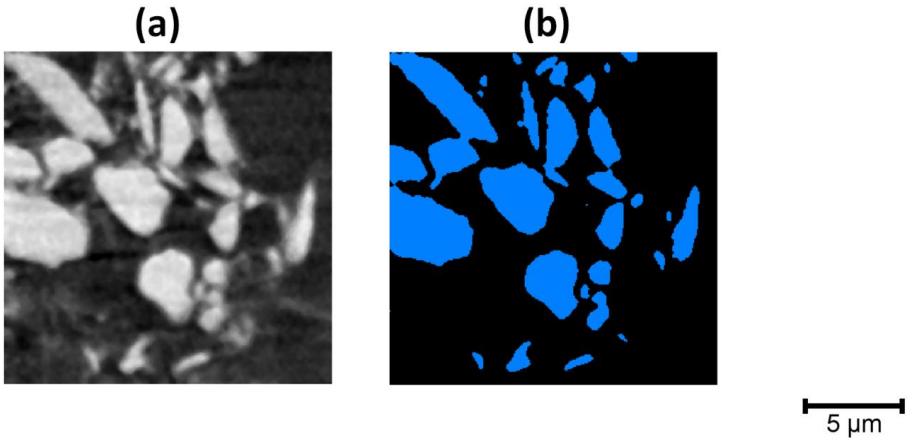

Figure 3.11. Cross-section of reconstructed image (a) before and (b) after applying threshold segmentation to extract the high attenuating particles.

Segmentation was performed using the "Edit Label Field" module in the Avizo software, which provided automatic segmentation tools such as threshold-based segmentation and region-growing for fast and less manual pixel labelling. Any background noise present with similar pixel intensity as the features of interest was carefully removed using label smoothing and island removal filters.

3.5.3 Feature separation and identification

After the segmentation or binarization process, features within the image such as grains or particles that seem to overlap can be separated and individually identified or labelled for further analysis. The feature separation operation can be performed in Avizo software using the "Separate Objects" quantification module (or 'binseparate' module in earlier software versions). The algorithm computes the 3D watershed on the binarized image stack which helps to identify connection lines between features or objects and separates them along these lines. The resulting output image of the process consists of the desirable feature separations, visualized as the outline of each feature. Subsequently, each individual feature is labelled automatically (using a connected component analysis [189]) for 3D visualization or for further analysis.

3.6 Microstructural quantification

After segmenting features of interest within the 3D image volume, microstructural quantification could then be performed on the segmented data in order to extract relevant structural parameters. In this work, key microstructural parameters of interest include phase volume fraction, specific surface area, particle size and size distribution, pore size and size distribution, and tortuosity. These parameters play a crucial role in understanding the relationship between electrode microstructure and performance in lithium-ion batteries. The calculation of the parameters is discussed in the following section.

3.6.1 Phase volume fraction

Phase volume fraction is calculated, using voxel counting approach, as the ratio of the total number of voxels in a particular phase to the total number of voxels in the analysed reconstruction volume. For instance, in a segmented 3D image containing a phase k, the volume fraction of phase k is given by:

$$Vol.frac.\ of phase\ k = \frac{\sum voxels\ labelled\ as\ phase\ k}{\sum voxels\ within\ analyzed\ volume} \quad (3.1)$$

Phase volume fraction is a dimensionless parameter and does not require imaging resolution information to be calculated. With porous materials, the volume fraction of the pore phase is also referred to as *porosity*. Porosity in lithium-ion battery electrodes influences battery electrochemical performance, especially when deciding between high energy and high power battery applications.

3.6.2 Specific surface area

With respect to battery electrodes, this parameter can provide both structural and performance-related information, as the interface between the electrode and the electrolyte serves as the reaction site for charge transfer during battery cycling. Larger surface area can be associated with smaller electrode particle size.

The volume-specific surface area can be defined as the ratio of the total 3D surface area of the sample's solid–porosity interphase to the total analysed sample volume. This microstructural parameter can be used to characterise how finely (or coarsely) a microstructural phase or constituent is dispersed in the 3D microstructural volume. Since specific surface is not a dimensionless parameter (unit: *1/length*), it is essential to know the image pixel resolution for its estimation.

In the segmented images, the 3D surface area was calculated as the area of a triangular surface mesh approximation of the solid phase/porosity interface. This was performed using the '*Surface Area-Volume*' quantification module in Avizo software. Here, a marching cubes algorithm [190] is applied to the segmented image to generate a triangulated surface. In order to capture phase interfaces, the marching cube algorithm in Avizo allows for generating interfaces between multiple segmented phases, and can use sub-voxel weights for surface smoothing. A constrained surface smoothing was applied using sub-voxel weights and with an optimal smoothing extent of 5 in the surface generation step. For this surface area calculation approach, mesh refinement was done and validated against the analytical solution of model image samples.

3.6.3 Tortuosity

Tortuosity, often denoted by τ, is another key structural parameter that is used to account for the complexity and interconnectedness of transport paths in porous

media. In lithium-ion batteries, the tortuosity of the pore phase describes the influence of electrode morphology on lithium-ion transport with the electrolyte. In the literature, the term has been defined from a diffusion transport point of view (as tortuosity factor, τ^2) and from a geometrical point of view [191].

With regards to diffusion phenomena in porous media, tortuosity can be described as the resistance to diffusion as a result of the twistedness of the pore network, and can be related to an effective diffusion parameter as shown in Equation (3.2), where ε represents porosity and D_{eff} and D are the effective and intrinsic diffusivities, respectively.

$$D_{eff} = D\frac{\varepsilon}{\tau^2} \tag{3.2}$$

Geometrically, tortuosity can be calculated using a definition provided by Shen [192] as the ratio of the effective length of a curve (L_e) to the length of the straight line between the curve's end points (L), i.e.

$$\tau = \frac{L_e}{L} \tag{3.3}$$

Throughout this thesis, the geometrical definition of tortuosity is employed. Tortuosity calculations were performed in 3D on the electrode pore phase, along the *x*, *y* and *z* axis directions. Tortuosities were calculated based on an approach presented by Jørgensen *et al.* [193] which involves distance map propagation. As demonstrated in Figure 3.12, a fast marching algorithm [194] is applied to the segmented image to generate a geodesic distance map of the propagating front which begins from a specified source point or starting boundary. After the distance map is created, the lengths of the shortest paths are then obtained from the end plane pixels/voxels. The reader can find more information about using the fast marching method to create distance distribution maps in Jørgensen *et al.* [193]. The tortuosity calculations were implemented using MATLAB.

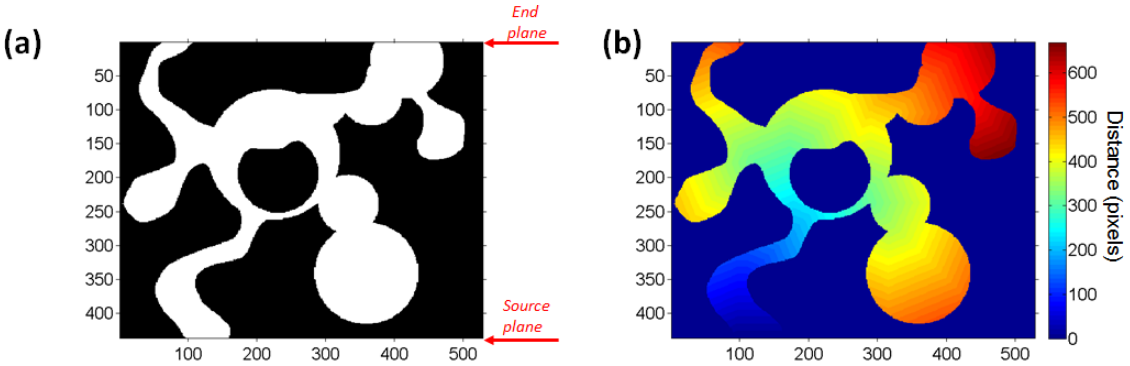

Figure 3.12. (a) A sample 2D binary pore network. White pixels denote the pore network. (b) Geodesic distance map image calculated using the fast marching algorithm. Distance values outside the pore network were assigned a value of zero to increase the contrast between the pore network and the surroundings.

3.6.4 Pore size

From a geometrical point of view, the pore radius for any section of the pore path in the network can be defined as the radius of the largest sphere that can be locally inscribed into that section of the network [193]. For the 3D pore size quantification, a pore radius distribution is usually extracted from the porous volume, from which a mean pore size can be calculated. Various methods exist for extracting pore radius distributions from 3D image volumes; however, in this work, we implement and compare these four methods:

(1) *Medial axis based method using fast marching (MA-FM)*: This method first extracts the medial axis (or skeleton) of the pore network by performing a skeletonization on the 3D pore image with the aid of an interfacial distance map generated using a multi-stencil fast-marching algorithm [195], and then takes the pore radius values assigned by the distance map to every point along the resulting topological skeleton as the distance to the nearest pore phase boundary. For pore radius quantifications on the 3D datasets using this approach in this work, a MATLAB algorithm was implemented that incorporated open-source MATLAB *m*-files for performing general multi-stencil, second-order fast marching calculations [196].

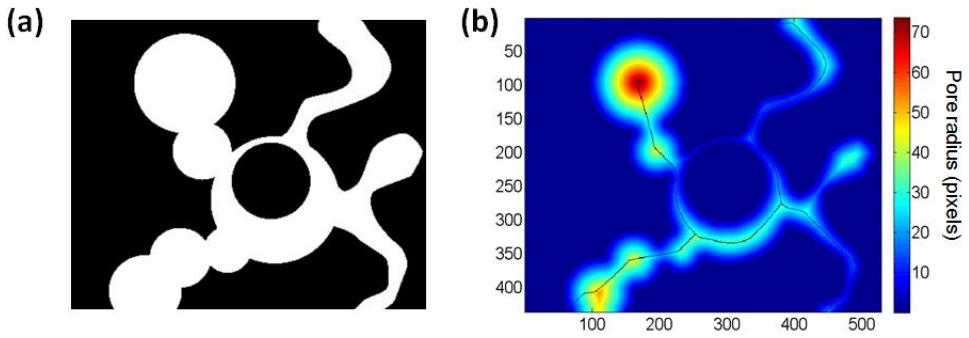

Figure 3.13.(a) A sample 2D binary pore network. White pixels denote the pore network.(b) The interfacial distance map calculated by the multi-stencil fast marching algorithm, with the resulting medial axis (black line) from a topological skeletonization sequence.

(2) *Medial axis-based method using distance-ordered homotopic thinning (DOHT)*: This method [197] also calculates pore radius as the distance from the nearest pore phase boundary to the pore skeleton, but performs the skeletonization by combining morphological thinning and distance map based techniques. First, a chamfer distance map of the 3D pore network is computed, which contains the shortest distance of each point in the pore space to the pore phase boundary, and then the resulting distance map is used to guide a morphological thinning algorithm. This approach was implemented using the Avizo software's 'Auto-Skeleton' module.

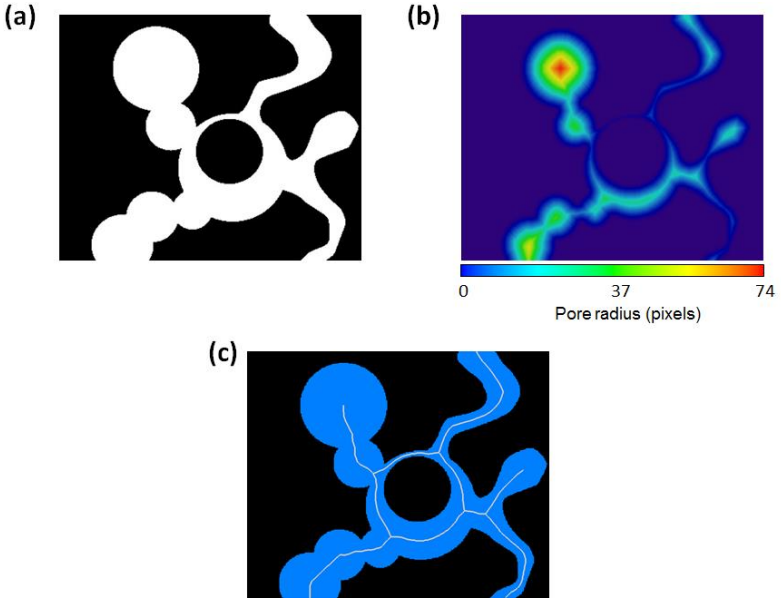

Figure 3.14. (a) A sample 2D binary pore network. White pixels denote the pore network. (b) Interfacial distance map computed by the Avizo 'Auto-Skeleton' module using a chamfer distance transform. (c) Resulting medial axis after morphological thinning guided by the chamfer distance map.

(3) *Successive morphological opening method (SMO)*: This method repeatedly applies the morphological opening operator on the 3D pore space with spherical structuring elements (SEs) of increasing radius [198–200]. Here, the operation of "opening" is a mathematical morphological operation which refers to the process of first eroding, and then dilating an image using a SE. Hence, if a spherical SE of 1 pixel radius is used to 'open' the 3D pore image, the resulting image will only have pores larger than 1 pixel in radius. In this method, the opening operation is repeated with increasing SE size until there are no more pores existing in the 3D pore volume. For each opening operation, the accumulated volume fraction of pores larger than a certain SE of radius *r* can be calculated as:

$$\upsilon(r) = 1 - \frac{\beta(r)}{\beta} \tag{3.4}$$

where β is the sum of the pore phase voxels in the initial 3D volume, $\beta(r)$ is the sum of pore phase voxels in the 3D volume after the morphological opening operation with a SE of radius *r* .

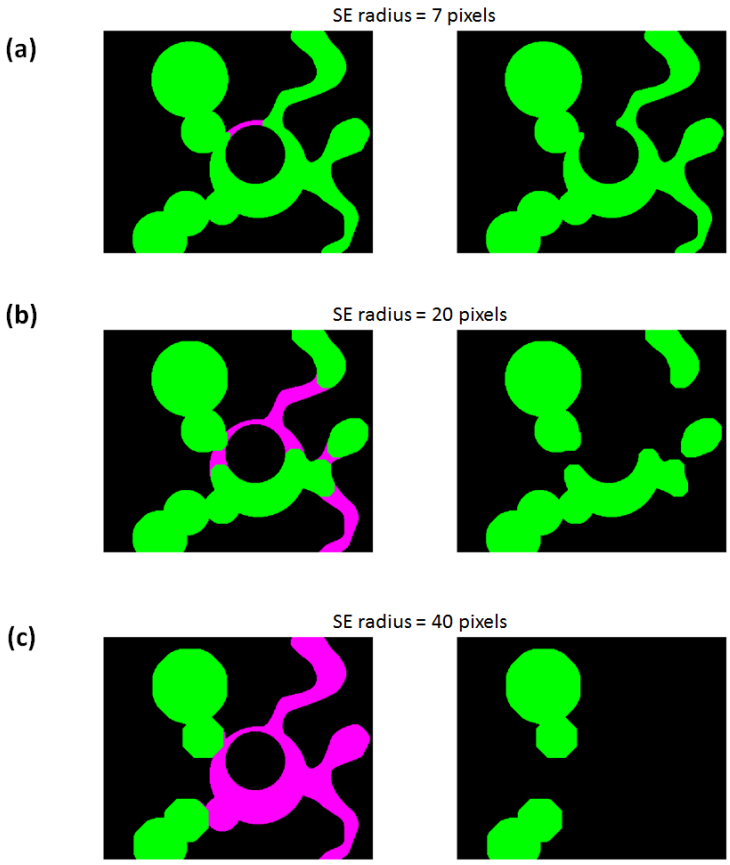

Figure 3.15. Pore size calculations using successive morphological opening. Effect of opening with circular SE of radius (a) 7 pixels, (b) 20 pixels, and (c) 40 pixels.

From this, the volume fraction of pores with a certain radius can be obtained by the difference of two successively accumulated volume fractions. The pore radius obtained using this method is called equivalent radius and it is equivalent to the radius of the maximal inscribed sphere in the pore. In this work, a bespoke MATLAB algorithm which utilized the MATLAB morphological operator function '*imopen*' was created to implement the SMO approach on 3D datasets.

(4) *Continuous pore size distribution method (CPSD)*: The 'continuous pore size distribution' method [201] is based on an algorithm which measures the pore volume that can be covered with a sphere of given radius. This algorithm can also be seen to represent, in this sense, the simulation of a pressure–induced intrusion with a poorly wetting fluid (e.g. mercury intrusion). Here, a continuous pore size distribution is obtained by incrementally reducing the radius and thereby filling a larger volume: by decreasing the radius, more constricted areas such as pore bottle-necks and narrow corners can be intruded. A cumulative PSD is obtained as a result by relating the incrementally filled volume with corresponding radii, which can then be normalized. Here, pore size calculations using the CPSD approach were performed on 3D datasets with the aid of an open-source pore size distribution algorithm implemented as a plugin in ImageJ software [201].

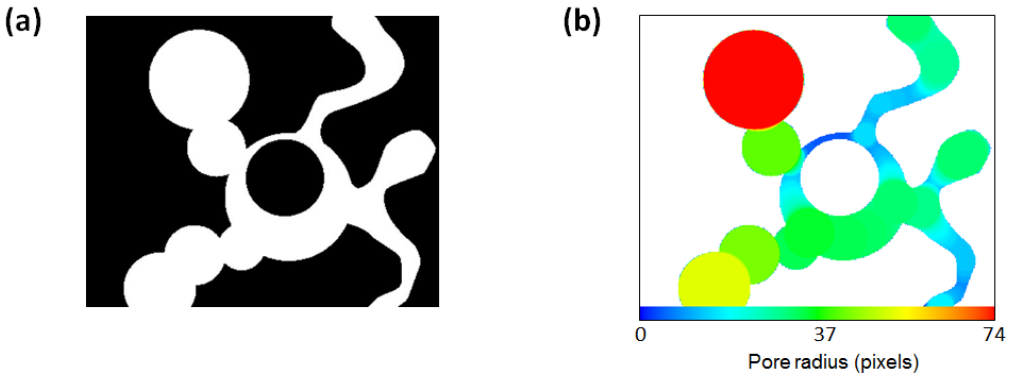

Figure 3.16. (a) A sample 2D binary pore network. White pixels denote the pore network. (b) Resulting pore size distribution image from the 'continuous PSD' simulation which measures the pore volume that can be occupied by a sphere of a given radius. By incrementally reducing the radius, increasingly larger areas of the pore network can be occupied.

3.6.5 Digital Volume Correlation

Digital volume correlation (DVC) is a 3D extension of the 2D digital image correlation (DIC) technique [202,203] which involves the measurement of in-plane displacement and strain fields of small regions of image pixels in two-dimensions. DVC involves tracking 3D changes in microstructural features between two consecutive volumetric images, typically acquired with X-ray micro-CT, and can provide full continuum-level displacement and strain field measurements in the process. Originally proposed by Bay *et al.* [204] in 1999 for strain calculations in trabecular bone tissue under compressive load, the technique has since found extensive application in the analysis of strain in a variety of materials [165], including the microstructure in lithium-ion batteries [175,205].

DVC analysis was carried out in this work using the Python-based software, 'TomoWarp2', which was developed between Universities of Lund and Grenoble and builds on the previously developed code, 'TomoWarp' by Hall *et al*. [206–208].

The procedure for DVC generally entails three main steps:

(1) *Acquisition of 3D volume images of the sample in its initial and deformed states* using X-ray micro-CT, and then digitally reading the volume images into the DVC program.

(2) *Measurement of a 3D discrete displacement vector field of distinct patterns or voxels throughout the sample by a correlation procedure*. Here, a regular 3D grid of discrete measurement points or 'nodes' is defined evenly throughout the CT volume, and a 3D image sub-set or 'correlation window' of user-defined size is centred about each node for the correlation analysis. The displacement for each node is determined by searching for the 3D translation vector, *v,* (Figure 3.17) that maximizes the cross-correlation of the gray-level data with the correlation window in the initial, un-deformed image and the translated correlation window in the deformed image. This initial displacement measurement provides an integer/voxel-level estimate of the displacement, and is used as an initial guess in sub-voxel displacement calculations. Sub-voxel resolved translation vectors are then determined based on the maximum of the interpolated correlation coefficient for a range of displacements around the initial integer value.

(3) *Calculation of the strain tensor field* based on the gradient of the computed displacement vector field over a [user-defined number]-point cubic element of neighbouring nodes.

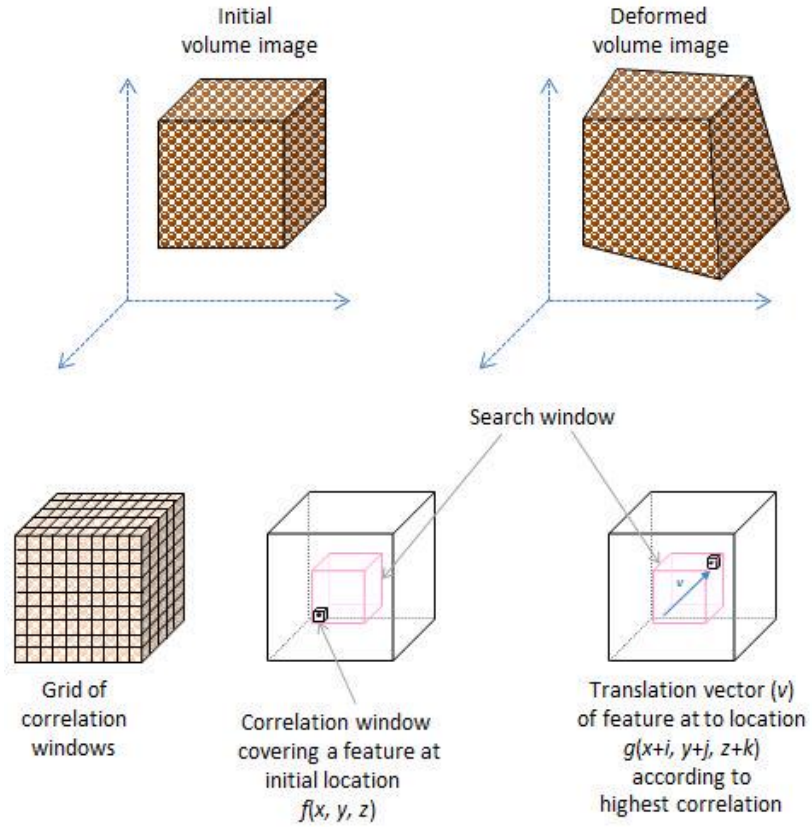

Figure 3.17. DVC correlation process showing the segmentation of a volume image into correlation windows (sub-volumes), followed by an example of a single sub-volume being correlated between the initial and deformed volume image, with the assignment of a displacement vector (*v*) corresponding to the region of highest correlation.

As shown in Figure 3.17, a 3D sub-volume (correlation window) containing a locally discrete pattern or group of voxels and centred at a point of measurement is defined in the initial (reference) volume image. The sub-volume, $f(x,y,z)$ is defined by a set of coordinates centred at the point of measurement (origin). The equivalent sub-volume, $g(x+i, y+j, z+k)$, is found in the deformed volume image, and a translation vector (v) is estimated to quantify sub-volume displacement. A shape function is typically assigned at this step, which allows for some deformation of the initial sub-volume while searching for a high correlation. The degree of match between the grey-level values of each voxel within f and the values within the corresponding voxels of g is defined by an appropriate correlation coefficient (CC), such as the sum of squares correlation or the cross-correlation coefficient [204,209]. An iterative process such as

the Levenberg-Marquardt or the Newton-Rhapson methods is employed for maximization of the CC and extraction of best-fit parameters for the volume correlation procedure. Translation is the main affine transformation of interest that is encompassed by the shape function, as it provides the displacement measurements required for subsequent strain calculations [204,210]. Other affine transformations include rotation, normal strain and shear strain. For more detail on the technique, the reader is referred to Bay et al [204] and Sutton *et al.* [202].

3.7 Electrochemical cell development for X-ray CT imaging experiments

The desire to understand how the structures of electrode materials affect the overall performance of batteries and the complex nature of lithium insertion reactions stimulated the undertaking of *in-situ* studies. Most of the microstructural studies on LIBs using X-ray tomographic imaging have been carried out *ex-situ*, which has usually involved either harvesting a small quantity of electrode material from (a) a freshly prepared electrode laminate, or (b) from a disassembled battery whilst avoiding any oxygen or water exposure or accidental battery short-circuiting, and then rinsing the harvested quantity with organic solvents to remove any traces of electrolyte salts. This approach, however, eliminates any chances of properly visualizing transient, real-time changes in the electrode material structure resulting from battery operation. *In-situ* and *in-operando* investigations involving the use of an electrochemical cell can help provide more accurate insight into electrochemical processes as well as degradation mechanisms that occur during LIB operation than conventional *ex-situ* methods that require cell disassembly.

Designing a stable electrochemical cell for *in-situ* X-ray tomographic imaging and 3D microstructural evolution studies during battery operation and repeated battery cycling is not trivial. One major challenge with this technique is that batteries are often encased in materials having high X-ray attenuation, and this can prevent adequate exposure of battery electrodes/innards to the X-rays. Macro-scale and cell level *operando* X-ray CT investigations have only recently been conducted using commercial Li batteries [179,205]. However, for higher resolution CT imaging studies on battery electrodes down to the particle level, using commercial cells is currently

very challenging. This challenge has spurred the design of bespoke electrochemical cells/batteries with X-ray transparent packaging/windows which facilitate high X-ray penetration through the sample of interest whilst keeping the cell operational. These cells are often modifications of standard electrochemical cell types used in laboratory research.

In this section, the design and development of an *in-situ* electrochemical cell suitable for examining the 3D microstructural evolution of LIB electrodes using X-ray tomographic imaging is discussed. Two *in-situ* cell designs, based on the coin cell-type and Swagelok-type cell geometries, were explored.

3.7.1 *In-situ* coin cell design

In order to conduct 3D X-ray imaging experiments during battery operation, the author initially worked with an *in-situ* battery cell design made by modifying standard 2032–type coin cell hardware. A diagrammatic representation of the modified cell design is shown in Figure 3.18(b).

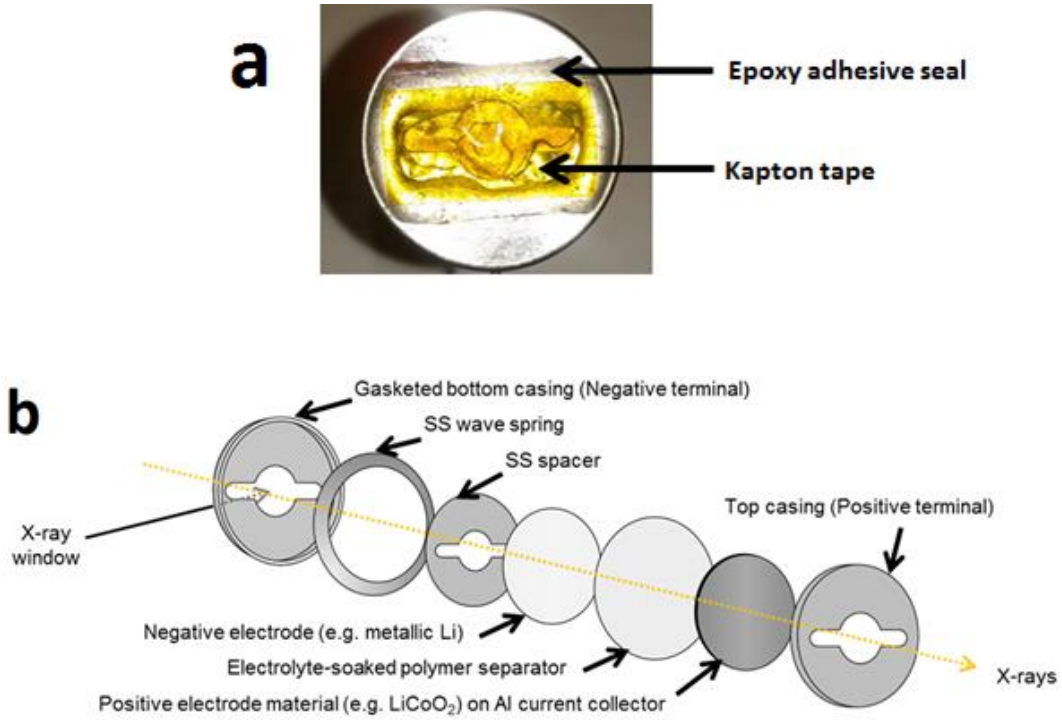

Figure 3.18. (a) Assembled *in-situ* coin cell designed for initial X-ray CT experiments. (b) Exploded view of the *in-situ* coin cell.

Previously reported *in-situ* coin cell designs have been used in real-time X-ray studies such as diffraction [211–213], absorption spectroscopy studies [214–216] and transmission X-ray microscopy [217–219]. However, these coin cell designs usually only

required a small aperture of a few millimetres wide to be made on one side (for experiments operating in reflection mode) or on both sides (for experiments operating in transmission mode) of the cell, which were sealed off with X-ray transparent materials (such as Kapton film or beryllium plates). Also, these small apertures could only accommodate small angular movements of the sample performed during the experiments without obstructing the path of the X-ray beam incident on the sample, thus limiting their application to X-ray CT experiments which require higher angular rotation of the sample about its long axis.

In the coin cell design presented in Figure 3.18, a 16 mm wide × 3 mm high letterbox-shaped aperture and a centered 6mm diameter circular hole were drilled into the can, cap and spacer components for 2032 type coin cells. Rectangular strips (*ca.* 19 mm × 5.5 mm) of 50 µm thick adhesive Kapton tape (Tesa, UK) were cut out and applied on both the inside and outside surfaces of the coin cell cap and can components to create an X-ray transparent window. Epoxy adhesive (Araldite, Germany) was then applied over the edges of the outside-surface Kapton strips, as shown in Figure 3.18(a), to create a hermetic seal around both windows. The circular hole in the centre of the cell hardware was designed to aid in sample alignment during tomography scans, while the letterbox shaped portion of the X-ray window was designed to provide a large enough angular rotation range during the tomographic scans whilst maintaining the coin cell's mechanical stability - this window design meant tomographic scans performed with the cell would be limited angle scans rather than full tomographic scans that acquire data through complete 180° or 360° sample rotation. During coin cell assembly, the X-ray windows on the cell casings and spacer components were carefully aligned in order to avoid beam attenuation by the dense metal components, ensuring a clear 'line-of-sight' for the X-ray beam being transmitted through the electrode material.

The suitability of this X-ray windowed 2032 coin cell design for tomographic imaging, prior to any *in-situ* and *operando* experiments during cell operation, was tested using synchrotron X-ray micro-tomography at the imaging branch of the I13 beamline at the Diamond Light Source, UK. Commercially obtained lithium manganese oxide (LMO) electrode laminates (MTI Corp., USA) were cut, dried and assembled within the *in-situ* coin cell. The cells were also assembled with a Celgard polypropylene

separator (25 µm thick), metallic Li foil as counter electrode, and electrolyte containing 1M $LiPF_6$ in EC: EMC (3:7 v/v).

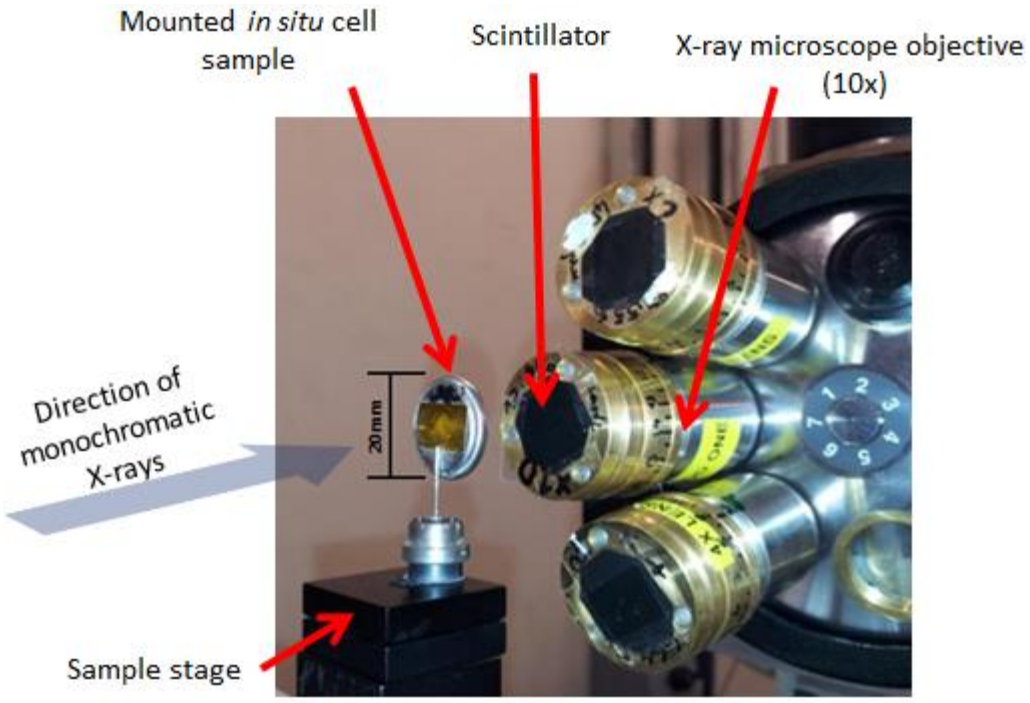

Figure 3.19. *In-situ* coin cell sample mounted for synchrotron X-ray CT

Figure 3.19 shows how the *in-situ* coin cell was mounted on the beamline sample stage and positioned before the X-ray microscope objective prior to the CT imaging test. The coin cells samples for imaging were placed on a high-precision rotating sample stage.

With the i13 beamline set in absorption-contrast imaging mode and in a parallel beam configuration at 16 keV, an interior CT scan of a LMO electrode sample assembled within the *in-situ* coin cell was performed through the Kapton window. The incident X-rays were monochromatized by a water-cooled double crystal Si <111> monochromator. At a sample–scintillator distance of 25 mm, an average useful rotation range of 147° was achieved with the X-ray (letter-box) window design. Projection images were acquired as the sample was rotated about its long axis through angular steps of 0.1°, with a 6 s X-ray exposure time for each projection image. X-rays transmitted or refracted through the sample were captured by a 9.6 µm thick GGG:Eu scintillator screen positioned in front of the microscope objective lens (10x) and converted to visible light that was focused onto a pco4000 camera with a CCD chip of 2*k* x 2*k* pixels and an effective pixel size of 0.365 µm. Tomographic reconstructions

were based on a standard filtered back projection (FBP) algorithm combined [220]. Cross–sectional views through the resulting tomogram are presented in Figure 3.20.

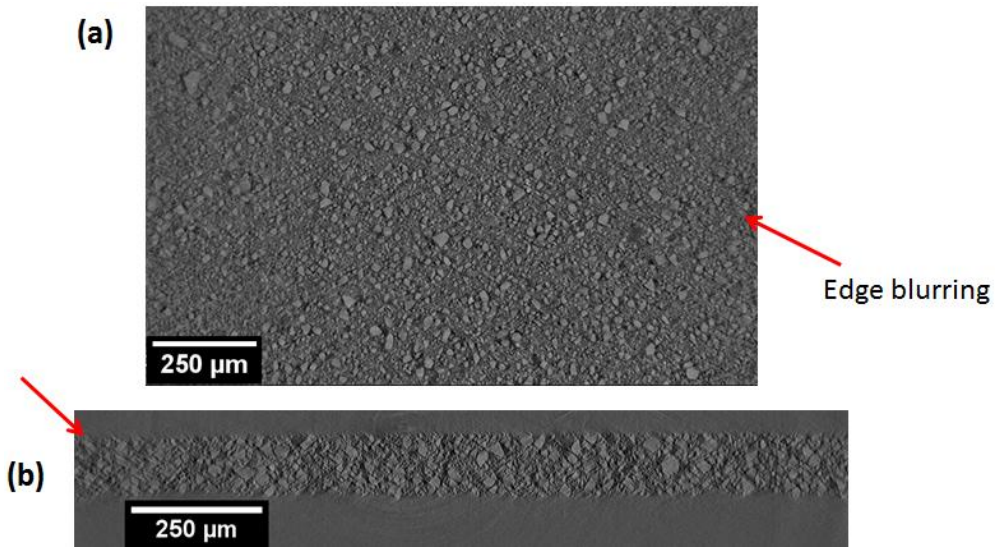

Figure 3.20. (a) Vertical and (b) horizontal cross sections through a tomogram of the LMO electrode taken through an assembled *in-situ* coin cell. The red arrows highlight the blurring artefacts resulting from the interior tomography scan.

With the exception of the edge blurring artefacts which often occur in limited angle CT scans, the image quality of the resulting tomograms of the LMO composite electrode was comparable to that obtained from *ex-situ* X-ray tomography scans (e.g. Figure 4.2c). Such blurring artefacts could be resolved with advanced iterative reconstruction algorithms [221,222].

The next step was testing whether the cycling performance and durability of Kapton-window coin cell was identical to that of the standard coin cell counterpart; in other words, to test the stability and hermeticity of the Kapton X-ray window design during cell cycling under atmospheric conditions. Performance durability tests were done with the windowed coin cells assembled with metallic lithium as counter electrode and graphite (electrode laminate, MTI Corp., USA) as the working electrode. Using the CC-CV charge cycling protocol at room temperature, cells were set up to cycle once at a C-rate of 0.05C (formation cycle) followed by multiple cycles at a C-rate of 0.1C. As a control experiment, some of the assembled windowed coin cells were not cycled but kept under atmospheric conditions.

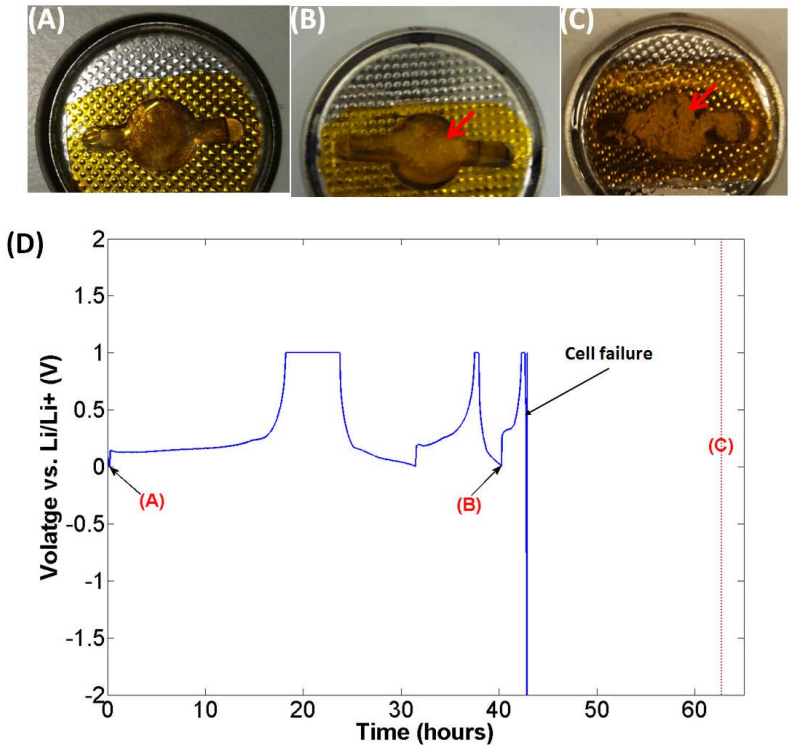

Figure 3.21. Optical images showing the appearance of the metallic lithium anode surface through X-ray window (a) immediately after coin cell assembly, (b) after 40 hours of charge cycling, and (c) after cell failure (> 60 hours from cell assembly). (d) The cell cycling performance declines over time up until cell failure. Red arrows highlight the presence of a white powder-like growth on the lithium metal electrode surface. Red-dotted line marks the time when the optical image in (c) was taken.

All *in-situ* cell samples which were set up for charge cycling displayed electrochemical behaviour similar to that of their standard coin cell counterparts up until *ca.* 40 hours of operation after which they experienced a significant decline in performance and eventual failure in the form of a large drop in cell potential down to negative values, as shown on the voltage versus time plot in Figure 3.21(d).

Also, the shiny, silvery surface of the lithium metal electrode which can be seen through the Kapton X-ray window of the cell [Figure 3.21(a)] gradually becomes tarnished over time. This was followed by the appearance and gradual growth of white, powder-like deposits (Figure 3.21b, highlighted by red arrow) on the surface of the Li metal, and with time, the lithium metal foil surface was completely transformed into the powder-like substance. In addition, significant gas accumulation displayed in the form of an outward bulge of the Kapton window was observed on the anode (Li) side of the coin cell, indicating an increase in cell pressure.

Post-mortem analysis on the internal structure of the failed *in-situ* coin cells was conducted in order to further investigate the cell failure. X-ray micro-CT of failed *in-situ* coin cells was performed using a Nikon XTH 225 ST laboratory X-ray microscope. Figure 3.22 shows reconstructed tomogram cross sections displaying the internal structure and assembly of a failed cycled *in-situ* coin cell.

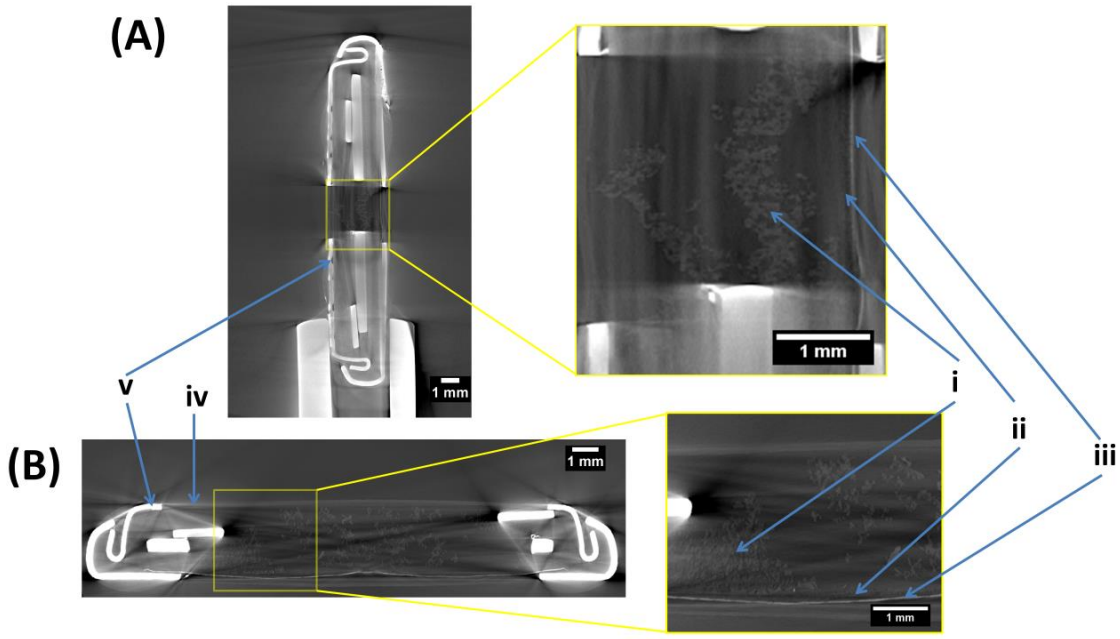

Figure 3.22. (a) Vertical cross section and (b) horizontal cross section through one of the failed cycled *in-situ* coin cell in Figure 3.21(c).

The imaging resolution and contrast was insufficient to confirm the presence of metallic Li which inherently has a low X-ray attenuation; however, the white powder-like surface growth was captured and is seen to have significantly spread within the cell housing.

Samples of the powder-like growth were carefully extracted from the failed cell and characterised using energy-dispersive X-ray spectroscopy (EDS) and Raman spectroscopy in order to obtain an idea of its chemical composition. The EDS spectra [Figure 3.23(a)] of the powder particles [shown in the inset SEM micrograph in Figure 3.23(a)] shows the presence of C and O elemental peaks, and a large low-*Z* peak on the left of the spectra which appears to be indicative of Li. However, the Raman spectra showed a sharp peak at 1088 cm^{-1} and smaller peaks 1458, 748 and 712 cm^{-1}; these

peaks were found to be characteristic of the Raman spectrum of lithium carbonate, Li_2CO_3 [223].

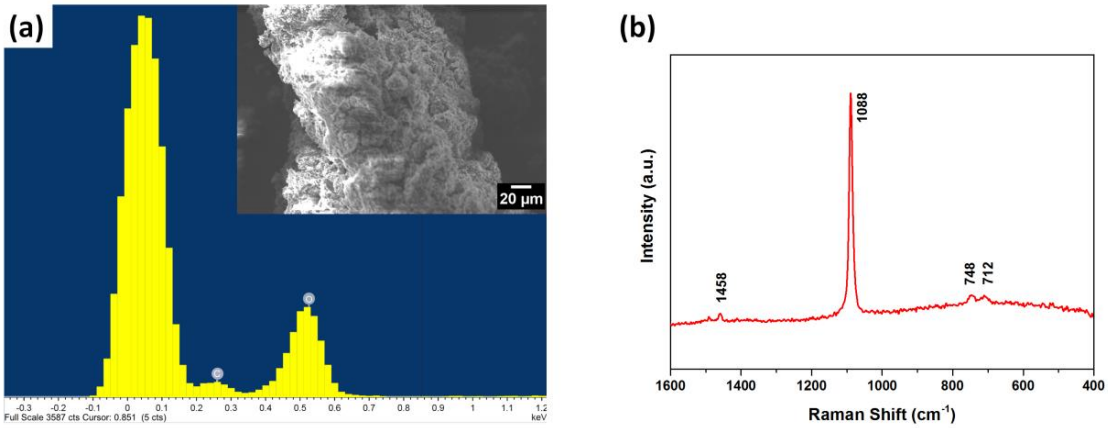

Figure 3.23. (a) EDS spectra and (b) Raman spectra of the white powder-like surface growth on the Li metal surface. Inset in (a): SEM micrograph of the powder particles.

It is suspected that the powder-like growth across the Li metal surface is associated with air contamination through the Kapton window seal of the cell upon introducing the sealed cell to atmospheric conditions from the argon environment in which it was assembled.

Because of their high reactivity with oxygen and water/moisture, both $LiPF_6$–based electrolytes and metallic lithium electrodes have to be kept under airtight conditions when used in lithium-ion cells, as the presence of water impurities in LIBs has negative effects on battery performance. Based on numerous research studies, Aurbach *et al*. [142] summarized a list of possible reactions that occur on Li surfaces in electrolytes solutions containing EC and DMC with the presence of water contaminants:

$$2EC + 2e^- + 2Li^+ \rightarrow (CH_2OCO_2Li)_2 \downarrow + CH_2 = CH_2 \uparrow$$

$$EC + 2e^- + 2Li^+ \rightarrow LiCH_2CH_2OCO_2Li \downarrow$$

$$DMC + e^- + 2Li^+ \rightarrow CH_3 \bullet + CH_2CH_2OCO_2Li \downarrow and/or\ CH_3OLi \downarrow + CH_3OCO \bullet$$

$$\boldsymbol{Trace\ H_2O} + e^- + 2Li^+ \rightarrow LiOH \downarrow + {}^1/_2\ H_2 \uparrow$$

$$LiOH + e^- + 2Li^+ \rightarrow Li_2O \downarrow + {}^1/_2\ H_2 \uparrow$$

$$\boldsymbol{H_2O} + (CH_2OCO_2Li)_2 \rightarrow Li_2CO_3 + CO_2 + (CH_2OH)_2$$

$$2CO_2 + 2e^- + 2Li^+ \rightarrow Li_2CO_3 \downarrow + CO \uparrow$$

Based on these reactions, it follows that water can react with the organic electrolyte solvents, causing pressure generation (due to contaminant gas formation), consumption of active materials (Li metal), as well as a decrease in the electrolyte concentration within the cells. From the reaction list, it is likely that the analysed surface growth also contained lithium alkyl carbonates, besides lithium carbonate. These reaction products possess no ion conductivity [224] and continued depletion of metallic Li in the cells towards lithium carbonate and lithium alkyl carbonates as well as electrolyte reaction and evaporation under atmospheric conditions are likely to have led to the failure of the cells. No further characterisation of the powder surface growth was performed in this work, as this was not the focus of the PhD project.

The powder-like surface growth also appeared in the control cells, eliminating any degradation effects due to initial electrochemical testing but thus questioning the effectiveness of the Kapton tape used in providing a hermetic window seal. Aluminized mylar windows were also tested in place of ordinary Kapton as the X-ray transparent window for the *in-situ* cell but this yielded similar result to the ordinary Kapton windows. These findings demonstrate that introducing the openings on the housing of coin cell-type cells for X-ray beam penetration can create an avenue for possible atmospheric contamination if the openings are not hermetically sealed.

It is noteworthy that previous diffraction and spectroscopy experiments that used *in-situ* coin cells were modified with much smaller windows or were kept in an inert chamber for the duration of the *in-situ* or *operando* experiment, so the chance of moisture or air contamination in such cases was relatively minimal. Moreover, long-term cell cycle longevity was often less important with such cell designs.

Although the X-ray window design of the coin cell implemented in this work appears to accommodate *in-situ* X-ray tomographic imaging, the cell's electrochemical performance and durability for relatively long term experiments needs to be significantly improved through cell re-design before it can be considered for use in *operando* X-ray studies.

3.7.2 *In-situ* Swagelok cell design

Due to the shortcomings experienced with the *in-situ* coin cell discussed in the previous section, an alternative *in-situ* cell design based on the Swagelok-type cell geometry was also explored.

By modifying perflouroralkoxy (PFA) type Swagelok tube fittings with an inner diameter of 0.125 inch (PFA-220-6, Swagelok, USA), custom-built X-ray transparent electrochemical cells were designed and assembled as shown in Figure 3.24. The polymeric-type Swagelok tube fitting was chosen because of the low X-ray absorption coefficient of polymers, as well as the excellent hermetic sealing provided by the commercial tube fitting. Moreover, this cylinder-like cell design provides an unobstructed view of the electrode of interest for X-rays through a complete 180° or 360° sample rotation [176].

Stainless steel (SS) rods with 0.125 inch (*ca.* 3.2 mm) diameter were used as current collectors for both electrodes; the rods were cut and both end surfaces were flattened and narrowed using a lathe cutting tool to enable a tight fit into the tube fitting. The cell electrode assembly is positioned in the centre of the union piece of the tube fitting between two machined stainless steel current collectors. In order to improve the X-ray transmission through the cell electrode assembly within the tube fitting, a groove was made with a lathe cutting tool around the centre circumference of the union piece hex, as shown in Figure 3.24 (a) and (b), leaving a 1.5 mm side wall thickness.

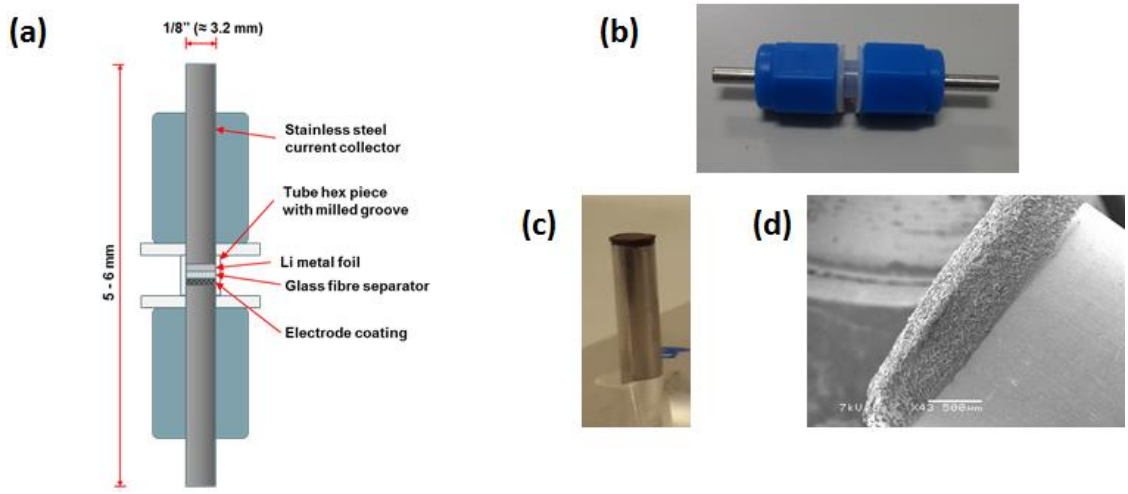

Figure 3.24. (a) Schematic diagram and (b) Optical image of the modified PFA Swagelok cell. (c) Optical image and (d) low resolution scanning electron micrograph of an electrode coating on the tip of a SS current collecting rod.

For the cell assembly process, the separator and Li metal counter electrode were cut into small discs using 0.125 inch diameter hole-punches, while the counter

electrode was dip-coated onto the tip of one of the current collecting rod, as shown in the image and scanning electron micrograph in Figure 3.24 (c) and (d) respectively.

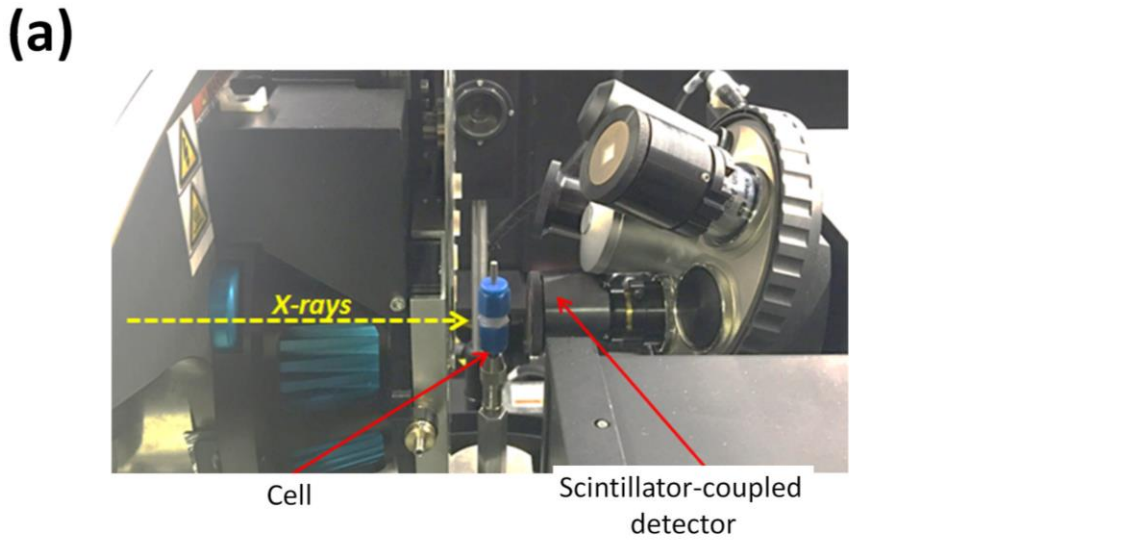

Figure 3.25. (a) Optical image of *in-situ* cell sample mounted for laboratory X-ray CT. (b) Vertical cross section through an X-ray tomogram of the Swagelok cell showing the half-cell assembly.

To test the cycling stability and durability of the *in-situ* Swagelok design, the modified Swagelok cells were assembled with a graphite electrode coating, a borosilicate glass fibre separator, a Li metal electrode and filled with liquid electrolyte (1M $LiPF_6$ in ethylene carbonate : ethyl methyl carbonate, in the ratio 3:7 by volume). A quality inspection of the assembled components within the Swagelok half-cell was

performed using laboratory X-ray micro-CT (ZEISS Xradia Versa 520) and an X-ray tomogram ortho-slice of the assembly shown in Figure 3.25.

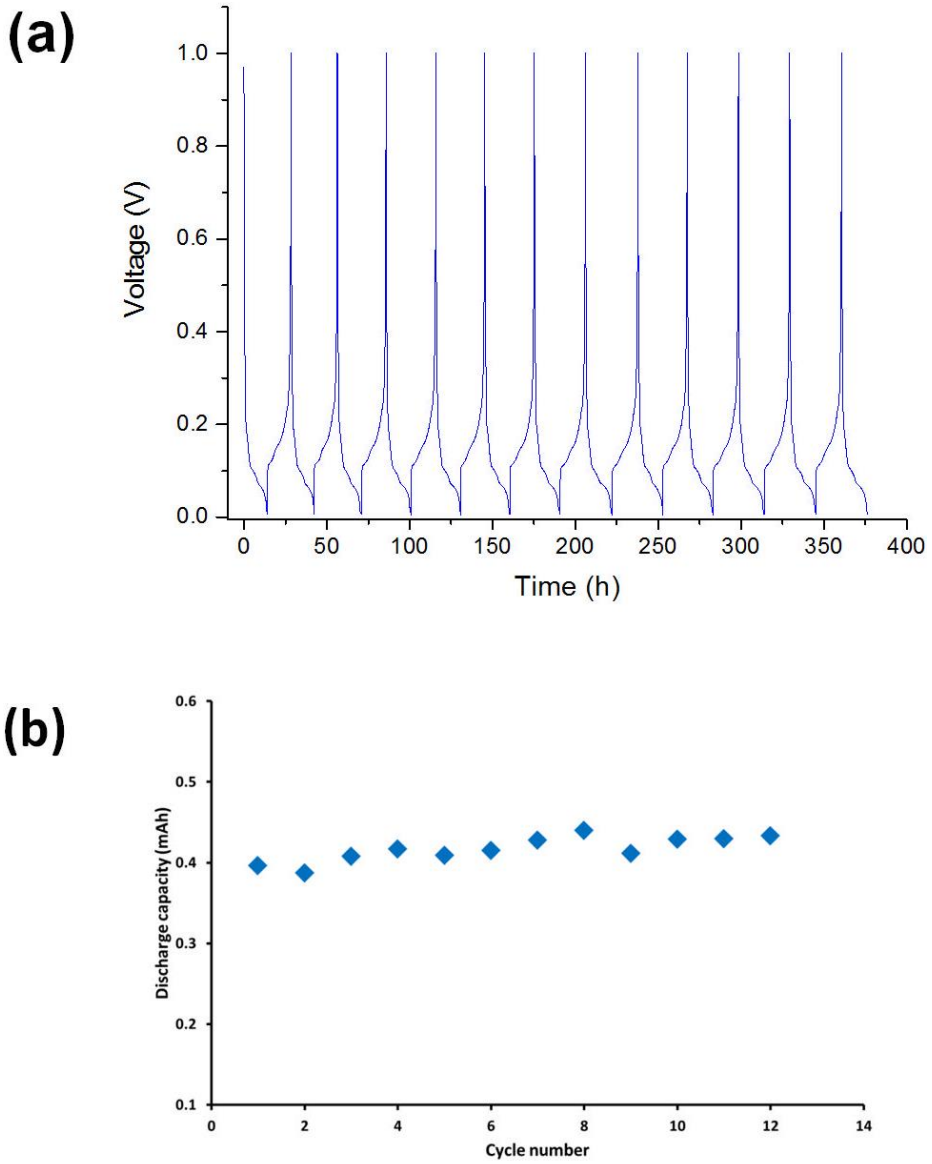

Figure 3.26 (a) Voltage vs. time profile and (b) Cycle performance of the assembled graphite/Li *in-situ* Swagelok cell at a C/14 C-rate.

The cycle performance of the *in-situ* Swagelok cell was then tested: graphite/ Li half-cells were setup for charge cycling on the Maccor 4300 series battery cycler at a C/14 rate between 0.005 V – 1 V for 12 cycles. Figure 3.26 shows the cycle performance of one of the tested graphite/Li Swagelok cells. The cells showed good durability and cycle repeatability after testing, and showed no signs of leakage around joints.

With the significant stability of the *in-situ* electrochemical cell design, the author went forward to conduct *in-situ* and *operando* X-ray CT experiments, which are reported in Chapters 5 and 6.

3.8 Summary

The experimental methods and techniques used the microstructural investigations reported later on in this thesis were introduced in this chapter. Sample preparation procedures, material characterisation and digital image analysis techniques used in the work were presented. Also, the design and development of an *in-situ* electrochemical cell used in later chapters to facilitate the study of 3D microstructural evolution in LIB electrodes using X-ray tomographic imaging was discussed.

Chapter 4

Comparison of 3D Analysis and Stereological Techniques for Quantifying LIB Electrode Microstructures

Material in this chapter is reproduced in part with permission from "Comparison of three-dimensional analysis and stereological techniques for quantifying lithium-ion battery electrode microstructures", O. O. Taiwo, D. P. Finegan, D. S. Eastwood, J. L. Fife, L. D. Brown, J. A. Darr, P. D. Lee, D. J. L. Brett, and P. R. Shearing, *Journal of Microscopy*, vol. 263, no. 3, pp. 280–292, Copyright (2016) John Wiley & Sons.

4.1 Introduction

A quantitative understanding of microstructure and transport pathways within lithium-ion battery electrodes is crucial for improving their design, manufacture, performance and durability. To this end, characterisation techniques for revealing all relevant, detailed microstructural morphology and for assessing quantitative geometric parameters are essential.

Three-dimensional microstructures can be quantitatively characterised using two principal approaches: the first is by stereological methods [225–228], which take measurements from planar 2D image slices through a sample material (typically obtained using two-dimensional cross sectional microscopy), and extrapolating the results to the geometric parameters of the 3D structure using statistical approaches and image analysis. The second approach is by direct viewing and measurement of 3D datasets obtained by tomographic imaging of the material of interest or serial sectioning techniques. X-ray tomography and FIB-SEM tomography are the most commonly applied imaging techniques for obtaining complete microstructural models of lithium-ion battery electrodes [24].

Although stereological procedures require significantly less experimental and computational effort, microstructural investigations using these methods are often inconclusive, particularly when attempting to characterise structural quantities that rely on phase connectivity in 3D. In contrast, 3D microstructural analysis from tomographic imaging can be time consuming and may require access to advanced tomography equipment.

This chapter will examine and compare both stereological prediction and 3D analysis techniques for quantitative measurements of key geometric parameters that characterise lithium-ion battery electrode microstructures. In this work, lithium-ion battery electrode samples were imaged using synchrotron-based X-ray CT, and for each electrode sample investigated, stereological analysis was performed on reconstructed 2D image slices extracted from tomographic imaging whereas direct 3D analysis was performed on reconstructed image volumes.

4.2 Materials and Methods

4.2.1 X-ray CT and image analysis

Three commercially-sourced lithium-ion battery electrodes laminates: lithium cobalt oxide (LCO), lithium manganese oxide (LMO) and graphite (all procured from MTI Corporation, USA) were imaged using synchrotron X-ray CT at the TOMCAT beamline of the Swiss Light Source (Paul Scherrer Institut, Villigen, Switzerland) [229]. Small sections of the electrode laminates were cut to a size which fit into the user-defined field of view, set to 1.6 × 1.4 mm^2 for this experiment. A parallel monochromatic beam was used in absorption contrast imaging mode, with the beam energy set to 10.5 keV for the graphite electrode and 18 keV for both LCO and LMO materials. For each tomographic scan, 1501 projections were acquired during a 180° rotation of the sample about its long axis, through angular steps of 0.12° with an exposure time of 200 ms for each projection image. The X-rays illuminated a 20-µm-thick LuAG:Ce scintillator, producing visible light which was focused onto a pco.Edge camera, providing an effective pixel size of 0.65 µm. Tomographic reconstruction of the acquired projection images was performed using the gridrec algorithm [230] after application of flat- and dark-field corrections to account for non-uniformity in the

incident beam and detector response, respectively. Table 4.1 is a summary of the parameters used to image the different samples.

Table 4.1. Tomography acquisition parameters for each sample

Scan parameters	LCO	LMO	Graphite
Beam energy (keV)	18	18	10.5
Number of projections	1501		
Radiograph exposure time (ms)	200		
Rotation range (°)	[0, 180]		
Effective voxel size (nm^3)	650 × 650 × 650		

Image pre-processing and volume rendering of the resulting reconstructed volumes was carried out using the Avizo software package. For each acquired tomographic volume (consisting of a stacked sequence of 2D greyscale images), a region-of-interest (ROI) was extracted for subsequent analysis. After ROI extraction, a non-local means smoothing filter was applied to the greyscale image sequences for image smoothing and de-noising, followed by threshold-based segmentation which utilizes the greyscale histogram of the tomographic images to separate out the solid phase from the pore phase, creating a binary image.

4.2.2 Microstructural parameters

In order to compare stereological and direct 3D quantification procedures, some common geometric parameters were analysed, namely: *pore volume fraction*, *volume-specific surface area*, *geometric tortuosity* and *pore radius*. Stereological or 2D-based predictions of 3D microstructural parameters are usually obtained by performing quantitative image analysis on 2D image sections—this could be done using a single 2D cross-sectional image slice or a statistical sampling of a few image slices. In this work, however, we perform stereological analysis on each 2D cross-sectional slice from each of the tomographic image sequences; thus, for each calculated parameter, a slice-wise distribution across the sample volume is generated over which an average is taken. Moreover, all stereological calculations for this work were algorithmically implemented into MATLAB. For each measured microstructural parameter, MATLAB algorithms which incorporated the necessary stereological relationships were created and run on the image datasets.

With direct 3D quantification, microstructural parameters were extracted from the tomographic image volume. In this approach, image sections can be read into a computer as a 3D volume using digital image analysis (as a matrix of volume pixels or voxels). The approaches used to calculate the aforementioned microstructural parameters both stereologically and in 3D are discussed below.

(i) *Pore volume fraction* (Φ): As previously, discussed in Section 3.6.1, this is the volume fraction of the pore phase with respect to the total volume of sample porous material being analysed. Pore volume fraction can be predicted stereologically using Delesse's principle [226,227] which estimates the volume fraction of a component/phase of interest within a 3D object from the area fraction of that component within a 2D cross-section through that object (A_A), that is, $\Phi = A_A$. Area fraction calculations were performed on each 2D cross-sectional slice generated from the tomography image sequences using a pixel counting approach as the ratio of the total number of pixels in the pore phase to the total number of pixels in the analysed image slice. Pore volume fraction was calculated directly from the tomographic image volumes, using a voxel counting approach, as the fraction of cubic voxels that make up the pore phase within the analysed 3D volume of interest.

(ii) *Volume-specific surface area* (S_V): For a given interface or phase boundary within an imaged sample volume, S_V can be defined as the ratio of the total surface area of that interface type in the sample to the sample volume. S_V for the solid phase/porosity in the lithium-ion battery electrode samples was predicted using a stereological approach which requires the measurement of L_A, the perimeter length of the total phase boundary observed within the given 2D cross-section per unit area of the image cross-section [226–228], that is,

$$S_V = \frac{4}{\pi}(L_A) \tag{4.1}$$

The variable S_V was directly quantified in 3D as the ratio of the total 3D surface area of the sample solid phase/porosity interface to the total analysed sample volume. The surface area of the solid phase/porosity interface was calculated as the area of a

triangular surface mesh approximation of the solid phase/porosity interface, which is discussed in Section 3.6.2.

(iii) *Geometric tortuosity* (τ): Geometrically, τ can be defined in 2D using the arc-chord ratio which is the ratio of the effective length of a curve (L_e) to the length of the straight line between the curve's end points (L), as is stated in Equation (3.3). However, extending this 2D definition to branching 3D networks, τ can be extracted between a source plane and a destination plane within a porous volume, and defined for each location x on the destination plane (i.e. in the *x*, *y* or *z* directions) where it intersects with the 3D network:

$$\tau(\mathrm{x}) = \frac{L_e(\mathrm{x})}{L(\mathrm{x})} \tag{4.2}$$

where $L_e(\mathrm{x})$ represents the shortest path length through the selected phase from the source plane to the location x and $L(\mathrm{x})$ represents the shortest path through any phase in the sample volume from the source to destination planes. With each of the examined 3D volumes, τ for the pore phase was calculated along the *x*, *y* and *z* axes.

Here, the tortuosities were calculated based on an approach presented by Jørgensen *et al.* [193] which involves distance map propagation and source backtracking from a propagation front with the aid of a fast marching algorithm. A brief description of the method is given in Section 3.6.3.

(iv) *Pore radius* (σ): Within 3D porous media, the pore size distribution is usually characterised by a mean pore size. Stereologically, such media can be characterised by a mean pore size that is not derived from a pore size distribution but from using the concept of mean intercept length [227]. From this, the stereologically predicted mean pore radius (σ_{2D}) can be defined by the following relation:

$$\sigma_{2D} = \frac{2\Phi}{S_V} \tag{4.3}$$

where Φ and S_V are the volume fraction and volume specific surface area of the pore phase, respectively. From a geometrical point of view, the pore radius for any section of the pore path in the network can be defined as the radius of the largest sphere that can be locally inscribed into that section of the network [193].

For the 3D pore size quantification, the mean pore radius is calculated by taking the average of a generated pore radius distribution and various methods exist for extracting pore radius distributions from 3D image volumes. However, in this work, 3D pore size was geometrically characterised and compared using the following four methods: *medial axis based method using fast marching (MA-FM)*, *medial axis-based method using distance-ordered homotopic thinning (DOHT), successive morphological opening method (SMO),* and *continuous pore size distribution method (CPSD)*. A brief explanation of how each of these 3D pore size calculations were implemented for this work can be found in Section 3.6.4.

4.2.3 Representative volume element analysis

To allow ease of manipulation for the direct 3D parameter quantification, the largest possible cuboid volume was cropped from each tomographic dataset (Table 4.2); however to ensure that these cropped electrode volumes were large enough to be representative of the macroscopic properties of the respective bulk electrode volumes, representative volume element (RVE) analysis was performed. The RVE is usually regarded as a volume of heterogeneous material which effectively includes a sampling of all microstructural heterogeneities present and is sufficiently large to be statistically representative for the entire structure. Further, the size of the RVE also depends on the investigated morphological or physical properties [231]. In practice, the RVE can be estimated deterministically by performing a systematic analysis of the influence of volume size on the overall geometric or physical properties of interest [232,233], with the minimum RVE given by the size of the volume for which the fluctuations in the effective property become insignificant, seen as a distinct plateau [i.e. the onset of region II in Figure 4.1(a)]. However, for real heterogeneous systems, the presence of region II may be difficult to delineate with confidence due to spatial variability [234,235].

Table 4.2. Volume dimensions of the analysed electrode samples

Electrode sample	**Analysed volume dimensions** $X \times Y \times Z$ **voxel**^{3} **(µm**^{3}**)**
LCO	744 × 1140 × 75 (483.6 × 741.0 × 48.8)
Graphite	1022 × 1176 × 85 (664.3 × 764.4 × 55.3)
LMO	990 × 1125 × 90 (643.5 × 731.3 × 58.5)

As a result, the selected volume of interest for each analysed electrode in this study was deemed a representative volume element if the absolute value of the relative error ($\varepsilon_{r,RVE}$) in the measured material parameter was less than or equal 2 %. For the RVE analysis, the ROI extracted for each electrode sample was split into sub-volumes, as shown in Figure 4.1(b) and Table 4.3, where each sub-volume was obtained by increasing the *x* and *y* lengths from an initial cuboidal volume selected from a vertex of the image, whilst keeping the *z*-length (i.e. electrode thickness) fixed for all sub-volumes. This was followed by computing the value of each microstructural parameter for the different incremental sub-volumes in attempt to realise converging RVE plots.

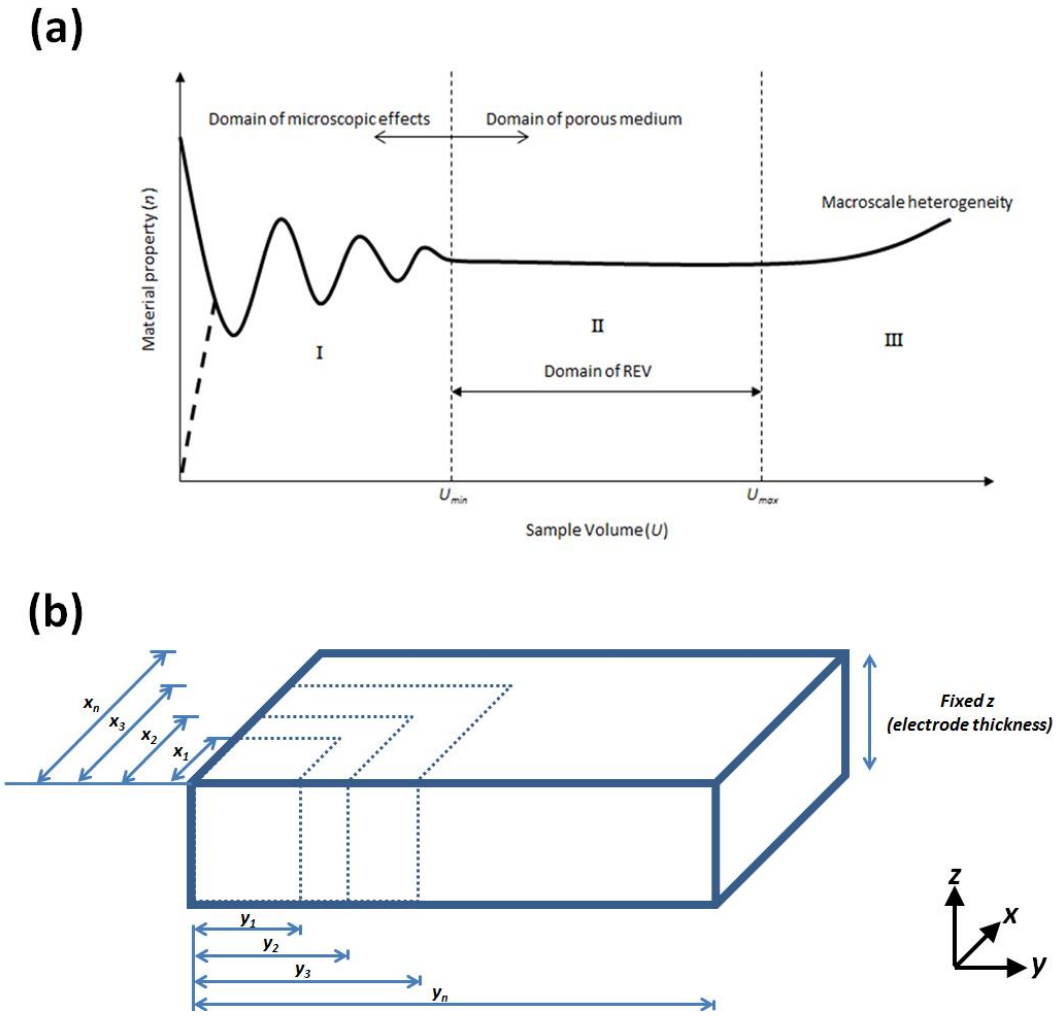

Figure 4.1. (a) Conceptual schematic representing the idealized relationship between material property (*n*) and the sample volume (*U*), and showing the representative volume element region. Adapted with permission from [233]. Copyright (2011) Journal of Microscopy. (b) Schematic representation of how the analysed electrode samples were split into sub-volumes by increasing *x* and *y* lengths, while keeping *z* thickness fixed.

Table 4.3. Extracted sub-volume dimensions from (a) LCO, (b) LMO, and (c) graphite electrode samples used in the representative volume element analyses.

(a)

Sample sub-volume	LCO X (μm)	LCO Y (μm)	LCO Z (μm)
1	40.3	61.8	48.8
2	80.6	123.5	48.8
3	120.9	185.3	48.8
4	161.2	247.0	48.8
5	201.5	308.8	48.8
6	241.8	370.5	48.8
7	282.1	432.3	48.8
8	322.4	494.0	48.8
9	362.7	555.8	48.8
10	403.0	617.5	48.8
11	443.3	679.3	48.8
12	483.6	741.0	48.8

(b)

Sample sub-volume	LMO X (μm)	LMO Y (μm)	LMO Z (μm)
1	42.9	48.8	58.5
2	85.8	97.5	58.5
3	128.7	146.3	58.5
4	171.6	195.0	58.5
5	214.5	243.8	58.5
6	257.4	292.5	58.5
7	300.3	341.3	58.5
8	343.2	390.0	58.5
9	386.1	438.8	58.5
10	429.0	487.5	58.5
11	471.9	536.3	58.5
12	514.8	585.0	58.5
13	557.7	633.8	58.5
14	600.6	682.5	58.5
15	643.5	731.3	58.5

(c)

Sample sub-volume	Graphite X (μm)	Graphite Y(μm)	Graphite Z(μm)
1	47.5	54.6	55.3
2	94.9	109.2	55.3
3	142.4	163.8	55.3
4	189.8	218.4	55.3
5	237.3	273.0	55.3
6	284.7	327.6	55.3
7	332.2	382.2	55.3
8	379.6	436.8	55.3
9	427.1	491.4	55.3
10	474.5	546.0	55.3
11	522.0	600.6	55.3
12	569.4	655.2	55.3
13	616.9	709.8	55.3
14	664.3	764.4	55.3

4.3 Quantification of microstructural parameters in 2D and 3D

In this work, we compare the geometric quantification of lithium-ion battery electrode microstructural parameters using both stereological and direct 3D measurement approaches. Figure 4.2 shows the result of threshold segmentation of a reconstructed greyscale image section and the resulting volume rendering of the region of interest analysed for each electrode sample. Note that each reconstructed 2D image section is a plane of single voxel thickness. For each electrode, parameter calculation using the stereological approach was performed on 2D image sections to yield slice-wise distributions, and RVE analysis was performed on the 3D reconstructed volumes to ensure bulk representation of the calculated parameters in three dimensions.

Based on a 2 % relative error criterion, the profiles for pore volume fraction, volume-specific surface area, as well as geometric tortuosity along the *x*, *y* and *z* directions presented in Figure 4.6(d), Figure 4.10(d) and Figure 4.17, respectively show that the three electrode sample volumes yield parameter values that are representative of the bulk electrode volume. These figures also show the graphite and LMO samples reach the minimum RVE at a much smaller sub-volume than the LCO sample, which can be attributed to lesser microscopic heterogeneity effects on the microstructural parameters in both graphite and LMO sample volumes.

4.3.1 Pore volume fraction

Figure 4.3 – Figure 4.6 show the slice-wise pore volume fraction profile for each of the three examined battery electrodes along each orthogonal direction. For each electrode sample, the mean pore volume fraction and standard deviation (SD) in each direction were also calculated over the 2D image sections. As expected, averaging the entire slice-wise 2D pore volume fraction distribution along each axis yields stereological mean pore volume fraction values (*Mean 2D*) which are identical to the value obtained from a 3D reconstruction of the pore phase, as seen in Table 4.4, but the pore volume fraction standard deviation varies in each direction.

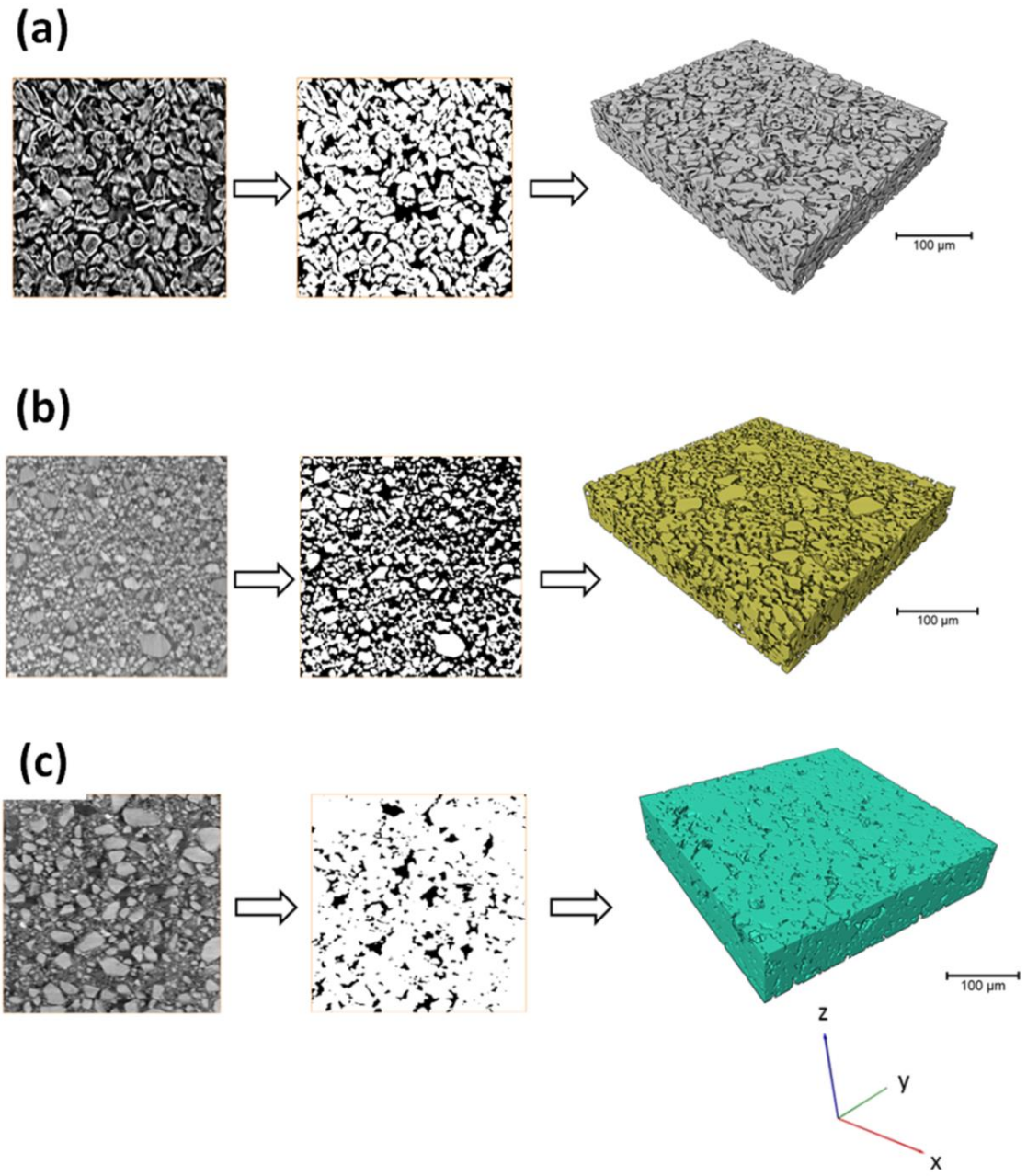

Figure 4.2. Transformation of reconstructed 2D greyscale image to binary image and a volume rendering of the (a) graphite, (b) LCO and (c) LMO electrode samples respectively, where white represents the solid phase and black represents the pore/electrolyte phase.

It was also seen that stereological prediction of pore volume fraction using 2D image sections along each axis yields a pore volume fraction profile that displays significant variation, thus highlighting localised microstructural heterogeneities. When compared to the pore volume fraction measured in 3D, all three electrodes showed larger maximum percentage underestimation (% U.E.) and maximum percentage overestimation (% O.E.) in the *x* and *y* directions than in the *z* direction. Moreover, the

results further indicate that basing pore volume fraction calculations for a 3D porous material with a heterogeneous microstructure on the area fraction of just a single planar section of such material could be misleading.

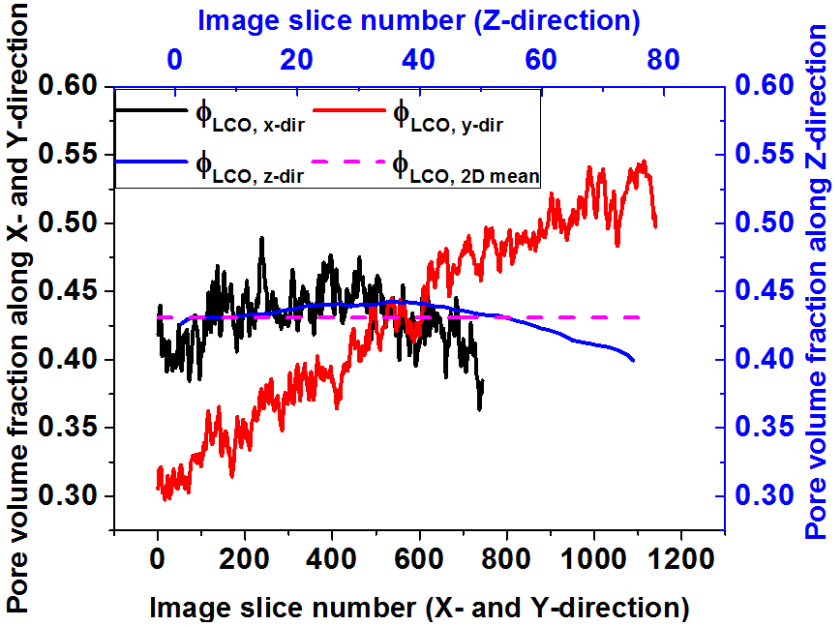

Figure 4.3. Pore volume fraction profiles for the LCO electrode sample showing variation in slice-wise pore volume fraction along the *x*, *y* and *z* directions.

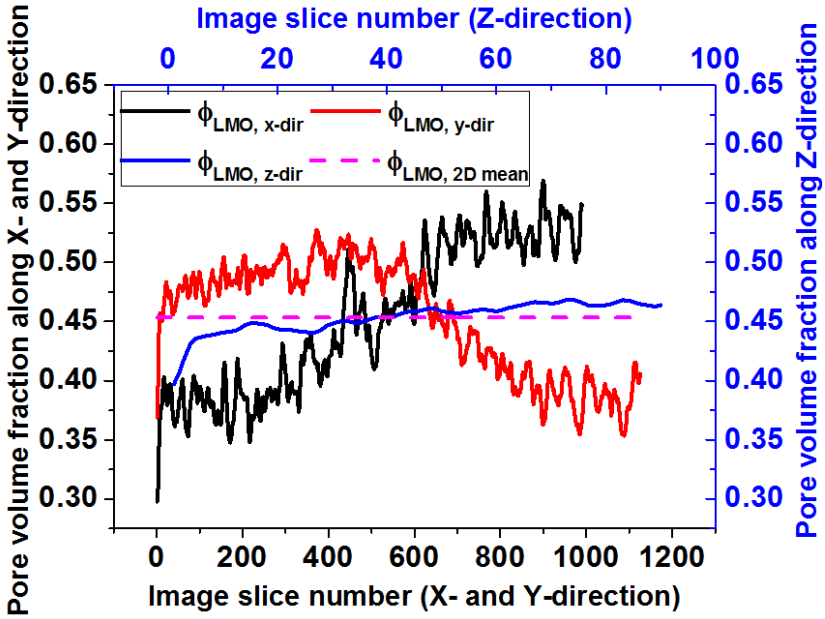

Figure 4.4. Pore volume fraction profiles for the LMO electrode sample showing variation in slice-wise pore volume fraction along the *x*, *y* and *z* directions.

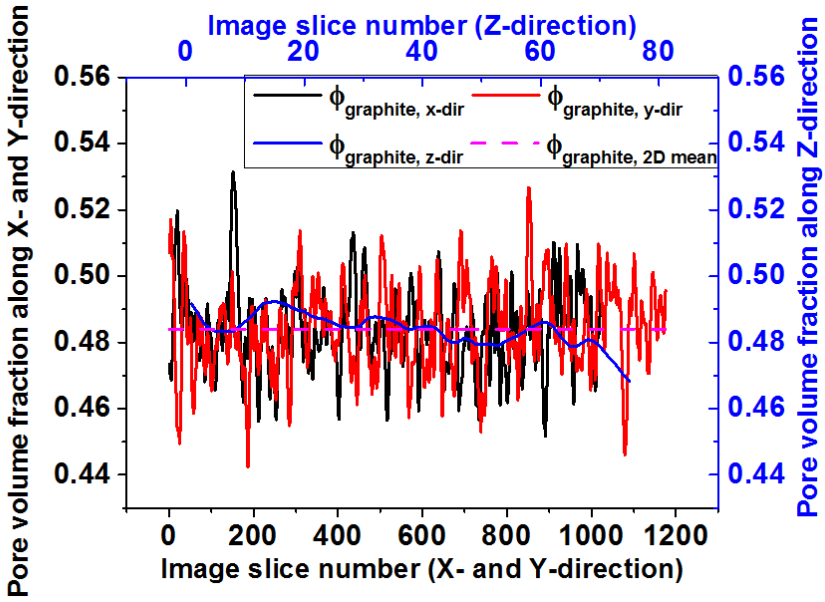

Figure 4.5. Pore volume fraction profiles for the graphite electrode samples showing variation in slice-wise pore volume fraction along the *x*, *y* and *z* directions.

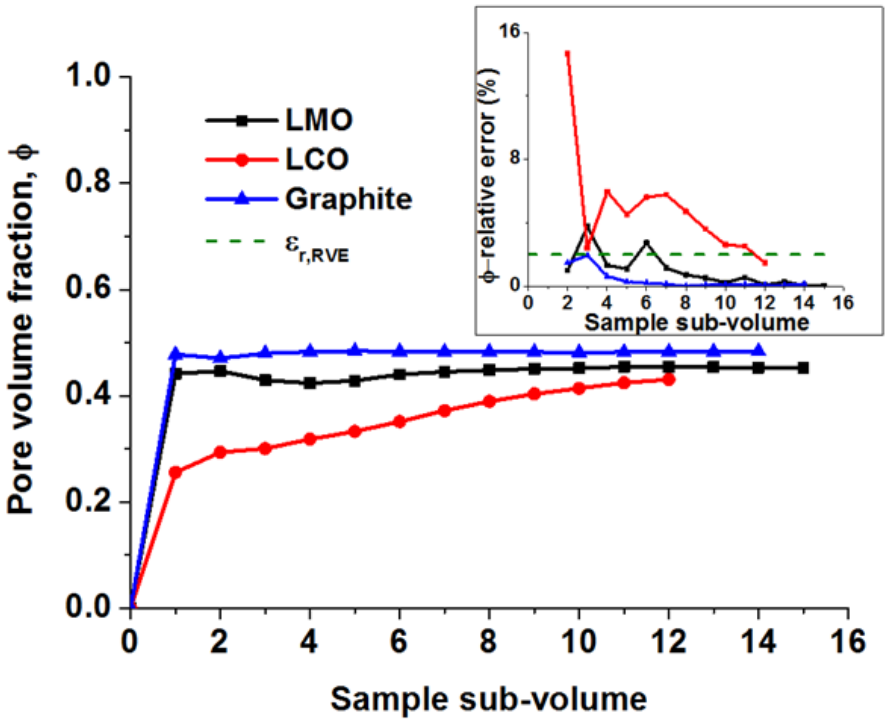

Figure 4.6. Evolution of 3D pore volume fraction (main) and the relative errors (inset) versus sub-volume size for each electrode sample.

Table 4.4. Comparison of pore volume fractions obtained by stereological predictions and 3D analysis.

Pore volume fraction, Φ							
Sample	**3D**	**Mean 2D**	**Std. Dev. 2D**	**Min 2D**	**% U.E.**	**Max 2D**	**% O.E.**
LCO	0.431	*x-dir*: 0.431	0.021	0.363	15.67	0.490	13.69
		y-dir: 0.431	0.070	0.297	30.96	0.546	26.69
		z-dir: 0.431	0.011	0.399	7.26	0.442	2.73
Graphite	0.484	*x-dir*: 0.484	0.013	0.452	6.67	0.531	9.81
		y-dir: 0.484	0.013	0.443	8.60	0.527	8.84
		z-dir: 0.484	0.005	0.468	3.24	0.492	1.73
LMO	0.453	*x-dir*: 0.453	0.062	0.298	34.36	0.569	25.58
		y-dir: 0.453	0.047	0.353	22.07	0.528	16.33
		z-dir: 0.453	0.013	0.397	12.47	0.469	3.38

4.3.2 Volume-specific surface area

Figure 4.7 – Figure 4.10 show the slice-wise volume-specific surface area profiles generated using the stereological relation shown in Equation (4.1) for each of the three examined battery electrodes along each orthogonal direction. Unlike the pore volume fraction results, it can be seen for all three samples that the mean stereological volume-specific surface area values obtained along each axis direction differ from each other and also from the mean volume-specific surface value obtained from 3D volume analysis; for instance, when compared with the mean volume-specific surface area obtained from 3D measurement shown in Table 4.5, a difference of up to 52 % was found in the LMO electrode sample. This error can be associated with the fact that the stereological method does not account for how each image slice interacts with the next one above or below it when estimating the length of the pore-solid phase boundary length. Furthermore, in the LMO and graphite samples, the 2D image sections extracted in the *x* direction yield a slice-wise profile with higher volume-specific surface area values than the profiles from the 2D sections in the *y* and *z* directions. This could be attributed to the anisotropic or non-spherical nature of the electrode particle shapes and/or to particle-to-particle ordering and orientation within the electrode samples as a result of electrode calendaring or the electrode manufacturing process. This could then lead to a variation in the length of the particle–

porosity phase boundary that would be captured in 2D sections along a given orthogonal direction.

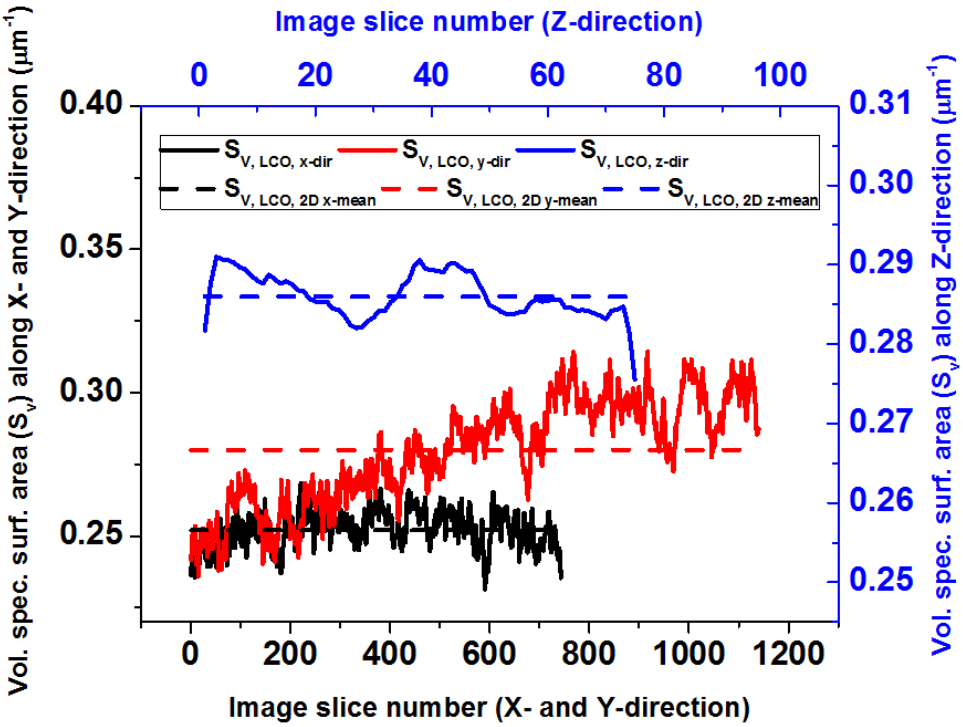

Figure 4.7. Volume-specific surface area profiles for the LCO electrode sample showing variation in slice-wise volume-specific surface area along the *x*, *y* and *z* directions.

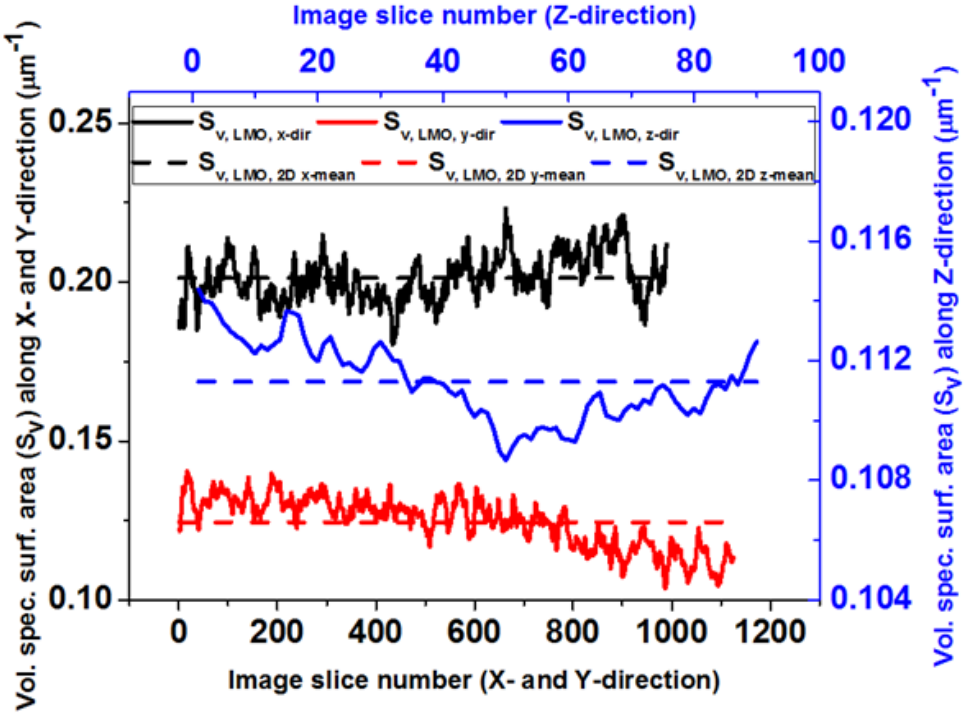

Figure 4.8. Volume-specific surface area profiles for the LMO electrode sample showing variation in slice-wise volume-specific surface area along the *x*, *y* and *z* directions.

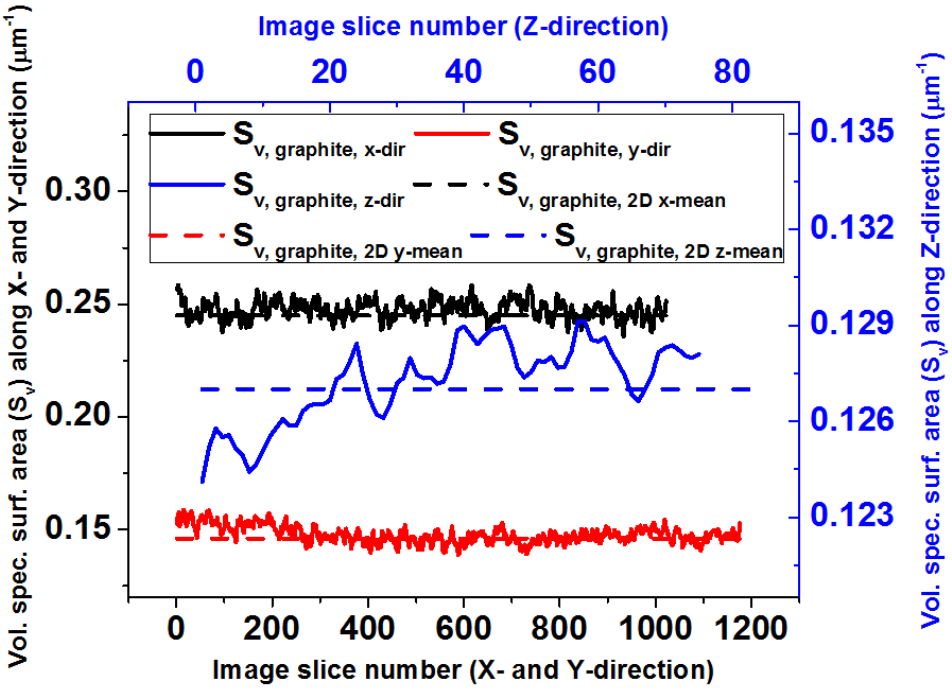

Figure 4.9. Volume-specific surface area profiles for the graphite electrode sample showing variation in slice-wise volume-specific surface area along the *x*, *y* and *z* directions.

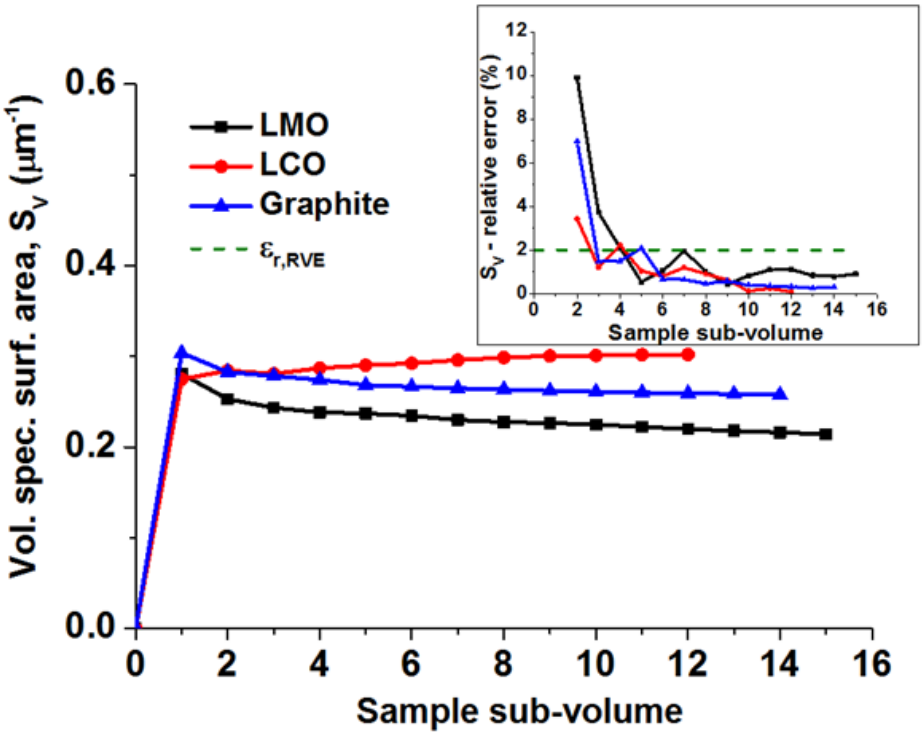

Figure 4.10. Evolution of 3D volume-specific surface area (main) and the relative errors (inset) versus sub-volume size for each electrode sample.

Table 4.5. Comparison of volume-specific area obtained by stereological predictions and 3D analysis

Volume-specific surface area, S_V							
Sample	**3D (μm^{-1})**	**Mean 2D (μm^{-1})**	**Std. Dev. 2D (μm^{-1})**	**Min 2D (μm^{-1})**	**% U.E.**	**Max 2D (μm^{-1})**	**% O.E.**
LCO	0.302	*x-dir*: 0.252	0.007	0.231	23.38	0.268	11.17
		y-dir: 0.280	0.018	0.236	21.83	0.314	4.08
		z-dir: 0.286	0.003	0.276	8.77	0.291	3.65
Graphite	0.258	*x-dir*: 0.248	0.004	0.236	8.64	0.258	0.21
		y-dir: 0.148	0.004	0.139	46.26	0.158	38.49
		z-dir: 0.127	0.001	0.124	51.89	0.129	49.95
LMO	0.214	*x-dir*: 0.325	0.012	0.180	15.69	0.223	4.32
		y-dir: 0.193	0.013	0.104	51.50	0.141	34.36
		z-dir: 0.169	0.002	0.109	49.41	0.114	46.55

4.3.3 Geometric tortuosity

Although the arc-chord ratio for calculating geometric tortuosity is not a relationship developed from stereological theory, it has been used on 2D image sections for estimating the tortuosity of inherently 3D structures [236]. Moreover, as illustrated in Figure 4.11 using a small ROI from the reconstructed LCO electrode pore network, 2D image-based estimations of the tortuosity of a 3D pore network along a given orthogonal direction means that the 2D planar images used for such estimations could be viewed or selected from two possible directions. For example, if we are estimating tortuosity along the *z* direction in a tomographically generated 3D image using the arc-chord ratio approach, the tortuosity estimates can be calculated using 2D image sections generated in the ZX or ZY planes, and in the *x* and *y* directions if the 3D image is re-sliced to generate image sections in the XZ or XY planes and YX or YZ planes, respectively. This results in two tortuosity profiles per axial direction, making a total of six possible tortuosity profiles, as illustrated in Figure 4.11.

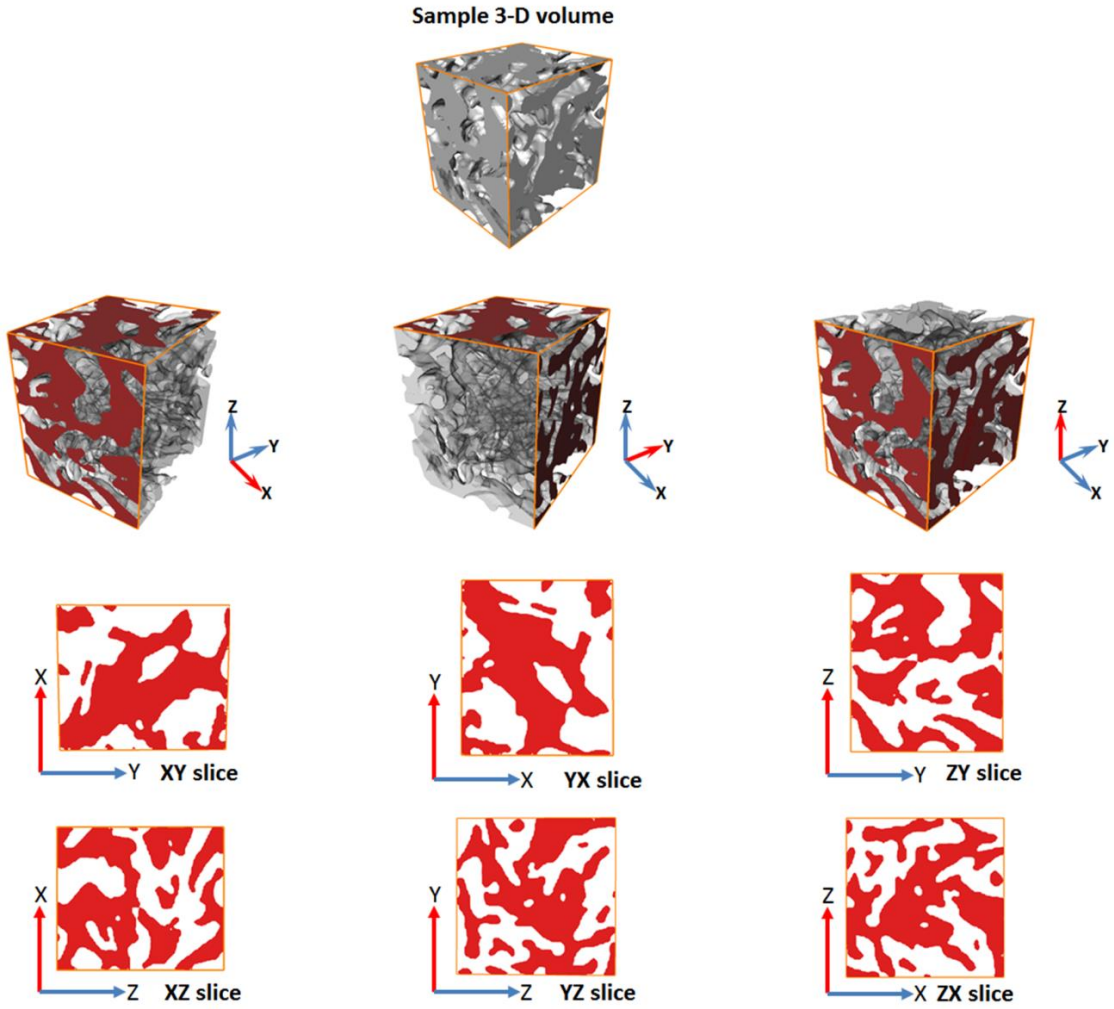

Figure 4.11. Schematic illustration of how a 3D structure can be viewed along each axis direction for 2D tortuosity calculations.

Although the pore phase in the examined electrodes showed good connectivity (>99 %) and percolation in three dimensions, we observe that the pore phase across some individual 2D sections generated was not connected, leading to discontinuities in the slice-wise tortuosity profiles. The tortuosity value across such sections is taken to be infinite. This further highlights how the stereological approach to microstructural parameter quantification can be misleading.

Figure 4.12 – Figure 4.14 show the discontinuities in the slice-wise tortuosity profile for each of the examined electrodes, which highlights the absence of a completely percolating pore phase across some 2D sections. These discontinuities were present in all the slice-wise profiles created along each possible plane. Figure 4.15 – Figure 4.17 show the evolution of 3D pore-phase tortuosity with increasing

sample sub-volume along the *x*, *y* and *z* directions using representative volume element analysis.

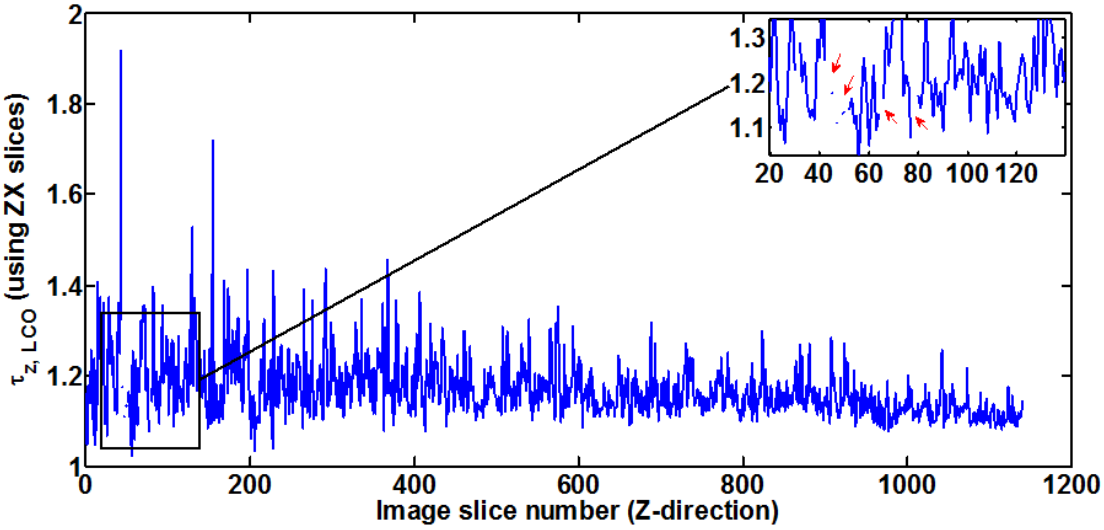

Figure 4.12. Slice-wise tortuosity profile of the LCO electrode pore phase across ZX image sections. Regions of tortuosity discontinuity highlighted by the red arrows in the inset plots signify no pore percolation across some image section(s) within that region of the sample.

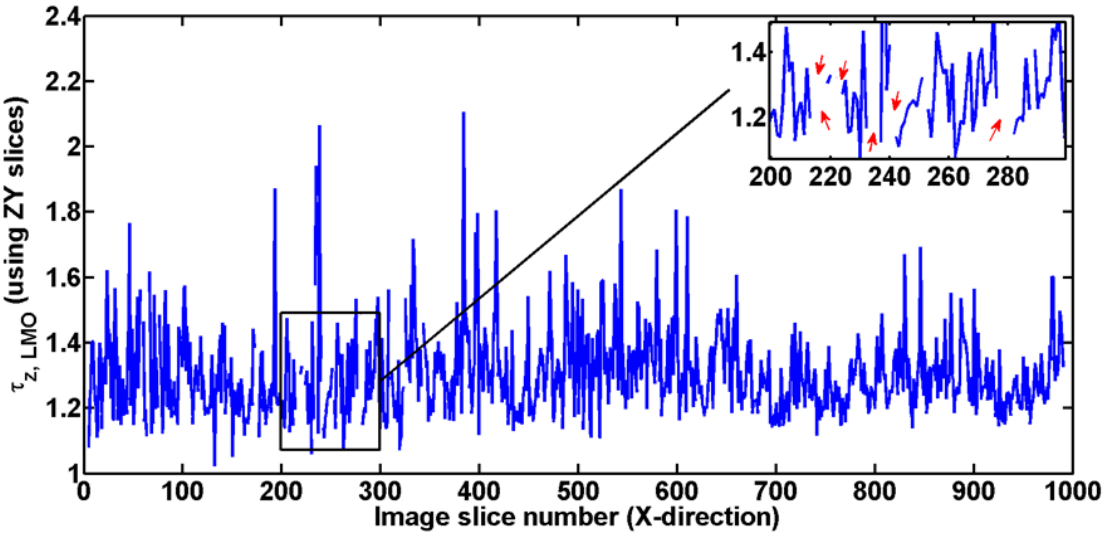

Figure 4.13. Slice-wise tortuosity profile of the LMO electrode pore phase across ZY image sections. Regions of tortuosity discontinuity highlighted by the red arrows in the inset plots signify no pore percolation across some image section(s) within that region of the sample.

The discontinuities in Figure 4.12 – Figure 4.14 show that the tortuosity within inherently 3D networks is nearly impossible to measure from 2D cross sections or planar slices, as it relies on exactly how and where the phase networks branch out and interconnect in three dimensions [23,237]. The 2D methodology does not consider this

3D phase network interconnectivity, and hence such an approach for estimation of 3D tortuosity is bound to be associated with ambiguity.

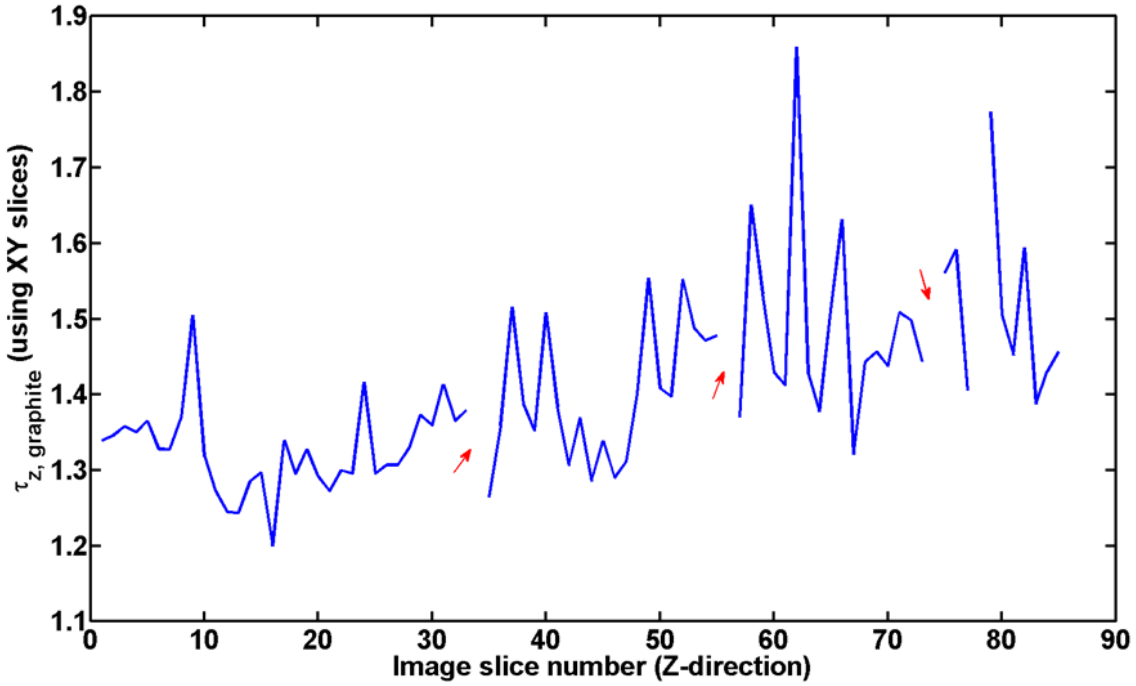

Figure 4.14. Slice-wise tortuosity profile of the graphite electrode pore phase across XY image sections.

Regions of tortuosity discontinuity highlighted by the red arrows in the inset plots signify no pore percolation across some 2D image section(s) within that region of the sample volume. Table 4.6 compares the stereological mean *z*-direction tortuosity (obtained using ZX image sections) with the directional tortuosities obtained directly from the 3D volumes. Here, the stereological mean *z*-direction tortuosities in each electrode sample appear to be largely overestimated as they are much higher than the *z*-direction tortuosities obtained from 3D analysis. This overestimation is most likely associated with the fact that the shortest pathway through such heterogeneous pore networks from a 2D cross-section is actually a much shorter route when the entire 3D pore network is considered.

Table 4.6. Comparison of geometric tortuosity obtained by stereological predictions and 3D analysis.

	Geometric tortuosity, τ						
Sample	**3D**	**Mean 2D (*z*-dir, *ZX* slices)**	**SD Dev. 2D (*z*-dir, *ZX* slices)**	**Min 2D (*z*-dir, *ZX* slices)**	**% U.E.**	**Max 2D (*z*-dir, *ZX* slices)**	**% O.E.**
LCO	τ_x : 1.078 τ_y : 1.060 τ_z : 1.011	1.170	0.069	1.023	1.18	1.919	89.82
Graphite	τ_x : 1.051 τ_y : 1.054 τ_z : 1.013	1.485	0.147	1.167	2.736	21.42	84.26
LMO	τ_x : 1.069 τ_y : 1.053 τ_z : 1.010	1.225	0.105	1.077	6.61	1.936	91.6

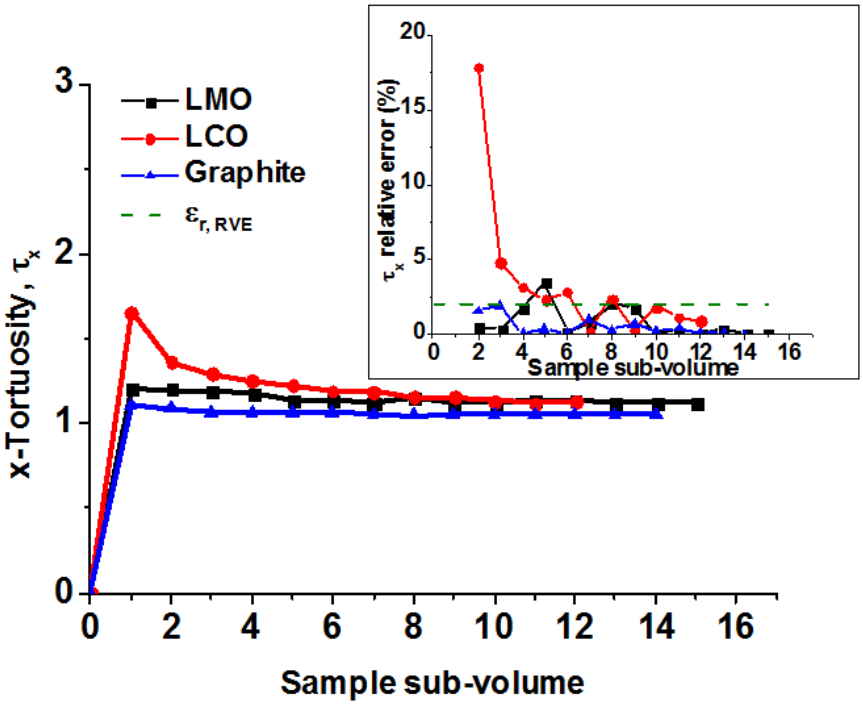

Figure 4.15. Evolution of 3D pore-phase tortuosity along the *x*-direction (main) and the relative errors (inset) versus sub-volume size for each electrode sample.

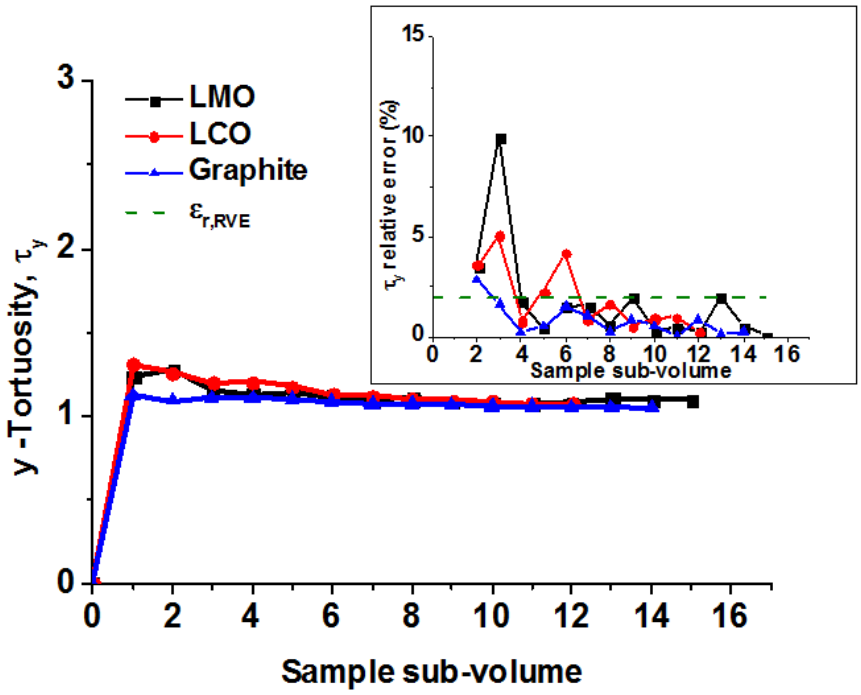

Figure 4.16. Evolution of 3D pore-phase tortuosity along the *y*-direction (main) and the relative errors (inset) versus sub-volume size for each electrode sample.

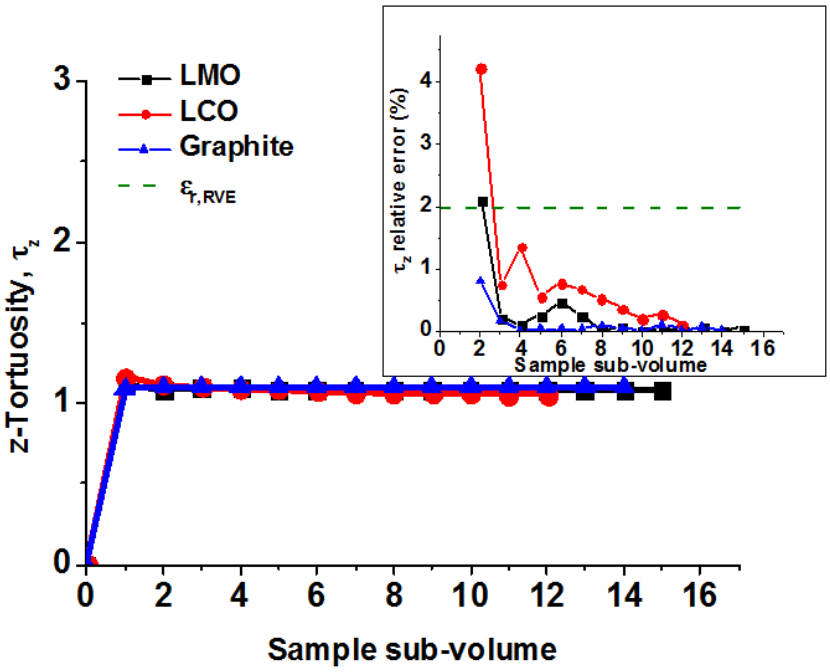

Figure 4.17. Evolution of 3D pore-phase tortuosity along the *z*-direction (main) and the relative errors (inset) versus sub-volume size for each electrode sample.

4.3.4 Pore radius

With the stereological approach, slice-wise profiles for mean pore radius were generated for each electrode sample using 2D sections generated along each axis. In all three samples, significant variations in pore radius are seen in each slice-wise profile along each axis. Moreover, in all three electrode samples, the mean pore radius values obtained along each axis direction appear to be in close range, as shown in Figure 4.18 – Figure 4.20 and in Table 4.7.

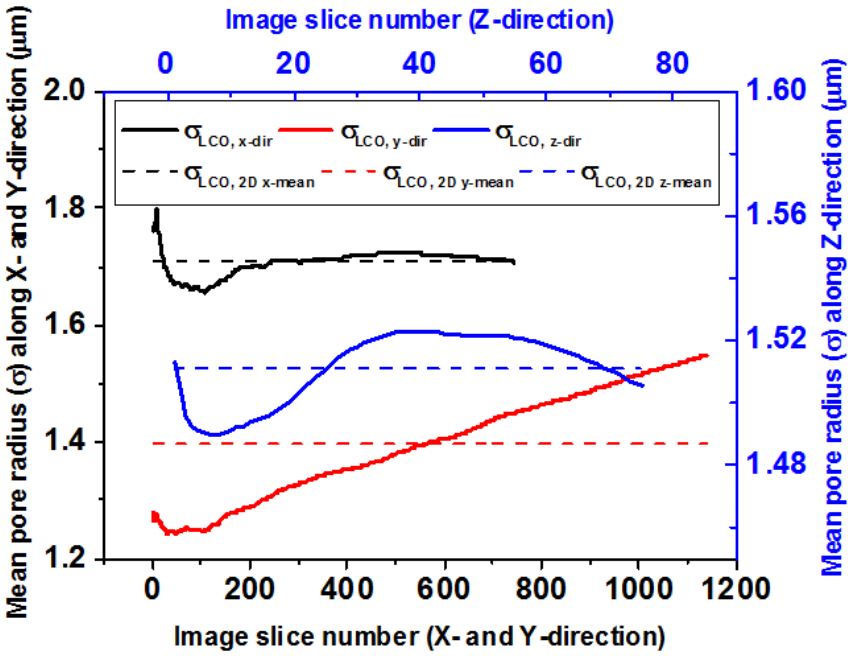

Figure 4.18. Mean pore radius profiles for the LCO electrode sample showing variation in slice-wise pore radii along the *x*, *y* and *z* directions.

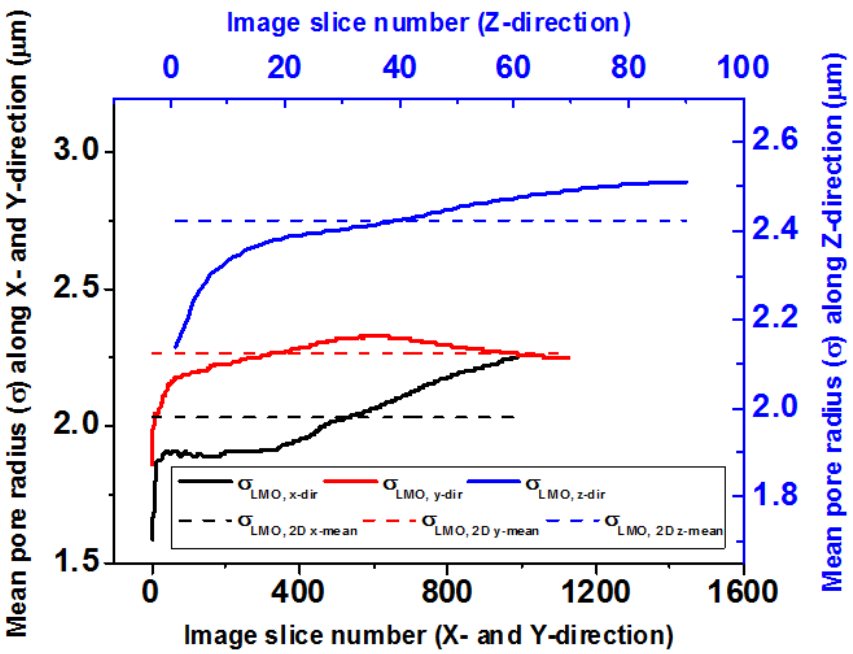

Figure 4.19. Mean pore radius profiles for the LMO electrode sample showing variation in slice-wise pore radii along the *x*, *y* and *z* directions.

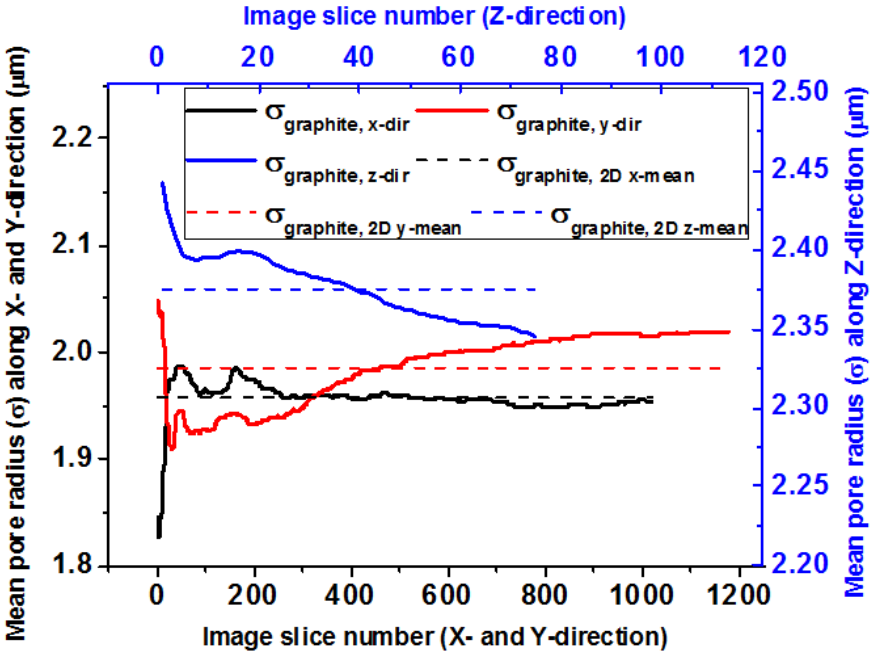

Figure 4.20. Mean pore radius profiles for the graphite electrode sample showing variation in slice-wise pore radii along the *x*, *y* and *z* directions.

Table 4.7. Comparison of pore radius obtained from stereological prediction and different 3D analysis methods.

Pore radius, σ							
Sample	**3D (μm)**	**Mean 2D (μm)**	**SD 2D (μm)**	**Min 2D (μm)**	**% U.E.**	**Max 2D (μm)**	**% O.E.**
LCO	DOHT: 1.049 MA-FM: 2.251 CPSD: 2.277 SMO: 2.394	*x-dir*: 1.708 *y-dir*: 1.397 *z-dir*: 1.511	0.021 0.092 0.011	1.656 1.243 1.490	27.26 45.43 34.56	1.797 1.549 1.523	21.07 31.99 33.12
Graphite	DOHT: 1.650 MA-FM: 3.531 CPSD: 3.031 SMO: 3.155	*x-dir*: 1.957 *y-dir*: 1.986 *z-dir*: 2.376	0.015 0.032 0.021	1.827 1.908 2.345	48.25 45.96 33.58	1.988 2.050 2.443	43.70 41.98 30.80
LMO	DOHT: 2.723 MA-FM: 3.680 CPSD: 3.408 SMO: 3.443	*x-dir*: 2.030 *y-dir*: 2.265 *z-dir*: 2.425	0.218 0.060 0.073	1.586 1.863 2.140	53.48 45.34 37.20	2.254 2.330 2.512	33.86 31.64 26.29

With regards to the 3D reconstructed volumes, four different approaches for extracting the mean pore radius parameter were examined, as outlined previously. Figure 4.21 shows a comparison of the pore radius distributions generated from these methods. Of all three electrode samples, the LMO electrode appears to have the broadest pore size distribution and the highest mean pore radius value.

It is also observed that the DOHT method gives a high frequency of smaller pores - this is associated with the tendency of the thinning algorithm to generate false branches and spurious nodes in the resulting skeleton, which are often induced by surface irregularities and image noise. However, these can be eliminated by “pruning” false branches within the skeleton, but this is a nontrivial process for such complex microstructures and could end up significantly altering the original topological skeleton.

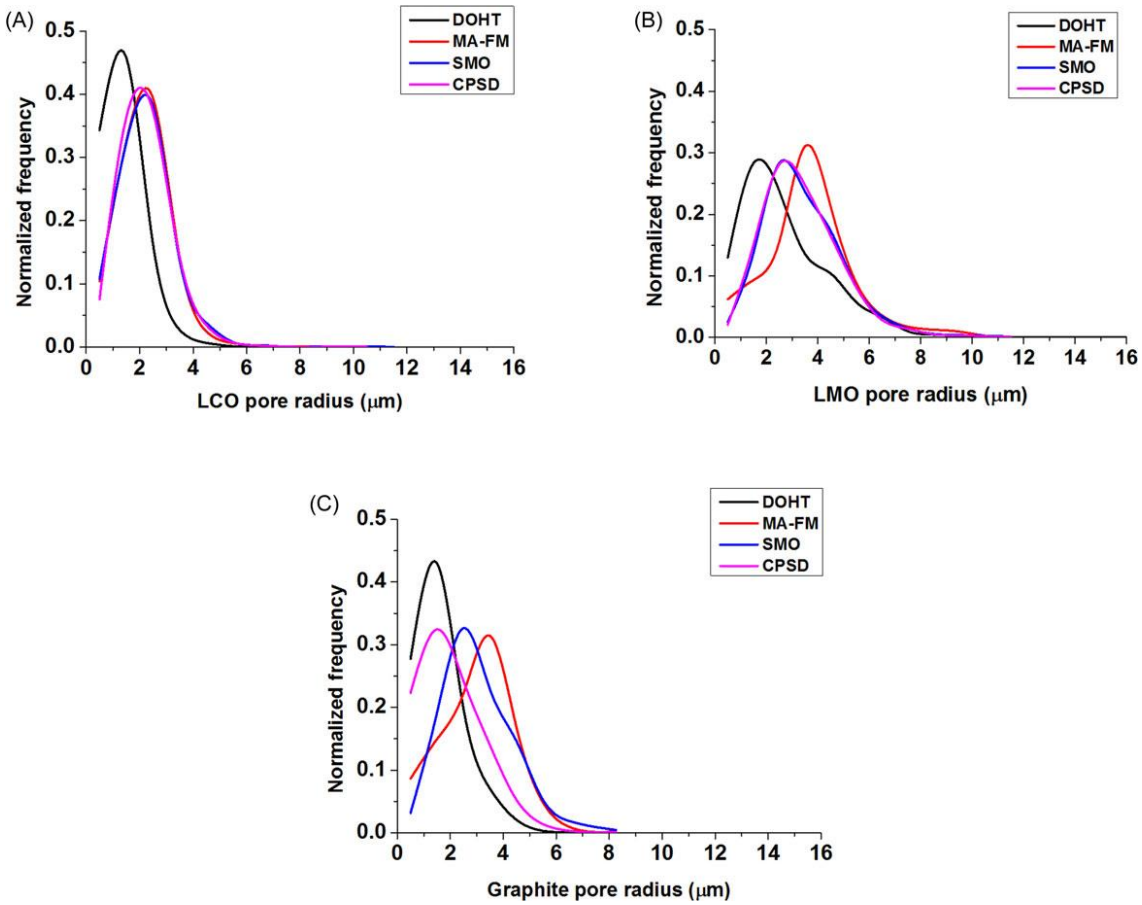

Figure 4.21. Pore radius distribution of the battery electrode samples (a) LCO, (b) LMO and (c) graphite.

The MA-FM method, however, shows a relatively higher frequency of larger pores. This is as a result of the characteristic of the fast marching algorithm employed to perform selective pore radius sampling on larger pore pathways rather than on every pore pathway due to the scaling of the speed map with the interfacial distance map [193]. The pore radius distribution generated with the MA-FM, SMO and CPSD methods are almost identical for the LCO sample. In both the LMO and LCO samples, the pore radius distribution curves from the CPSD and SMO methods are similar. However, this trend is absent in the graphite electrode sample, with the SMO method displaying a broad pore radius distribution.

It is noteworthy that pore-scale quantification of tomography data has been extensively validated against conventional porosimetry techniques [238–240]; moreover, the CPSD algorithm was developed to mimic the physical process of mercury porosimetry to extract values from tomography data that can be directly compared with porosimetry measurements.

Although these 3D pore size extraction methods are commonly used in pore-scale characterisation of porous materials, each of them has its advantages and drawbacks (e.g. DOHT method is easily affected by image noise and could create false skeleton branches and nodes, whereas the MA-FM method selectively samples pore pathways) and the differences in calculated pore radius values suggests that there stands the risk of confusion about the geometric definition of pore size and size distribution. However, the CPSD method would be expected to have a high degree of accuracy as it includes all possible pathways including narrow bottlenecks and dead-ended pores, and is not limited by possible errors from topological skeleton creation.

Therefore, it is recommended that one proceed with caution when selecting amongst these pore size calculation methods for quantifying complex porous microstructures, and consequently any comparison of 3D pore size distribution should fully account for inherent differences that may be present in the calculation methodology. Moreover, even as all pore size calculations should be independent of imaging resolution (as the digital image resolution dependencies decrease once the voxel size falls below that of the structures to be resolved), it is useful to image the porous material of interest at a sufficiently high resolution to reduce the effect of possible artefacts from image processing. Applying a multiscale 3D imaging approach [24] will provide a good validation for microstructural quantification. Furthermore, when the stereological mean pore radii values were compared with the mean pore radius values obtained using the CPSD method, large underestimations (and overestimations) of over 20 % were observed.

4.4 Conclusion

In this chapter, both stereological prediction and 3D analysis techniques for quantitative assessment of key geometric parameters for characterising lithium-ion battery electrode microstructures were examined and compared. Quantitative analysis was carried out on image data obtained from imaging battery electrode samples using synchrotron-based X-ray tomographic microscopy. For each electrode sample investigated stereological analysis was performed on 2D planar image slices generated from tomographic imaging, whereas direct 3D analysis was performed on rendered

image volumes. Representative volume element analysis was performed to ascertain the selected 3D volumes examined were representative of the bulk electrodes.

The results showed that stereological estimation of inherently 3D microstructural parameters using a single 2D image section is bound to be associated with ambiguity and may lead to significant parameter under- or overestimation. Significant variation in measured parameters observed using 2D planar image sections highlights the presence of localised microstructural heterogeneities within the electrode materials. Pore volume fraction measurements using stereological prediction showed smaller parameter variations using planar slices normal to the *z* direction; in this case, stereology could be useful to obtain an initial approximation for pore volume fraction but in order to obtain complete information on a statistically non-homogenous microstructure, direct 3D measurement cannot be replaced by stereological relationships. Discontinuities in the planar tortuosity profiles show that the tortuosity within inherently 3D networks cannot be geometrically measured from 2D cross-sections or planar slices, as tortuosity relies on exactly how and where the phase networks branch out and interconnect in three dimensions. This also demonstrates that 3D measurement of non-convex, irregular and interconnected pore networks are more suited for accurately quantifying spatial parameters, like tortuosity and phase connectivity.

Also, four different methods to extract pore size distributions in 3D are compared. The CPSD and SMO methods give similar pore-size distributions curves as they consider the entire network including dead-ended and isolated pores, as opposed to the MA-FM method which tends to sample major pore pathways. It is recommended that comparison of 3D pore size distributions should fully account for inherent difference that may be present in each calculation methodology.

Three-dimensional characterisation has undoubtedly furthered the understanding of LIB electrodes, revealing the complexity of their microstructural features. Establishing suitable quantification techniques for analysing 3D reconstructed battery electrodes with statistical confidence will aid in providing representative information on microstructural parameters and show how these parameters evolve during battery operation and even degradation, as in demonstrated in the following chapters.

Chapter 5

4D Characterisation of Metallic Lithium Electrode Microstructures using X-ray Micro-CT

5.1 Introduction

A range of diagnostic tools have been used by researchers to study the formation of dendritic/mossy microstructures in lithium batteries. Optical and electron microscopy have been used for two-dimensional (2D) characterisation of electrodeposited Li microstructures and lithium metal surface morphology changes [11,241–243], providing a wealth of qualitative information on their inherently three-dimensional (3D) structure. However, most of these studies were performed *ex-situ*, thus requiring cell disassembly and removal of the lithium microstructures from their *as grown* environment. NMR and MRI investigations are non-invasive and have been successfully carried out *in-situ* to capture the formation of dendritic and electrodeposited lithium structures [19,128]; however the resolution of MRI is limited, typically 100 µm [244], and the presence of metals can introduce imaging artefacts [245]. There have also been reported attempts to theoretically model different electrodeposited Li growth with regards to their morphologies and feature size distributions [143,246–248].

X-ray computed tomography (CT) enables non-invasive acquisition of high spatial resolution 3D images of materials *in-situ*; however, applying tomographic imaging to Li can be rather challenging due to its low attenuation coefficient which limits X-ray absorption contrast. Recently, X-ray CT has been used to visualize metallic Li microstructures. Harry *et al*. [129] first used synchrotron-based X-ray CT to image metallic Li microstructures in Li-polymer cells, demonstrating the role of subsurface dendritic structures within a Li metal electrode in the failure of lithium batteries. With bespoke Li/Li symmetrical cells, the author, in a collaborative study with Eastwood *et al*. [249], used synchrotron X-ray phase contrast imaging to characterise different

forms of Li microstructures. In this previous study, the author with Eastwood *et al.* were able to distinguish between mossy metallic Li microstructures from high surface area lithium salt deposits by their contrasting X-ray attenuation. However, X-ray CT can be extended to explore temporal evolution of material microstructures within batteries during operation or failure, thus giving rise to the notion of "4-dimensional" tomography (i.e. 3D plus time) and even enabling quantitative information on 3D microstructural dynamics to be extracted.

In this chapter, the use of both synchrotron and laboratory-based X-ray micro-tomography to perform both *in-situ* and *operando* characterisation of the morphological evolution that occurs at the surface of Li metal electrodes is demonstrated.

5.2 Electrode preparation and cell assembly

Using the *in-situ* Swagelok cell design described in Section 3.7.2, half-cells were assembled in an argon-filled glove-box (O_2 and moisture level maintained at < 0.5 ppm) using metallic lithium as positive electrode, graphite as negative electrode, a borosilicate glass microfiber separator (Whatmann GF/B grade, GE, UK), and 1M $LiPF_6$ in 3:7 vol/vol of ethylene carbonate (EC) : ethyl methyl carbonate (EMC) as electrolyte. Graphite electrodes were prepared as a slurry mixture containing graphite powder (TIMREX® SLP30, TIMCAL, Switzerland), carbon black (Super P, Sigma Aldrich, UK), and PVDF binder (Pi-KEM, UK) in the respective percentage weight ratios 87:3:10 in *n*-methyl-2-pyrrolidone (Pi-KEM, UK). This slurry was coated onto the tip of stainless steel current collecting pins, and dried at 80 °C under vacuum for 24 h. The metallic lithium electrodes were cut out from a 200 µm thick lithium foil (Pi-KEM, UK) into 3.2 mm diameter discs.

5.3 *Operando* synchrotron X-ray tomography study during single discharge

The morphological changes at the surface of a Li metal electrode during the first discharge of an assembled graphite/Li half-cell were examined using *operando* X-ray CT. Synchrotron X-ray CT experiments were conducted at the Diamond-Manchester Imaging Branchline I13-2 of Diamond Light Source, UK. The experimental setup is shown in Figure 5.1. The mounted half-cell sample was electrically insulated

from the sample stage to prevent interference. A partially-coherent, polychromatic 'pink' beam (5 to 35 keV) of parallel geometry was used with an undulator gap of 5 mm. The pink beam was chosen as it can provide higher signal-to-noise images with shorter exposure times, high temporal resolution and improved spatial resolution (due to decreased blurring), relative to a monochromatized beam. Compared to a monochromatic beam, the photon flux of the pink beam is about 50 – 100 times higher [250].

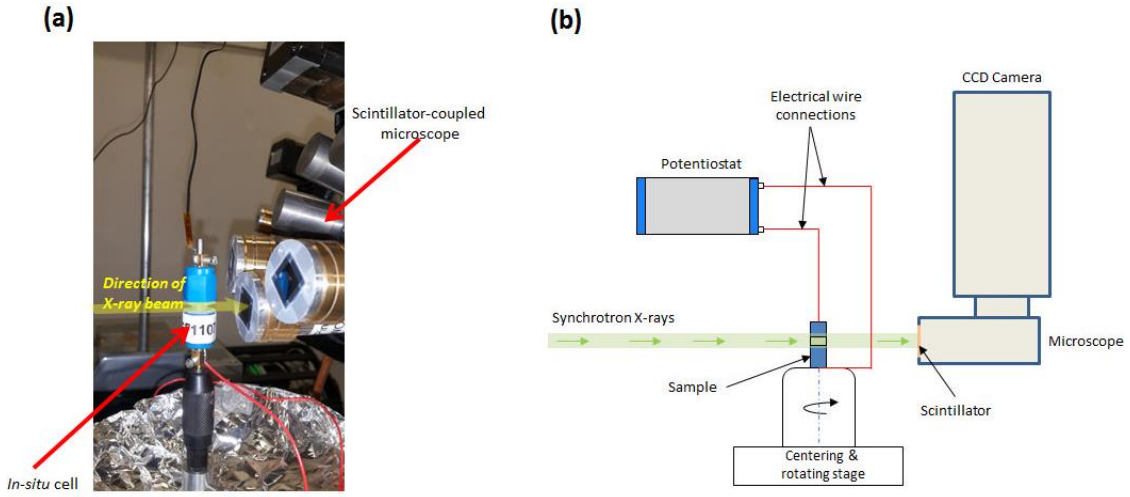

Figure 5.1. (a) Optical image of the *in-situ* cell mounted for synchrotron X-ray CT. (b) Schematic representation of the experimental beamline setup for *operando* synchrotron X-ray CT.

The beam coming into the experimental hutch was reflected from the platinum stripe of a grazing-incidence focusing mirror and filtered with 950µm-thick pyrolytic graphite, 2 mm-thick aluminium and 20 µm-thick nickel filters. For each tomogram of the examined half-cell sample, 4000 projection images of exposure time 160 ms each were recorded at equally-spaced angles over 180° of continuous rotation (along the sample's long axis) by a pco.edge 5.5 (PCO AG, Germany) detector. The detector was coupled to a 500µm $CdWO_4$ scintillator and visual light optics, providing 8x total magnification, a field of view of 2.1 × 1.8 mm (2560 × 2160 pixels) and an effective pixel size of 0.81 µm. A propagation distance (between the sample and the detector) of approximately 25 mm was used to provide minimal inline phase contrast. Prior to reconstruction via filtered back projection with DAWN 1.7 software [251], projection images were flat- and dark-corrected and ring artefact suppression was performed [252].

Galvanostatic discharge of the half-cell from open circuit voltage to 0.005 V was performed using a potentiostat (Ivium Compactstat, Ivium Technologies) at a rate of 20 mAg^{-1}, which is estimated to be a C/20 C-rate based on graphite material mass. Tomograms of a central region within half-cells were successively acquired every 15 min during discharge, including a rest period of 120 s between each successive tomogram acquisition, and a total of 44 successive X-ray tomograms were acquired in the course of the half-cell discharge.

Figure 5.2(a) shows a vertical cross section through the tomogram of a half-cell sample before operation, and Figure 5.2(b) shows a selected sequence of time-resolved tomogram cross-sections of a magnified region of interest that captures gradual pit formation along the Li metal electrode surface as a result of electrochemical discharge. Volume renderings of this magnified region [presented in Figure 5.3 and Figure 5.4(a)] provide qualitative insight into the 3D morphological structure and evolution of these pits. The pits appear roughly hemispherical in shape and are seen to gradually increase in both diameter and depth as the half-cell discharge progresses. In Figure 5.4(b), a gradual increase in the volume fraction of pits within the analysed sample volume is clearly observed as a result of the cell discharge.

The occurrence of similar pit-like holes on the surface of cycled lithium electrodes has previously been identified using electron microscopy [138,144,242,253]. It was found that pit morphology and growth rate along the metallic Li electrode surfaces can be a function of electrolyte composition and applied current density. In addition, such electrochemically–induced pitting has been previously observed to be associated with the breakdown of the passive layer on the metal surface, which could be as a result of the penetration of PF_6^- anions from the electrolyte through the layer, causing localized variations in interfacial energy and thus resulting in the local dissolution of the lithium metal surface [254]. Moreover, previous investigations also show that such lithium dissolution could take place preferentially along surface defects such as those induced during manufacturing or prior handling of the Li metal electrode [242,255].

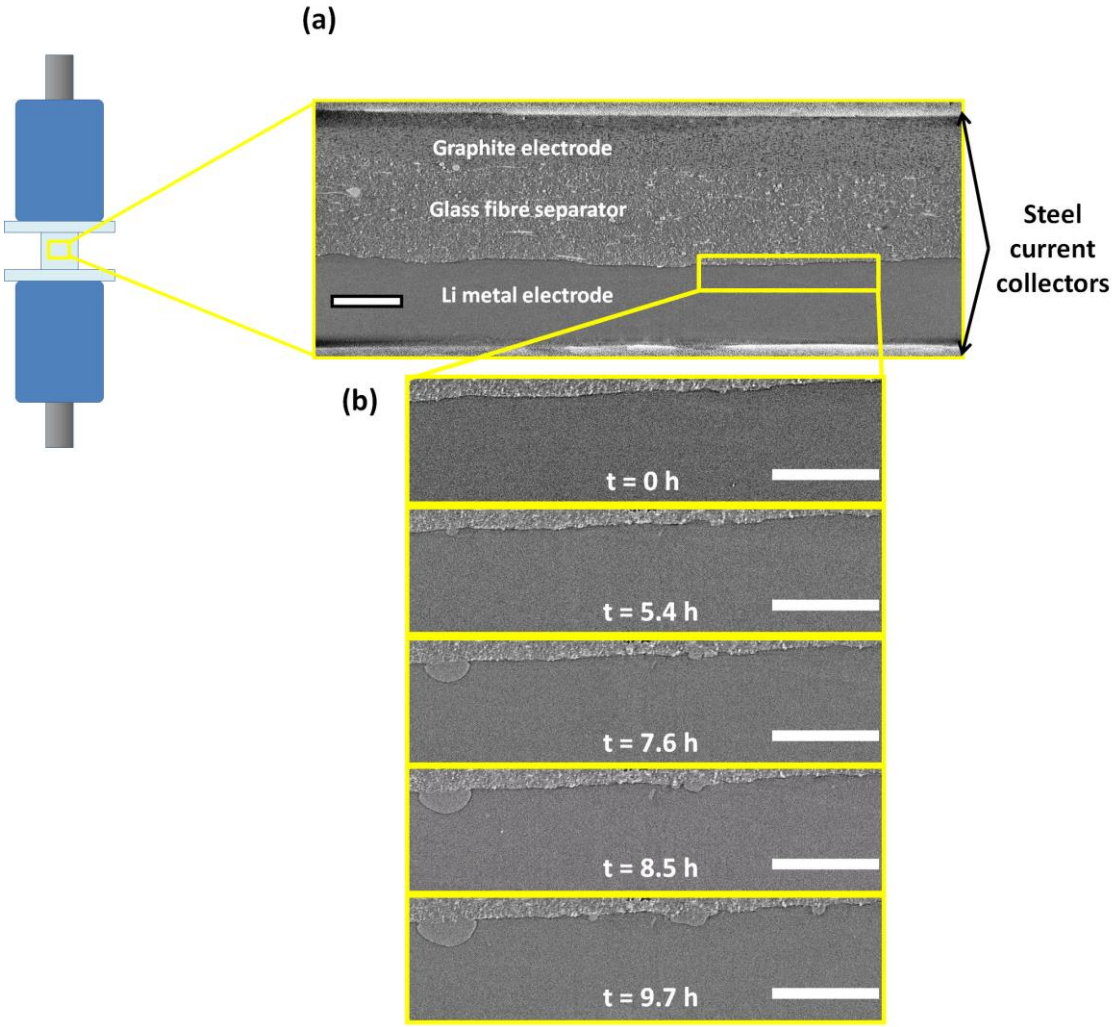

Figure 5.2. (a) X-ray tomogram cross-section through the half-cell assembly. (b) Magnified region of tomogram section showing gradual pit formation on the Li metal surface during cell discharge at a constant rate of 20 mAg^{-1}. Scale bars represent 200 µm.

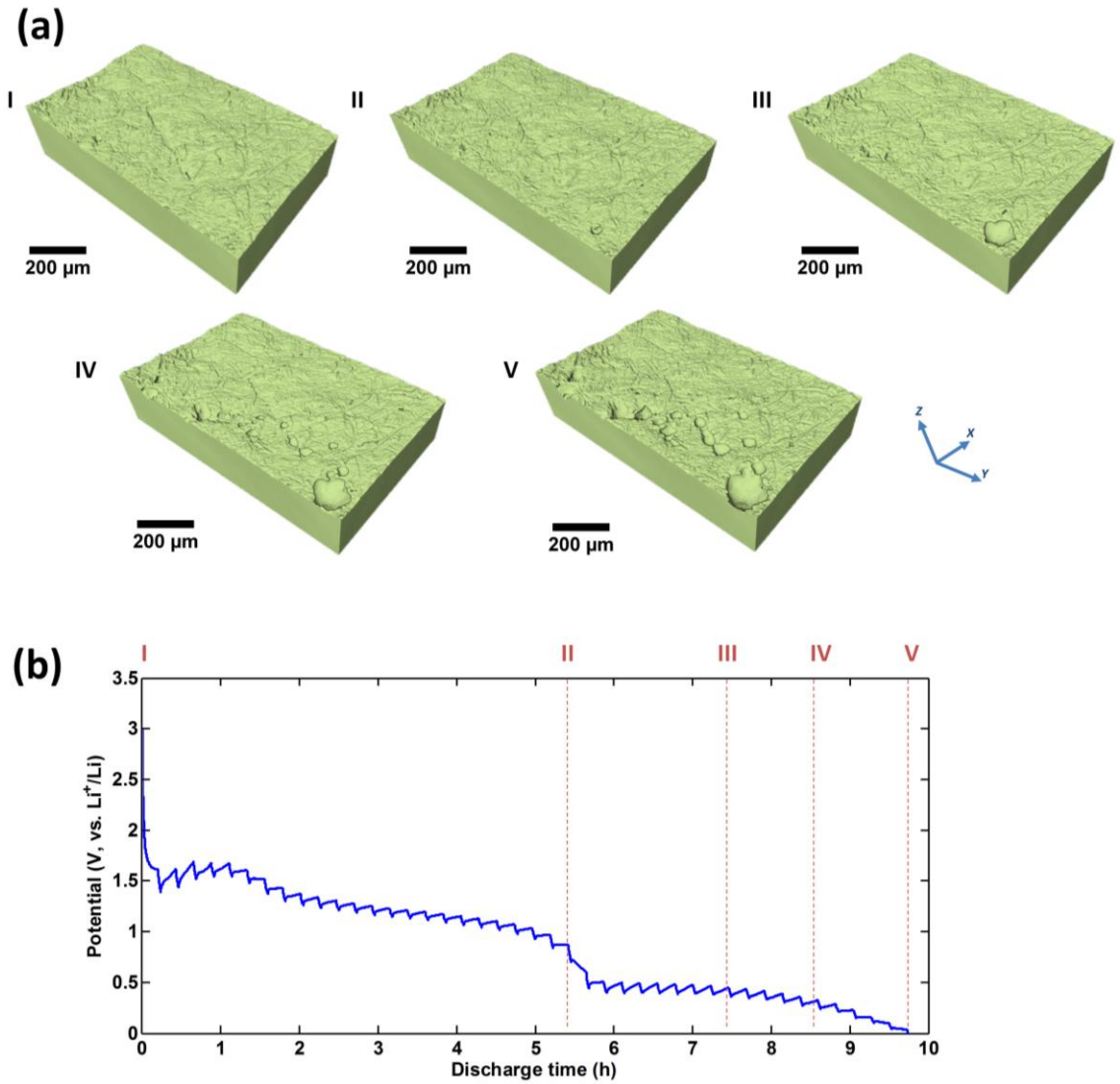

Figure 5.3. (a) 3D renderings of the lithium metal surface within the magnified region in Figure 5.2b at different stages during the half-cell discharge at a constant rate of 20 mAg^{-1}. The discharge voltage profile of the cell is plotted in (b) and relates the 3D renderings to time.

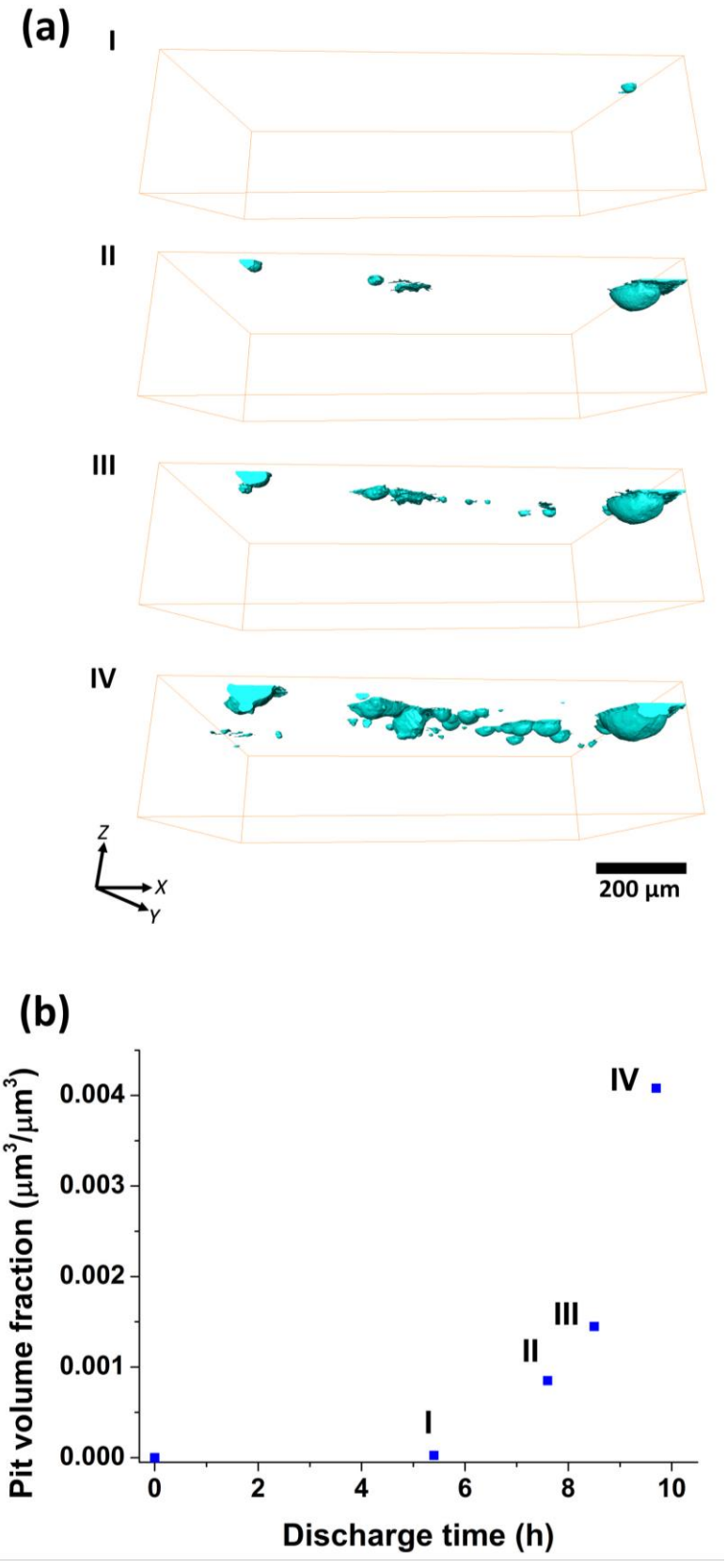

Figure 5.4. (a) Volume rendering of the pits formed along the lithium metal surface within the magnified region in Figure 5.2b at different stages of the half-cell discharge. (b) Variation of pit volume fraction with discharge time within the analysed sample region.

Although the primary investigation here was to visualize and track morphological changes occurring at the surface of the lithium metal electrode during the course of a single discharge, some other interesting observations were made. During exposure of the operating half-cell to the intense synchrotron radiation, a loss in cell performance as well as a deviation from the normal half-cell electrochemical behaviour was observed. Figure 5.5 shows the resulting electrochemical discharge profile of the graphite/Li half-cell during *operando* synchrotron X-ray CT. Sequential fluctuations or 'upward humps' in the voltage profile of the graphite/Li half-cell were seen, with their occurrence corresponding with tomogram acquisition periods when the sample was exposed to the pink beam. A typical graphite/Li half-cell discharge is normally associated with a decline in the cell voltage as shown by the red-dotted voltage profile in Figure 5.5. However, with the half-cells used in the X-ray experiments, increases in the half-cell voltage occurred each time the X-ray shutter was open, such as during each tomogram acquisition and flat-image acquisition where the half-cell sample was exposed to the high flux X-rays. Between each successive tomogram acquisition was a 120 s rest period during which the X-ray shutter was closed: during this period, the half-cell voltage reverts to the expected decreasing profile. These fluctuating trends in electrochemical behaviour are found to be similar to that previously observed during intermittent X-ray irradiation of TiO_2 film electrodes, where exposure to synchrotron X-rays promoted photoelectrochemical reactions [256], and also during exposure of low temperature fuel cells to high intensity synchrotron radiation [257–259].

Significant degradation in half-cell discharge performance during exposure to the high intensity X-ray beam was also observed – the discharge of the irradiated half-cell was completed in *ca.* 10 hours rather than an expected 20 hours based on the estimated C/20 current rate. Moreover, a lower specific discharge capacity of 159 $mAhg^{-1}$ was obtained with the irradiated cell while a discharge capacity of 370 $mAhg^{-1}$ achieved with no X-ray exposure.

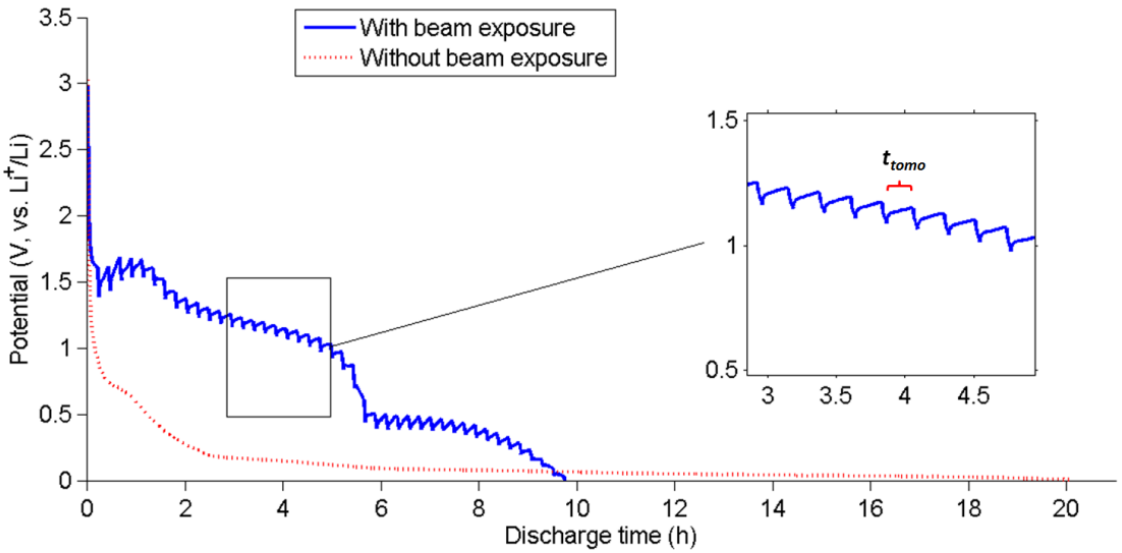

Figure 5.5. Discharge profile of the graphite/Li half-cell during operando CT (blue line) and without any exposure to the pink beam (red dotted line). Both half-cell discharges were performed at a C/20 current rate. Each tomogram acquisition period (t_{tomo}) corresponded with the period of abnormal discharge voltage behaviour.

To ensure that the observed performance degradation phenomenon was not caused from interference to the cell's electrical connections from sequential sample rotation / tomography acquisition, the beamline was set to radiography mode (i.e. no sample rotation) and the open-circuit voltages of more identical graphite/Li half-cell samples were repeatedly measured during discharge with and without X-ray irradiation (i.e. when the X-ray shutter was in open or closed state). It was observed that even in radiography mode, oscillations in cell voltage similar to those seen in Figure 5.5 occurred in each of the irradiated cell samples whenever the X-ray shutter was opened or closed, in addition to shorter discharge times and lower discharge capacities. From these observations, it could be said that the exposure of the sample to the intense X-ray beam induced performance degradation in the half-cell.

It is suspected that the observed performance degradation behaviour is the result of sample interaction with the ionising beam, causing increased internal resistances within the half-cell and thus a loss in performance. Similar degradation phenomena in electrochemical behaviour have been detected in lithium-ion full cells and half-cells containing $LiPF_6$-based electrolytes that were exposed to ionising radiation: Ding *et al*. observed substantial deterioration in cell performance after gamma radiation exposure [260–262] and attributed the decline in performance to the

production of carboxyl groups in the electrolyte which react with active lithium metal, causing an increase in cell impedance and a decrease in charge and discharge capacity. Gamma radiation – induced capacity degradation has also been observed in lithium polymer cells [263], with increased radiation dose in cells leading to shorter discharge time and lower specific capacity. Such electrochemical behaviour was not observed during synchrotron X-ray CT experiments previously reported [176,264] which employed a lower intensity monochromatic X-ray beam. Moreover, these findings highlight the need for careful consideration of radiation dose that would prevent performance losses in functional materials when using ionising beams such as X-rays are used as a diagnostic tool.

5.4 Time-lapse laboratory X-ray tomography study during repeated cycling

To observe the effect of repeated charge-discharge cycling on the surface morphology of Li metal *in-situ*, X-ray CT was performed on another assembled graphite/Li half-cell using a microfocus tube 'laboratory source' X-ray microscopy system equipped with a tungsten anode target (ZEISS Xradia Versa 520, Carl Zeiss X-ray Microscopy Inc., USA). X-ray CT scans were performed on the half-cell in its original state immediately after assembly and after 10, 70 and 135 charge-discharge cycles. The half-cell was galvanostatically cycled at a C/5 C-rate between 0.005 V and 1.0 V using a battery cycler (Maccor 4300 series, USA).

For each tomographic image acquisition, the half-cell was mounted firmly onto a sample holder and placed on the rotating sample stage between the X-ray source and a 2*k* × 2*k* detector, as previously shown in Figure 3.25. Tomography datasets were collected at 20× magnification in absorption-contrast mode. The projection image datasets were reconstructed using a commercial image reconstruction software package (ZEISS XMReconstructor, Carl Zeiss X-ray Microscopy Inc., Pleasanton, USA) which employs a filtered back-projection algorithm. Details of the experimental parameters for each tomographic scan are presented in Table 5.1. The tomograms were 3D median filtered using Avizo software to reduce random image noise.

Figure 5.6(a) shows tomogram cross-sections through the graphite/Li half-cell at different stages in its cycle life. As seen in Figure 5.6(a), the half-cell components

were distinctly resolved: the dark-grey topmost layer is the low-attenuating Li metal electrode; the middle layer is the glass-fibre separator with relatively highly attenuating microfibers and the porous graphite electrode at the bottom. Also captured in the tomogram is a clear outline of the Li metal surface in contact with the glass-fibre separator. The Li metal surface is originally smooth and almost featureless prior to cell assembly; however, pressure applied to the cell during assembly causes the separator microfibers to leave imprints upon contact with the soft Li metal surface, as seen in the volume renderings of the Li surface in Figure 5.3.

Table 5.1. Scan parameters for tomographic experiments

Scan Parameters	0 cycles	10 cycles	70 cycles	135 cycles
Source voltage (kV)	50	35	50	50
Radiograph exposure time (s)	75	66	66	66
Number of projections	1601	3201	2151	2201
Source-detector distance (mm)	29	29	29	29
Effective voxel size (µm)	0.75	0.75	0.75	0.75

After 10 cycles, the presence of a low attenuation, morphologically distinct layer is observed on the Li metal surface. The corresponding 3D rendering in Figure 5.6(b) shows this layer to be a moss-like deposit, which appears to penetrate the surface of the fibrous separator. Such moss-like deposits, as well as dendrite formation, are known to occur as a result of non-uniform lithium electro-deposition during repeated charge and discharge cycles. Previous investigations using electron microscopy (e.g. [241,242,255,265]) have shown that lithium moss and dendrite nucleation and growth upon subsequent Li deposition during charge cycling takes place preferentially along dissolution pits such as those identified in the *operando* CT study. This has been attributed to locally enhanced current densities at such regions on the electrode surface. As the cell cycling progresses, the lithium moss is seen to gradually increase in thickness and penetrate through the fibrous separator [Figure 5.6(b)]. These deposits can continually grow through the separator to create contact between both electrodes and initiate internal short-circuits, which could lead to hazardous battery failure via short circuiting. Dendritic growth within lithium batteries continues to present significant safety risks; as such, there are currently research efforts into their early detection within the batteries before short circuiting occurs

[266]. Furthermore, these imaging results highlight the influence of separator selection on the overall performance and safety of lithium batteries: highly tortuous, less porous separators are favourable in suppressing dendrite growth and contact between electrodes that can cause short circuits; however, such separator structure does not promote high rate capability and fast ion transport.

The cycling performance of the graphite/Li half-cell is presented in Figure 5.7(a). After 135 cycles, the graphite/Li half-cell showed a 51 % drop in capacity. The apparent capacity fade seems typical of cells containing Li electrodes, as repeated cycling of Li electrodes leads to continuous SEI layer formation, causing significant Coulombic efficiency losses, lithium consumption, and increased cell impedance [267].

The mossy lithium deposited on the metallic Li electrode surface forms a porous, micro-structured layer that gradually penetrates through the microfiber separator. As shown in Figure 5.8, the volume and thickness of the mossy Li layer increase as cell cycling progresses. The mean thickness of the mossy layer measured from the surface of the metallic Li electrode after 10 cycles was 35 µm. After 70 cycles, the mossy layer thickness increased to 130 µm (with 65 µm of the mossy layer penetrating the microfiber separator) and eventually to 180 µm (with 100 µm of the layer penetrating the microfiber separator) after 135 cycles. Moreover, the thickness and volume of the residual (unreacted) lithium electrode is seen to decrease as the cell cycling progresses. These observations are in good agreement with Lopez *et al*. [241] who, using scanning electron microscopy, identified the presence of a thin dendritic layer (a few micrometres thick) on top of a dense porous mossy layer (several tens of micrometres thick) growing above the residual Li metal, and observed that the thickness of the micro-structured layers increase significantly with repeated cycling.

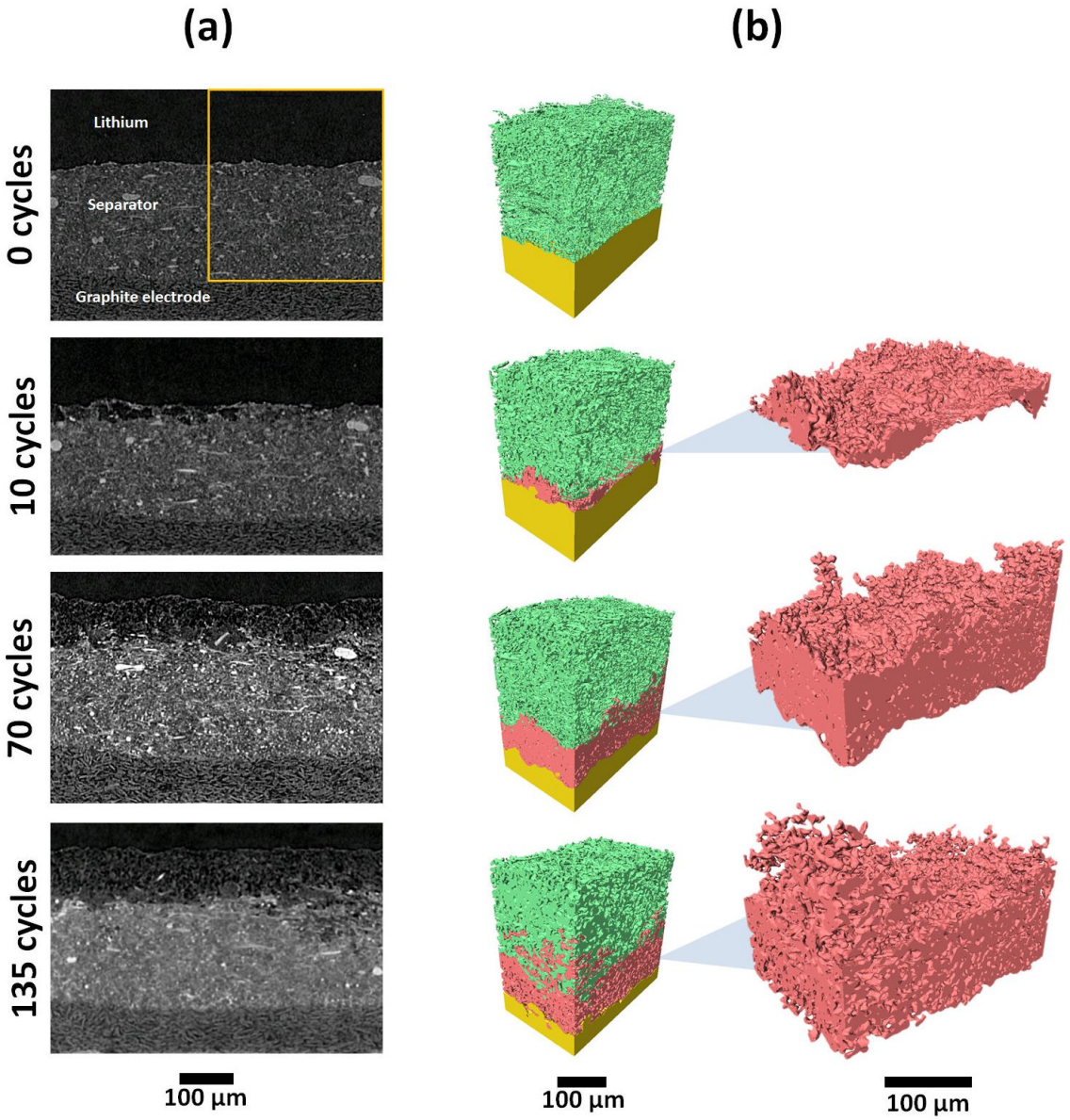

Figure 5.6. (a) Vertical cross-sections through the tomogram of the half-cell at different cycle number. The orange rectangle in the panel at 0 cycles indicates the sub-volume of interest extracted in each acquired tomogram for subsequent analysis. The white scale bars represents 100 µm. (b) Corresponding 3D renderings of the sub-volume of interest highlighted at different cycle number, where the separator is shown as green, the mossy lithium phase is shown as pink and the non-porous residual lithium layer is shown as yellow.

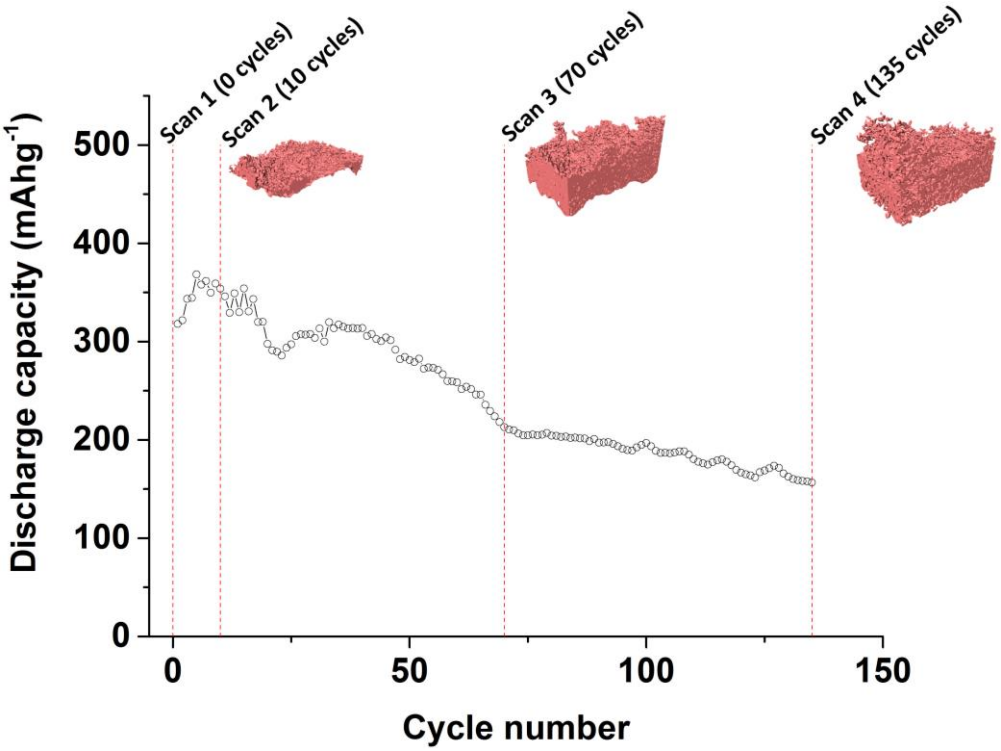

Figure 5.7. Cycle performance of the *in-situ* graphite/Li half-cell. Red dashed lines mark each tomogram acquisition point, and volume renderings of the mossy lithium formed are shown at each marked cycle stage.

Phase volume fraction and pore size distribution information were also extracted from the mossy layer in the image reconstructions. Here, the moss volume fraction is taken as the fraction of the mossy lithium volume within the analysed sample volume, and pore size calculations were performed only on the porous mossy lithium layer using the continuous pore size distribution method [201]. In Figure 5.8, the 3D moss volume fraction within the analysed sample volume increases from 0.026 after 10 cycles to 0.16 after 70 cycles and appears to remain fairly constant at 135 cycles. However, after a 2D slice-wise examination of the moss volume fraction using a stereological relationship [268], a decrease in slice-wise volume fraction of the Li moss is observed along the *z*-height (through-plane direction) of the sample volume between 70 and 135 cycles, as shown in Figure 5.9. This decrease can be attributed to the increase in porosity of the mossy layer with repeated cycling. In the tomogram taken after 70 cycles, the porous nature of the mossy layer was revealed with a measured porosity of 13.4 % which increased to 39 % after 135 cycles. Porosity information on the mossy layer was not extracted after 10 cycles, as the porous nature

of the mossy microstructure could not be sufficiently resolved at the employed imaging length scale.

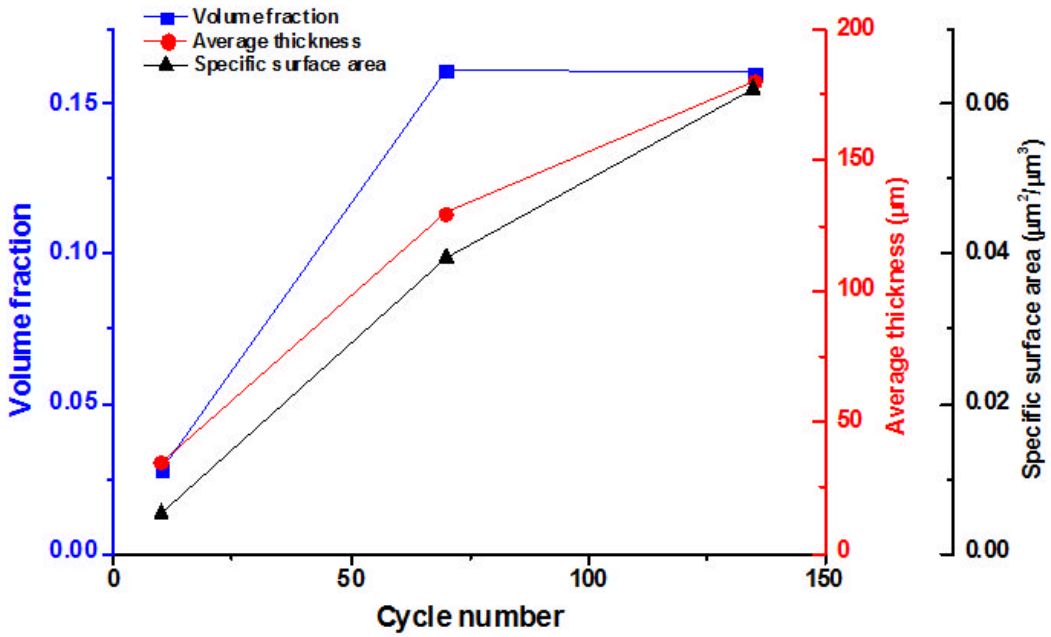

Figure 5.8. Variation in 3D moss volume fraction, average thickness and specific surface area of the entire porous mossy lithium layer with cycle number.

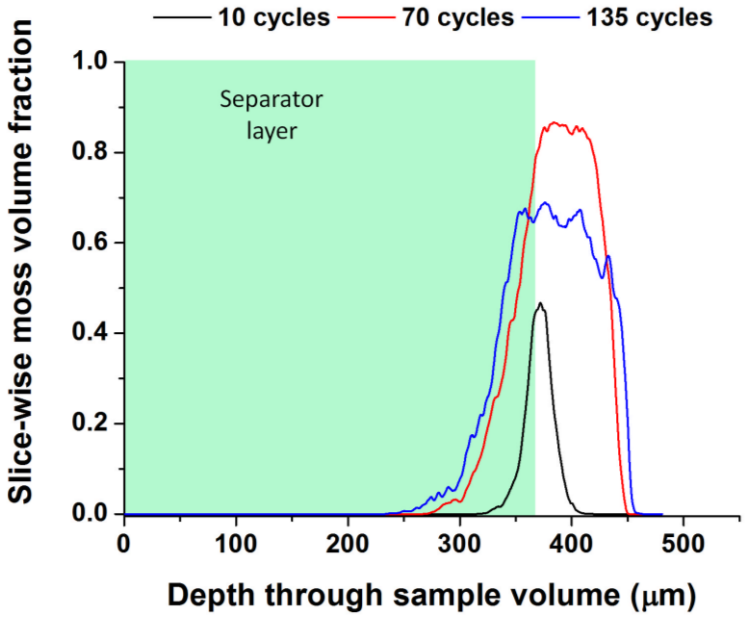

Figure 5.9. Slice-wise variation of Li moss volume fraction along the *Z*-axis direction (sample volume depth) at different cycle number.

Moreover, the pore size distribution information extracted from within the mossy layer, which is presented in Figure 5.10, shows that there is a clear increase in

the pore size within the mossy lithium layer, with the average pore size increasing from 3.1 µm to 5.3 µm between 70 and 135 cycles. The observed increase in porosity and pore size could be attributed to occurrence of heterogeneous dissolution within the mossy microstructure during repeated charge cycling, which could also lead to the formation of electrically isolated Li [269]. The pore sizes obtained are in good agreement with previous research [241]. Also, the specific surface area of the mossy lithium microstructure is seen to increase with cycling in Figure 5.8, which can be related to the increase in porosity and pore size within the mossy layer.

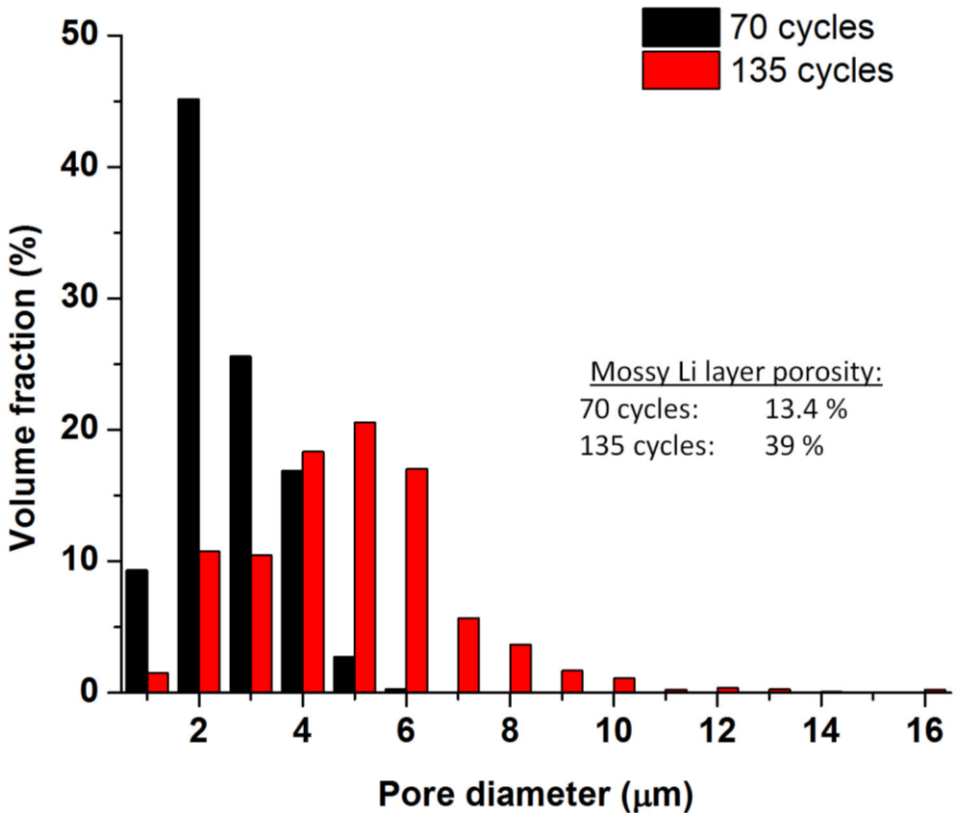

Figure 5.10. Pore size distribution within the porous mossy lithium layer at 70 and 135 cycles. Pore size distribution was calculated using the continuous pore size distribution method.

5.5 Conclusion

The morphological changes that occur at the surface of lithium metal electrodes in rechargeable lithium batteries have been characterised *in-situ* and *operando* with X-ray tomographic imaging using both synchrotron and laboratory based X-ray sources. *Operando* synchrotron X-ray CT enabled the real time 3D visualization of pit formation at the Li metal surface due to Li dissolution. Time-lapse laboratory X-ray CT imaging was used to track the growth of moss-like lithium deposits

at the Li electrode surface over longer periods of cycling. The 3D imaging data showed the appearance of pit-like holes on the Li metal surface as a result of Li dissolution during the first discharge, and the formation of a mossy, micro-structured lithium layer that increased in thickness with repeated cell cycling, penetrating the separator in the process. The results also highlight the importance of separator morphology in controlling or preventing dendrite growth in high tortuosity separators within commercial lithium batteries

Microstructural parameters such as phase volume fraction, pore size distribution and specific surface area were used to quantitatively track the evolving microstructure of the metal electrode surface. The porosity and specific surface area of the mossy lithium layer formed upon repeated cycling are seen to increase with cycle number, most likely due lithium dissolution, and further dissolution could lead to the formation of electrically isolated lithium and thus reduced cell capacity.

Analysis of the mass balance of Li between the mossy micro-structured layer and the residual unreacted Li layer was not conducted here because the Li metal electrode used in this study (3.2 mm diameter) was larger than the X-ray field of view (*ca.* 1 mm wide). However, the aid of an electrode assembly design smaller than the employed X-ray field of view, future experiments will look at quantitatively tracking the amount of Li consumed during Li dissolution and the amount of mossy Li deposited via material balance calculations.

Although the high flux of the synchrotron pink beam provided sufficient resolution and contrast that enabled identification and tracking of surface morphology changes within the low attenuating Li metal, beam exposure to the sample led to performance degradation. Based on the findings from the synchrotron CT experiments, the X-ray radiation dose to the cell samples must be carefully considered to prevent material degradation and cell performance losses.

This 4D microstructural investigation approach using X-rays can also be extended to study a variety of electrode materials, especially those that experience significant volume changes in microstructure as a result of battery operation, such as silicon – which is the focus of the next chapter.

Chapter 6

4D Characterisation of Silicon Electrode Microstructures using X-ray Micro-CT

Portions of this chapter are reproduced in part with permission from the following publications: “4D analysis of the microstructural evolution of Si-based electrodes during lithiation: Time-lapse X-ray imaging and digital volume correlation”, J. M. Paz- García, O. O. Taiwo, E. Tudisco, D. P. Finegan, P. R. Shearing, D. J. L. Brett, and S. A. Hall, *Journal of Power Sources*, vol. 320, 196 – 203, Copyright (2016) Elsevier; “Microstructural degradation of silicon electrodes during lithiation observed via operando X-ray tomographic imaging”, O. O. Taiwo, J. M. Paz- García, S. A. Hall, T. M. M. Heenan, D. P. Finegan, R. Mokso, P. Villanueva-Pérez, A. Patera, D. J. L. Brett, and P. R. Shearing, *Journal of Power Sources*, vol. 342, 904 – 912, 2017. Copyright (2017) Elsevier. The DVC analysis was performed in collaboration with J. M. Paz-García.

6.1 Introduction

Visualization of morphological changes that occur in Si, as well as other alloying-type electrode materials, during electrochemical cycling have previously been carried out *in-situ* using two-dimensional (2D) imaging techniques; for example, using *in-situ* transmission electron microscopy [270–273], and *in-situ* atomic force microscopy [12,87,274]. However, three-dimensional imaging using X-ray CT, with the aid of both laboratory and synchrotron X-ray sources, can provide further microstructural insight as well as a platform for *in-situ* and *operando* examination of temporal changes in electrode materials resulting from battery operation or failure.

Recently, Gonzalez *et al*. [275] performed *in-situ* visualization of microstructural evolution in Si-based electrodes using laboratory X-ray micro-CT at different stages of electrode lithiation. In this study, volume expansion and phase transformation could be analysed at electrode and particle levels. Also, lithiation-induced delamination of a composite Si-based electrode from the current collector was captured using

laboratory-based X-ray radiography and tomography by Tariq *et al* [276]. The higher X-ray flux achievable with synchrotron X-ray sources [165] leads to significantly faster image acquisition times, enabling higher spatial and temporal resolution imaging. Therefore, synchrotron CT enables dynamic morphological evolution and degradation of materials to be captured in real time; for instance, during continuous battery operation.

In this study, both laboratory and synchrotron X-ray CT was used to track microstructural evolution within silicon-based electrodes at different stages during the first lithiation process at the electrode and particle levels. Microstructural volume changes due to electrode lithiation were quantified using full 3D strain field measurements via digital volume correlation (DVC) analysis, and lithiation-induced phase transformation and fracturing within individual silicon particles were captured and tracked in real time.

6.2 Electrode preparation and cell assembly

For the electrode slurry preparation, micron-sized Si powder (< 300 mesh, 99% purity), conductive carbon and polyvinylidene fluoride (PVDF) were mixed with N-methyl-2-pyrrolidone (NMP) in a ULTRA-TURRAX IKA® homogenizer. Two different slurries were prepared: for the laboratory X-ray CT study, a slurry mixing ratio of 80 wt% Si, 10 wt% C and 10wt% PVDF was used, while a mixing ratio of 30 wt% Si, 60 wt% C and 10 wt% PVDF was used in the synchrotron study. A smaller Si content was employed in the latter to ease the tracking of individual Si particles between successive CT images. All chemicals used in the electrode slurry preparation step were procured from Pi-KEM Ltd., UK.

After mixing, the resulting slurry was then coated onto the tip of stainless steel current collecting rods (*ca.* 3.2 mm in diameter); coated rods were placed in a vacuum oven at 80 °C to dry for 12 h. The mass of Si within the dried electrode was estimated by weighing the current collecting rods before and after slurry coating.

Half-cells were then assembled in the custom Swagelok setup, in an argon-filled glove-box (oxygen and moisture levels in the glove-box were both maintained at < 0.5 ppm) with a metallic lithium foil counter electrode (Pi-KEM Ltd.), a borosilicate glass fibre separator (Whatmann GF-D grade, GE), and electrolyte containing 1M $LiPF_6$

dissolved in a mixture of ethylene carbonate (EC) : ethyl methyl carbonate (EMC) in the ratio 3:7 by volume.

6.3 Time-lapse laboratory X-ray CT study of bulk Si electrode during lithiation

X-ray CT imaging was performed on an assembled *in-situ* Si/Li half-cell using the laboratory micro-CT system (ZEISS Xradia Versa 520-XRM). For this experiment, the silicon electrode assembled within the half-cell contained 80 wt % active Si. The half-cell was partially discharged at successive intervals in 10 consecutive steps at a constant rate of 12 mAg^{-1} (or an applied C/200 rate). Such slow discharge rate was employed to allow sufficient lithiation of the relatively thick electrode and large particles used and to prevent the occurrence of any side reactions associated with fast discharge currents. The first partial discharge step was performed for 10 h after which the electrode was lithiated by 3.36%. Consecutive steps had 20 h duration each, and the electrode was lithiated by *ca.* 6.72% in each step. Further lithiation of the cell after the tenth step was not possible, most likely due to breakdown of the separator, which is discussed later. Figure 6.1 shows the cell potential readings during the gradual lithiation of the Si electrode.

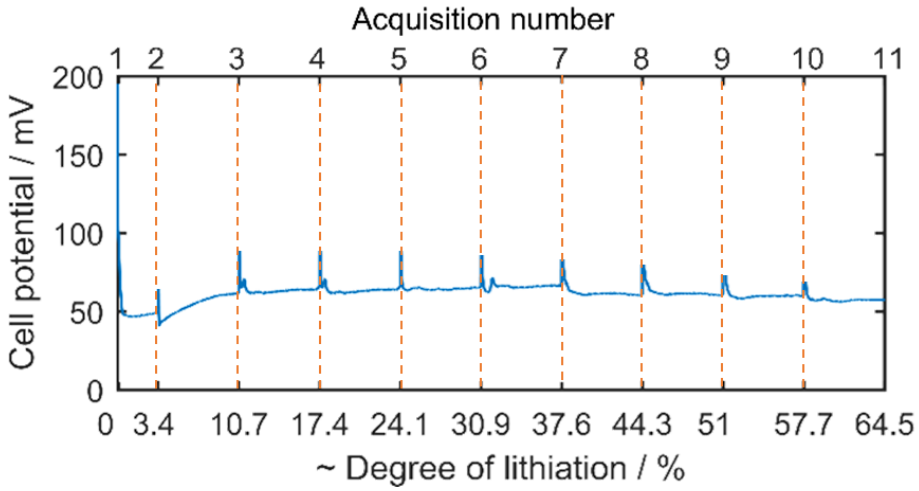

Figure 6.1. Discharge voltage profile (blue line) during the galvanostatic lithiation of the Si electrode using a constant current of 12 mAg^{-1}. The duration of the first step was 10 h, and consecutive steps had 20 h duration. After each partial discharge step, X-ray CT image scans were acquired (marked by brown dashed lines).

A total of 11 X-ray tomography scans of the half-cell assembly were performed (one at the initial state and after each of the 10 partial discharge steps) in absorption-

contrast mode. For each of the scans, the half-cell sample was mounted firmly between the X-ray source and a 2*k* × 2*k* detector as shown in Figure 3.25(a), with the source–detector distance set at 30 mm. An effective pixel resolution of 1.7 µm was achieved using a 4× optical magnification. Tomography scans were carried out with an X-ray source tube voltage of 45 kV with exposure time of 30 s per projection image, and a total of 2001 projection images were collected per scan. The projection image datasets were reconstructed using a commercial image reconstruction software package (ZEISS XMReconstructor, Carl Zeiss X-ray Microscopy Inc., Pleasanton, USA) which employs a filtered back-projection algorithm.

During lithiation, the Si electrode undergoes chemical transformation (which, in X-ray CT images, is associated with changes in X-ray attenuation) and the resulting volume expansion of the electrode causes material displacement within the electrode. In order to quantitatively analyse the 3D microstructural volume changes in the electrode, DVC was applied directly to the reconstructed 3D datasets prior to any initial image processing or enhancement steps. DVC analysis was performed using the Python-based software, TomoWarp2. A further description of the DVC approach can be found in Section 3.6.5. For the DVC calculations, a regular 3D grid with 25-voxel node spacing in each direction and a correlation window with a volume of 51 × 51 × 51 voxels^3 (i.e. 86.7 × 86.7 × 86.7 µm^3) were found to perform optimally on the extracted sub-volumes.

Figure 6.2 and Figure 6.3 show, respectively, vertical and horizontal cross-section images from the acquired tomograms. The tomograms reveal the half-cell assembly based on the X-ray attenuation. The lithium metal electrode is captured as the dark, low-attenuation layer, while materials with higher density, such as Si particles and glass fibre separator, are marked by high greyscale values.

The lithiation process is clearly accompanied by a significant volume expansion of the Si-based electrode. The volume of the electrode at 64.5% lithiation is significantly larger than that in the initial state. The separator's mechanical stability contributes immensely to the safety and performance of LIB cells. The huge volume changes within the tested half-cell induced rupturing of the separator, which is seen to propagate across the top of the separator in Figure 6.4. Further lithiation of the electrode beyond 64.5 % could not be achieved within the tested half-cell upon

continued galvanostatic discharge due, presumably, to the growth of dendritic lithium growth across the ruptured separator, causing a short circuit upon contact with Si electrode.

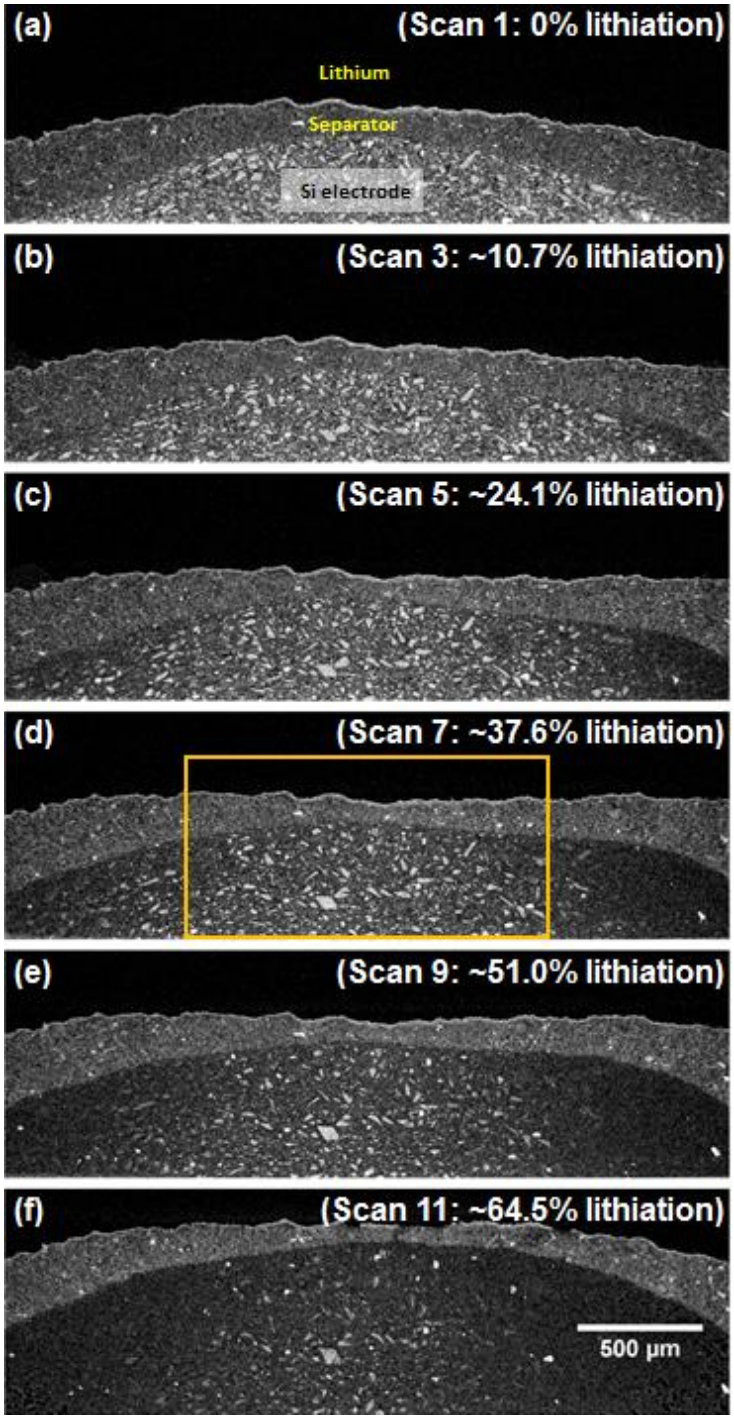

Figure 6.2. (a–f) Vertical cross-sections through the half-cell at different degrees of lithiation. Cross sections 6 out of the acquired 11 image volumes are shown. Yellow rectangle in (d) indicates the location of the extracted sub-volume used for subsequent DVC analysis.

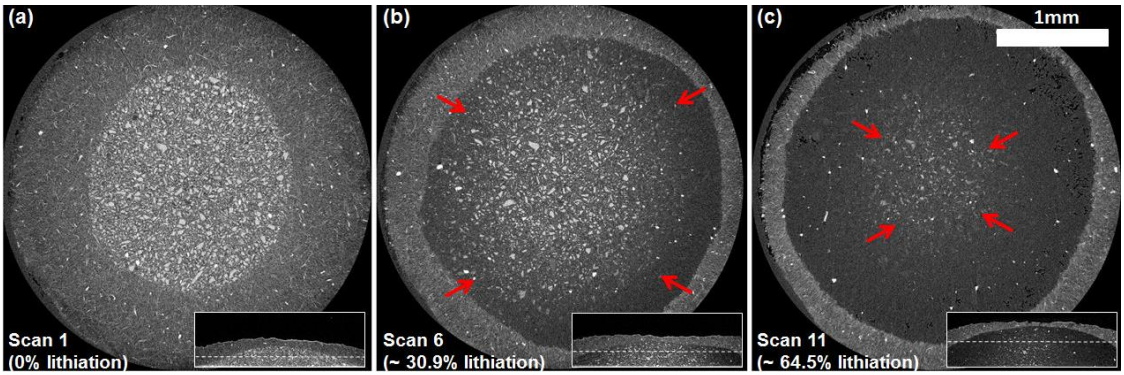

Figure 6.3. (a-c) Horizontal cross sections through the half-cell at different degrees of electrode lithiation. Cross-sections from 3 out of the acquired 11 image volumes are shown. Inset images indicate the vertical position of the cross-section within image volume. Yellow rectangle in (b) indicates the location of the extracted sub-volume used for subsequent DVC analysis. Red arrows highlight an inward propagation of the lithiation front towards the central region of the cell.

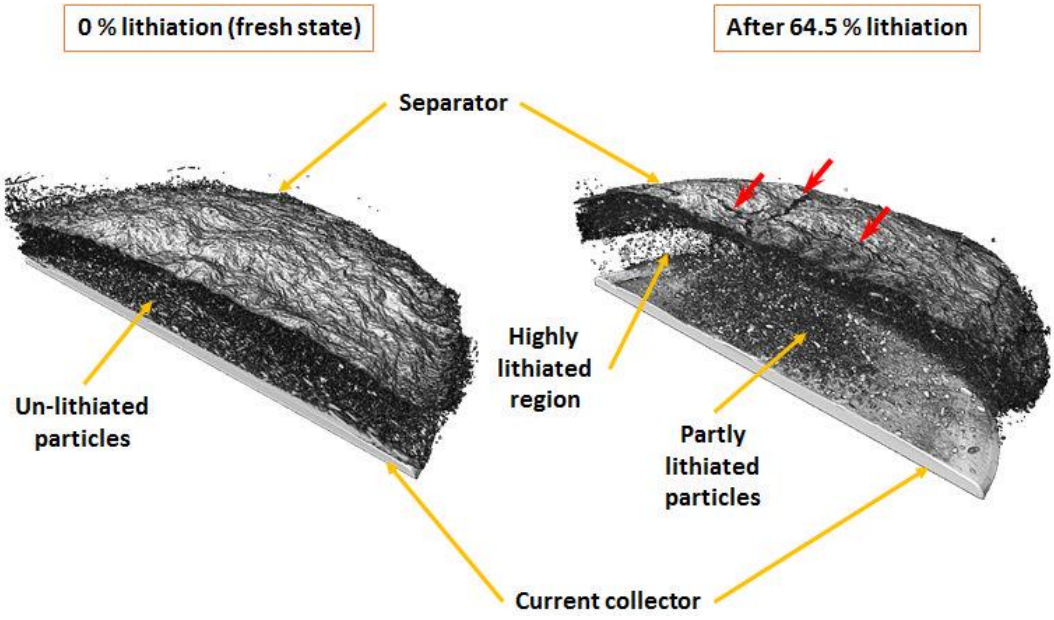

Figure 6.4. Cut-through 3D renderings of the half-cell assembly at 0 % and 64.5 % degree of lithiation, showing the volume change experienced by the Si electrode and separator rupture characterised by crack formation (marked by red arrows). The highly lithiated region within the Si electrode is characterised by a decrease in the attenuation of the Si particles (low attenuating areas are shown as transparent in the rendered image).

During the lithiation process, the glass-fibre separator was seen to suffer a vertical displacement towards the lithium electrode as a result of the volume expansion of the Si-based electrode. Also, the separator was seen to suffer

compression particularly towards the middle of the cell, indicating than the volume expansion of the Si electrode exceeds the volume of lithium consumed at the lithium metal electrode due to oxidation into Li^+ ions. Moreover, in Figure 6.3, the lithiation front (i.e., the front of decrease in the attenuation within the images) is observed to progress in radial direction towards the inner-central part of the electrode. This may be as a result of the uneven initial thickness seen across the porous glass fibre separator (attributed to the dome-like shape of the Si electrode), indicating a higher level of (fibre) compression within the central part of the separator. This initial compression effect would create a decrease in the fibrous separator's porosity in the central region, and could consequently cause a local decrease of the lithium diffusivity in that region, with Li^+ ions appearing to go across the separator preferentially through the outer, less compressed region. This compression effect within the separator was detected by DVC analysis, discussed later on in this section.

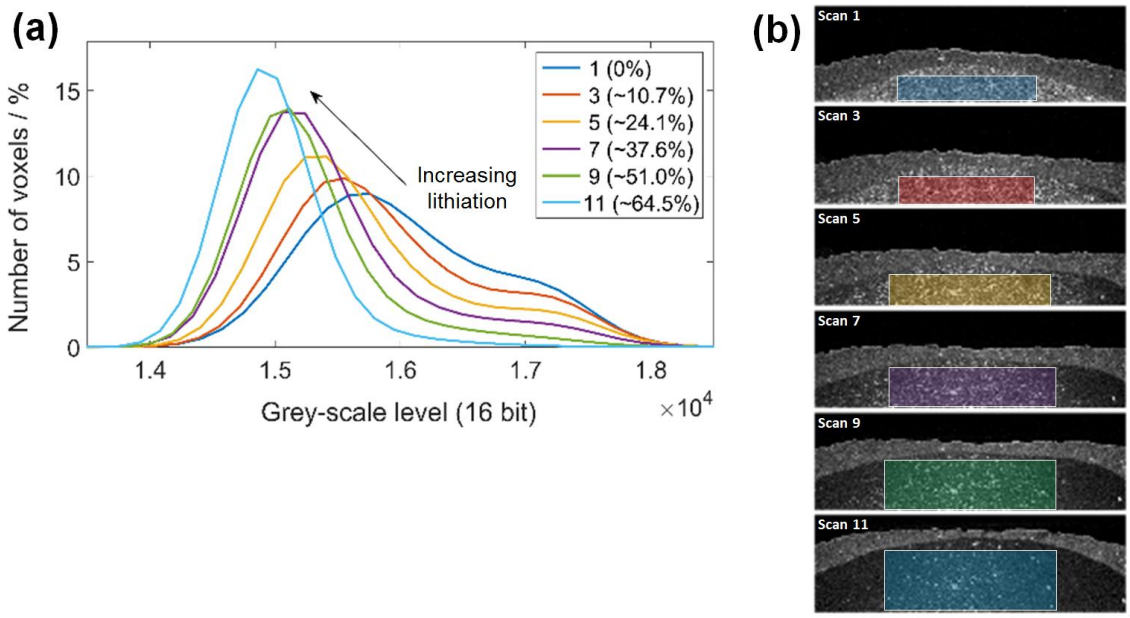

Figure 6.5. (a) Evolution of the greyscale intensity histogram of a sub-volume within the Si-based electrode, capturing changes in attenuation at different states of electrode lithiation. Legend highlights the scan number and degree of lithiation of the electrode. Coloured boxes in (b) indicate the sub-volumes of the expanding electrode where the greyscale histograms were computed.

Changes in X-ray attenuation within the Si electrode as a result of the lithiation process are also clearly observed. As the lithiation takes place, the Si particles react with the lithium ions to form lithiated-Si phases (Li_xSi_y) which have lower X-ray attenuation and, therefore, appear darker in the tomograms. Figure 6.5 shows the

evolution of the greyscale histogram for extracted sub-volumes in each successive tomogram corresponding to the same region within the Si electrode (i.e. excluding the separator and the lithium foil regions of the Si electrode), taking into account the dilation of the electrode. For the original tomogram at 0 % lithiation, a bimodal greyscale intensity distribution is seen, where the lower intensity peak at a greyscale level of 15,800 corresponded to the electrode matrix (mainly consisting of conductive carbon, binder and pores filled with electrolyte) and the high intensity peak at a greyscale level of 17,000 was affiliated with the Si particles. The histogram evolution during the lithiation process shows a clear decrease of the X-ray attenuation, with the intensity peaks shifting towards lower greyscale levels due to the formation of the low-attenuating lithiated-Si phase.

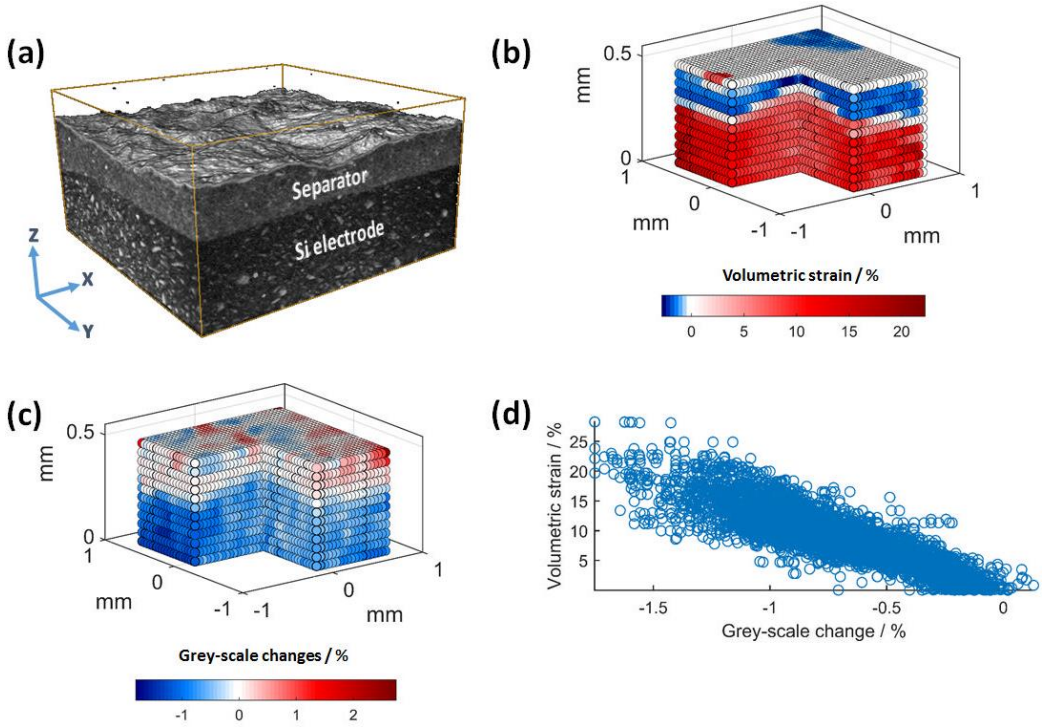

Figure 6.6. (a) 3D rendering of the extracted sub-volume (from scan 7) used in the DVC analysis showing the separator and the Si electrode phase. The boundary of the extracted sub-volume is highlighted in Figure 6.2. (b) 3D volumetric strain field and (c) percentage changes in greyscale within the same sub-volume between CT scans 6 (*ca*. 30.9 % lithiation) and 7 (*ca*. 37.6 % lithiation). The relationship between the volumetric strain and the local greyscale changes between the two sub-volumes is plotted in (d).

In order to quantify volume changes resulting from the expansion of the Si electrode respectively, DVC measurements were performed on sub-volumes with dimensions 1000 × 1000 × 500 voxels^3 (*ca.* 2.46 mm^3) extracted from the central part

of the half-cell assembly [Figure 6.2(d) and Figure 6.6(a)]. Each extracted sub-volume includes the Si electrode, separator and a portion of the lithium electrode.

Confirming the compressive effect that the dilated Si electrode had on the fibrous separator as a result of the lithiation process, Figure 6.6(a) shows the 3D volumetric strain map obtained from the DVC measurements between two consecutive sub-volumes, (from CT image acquisitions 6 and 7, which corresponds to electrode lithiation degrees of *ca.* 30.9 % and ca. 37.6 % respectively). The 3D volumetric strain data in this figure was plotted using a blue-white-red color scale, where red (positive) strain values indicate expansion and blue (negative) strain values indicate compression.

Using the same two sub-volumes from the DVC strain calculation, the local change in greyscale level was also computed. Figure 6.6(c) shows the corresponding relative percentage changes in greyscale, where red (positive) indicates an increase in the greyscale level between the sub-volumes, and blue (negative) indicates a decrease in greyscale level.

In the upper regions of the 3D fields in Figure 6.6 (b) and (c) (which is the region of the separator), mainly negative volume strain and slight increases in greyscale level are seen, respectively, both of which are consistent with the observed compression and densification of the porous separator in the X-ray tomograms. The lower regions of the 3D fields (corresponding to the Si electrode) indicate the presence of positive volumetric strain in the lithiated electrode, as well as with a clear decrease in greyscale (and X-ray attenuation). Upon relating the local positive volumetric strain measurements with the local changes in greyscale intensity within the Si electrode only, a linear trend was observed, as shown in Figure 6.6 (d).

The evolution of the positive volumetric strain within the Si electrode at each of the different degrees of lithiation was also tracked. Figure 6.7 shows the positive 3D volume strain results from DVC measurements between consecutive pairs of the acquired tomograms, within a common extracted sub-volume [Figure 6.6 (a)]. As lithiation progresses, volumetric strain is seen to increase locally at different rates within the electrode, highlighting the inhomogeneous nature of the lithiation process across the bulk electrode.

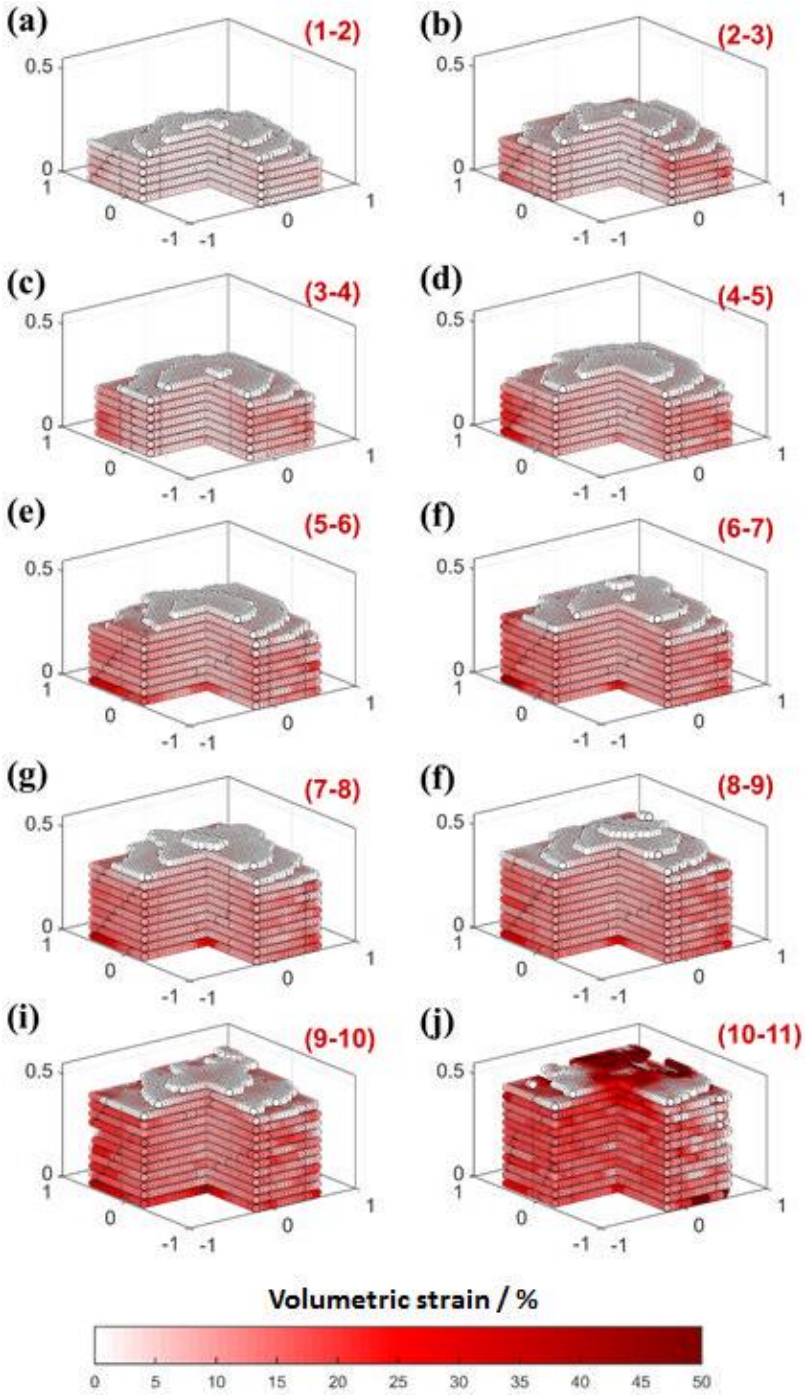

Figure 6.7. (a-f) 3D volumetric strain maps of the Si electrode region generated via DVC measurements between consecutive pairs of acquired tomograms (indicated in red brackets). Axes of each 3D strain map are in millimetres (mm).

In Figure 6.8, cumulative values for the volume expansion of the Si electrode are plotted as a function of the degree of lithiation. A second-degree polynomial curve fitting of the volume change increment data suggests a quadratic relation to the bulk electrode lithiation degree. At 64.5 % global electrode lithiation, the volume increment was calculated to be *ca.* 155 %. Extrapolating the second-degree polynomial curve to a

100 % (full) lithiation of the Si electrode gives a predicted volume expansion of 350 %, which is in good agreement with the volume expansion information previously reported in the literature for the complete lithiation of Si electrode [275,277].

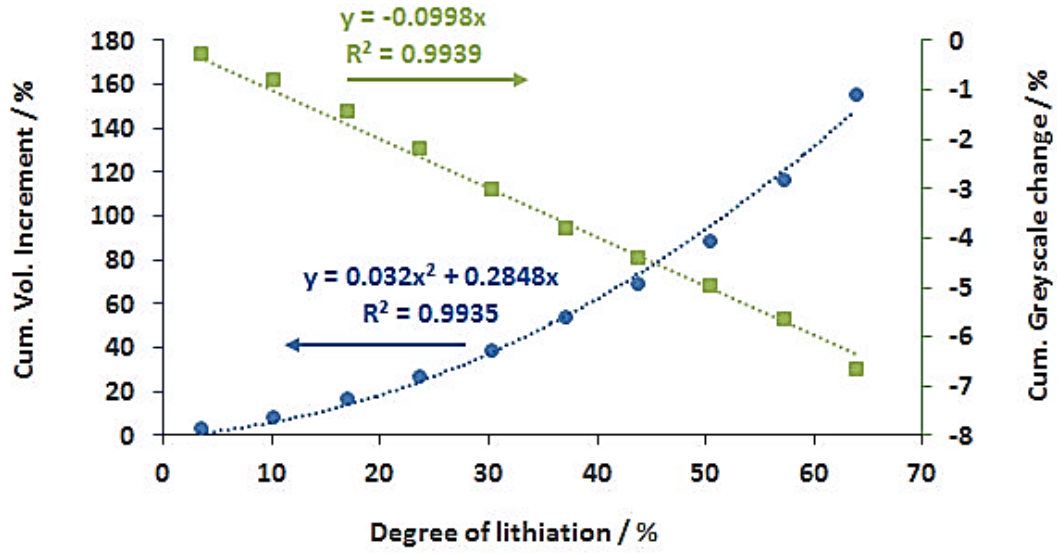

Figure 6.8. Cumulative volume increment of the Si electrode (blue circles, left vertical axis) and greyscale changes (right vertical axis) with reference to degree of lithiation. Greyscale changes (green squares) within the electrode sub-volume were computed directly using the global intensity histograms in Figure 6.5 (a).

Figure 6.8 also shows the cumulative values for greyscale changes in the electrode with increased lithiation. Greyscale intensity change calculations were performed using the global intensity histograms in Figure 5.6 (a), and were seen to show a linear trend with respect to the degree of lithiation.

6.4 *Operando* synchrotron X-ray CT of Si electrode particles during lithiation

To examine how the 3D microstructure and morphology of micron-sized Si particles gradually evolved during battery operation, *operando* X-ray CT imaging was conducted. For this experiment, the electrode fabrication and half-cell assembly procedures were identical to that described in Section 6.2; the only exception was that the mass loading of Si within the electrode was set to 30 wt. % in order to ease individual particle tracking and feature extraction from the resulting tomography data.

Operando X-ray CT imaging was performed at the TOMCAT beamline of the Swiss Light Source (Paul Scherrer Institut, Villigen, Switzerland) which enables fast,

non-invasive imaging at sub-micron resolution [229]. The experimental setup for the *operando* tomographic imaging is shown in Figure 6.9(a). An assembled Si-Li half-cell was mounted on the sample stage as shown in Figure 6.9(b) to enable galvanostatic cell discharge whilst simultaneously acquiring tomographic images.

The half-cell was imaged in a 17 keV parallel monochromatic X-ray beam with a field-of-view (FOV) of 1.6 mm × 1.4 mm, corresponding to half the size of the cell assembly. At the TOMCAT beamline, this FOV is associated with the 10× optical magnification mode of the X-ray microscope. The sample stage rotation axis was positioned at the edge of the FOV, such that it was possible to capture the entire cell assembly by a full 360° rotation. 3001 projection images were acquired during the rotation of the sample about its long axis, through angular steps of 0.12° with an exposure time of 110 ms for each projection image.

The transmitted X-rays illuminated a 20 µm thick LuAG:Ce scintillator (Crytur Ltd., Turnov, Czech Republic), producing visible light which was focused onto a PCO.Edge camera with a high-speed CMOS detector. A scan time of 5.5 min per tomogram was achieved with an effective voxel size of 650 nm, a significant improvement in both temporal and spatial resolution to previous laboratory-based X-ray tomography studies on Si electrodes [275].

Galvanostatic cell discharge was performed using a potentiostat (Ivium Compactstat, Ivium Technologies, Netherlands). Tomograms of the entire electrode were acquired every 18 min during galvanostatic discharge at a rate of 50 mAg^{-1} (estimated at C/72 C-rate based on the mass of active material within the sample). At this discharge rate, the lithiation kinetics, and thus microstructural dynamics of Si, was slow enough to be effectively captured in successive tomograms, and negligible material displacement was observed at the employed imaging frequency. However, only partial lithiation of the electrode was achieved in the limited synchrotron beamtime available.

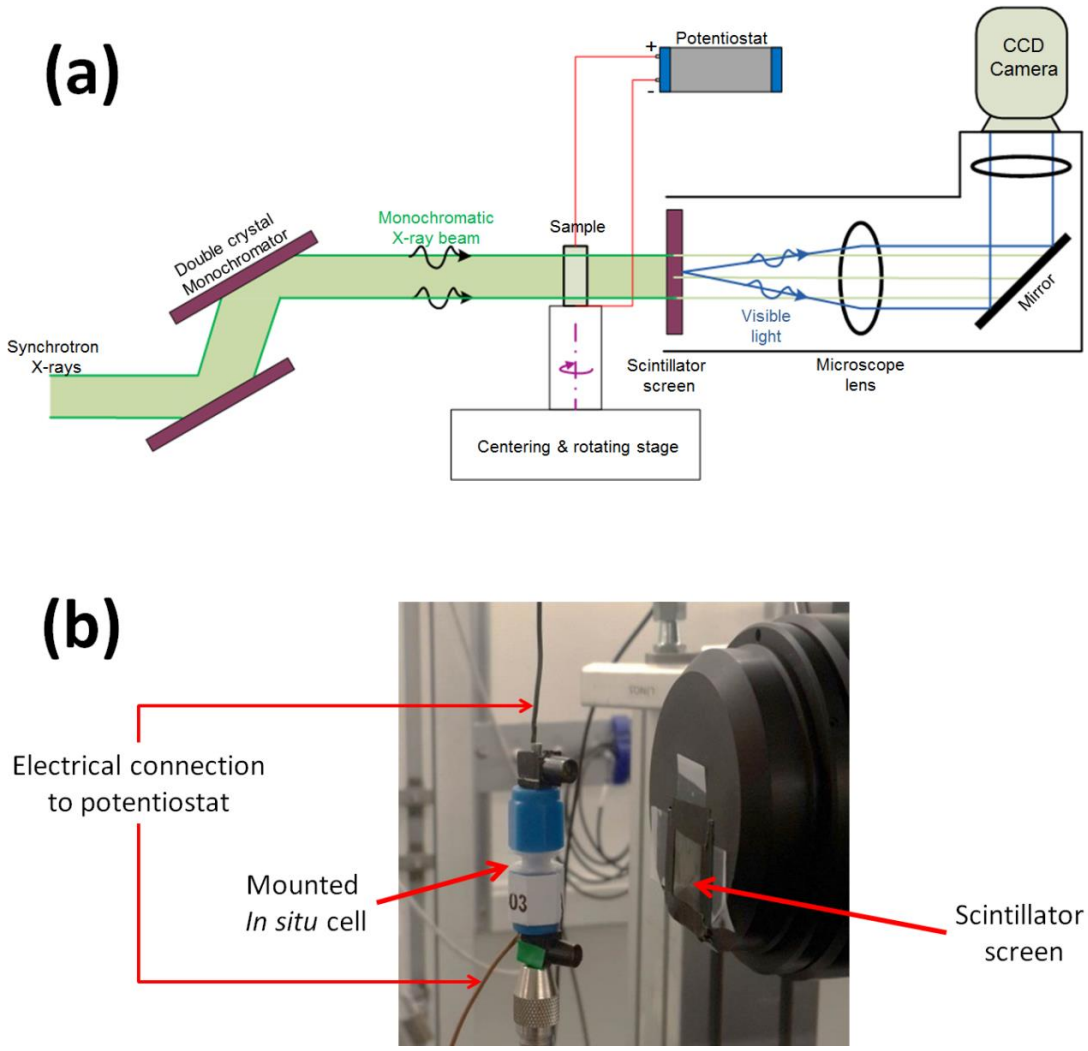

Figure 6.9. (a) Schematic illustration of the experimental setup at the TOMCAT beamline. (b) Optical image of the *in-situ* cell set up for operando synchrotron X-ray imaging.

A total of 72 datasets were collected, involving 3001 projections in 16-bit image stacks in TIFF format. Each projection image was corrected with the respective dark- and flat-field image, and single-image phase and intensity extraction was applied to all projection images with the aid of the Paganin phase-retrieval algorithm [278]. 3D reconstruction of the data was achieved using the gridrec algorithm [230].

Following the electrode-level microstructural investigations using time-lapse laboratory CT, *operando* synchrotron X-ray imaging was used to track the dynamic evolution of bulk Si particles within the composite electrode during the first lithiation stage.

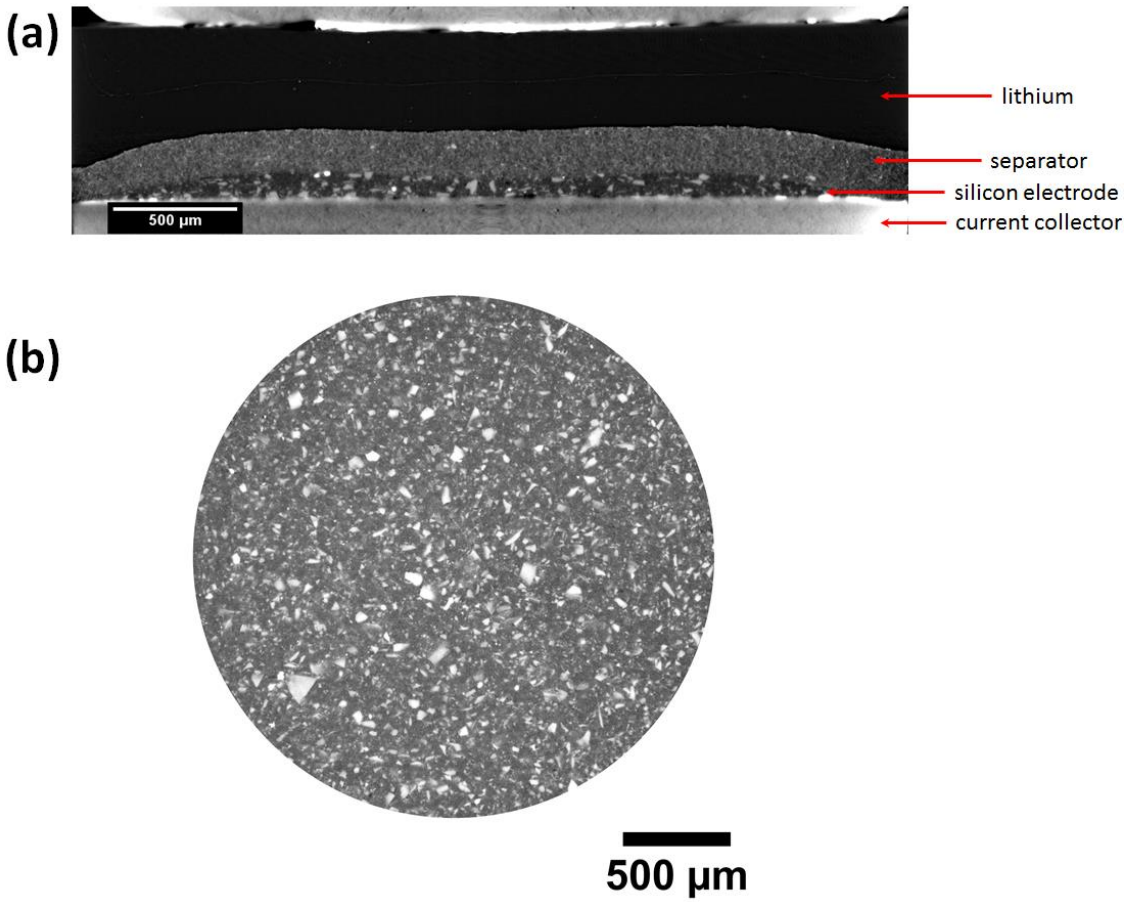

Figure 6.10. (a) Vertical cross-section through X-ray tomogram, showing the entire cell assembly. (b) Transverse cross-section through the X-ray tomogram, showing the Si composite electrode.

Vertical and horizontal cross-sections through an X-ray tomogram of the half-cell assembly prior to electrochemical testing are presented in Figure 6.10; the horizontal section intersects the cell at the level of the Si electrode. The dense Si particles can be differentiated from the conductive matrix and electrolyte/pore phases by their higher X-ray attenuation, and were thus isolated via threshold segmentation before rendering in 3D. On close inspection of the electrode volume rendering [Figure 6.11(d)], the non-uniform shape distribution of the Si microparticles can be seen.

Figure 6.11(c) shows the volume distribution of Si microparticles within the electrode prior to any electrochemical reduction, with particle count plotted against particle volume (*x* axis is plotted with logarithmic scale). The electrode sample shows a high frequency of small sized Si microparticles and measured particle volumes ranged between 6.60 μm^3 and 11 × 10^4 μm^3. Assuming spherical shaped particles, these

volumes would correspond to equivalent minimum and maximum particle diameters of 2.33 µm and 60.1 µm, and a mean particle diameter of 11.7 µm.

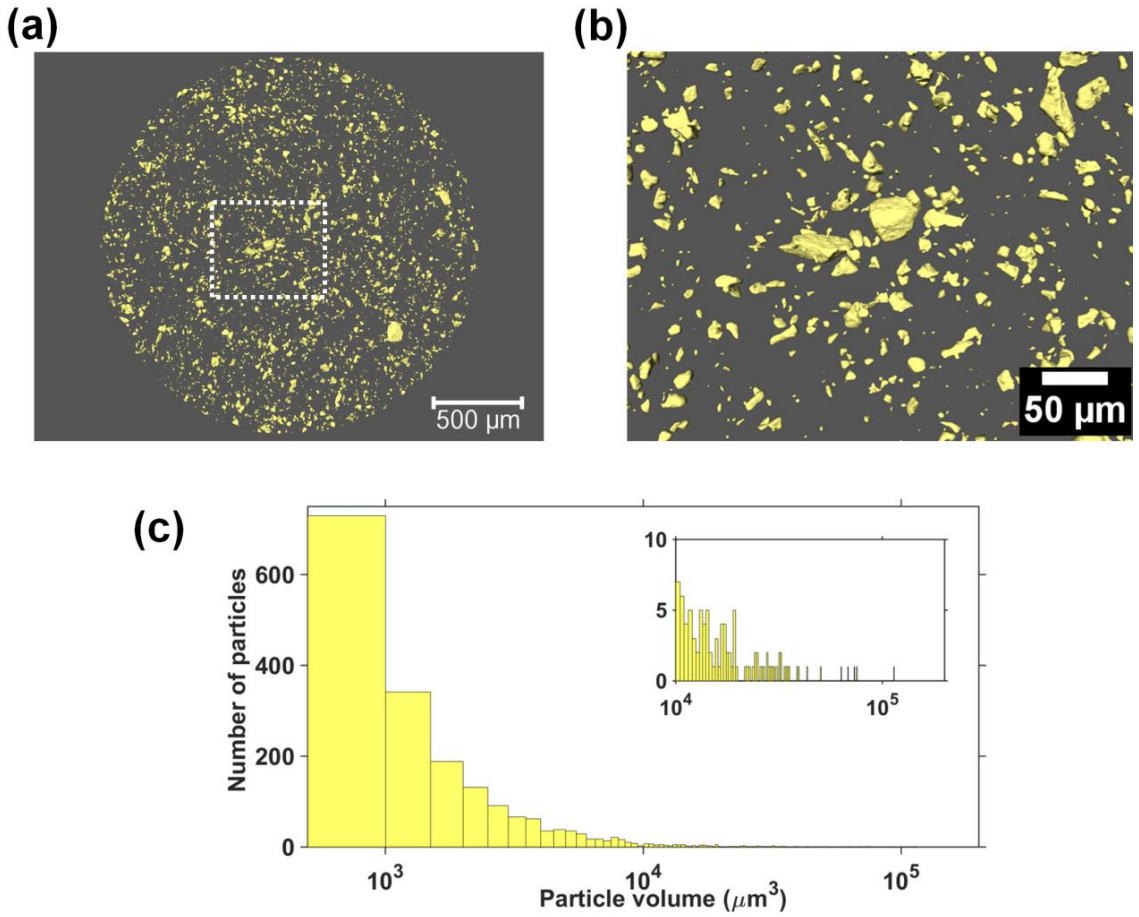

Figure 6.11. (a) 3D rendering of the thresholded tomogram showing dense Si particles within the composite electrode before cell discharge. (b) Zoomed-in image of rendered particles shows their non-uniform shape distribution. (c) Si particle volume distribution within the entire electrode before cell discharge. Inset: volumetric distribution at volumes greater than 1×10^4 μm^3.

Figure 6.12 shows the voltage versus time plot of the half-cell discharge. During the course of the galvanostatic discharge of the pristine Si/Li half-cell (*ca*. 22 hours), the entire Si electrode undergoes partial lithiation (*ca*. 30 % lithiation), reaching a specific discharge capacity of 1094 $mAhg^{-1}$ out of an achievable 3579 $mAhg^{-1}$ for the given electrode material. Time-lapse videos of the partial electrode lithiation were made from both the radiography and reconstructed image slice sequences, and can be found in www.sciencedirect.com/science/article/pii/S0378775316317736. To track changes within the half-cell assembly, 12 of the 72 tomograms acquired during discharge were selected (marked by red dots in the plot in Figure 6.12).

During cell discharge, the irregular-shaped Si microparticles in the electrode sample showed varying initial microstructural responses to lithiation-induced stresses, such as phase transformation and fracturing. These varying structural responses were identified by selecting some of the largest Si microparticles within the composite electrode and tracking their temporal evolution during the lithiation process. From here on, the tomograms are referred to by time-stamps as referenced to the electrochemical cycling data in Figure 6.12.

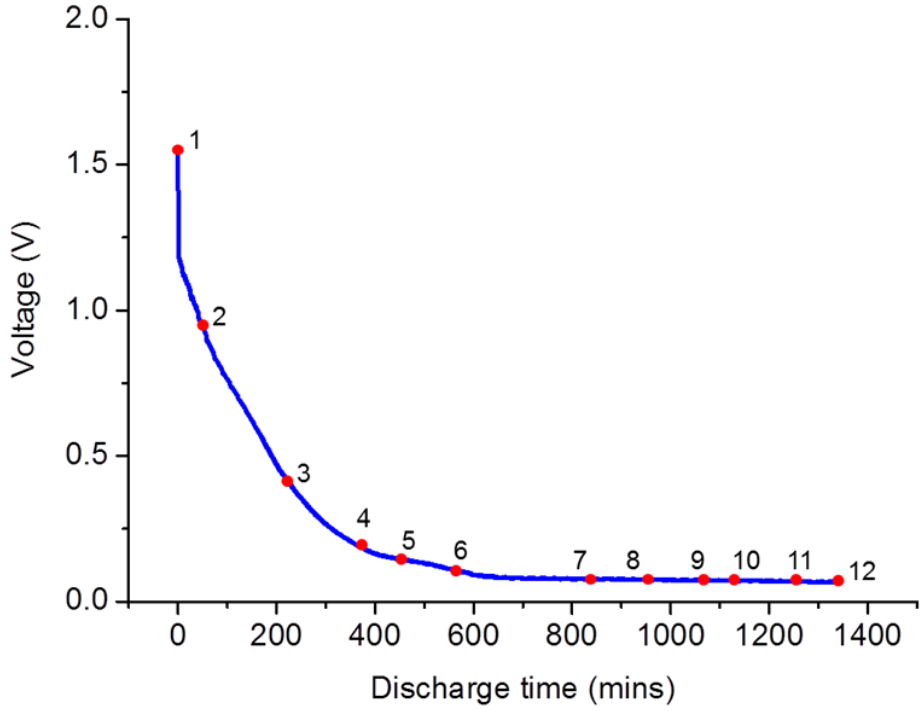

Figure 6.12. Galvanostatic discharge profile of the Si/Li half-cell at a constant rate of 50mAg^{-1}. 12 of the 72 tomographic scans taken at different stages during discharge (marked by red dots) are selected for subsequent analysis.

Between 1036 min and 1314 min, the X-ray tomogram sections of the particle in Figure 6.13(a) show an uneven, inward growth of a low attenuating front from the surface of particle surface. This low attenuating layer is associated with the formation of the low density Li_xSi_y phase upon electrochemical lithiation of Si via a two-phase mechanism on the surface of the crystalline Si [112,279,280], forming a core-shell like structure. The non-uniform growth of the low attenuating Li_xSi_y layer observed around the crystalline Si particle can be explained by a number of experimental and modelling studies that have shown that the growth of the lithiated silicon phase is anisotropic due to lithiation occurring preferentially in a particular crystal plane direction [281–284]. An intensity line scan performed across the crystalline Si, lithiated Si and the

surrounding conducting matrix in the X-ray tomogram section at 1314 min [Figure 6.13(d)] shows a significant difference in contrast between the high X-ray absorbing crystalline Si phase and low absorbing lithiated Si layer, but with less contrast between the lithiated phase and the surrounding conductive matrix. This makes threshold-based segmentation between both low density phases challenging, thus requiring the use of other image segmentation approaches such as 3D region growing [285].

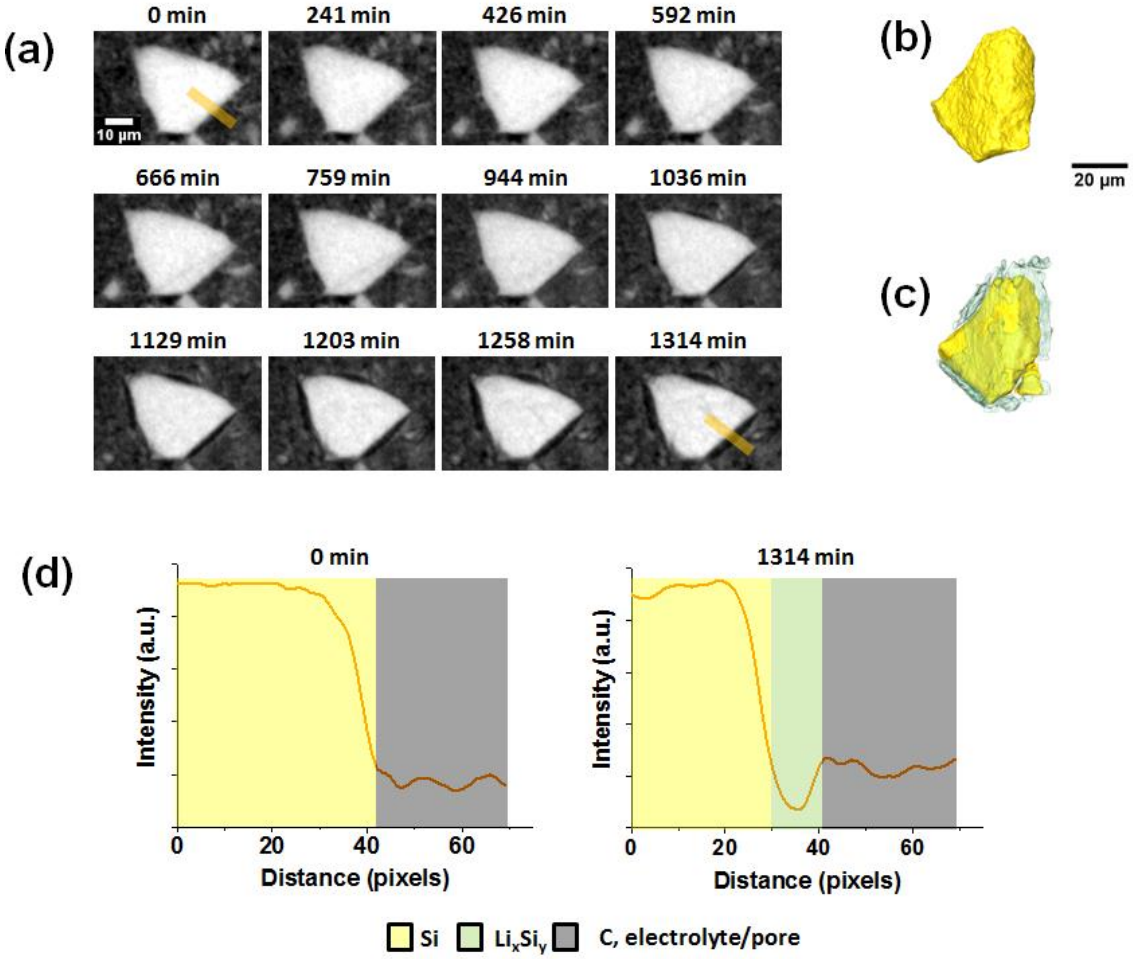

Figure 6.13. (a) X-ray tomogram sections of a selected Si microparticle showing phase transformation at the particle boundary as a result of lithiation. (b,c) 3D renderings of the particle in (a) at 0 min and 1314 min respectively. The histograms in (d) are the result of an intensity line scan [orange line in tomogram section at 0 min and 1314 min in (a)] showing the phase transformation at the particle boundary. The yellow, green and grey sections in the histograms highlight the crystalline Si, Li_xSi_y and surrounding carbon phases respectively.

In Figure 6.14, two Si particles adjacent to each other within the electrode were tracked. From the X-ray tomogram 2D sections, there is a difference in the morphological evolution of these two particles in response to lithiation-induced stress.

With progressive lithiation of crystalline Si, surface cracks form due to tensile hoop stress development [286,287], and anisotropic volume expansion of the particles occurs which leads to stress intensification and eventually fracture at certain locations.

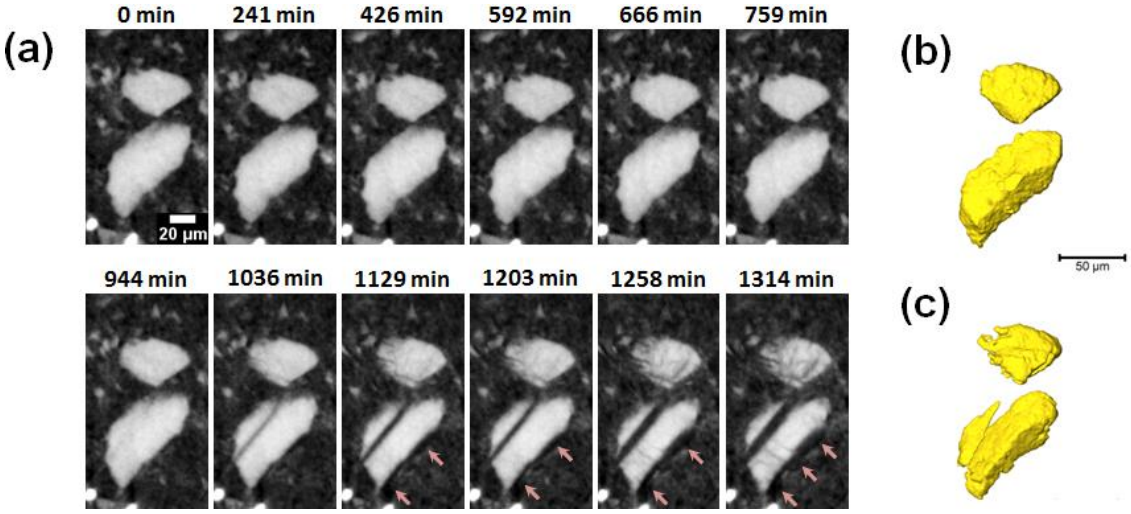

Figure 6.14. The two adjacent particles in (a) respond differently to lithiation stresses: both particles experience micro-cracking which eventually leads to the formation of complex crack microstructure in the top particle and fracturing in the bottom particle. Pink arrows highlight the gradual formation of the low attenuating Li_xSi_y phase. (b,c) 3D renderings of the particle in (a) at 0 min and 1314 min respectively

In the tomogram captured at 1036 min in Figure 6.14(a), the formation of micro-cracks is observed in both particles. As lithiation progresses, the main crack in the lower particle propagates until particle fracture occurs; however, a complex vein-like network of micro-cracks forms in the top particle. In the lower particle, formation of the low attenuating Li_xSi_y phase appears to take place preferentially on one surface parallel to the main crack, as indicated by the pink arrows in the tomograms in Figure 6.14(a). Choi *et al*. [288] observed that the nature of micro-crack generation and propagation to form complete fractures in crystalline Si was dependent on the crystal orientation. Using TEM, they revealed the formation of micro-cracks in crystalline Si upon initial lithiation, which subsequently contributed to the formation of a complex vein-like network of Li_xSi_y within the crystalline Si matrix, proposing that these micro-cracks act as fast diffusion paths for lithium, and generate a network of interconnecting cracks within the crystalline Si.

Figure 6.15 shows how different morphologies of micro-cracks form within two further Si microparticles over the same lithiation period. At 1314 mins, a more complex

network of small multiple cracks is seen in the Si microparticle in Figure 6.15(a), while longer and wider cracks are seen in the Si microparticle in Figure 6.15(d).

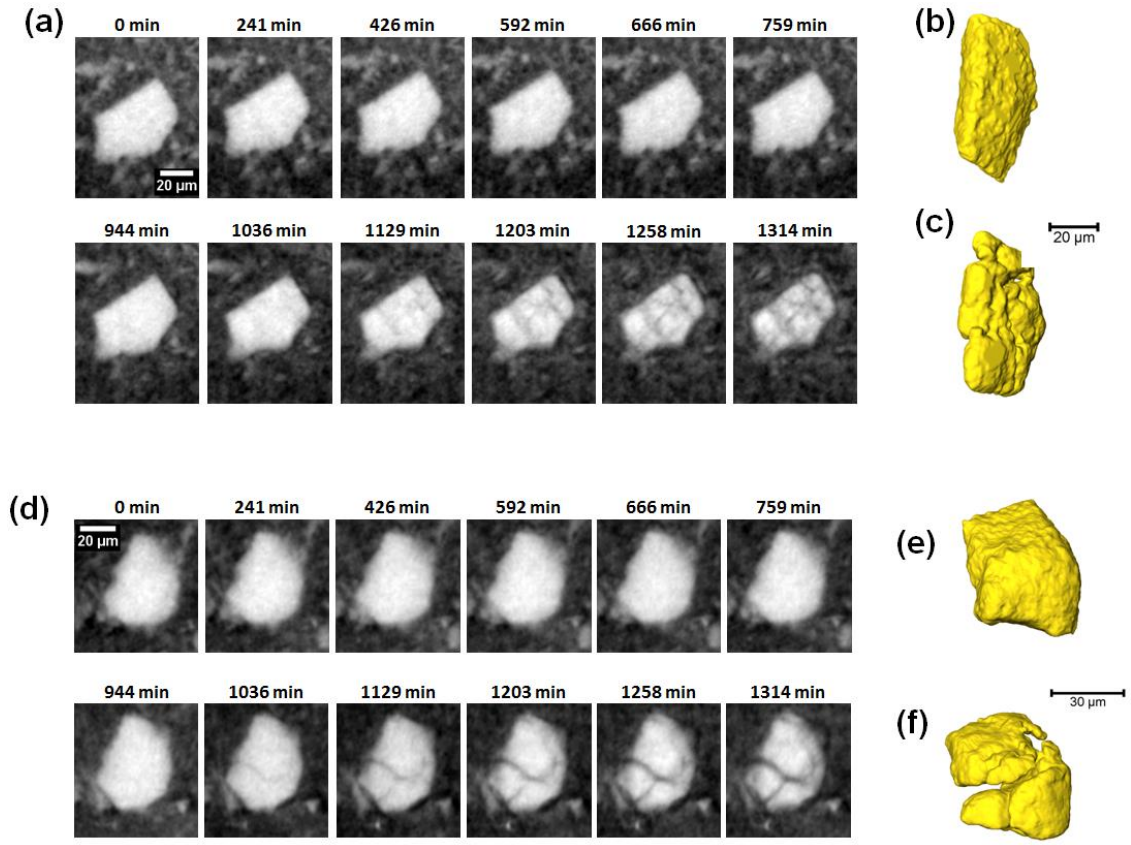

Figure 6.15. Micro-crack initiation and propagation in selected Si microparticles. X-ray tomogram cross sections show that micro-cracks could initially propagate within a Si microparticle to form a complex network of small cracks as in (a) or form longer and wider cracks as in (d). 3D renderings show the crystalline Si phase in particles (b,e) before lithiation and (c,f) after lithiation.

It is noteworthy that the varied structural responses observed amongst the highlighted individual Si microparticles could be due to any of (or a combination of) the following factors: anisotropic kinetics of the lithiation process at the Si/Li_xSi_y interface, presence of manufacture-induced surface defects prior to electrochemical reduction, formation of lithiation-induced defects that provide faster Li^+ diffusion pathways, or the quality of electrical contact between active particles and the conducting phase.

At the imaging resolution employed, no size-dependent fracturing was observed amongst the Si microparticles within the electrode upon lithiation. However, higher resolution *in-situ* TEM imaging studies have shown that there exists a critical particle size above which fracturing occurs during lithiation and delithiation, and it is

seen to be typically *ca.* 150 nm in Si nanoparticles [286] and *ca.* 250 nm in Si nanowires [289]. Such critical particle size investigations could not be confirmed with the imaging resolution used here, but could be attempted using nanometre-scale X-ray CT. However, a number of large Si microparticles in this study were observed to not display severe fracturing over the course of the lithiation process; the particle captured in Figure 6.13(a) is a typical example.

The extent of particle lithiation as a function of distance from electrode current collector was also examined. Overall, it was observed that Si particles closest to the electrode-separator interface experienced the most morphological change upon lithiation of the electrode, whereas particles furthest from the separator showed little or no transformation during the cell discharge – this is consistent with ionic transport limited processes. Figure 6.16 and Figure 6.18 show the morphological evolution of two large particles (labelled as Particle A and B) selected from the centre region of the electrode layer tracked over the lithiation process. A region of interest surrounding Particle A is cropped from the top of the composite electrode, just below the separator while Particle B is cropped above the surface of the Si electrode current collector. The changes in the greyscale intensity (which is directly proportional to X-ray attenuation) within the cropped region of interest containing each particle was also tracked over the course of the cell discharge. Compared to Particle A, Particle B experienced minimal morphological and attenuation changes as a result of the lithiation process, which suggests that particle lithiation within the electrode in this study is limited by Li^+ transport, and not by electronic conductivity. The morphological evolution of Si phase in the two SiMPs upon lithiation is shown in 3D as a time-lapse movie which can be found in www.sciencedirect.com/science/article/pii/S0378775316317736.

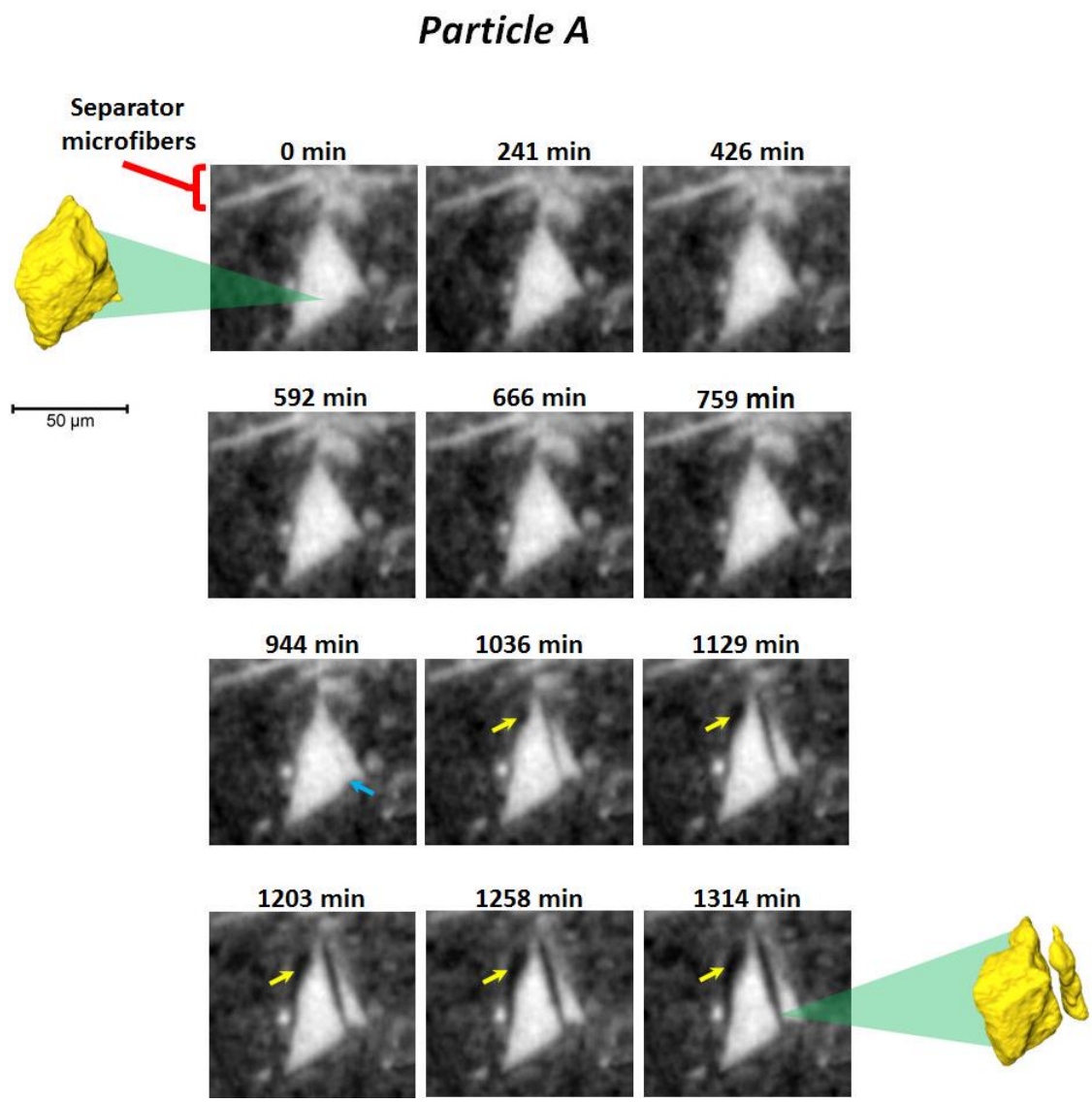

Figure 6.16. Morphological evolution of Particle A during electrode lithiation. Particle A is located very close to the lithium source (just below the separator). Blue arrow indicates point of crack initiation, yellow arrows highlight gradual Si phase transformation at the particle boundary.

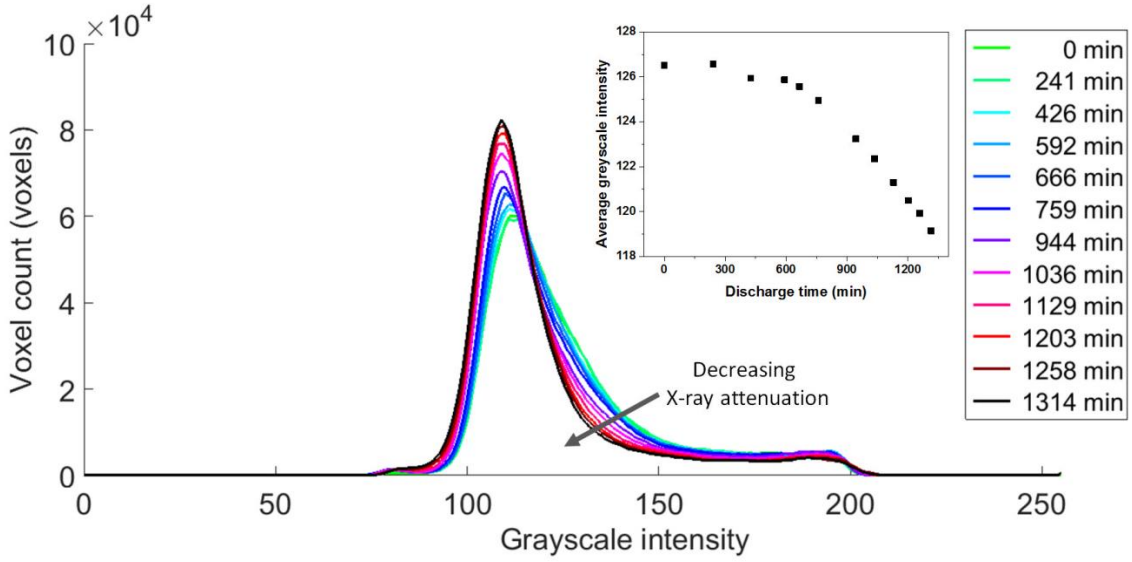

Figure 6.17. Evolution of the greyscale intensity histogram of the cropped region of interest containing Particle A (Figure 6.16) during the lithiation process. Inset: change in average greyscale intensity of the region of interest during cell discharge.

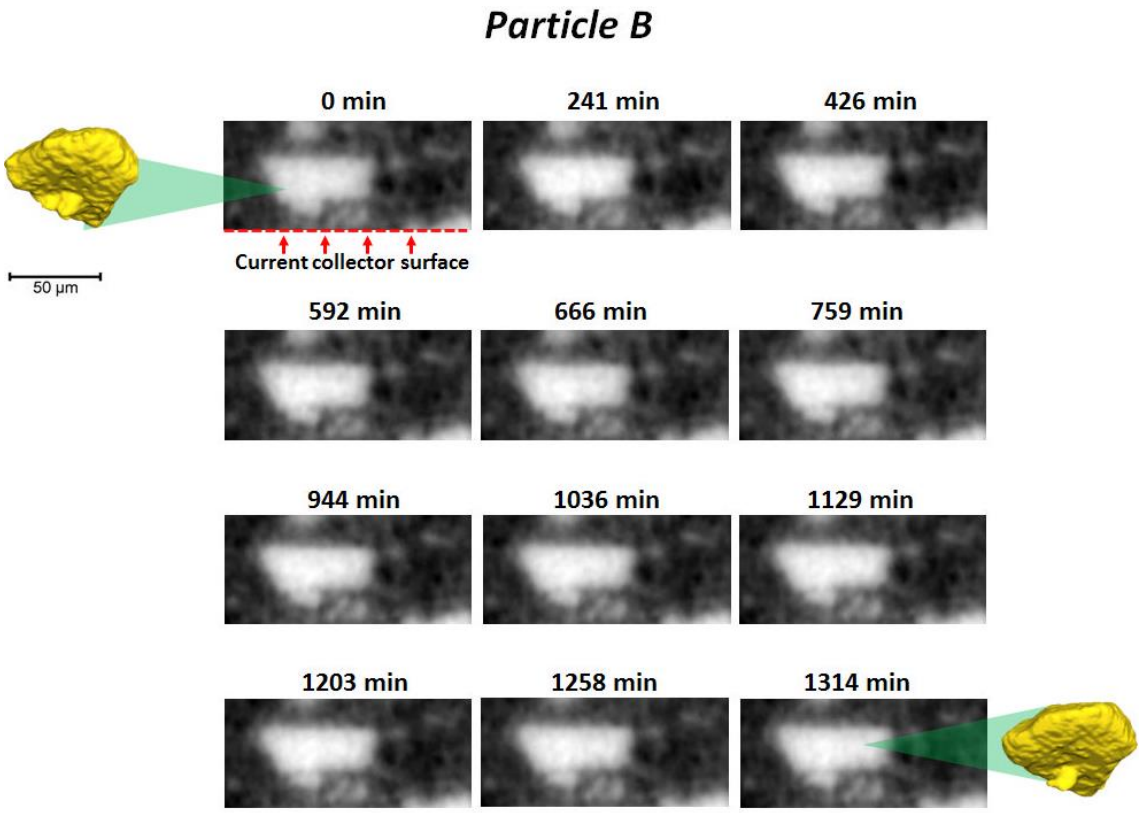

Figure 6.18. Morpholoigcal evolution of Particle B during electrode lithiation. Particle B is located at the surface of the electrode current collector.

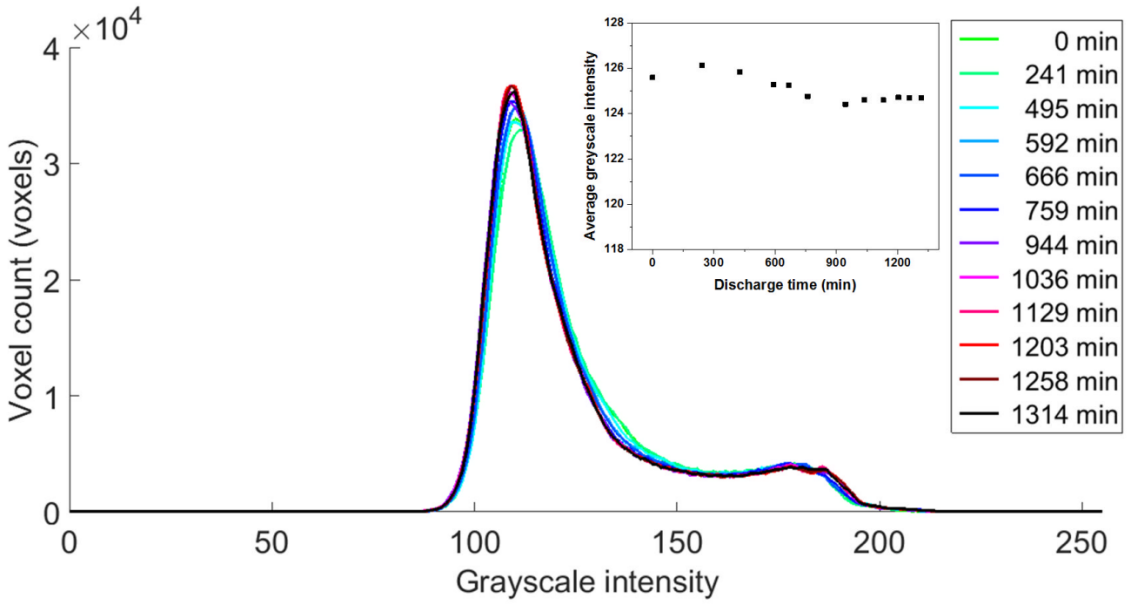

Figure 6.19. Evolution of the greyscale intensity histogram of the cropped region of interest containing Particle B (Figure 6.18) showing little change during the lithiation process. Inset: change in average greyscale intensity of the region of interest during cell discharge.

As the cell discharge progresses, Particle A gradually lithiates, with micro-crack formation seen at 994 min [marked by the blue arrow in Figure 6.16(a)]. The crack then propagates up until complete particle fracture occurs, with the particle breaking down into smaller fragments. The fracture process could cause a loss of electrical contact between the active Si surface and the conductive matrix, and increase the crystalline Si surface area for additional SEI formation. Growth of the weakly attenuating Li_xSi_y phase appears to initiate locally (at 1036 min) and spread along the particle surface [marked by yellow arrows in Figure 6.16(a)]. The increase in magnitude of the greyscale intensity peak and the slight peak shift to even lower greyscale values seen in Figure 6.16(b) can be associated with lithiation-induced phase transformation within and around Particle A. A significant decrease in the average greyscale intensity is seen to occur in the region of interest around Particle A (Figure 6.17 inset). This also shows evidence of phase change within the conductive matrix surrounding the main particle as well as the occurrence particle crack formation.

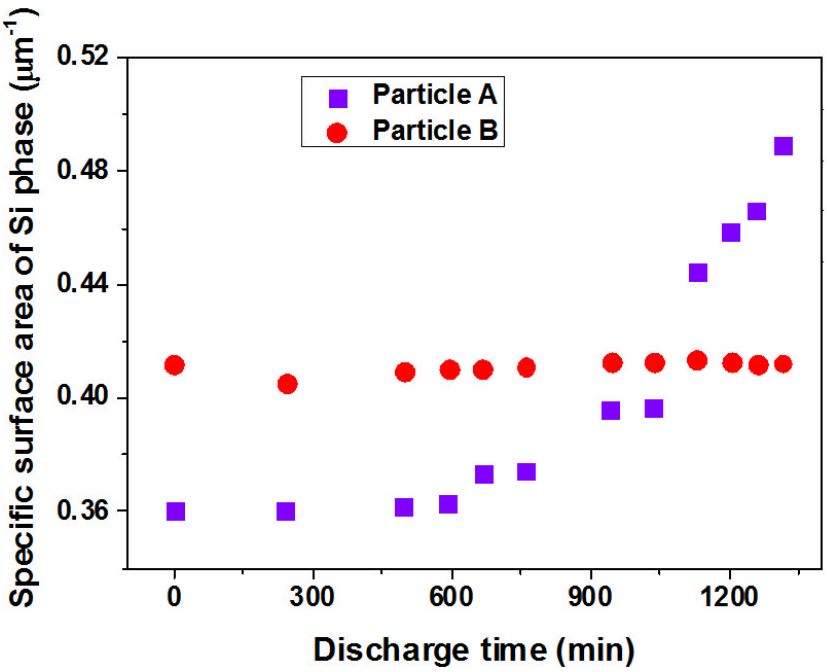

Figure 6.20. Change in volume specific surface area of the crystalline Si phase for Particle A and Particle B as a function of electrode specific capacity.

Change in volume-specific surface area of the crystalline Si phase in both sampled particles was tracked as a function of cell discharge and is shown in Figure 6.20. The sudden increase in volume-specific surface area of the dense Si phase in Particle A after 759 min can be associated with particle fracturing seen in Figure 6.16 which leads increase in exposed Si surface. Minimal surface variation was observed in Particle B over the course of the cell discharge.

6.5 Conclusion

In this study, 4D microstructural evolution occurring within Si/Li half-cells during electrochemical discharge was visualized and quantified. Time-lapse *in-situ* laboratory X-ray CT, in combination with DVC analysis, was used to track and quantify lithiation-induced microstructural volume changes within the bulk Si electrodes. The extent of lithiation of silicon electrode was been measured in 3D from the greyscale changes of the acquired tomography images. 3D volumetric strain was observed to increase locally at different rates, highlighting the inhomogeneous nature of the lithiation process across the bulk electrode.

With higher spatial resolution using synchrotron X-rays, *operando* 3D X-ray imaging enabled visualization of phase transformation and fracturing in individual silicon microparticles. Selected Si microparticles showed varied structural responses to

lithiation-induced stresses by surface growth of low-absorbing Li_xSi_y phase and developing micro-cracks which propagate and lead to particle fracture. Particles closest to the separator surface (or to the Li^+ source) underwent the most lithiation and experienced severe fracturing, indicating that the lithiation in the composite electrode under study is not limited by electronic conductivity, but by the diffusion of Li^+ ions through the electrode layer. In the following chapter, These Si particle level investigations are further extended using even higher resolution X-ray CT imaging.

Chapter 7

X-ray Nano-Tomography Characterisation of LIB Electrode Microstructures

Portions of this chapter are reproduced in part with permission from “The use of contrast enhancement techniques in X-ray imaging of lithium–ion battery electrodes”, O. O. Taiwo, D. P. Finegan, J. Gelb. C. Holzner, D. J. L. Brett, and P. R. Shearing, *Chemical Engineering Science*, vol. 154, pp. 27–33, Copyright (2016) Elsevier.

7.1 Introduction

The capability of X-ray CT has been demonstrated at the micrometre length scale earlier in Chapters 4, 5 and 6. X-ray microtomography systems can achieve true spatial resolutions around 1 µm [290]. However, with the introduction of nano-scale X-ray CT systems, even finer resolutions can now be achieved. The implementation of X-ray optics has been largely responsible for the improvements in X-ray CT resolution observed in recent years: for instance, systems with zone plate lenses can achieve spatial resolutions better than 50 nm on suitable specimen [291]. Such high resolution can be applied to the study of nano-sized materials and sub-micron features within micron-sized materials.

In this chapter, two different microstructural studies employing X-ray nanotomography are reported. In the first study, X-ray nanotomography is used to investigate the morphological changes in micron-sized silicon electrode particles due to repeated electrochemical cycling. The second demonstrates an approach for obtaining improved nano-scale image contrast on a laboratory X-ray microscope by combining information obtained from both absorption–contrast and Zernike phase-contrast X-ray images.

7.2 Characterisation of microstructural evolution of Si-based electrodes using X-ray nano-CT

During the first lithiation stage, Si undergoes huge volume changes which induce both structural and material degradation within the electrode; this degradation becomes more significant with prolonged cycling. In Chapter 6, micrometre-scale X-ray CT was used to capture the 3D microstructural changes in bulk silicon electrodes during the early stages of battery operation, achieving spatial resolutions around 1–2 µm. With X-ray nanotomography (nano-CT), even higher spatial resolution can be achieved (down to a tens of nanometres), facilitating detailed microstructural investigations at the nanometre scale. However, at such length scale, designing *in-situ* electrochemical setups for microstructural evolution studies is non-trivial, often leading to the use of *ex-situ* nanotomographic analysis [9,33]. Moreover, the *in-situ* cell used in the previously reported experiments in this work was designed more to accommodate micrometre scale investigations.

In this study, the morphological changes in micron-sized silicon particles due to electrochemical cycling are examined. Electrode samples made from micron-sized Si particles were repeatedly cycled and their 3D microstructure was subsequently imaged *ex-situ* using laboratory X-ray nano-CT.

7.2.1 Materials and methods

7.2.1.1 Electrode preparation and cell assembly

In order to enable the examination of a more statistically representative electrode sample volume within the limited X-ray field-of-view of the nano-CT instrument, powdered Si with relatively smaller-sized microparticles (Elkem Silgrain e-Si, d50 3.1 µm, 99.7 % purity) – compared to that used in the micro-CT studies in Chapter 6 – was used as active material for the preparation of Si electrodes. Carbon black (Alfa Aesar, Acetylene Black, purity, 99.9+ %) and graphite (TIMREX SF56, purity 99.93 %) were used as conductive agents and a sodium salt of polyacrylic acid (Na-PAA) as binder. The binder was prepared by dissolving PAA in de-ionised water and then partially neutralizing the solution with sodium carbonate. Further details of the binder preparation can be found in [292].

The powdered Si, carbon black, graphite and the partially neutralized Na-PAA solution (in a percentage weight ratio of 70:10:6:14, respectively) were mixed with de-ionised water, and stirred using a high shear mixer (Primix Homodisper Model 2.5) for 30 mins. Electrode laminates were then created by casting the resulting electrode slurry onto 10 µm thick Cu foil (Oak Mitsui, electrodeposited) using a film applicator (RK PrintCoat Instruments, UK), with partial vacuum applied to the Cu foil and a doctor blade gap set to 100 µm. Slurry-coated Cu foils were dried on a hot plate at 80 °C for 2 mins followed by vacuum drying at 70 °C for 12 h. The dried electrode laminates were cut into 10 mm diameter discs, each of which was weighed in order to obtain the mass loading of Si.

Half-cells were fabricated using PFA-type Swagelok hardware (PFA-820-6, 0.5 inch diameter, Swagelok, USA) in an argon-filled glove-box (oxygen and moisture levels in the glove-box were both maintained at < 0.5 ppm) with a metallic lithium foil counter electrode (Pi-KEM Ltd, cut to 11 mm diameter), a borosilicate glass fibre separator (Whatmann GF-D grade, GE, cut to 12 mm diameter), and electrolyte containing 1M $LiPF_6$ in mixture of ethylene carbonate (EC) : ethyl methyl carbonate (EMC) in the ratio 3:7 by volume.

7.2.1.2 Electrochemical characterisation

Electrochemical cycling of assembled Swagelok cells was performed at room temperature using a Maccor 4300 series battery cycler between 1 – 0.005 V vs Li/Li^+. Cells were selected to be cycled for 1, 10 and 100 cycles. A C/5 rate was used for Si electrodes cycled for 1 and 10 cycles. For electrodes cycled for 100 cycles, the first cycle was performed at a C/5 rate to promote SEI formation, and subsequent cycles were performed at a C/2 rate. The C-rates were calculated based on the theoretical capacity of Si at room temperature (Q = 3579 $mAhg^{-1}$).

7.2.1.3 SEM and e*x-situ* X-ray nano-CT

After electrochemical testing, the cells were then carefully disassembled in the argon-filled glove box. The Si electrodes (in delithiated state) were carefully extracted from the disassembled cells and then thoroughly rinsed in pure diethyl carbonate (DEC) solution for 6 h to remove traces of electrolyte. The washed electrode was dried

by storing it in a vacuumed antechamber of the glove box at room temperature to remove any DEC present.

Both the pristine (uncycled) and the washed, cycled versions of the Si electrode sample were then dissected under a visible light microscope into smaller sample sizes suitable for nanoscale X-ray CT imaging and mounted onto the tip of stainless steel needles using epoxy resin. Remaining portions of the pristine and electrode were reserved for SEM characterisation. Scanning electron micrographs of electrode sample in its pristine and cycled states were captured with the aid of a ZEISS EVO MA 10 microscope.

X-ray nano-CT was conducted on the electrode samples using a laboratory-based XRM system (ZEISS Xradia 810 Ultra, Carl Zeiss Microscopy Inc., Pleasanton, USA) in absorption–contrast mode. For each investigated sample, X-ray radiographs were acquired over a 180° sample rotation in small successive angular increments. Details of the tomographic imaging parameters for each sample are presented in Table 7.1. The acquired radiograph images were then reconstructed with the aid of the ZEISS XMReconstructor software (Carl Zeiss X-ray Microscopy Inc., Pleasanton) which employs a filtered-back projection algorithm.

Table 7.1. Nano-XRM image acquisition details

	Pristine	**1st cycle**	**10th cycle**	**100th cycle**
Field of view dimensions	65 µm x 65 µm			
Detector binning	1			
No. of radiographs recorded	1601	2001	2001	2001
Radiograph exposure time (s)	23	15	20	14
Effective voxel size (nm)	63.1			
Photon energy (keV)	5.4			

7.2.2 Observing cycling-induced microstructural changes in Si electrodes

The cycling behaviour of the silicon electrode material over a 100 charge-discharge cycle period is shown in Figure 7.1. A discharge capacity of *ca.* 2700 $mAhg^{-1}$ was obtained in the first cycle but this sharply drops to *ca.* 1460 $mAhg^{-1}$ in the second cycle. This significant capacity loss after the first cycle is attributed to the formation of SEI on the surface of the silicon electrode particles. The capacity slightly recovers to over 1600 $mAhg^{-1}$ after the fifth cycle, and remains relatively stable until the 15th cycle

after which a steady decline in electrode performance is seen with progressive cycling. This result indicates that the cycling-induced electrode volume expansion and contraction effect on the electrical connectivity between the Si particles and the conductive matrix is more significant in the first cycle than in subsequent cycles. The Coulombic efficiency (CE) was calculated as the percentage ratio of the electrode's delithiation capacity to its lithiation capacity. As the SEI layer on LIB electrodes matures and its growth slows down with cycling, the CE is expected to increase and then stabilize shortly after the first few cycles [293]. The CE of Si was 93.3 % in the first cycle, and it is seen to increase and then stabilize above 98 % after 20 cycles.

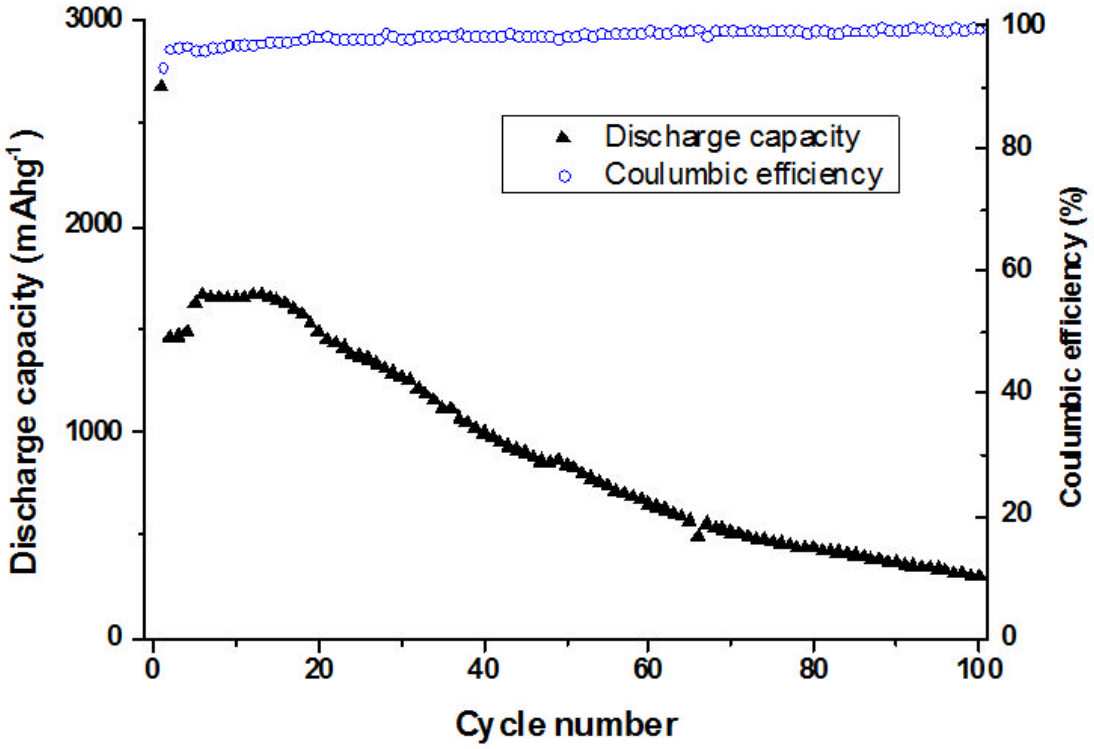

Figure 7.1. Discharge capacity and Coulombic efficiency versus cycle number for the Si electrode.

Figure 7.2(a-d) shows the top-view SEM images of the surface morphology of the silicon electrode in its pristine state (before cycling), after the 1st cycle, after the 10th cycle, and after 100th cycle. In Figure 7.2(a), the individual silicon particles can be easily identified by their detailed sharp edges and flat facets. After 1 cycle (Figure 7.2b), the electrode still maintains its integrity; however, the sharp edges and faces become less prominent as a result of the SEI layer formation and volume changes. The surface film is becomes more significant after 10 cycles (Figure 7.2c), along with the

occurrence of cracks propagating across the electrode surface. The SEM image taken after 100 cycles shows severe fracturing of electrode particles into smaller fragments.

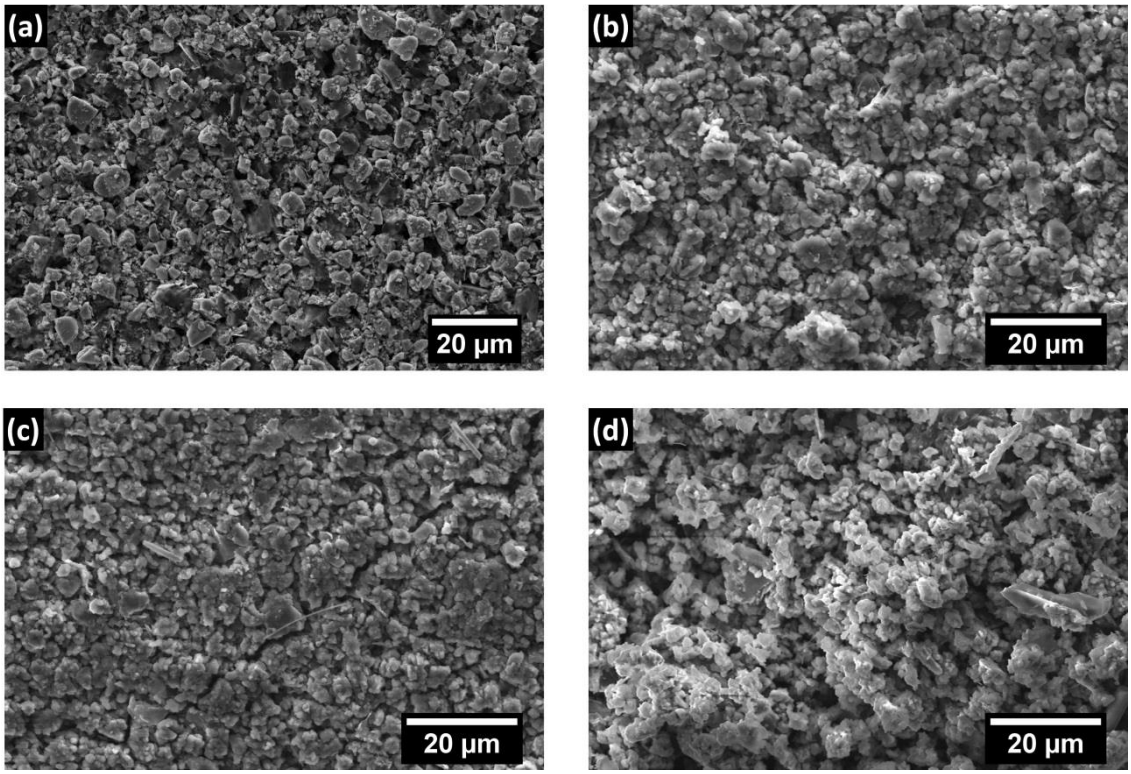

Figure 7.2. SEM images of the silicon electrode (a) in its pristine state (b) after 1 cycle, (c) after 10 cycles, and (d) after 100 cycles.

In order to gain further insight into the morphological evolution of the Si electrode material, 3D nano-scale X-ray tomography was also performed on the pristine and cycled electrodes. Within each acquired tomogram, a volume of interest (36 µm × 27 µm × 26 µm) was extracted for further analysis. Figure 7.3 shows greyscale image cross-sections through the X-ray tomograms of the Si electrode before cycling, after 1, 10 and 100 cycles. In order to facilitate the comparison between the different tomograms, the greyscale intensity histogram of each X-ray tomogram was normalized with respect to the initial tomogram of the pristine electrode. Within the pristine electrode (Figure 7.3a), the Si particles are clearly distinguished by their higher X-ray attenuation as the bright, irregular-shaped regions with no visible cracks or fracturing. The darker, less attenuating region surrounding the Si particle corresponds to the porous matrix containing the conductive material and binder phases.

Following the 1st cycle, Figure 7.3b, significant cracking can be seen to occur within the Si particles (denoted by yellow arrows) as a result of volume change caused by lithiation and delithiation processes. In addition to particle cracking, the Si particles

begin to lose the (greyscale) intensity around their edges, with the presence of a relatively low intensity phase observed around the outer surface of the particles. This decrease in greyscale intensity directly correlates with a decrease in X-ray absorption or a change in material density [275]. The formation of the low attenuating phase can be attributed to the phase transformation that occurs due to the alloying of Li and Si, as well as the significant formation of SEI-based products from electrolyte breakdown. Excessive SEI formation in Si electrodes can be controlled through the use of electrolyte additives [93,94].

After 10 cycles (Figure 7.3c) and 100 cycles (Figure 7.3d), numerous Si particles appear to have further undergone phase transformation and volume change, and this is accompanied by a significant increase in the low attenuating phase surrounding the remaining Si fragments. However, at 100 cycles, the region that was imaged within the electrode appeared to have darker attenuating regions (highlighted by blue arrows) which could be attributed to the bulk fracturing and material displacement within the electrode matrix as a result of repeated volume change during progressive cycling. This could influence the electrical contact of some Si particles within the bulk electrode, causing their isolation from the conductive matrix and could contribute to the loss in electrode capacity.

The evolution of the 3D structure of the Si electrode was also visualized with the aid of 3D renderings of the electrode. Figure 7.4 shows a 3D rendering of the Si phase within the electrode prior to any cycling. The Si particles (colored in yellow) were rendered after threshold segmentation of the highly attenuating Si particles shown in Figure 7.3, while the rest of the electrode matrix (conductive carbon, binder and pore phases) were set to be invisible.

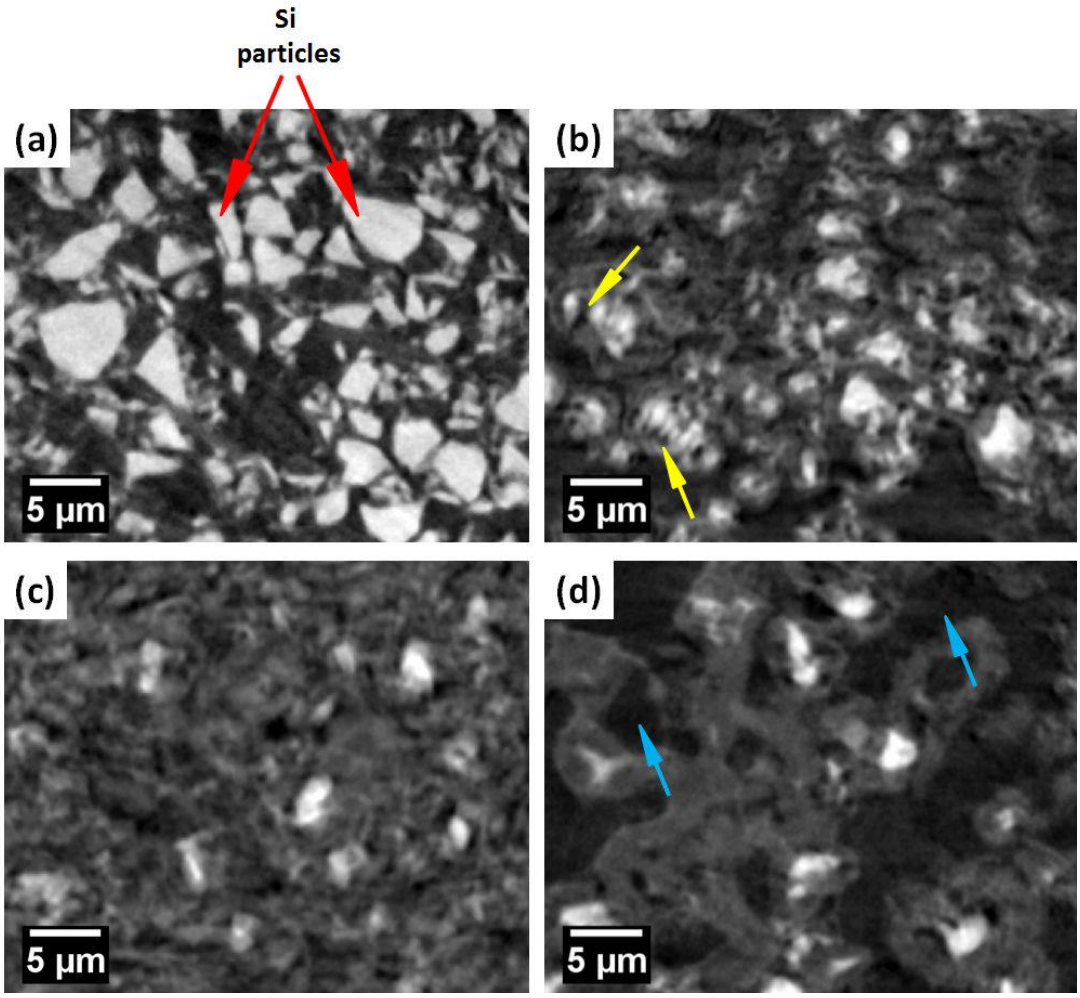

Figure 7.3. Cross-sections through X-ray tomograms of the Si electrode (a) in its pristine state, (b) after 1 cycle, (c) after 10 cycles, and (d) after 100 cycles. The yellow arrows in (b) highlight fracturing in the bulk Si particles while the blue arrows in (d) highlight possible voids formed from fracturing and material displacement due to repeated electrode volume changes.

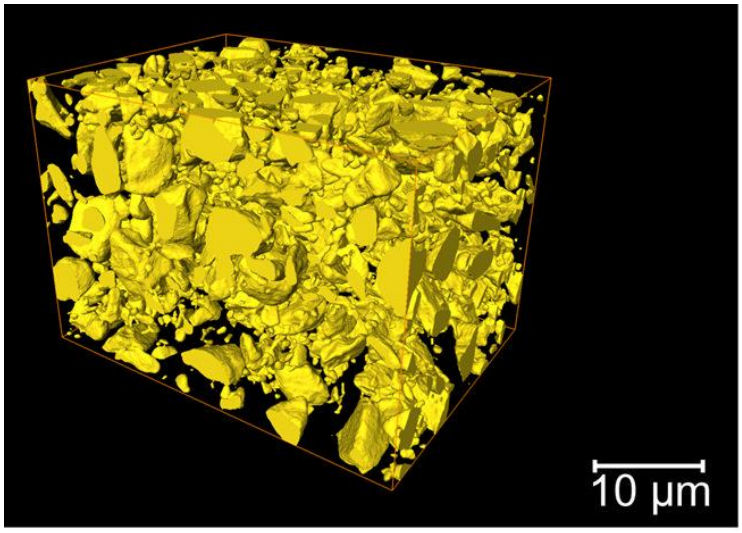

Figure 7.4. 3D rendering of Si phase in the pristine electrode.

3D renderings of the electrode, including individual renderings of the Si and low attenuating phases, after 1, 10 and 100 cycles are presented in Figure 7.5 – Figure 7.7. With progressive cycling, continuous lithiation-induced phase transformation of Si, as well as SEI layer growth, occurs which is associated with formation of the low attenuation phase (colored in green). As a result, there is a significant reduction in the volume fraction of the Si phase in the analyzed electrode volume, from 21.30 % in its pristine state to 3.65 % after 100 cycles (Table 7.2). The specific surface area of the Si phase is seen to increase between the analysed 3D volumes from 2.86 μm^{-1} in the pristine electrode to 4.29 μm^{-1} after 1st cycle; this change can be associated with the increased Si surface area exposed due to particle fracturing upon volume expansion. The surface area drops slightly in the examined electrode volume at 100 cycles to 3.45 μm^{-1} most likely due to a lesser volume fraction of Si particles / fragments present.

Table 7.2. Morphological parameters extracted from the 3D reconstructions of the electrode before and after cycling.

Cycle number	**Phase volume fraction (%)**		**Pure Si specific surface area (μm^{-1})**
	Pure Si phase	**Low-attenuating phase**	
0	21.30	-	2.86
1	5.84	44.10	4.29
10	5.48	79.92	4.36
100	3.65	46.01	3.45

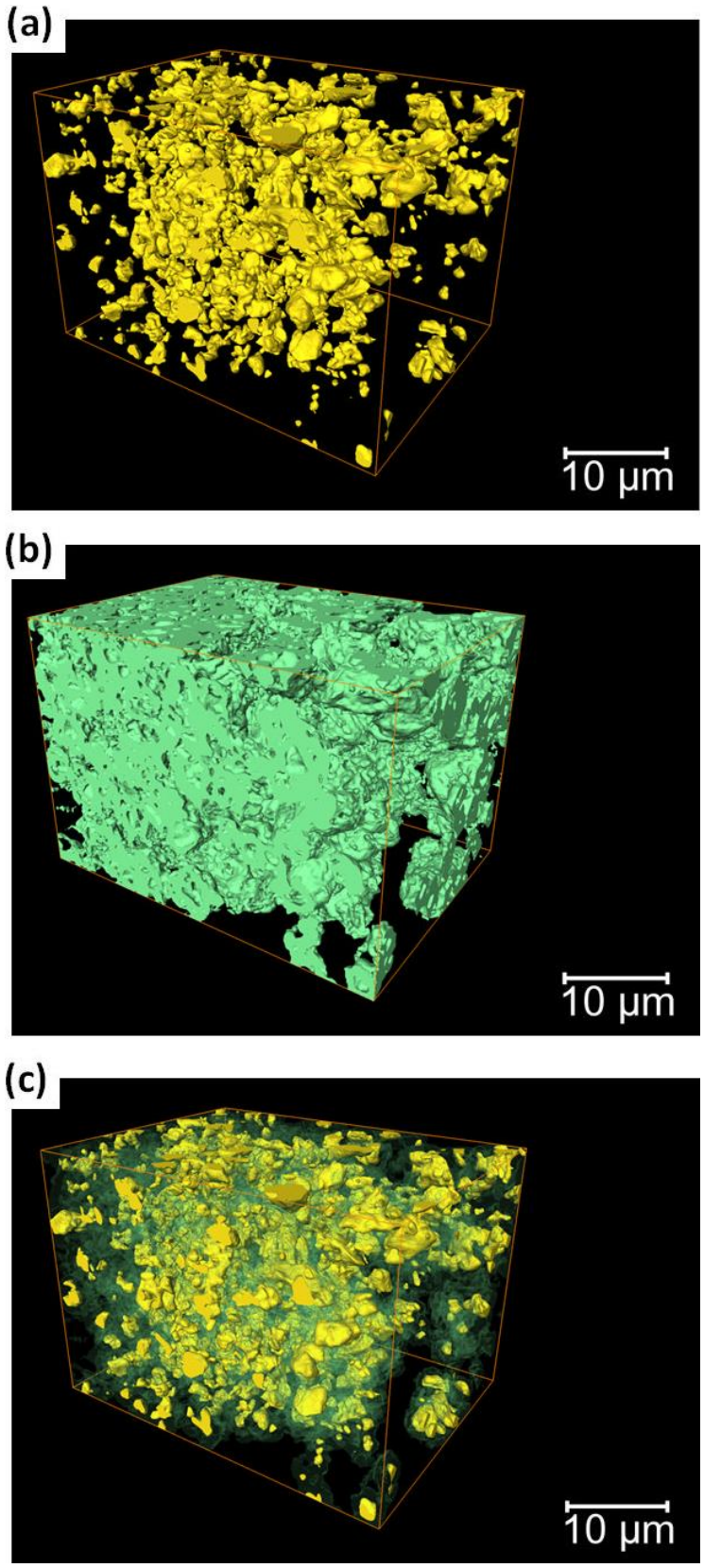

Figure 7.5. 3D rendering of the (a) Si phase, (b) low-attenuating phase, and (c) both phases combined after 1 cycle. The low attenuating phase made transparent in (c).

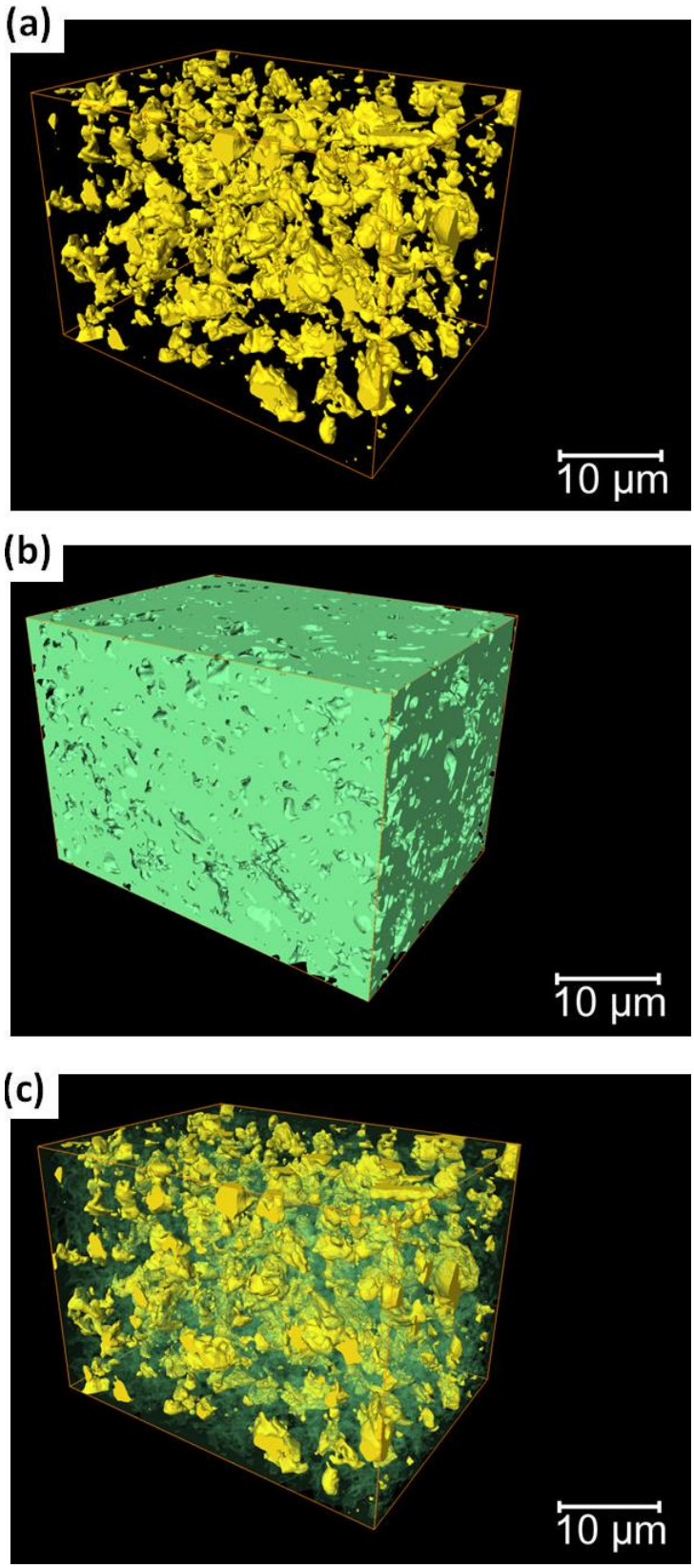

Figure 7.6. 3D rendering of the (a) Si phase, (b) low-attenuating phase, and (b) both phases combined after 10 cycles. The low attenuating phase made transparent in (c).

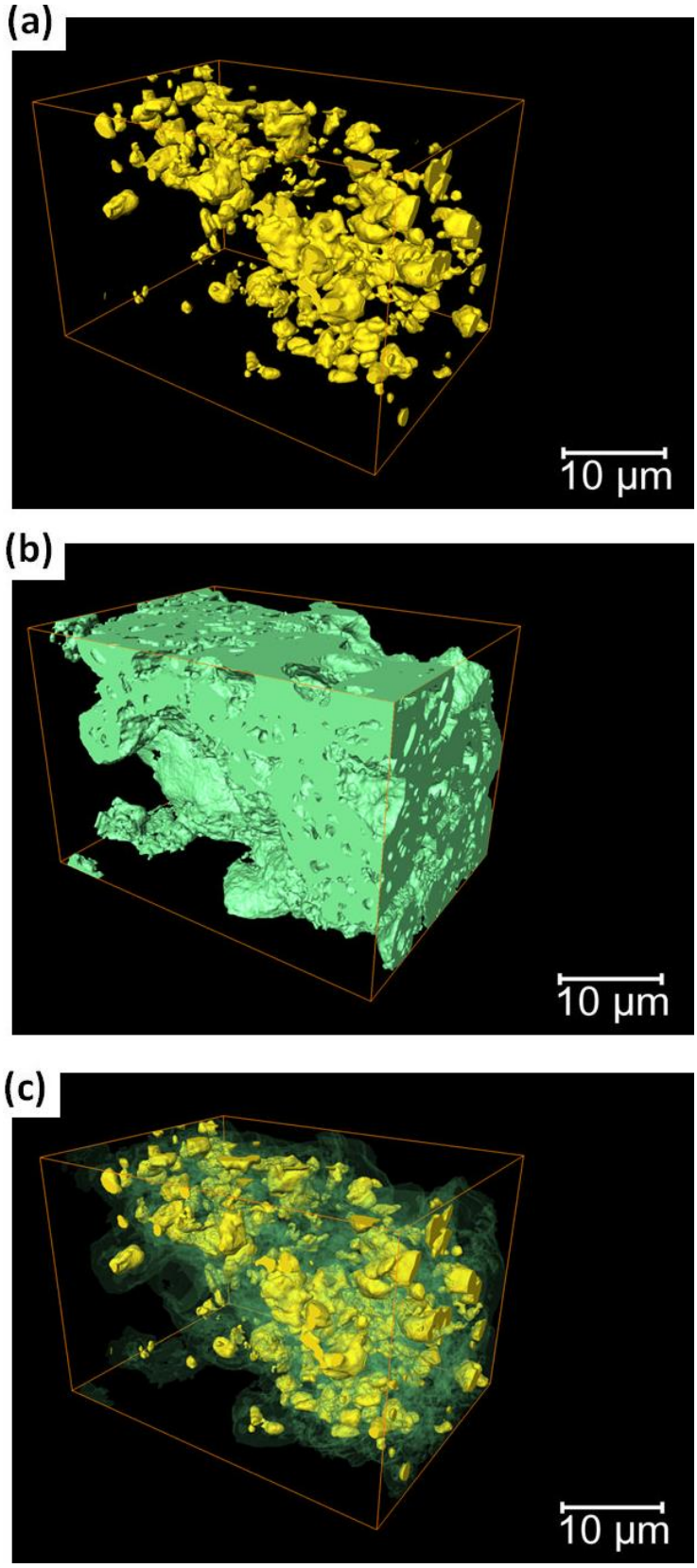

Figure 7.7. 3D rendering of the (a) Si phase, (b) low-attenuating phase, and (c) both phases combined after 10 cycles. The low attenuating phase made transparent in (c).

7.2.3 Conclusion

Upon cycling, Si electrodes experience significant degradation in their electrochemical performance which can be related to changes within the electrode microstructure. Here, X-ray nano-tomography was used to investigate the cycling-induced morphological evolution of the 3D microstructure of a Si-based electrode. Fracturing and phase transformation of Si particles within the electrode material were highlighted. The evolution of morphological parameters such as phase volume fraction and specific surface area as a result of the electrode cycling were quantified in 3D. Such high-resolution nanometre-scale X-ray imaging provides opportunities to obtain better understanding of the electrochemically induced degradation mechanisms in lithium-ion batteries.

7.3 Contrast enhancement techniques in X-ray imaging of LIB electrodes

Tomographic imaging has been used to examine battery cathode materials at multiple length scales [24]; however, for low atomic number (low-*Z*) anode materials (e.g. graphite), conventional tomographic imaging approaches have some limitations. For instance, the Ga^+ focused-ion beam interacts with graphitic structures, often resulting in highly non-uniform surface milling. Moreover, with conventional absorption contrast X-ray imaging, it is difficult to obtain high-contrast images due to the extremely small X-ray absorption coefficients of low-*Z* materials, especially at the nanometre length scale.

The proliferation of phase-contrast X-ray imaging modalities [168–172] has helped enhance contrast in X-ray images of weakly absorbing materials by utilizing phase shifts across the incident X-ray beam. For nanoscale imaging in particular, Zernike phase contrast X-ray imaging has been used to improve the contrast in CT images of graphite anodes [294] and of the conductive additive-binder phase in a LIB cathode [295], enhancing the visibility of sub-micron features of interest within the electrode materials. Unfortunately, Zernike phase-contrast tomography on low-*Z* materials produces artifacts, such as “halos” and “shade-offs” [296], which preclude the use of traditional image segmentation techniques that employ a single value

threshold; however, images laden with such artifacts may be restored with use of algorithms which model the phase contrast optics [297].

In this section, a combined contrast approach was developed and applied to characterise the three-dimensional microstructure in a graphite-based electrode material using image information obtained subsequently from both absorption–contrast and phase-contrast X-ray CT imaging. Previously, Komini Babu and co-workers [295] successfully used Zernike phase-contrast and absorption–contrast X-ray CT imaging to separately resolve the active material and carbon-binder phases in a $LiCoO_2$ cathode material by merging the resulting segmented image data from both X-ray CT images with mathematical image operations. Here, however, the combination of absorption and phase contrast information from sequential X-ray imaging in a laboratory X-ray microscope without prior image segmentation is demonstrated by blending and optimising the weighting of the signal from both X-ray images in order to create a final enhanced image with improved contrast. This technique leverages the benefits of both phase and absorption imaging: maintaining the fine detail of electrode cracks characteristic of phase images with the ease of image analysis of absorption imaging, which enables the use of single-threshold image segmentation and minimal post-processing of image reconstructions.

Microstructural investigations at two length scales are also performed: using laboratory X-ray micro-CT, to image the bulk electrode and then to identify a region of interest for subsequent investigation using nano-scale X-ray CT. For the first time, the results of high-resolution studies on a graphite anode material using the unique combined phase/absorption approach are presented.

7.3.1 Materials and Methods

Graphite electrodes were prepared by mixing graphite powder (TIMREX® SLP30, TIMCAL, Switzerland), carbon black (Super P, Sigma Aldrich), and PVDF binder (Pi-KEM) in the respective percentage weight ratios 87:3:10 with *n*-methyl-pyrrolidone (Pi-KEM) in an ULTRA-TURRAX IKA mixer (IKA®-Werke GmbH, Germany). The resulting slurry was dried at 80 °C under vacuum for 24 hours. Scanning electron micrographs of the prepared electrodes were captured with the aid of a ZEISS EVO MA 10 microscope.

Following electrode preparation, the three-dimensional microstructure of an electrode sample was examined using two X-ray tomography platforms: micron-scale

X-ray CT and nano-scale X-ray CT, using the laboratory-based ZEISS Xradia Versa 520 and the ZEISS Xradia 810 Ultra respectively. The coupling of these two systems enables multi-scale insight into the microstructure of battery electrodes, which can be used to optimise material design and manufacturing for high performance cells.

3D datasets were collected at 20× magnification in absorption-contrast mode using the micron-scale X-ray CT instrument. To obtain a high signal-to-noise ratio, a total of 3201 radiographs were acquired over a 360° sample rotation range with an exposure time of 40 s per radiograph. The electrode sample was placed between the X-ray source and a $2k \times 2k$ detector, with a source-detector distance of 23.6 mm providing a voxel resolution of *ca.* 670 nm with the detector set to 2 × 2 pixel binning.

After the micron-scale analysis, the graphite electrode sample was then carefully dissected with a scalpel under a visible light microscope into smaller samples sizes for nano-CT studies. For the nano-scale X-ray CT experiments, both absorption-contrast and phase-contrast images of the graphite electrode were acquired in the "large field-of-view" mode (65 µm × 65 µm in dimension). A total of 1601 projections were collected per 180° sample rotation with an exposure time of 3 s for the absorption-contrast imaging and 8 s for the phase-contrast imaging. This yielded two sets of raw image data, both with an isotropic voxel resolution of *ca.* 130 nm using a detector pixel binning of 2.

In order to generate a nano-scale dataset of the graphite electrode large enough for some microstructural quantification, separate tomography images were successively acquired and then vertically stitched together to form taller single tomographic image. This enabled imaging of samples which are taller or wider than the X-ray instrument's standard field-of-view. Vertical stitching is a technique which enables the combination of multiple 3D datasets from multiple regions along the vertical length of a sample. Phase-contrast and absorption-contrast images were first collected for each region of interest to achieve contrast-enhanced reconstructions. Vertical stitching was then performed using an automated image stitching algorithm (*Plugin_Stitch.dll*) in the ZEISS XMController software. To enable optimum execution of the image stitching procedure, a recommended vertical overlap of 15% between the field of view of both image scans was applied.

The raw transmission images from both micro- and nano-scale X-ray CT imaging experiments were reconstructed using the ZEISS XMReconstructor software, which employs a commercial filtered back-projection algorithm (Carl Zeiss X-ray Microscopy Inc., Pleasanton, CA). Tomographic scan details are shown in Table 7.3.

Table 7.3. Tomography acquisition details.

Scan parameter	**VersaXRM-520**	**810 Ultra**	
Contrast mode	Absorption	Phase	Absorption
Source voltage (kV) or Photon Energy (keV)	30 kV	5.4 keV	5.4 keV
Camera binning	2	2	2
Number of projections	3201	1601	1601
Radiograph exposure time (s)	40	8	3
Voxel size (nm)	670	130	130
Magnification/Field-of-view (FOV)	20X	LFOV	LFOV

7.3.2 Multi-scale microstructural characterisation

Scanning electron micrographs of the prepared electrode (Figure 7.8) revealed a platelet–like shape of the graphite particles, defects on particle surfaces, particle arrangement mostly along the graphite particle basal plane, and a nearly uniform particle size distribution. Whilst the micrographs show a wealth of qualitative structural information, SEM imaging is limited in its ability to provide accurate quantitative information on inherently three-dimensional structural parameters, such as tortuosity and pore-phase connectivity – such parameters directly influence the performance of the electrode in the cell, thus motivating material microstructural studies in three dimensions [7].

The reconstructed 3D image volume from the micron-scale X-ray CT imaging was segmented using the Avizo software package. The reconstructed volume showed a high signal-to-noise ratio due to the large number of projection images [Figure 7.9(a)] collected during the CT scan, thus making image segmentation straightforward. Figure 7.9(b) and Figure 7.9(c) show a single reconstructed greyscale 2D slice of the graphite electrode sample and the resulting binary image from segmenting the solid electrode and pore phases respectively. A representative region of interest (ROI) was then extracted from the full micro X-ray CT 3D dataset by cropping a volume of interest (*ca.* 447 mm × 402 mm × 65 mm) which fulfilled representative volume element conditions (highlighted in Section 4.2.3) for subsequent analysis.

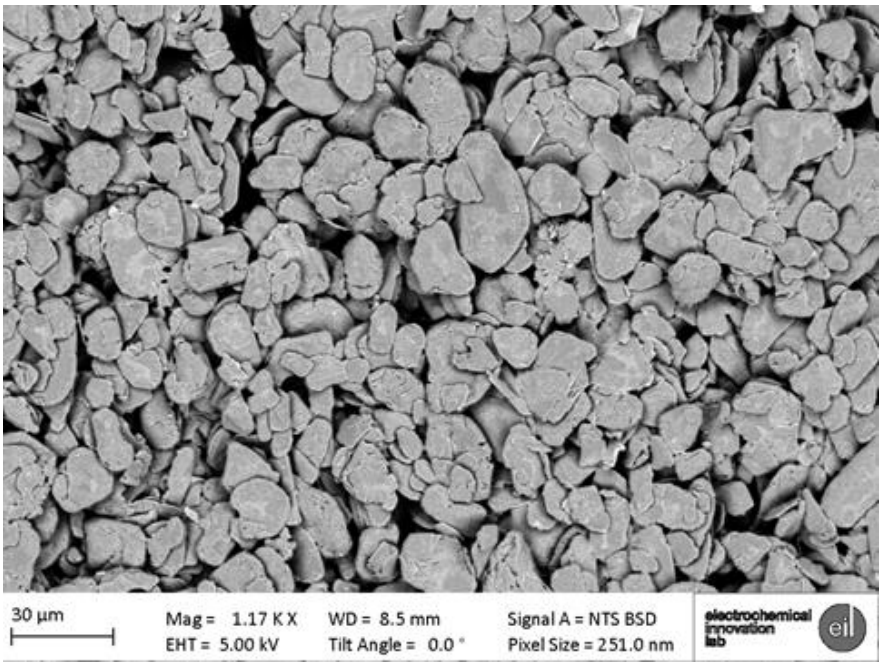

Figure 7.8. Scanning electron micrograph of the prepared graphite electrode.

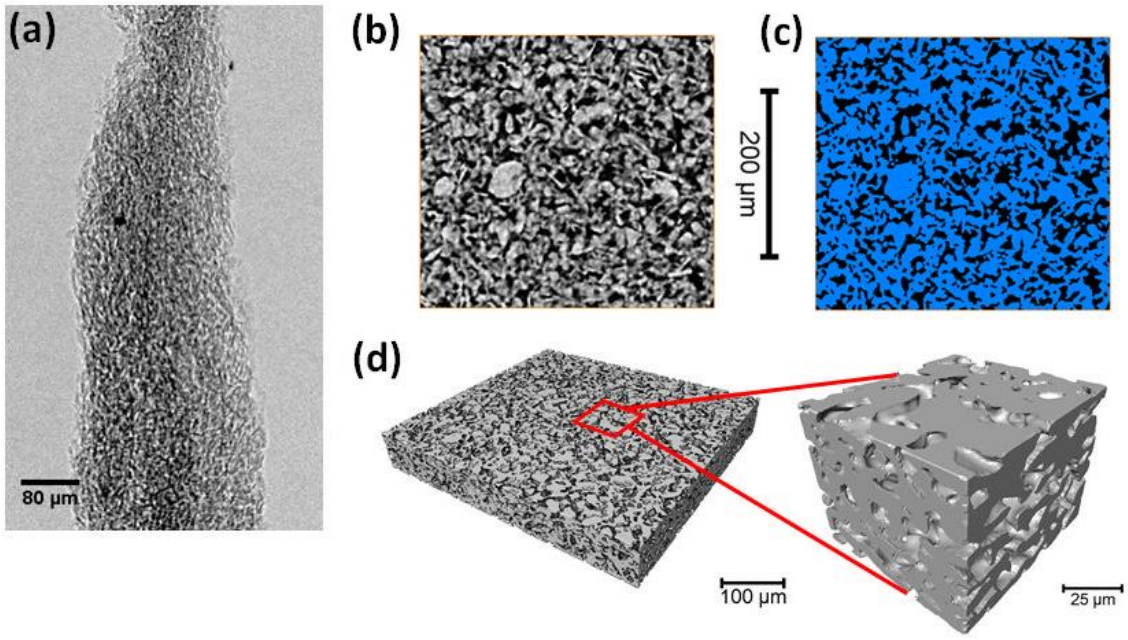

Figure 7.9. (a) A single X-ray projection image of the graphite electrode material acquired from absorption-contrast micron-scale XRM. (b) A single 2D reconstructed slice of a cropped region of interest from the micro-XCT graphite 3D greyscale dataset and (c) the resulting binarized image. (d) 3D renderings of the binarized dataset (left) and a zoomed-in region showing the microstructural detail (right).

X-ray radiographs from nano-scale CT imaging in absorption and Zernike phase-contrast imaging modes are presented in Figure 7.10(a) and Figure 7.10(b) respectively, and resulting reconstructed slices in Figure 7.10(c) and Figure 7.10(d).

From the radiographs, it can clearly be seen that the Zernike phase contrast imaging enhances features and edges of the graphite electrode particles compared to the absorption-contrast imaging; this is also observed in the reconstructed images. Each image has its merits: the phase-contrast image provides more boundary edge contrast information, revealing the internal inclusions and cracks in the graphite microstructure, while the absorption–contrast image represents density information, which is particularly important for reliable, automated image segmentation. In order to take advantage of the merits of both imaging techniques, the information from both absorption–contrast and phase–contrast images was merged to yield a "combined contrast" image; this was performed using image registration and dual–scan analysis with aid of the ZEISS Xradia Dual Contrast Visualizer software [298,299].

Most commonly used in dual-energy imaging (see e.g. [300]), the dual-scan analysis software enables blending of the absorption and phase contrast images by aid of a two-dimensional intensity histogram, with the goal to preserve the favourable contrast behaviour of the two imaging modes: edge enhancement from phase contrast and density information from absorption.

The variations of greyscale intensity across the graphite particles can significantly determine threshold segmentation accuracy. The 2D histogram of a line profile across a graphite particle in the reconstructed image shown in Figure 7.11 was plotted for all three acquired images. With the phase-contrast image, the histogram clearly shows that the graphite particle boundary edges can be clearly mapped by the presence of distinct intensity fringes (unlike in the absorption-contrast image). However, a complete and accurate threshold-based segmentation of the graphite particle based solely on the phase information will prove troublesome due to the presence of "shade-off" (i.e. due to the similarities in the greyscale intensity within the graphite particle interior and exterior).

The absorption-contrast image, however, shows a substantial attenuation contrast distribution between background and the graphite particle, but not as much detail on particle defects and boundary edges as the phase-contrast image. As highlighted in Figure 7.11, sub-particle defects, visible in phase contrast, are difficult to detect from the absorption contrast dataset alone. Combining boundary edge and attenuation information from both phase-contrast and absorption-contrast images

provides a sufficient distribution of greyscale intensity to ease automated threshold-based segmentation; whilst maintaining the unique benefits of phase contrast imaging to describe physical edges and cracks in the electrode. Image segmentation of the combined contrast nano-scale X-ray CT dataset was also performed in Avizo software.

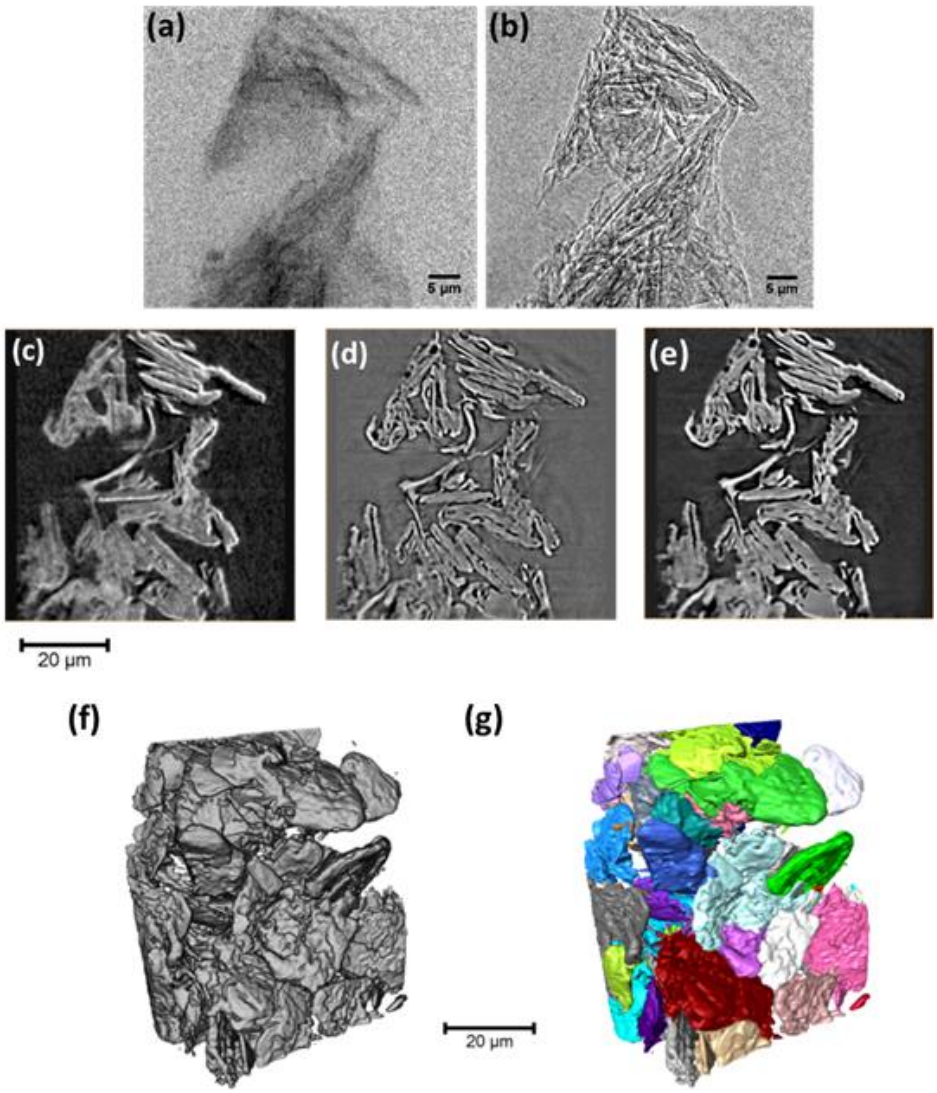

Figure 7.10. A single X-ray projection image of the graphite electrode material acquired from (a) absorption-contrast nano-scale X-ray CT, (b) Zernike phase-contrast nano-scale X-ray CT. Single reconstructed slices from nano-scale X-ray CT of a small region of interest within the graphite electrode (c) in absorption-contrast mode (d) in phase-contrast mode, and (e) after combined-contrast enhancement. (f) Resulting volume rendering of the graphite electrode region of interest, and (g) after algorithmic particle separation and identification.

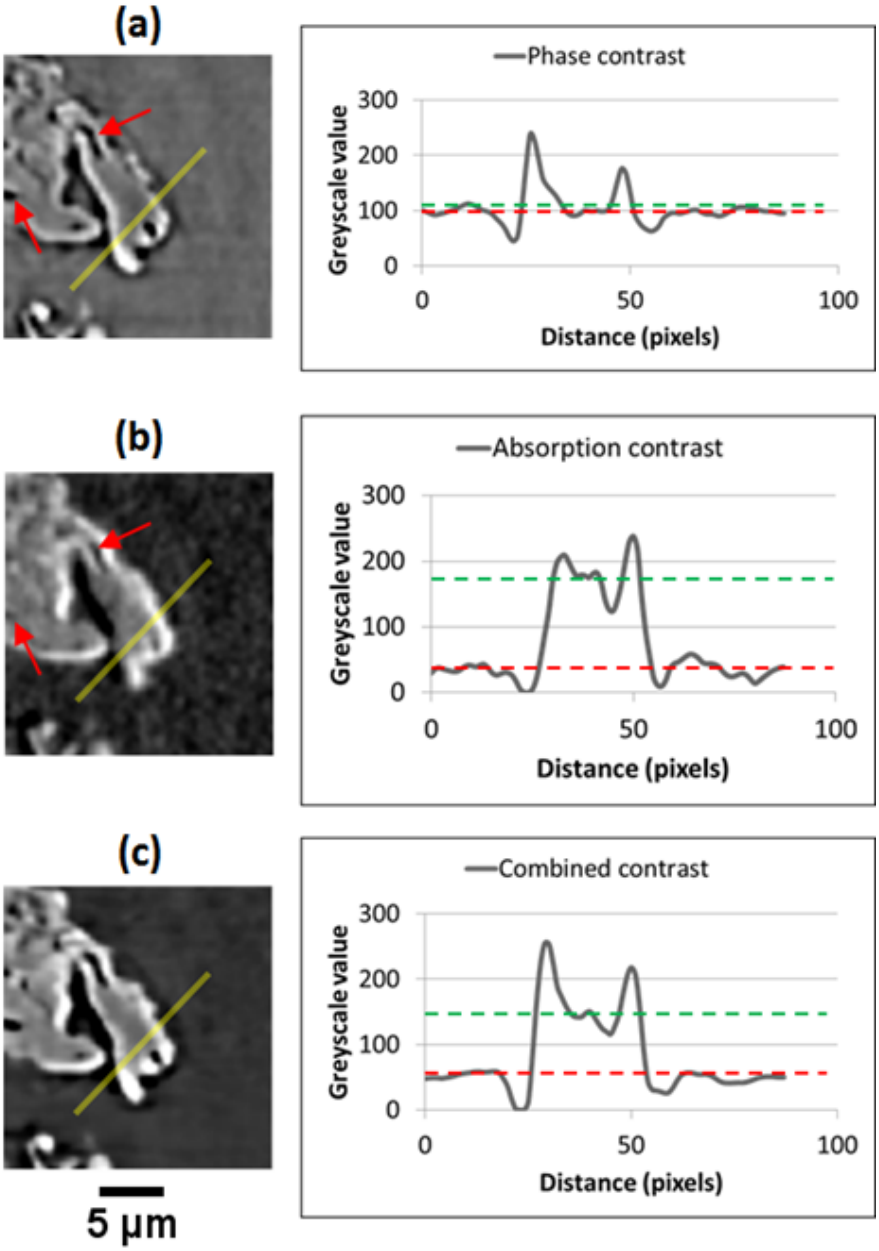

Figure 7.11. Variation in greyscale intensity across a graphite particle in reconstructed images generated from (a) phase contrast imaging, (b) absorption contrast imaging and (c) combined contrast enhancement. Improved attenuation information and boundary edge detection is achieved with the combined contrast image, easing image segmentation. Red arrows highlight particle inclusions and cracks which are visible in Zernike phase-contrast image but not as clear in absorption-contrast image. In each graph, the green and red dashed-line mark the average greyscale within the graphite particle and background respectively.

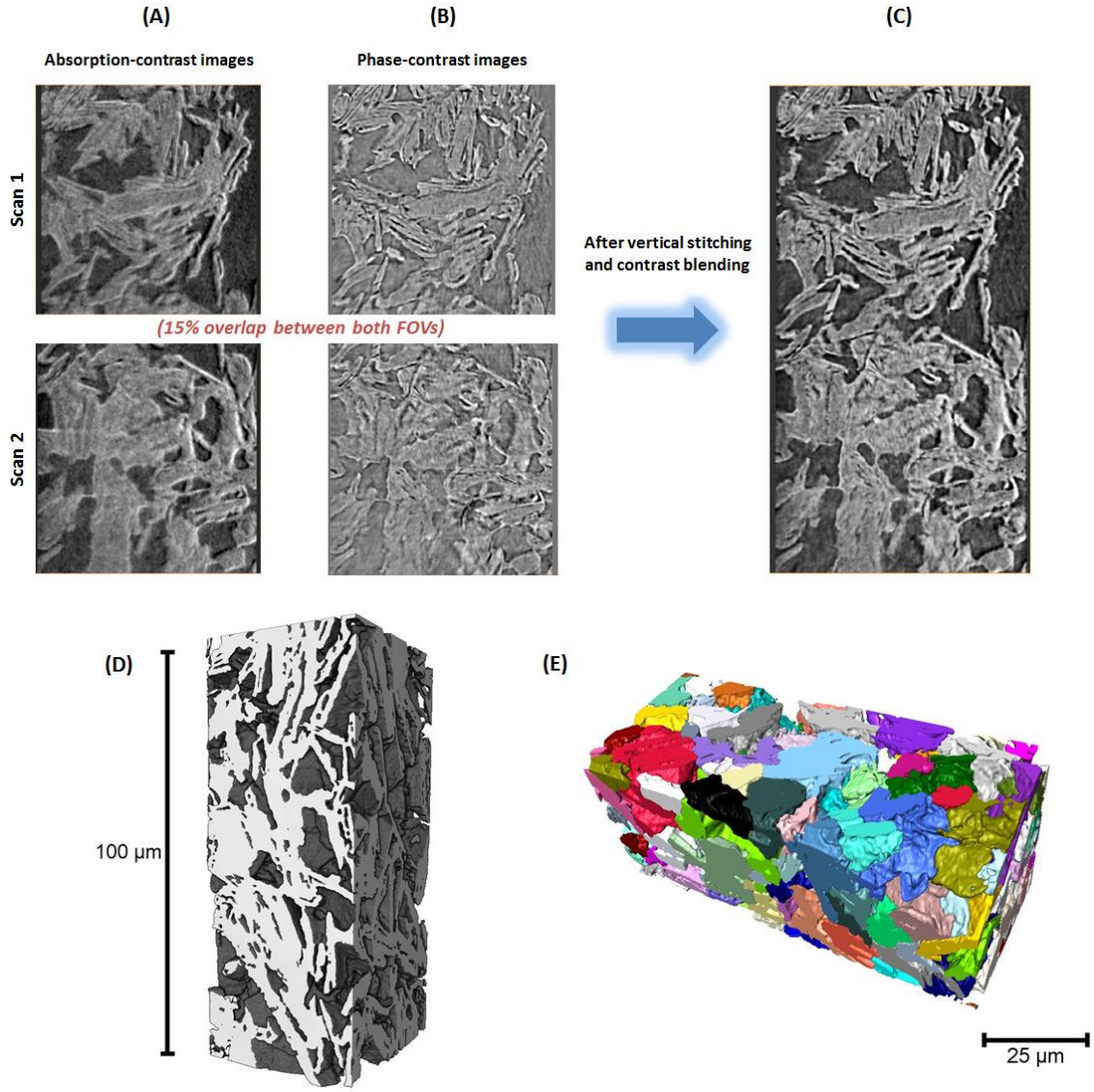

Figure 7.12. Single reconstructed slices from successive nano X-ray CT scans acquired along the length of a larger graphite electrode sample (a) in absorption-contrast mode (b) in phase-contrast mode. (b) Single reconstructed slice from 3D dataset resulting from vertical stitching and contrast blending of the absorption and phase-contrast 3D datasets. A 15 % overlap between the successive scans was used to allow optimum operation of the vertical stitching procedure. (d) Volume rendering of the fully stitched dataset. (e) Volume rendering after algorithmic particle identification.

A larger and more representative nano-scale 3D dataset (*ca.* 43 mm × 98 mm × 41 mm) for subsequent quantitative analysis was obtained by acquiring successive tomography images along the length of the sample and then vertically stitching them together. Figure 7.12 shows reconstructed slices from two successive fields of view along the length of a scanned graphite electrode sample taken in absorption and phase-contrast modes. After contrast blending and vertical stitching, the resulting

enhanced 3D dataset was segmented using the auto-thresholding tool in Avizo software. A volume rendering of the segmented dataset is shown in Figure 7.12 (d).

Moreover, the improved contrast nano-CT datasets enabled individual particle separation and identification to be performed. Particle separation and identification was performed using the 'Separate Objects' quantification module in Avizo software, and Figure 7.10(e) and Figure 7.12(e) show the resulting volume rendering of separated graphite particles using the algorithm. Attempts to separate the micro-CT dataset into individual particles using the Separate Objects algorithm were not successful, with the electrode volume being split electrode volume into large clusters of particles at that imaging resolution.

Quantitative analysis was performed on the micro- and enhanced nano–CT datasets to extract microstructural parameters: namely, porosity, volume-specific surface area, pore-phase tortuosity, and mean pore size (see Table 7.4).

Table 7.4. Electrode microstructural parameters extracted from tomography data.

Imaging platform	Pixel size (µm)	Porosity (%)	Geometric Tortuosity			Specific surface area (μm^{-1})	Average pore size (µm)
			x	y	z		
Micro-CT	0.670	42.52	1.09	1.05	1.26	0.411	2.71
Nano-CT	0.130	42.95	1.14	1.17	1.32	0.861	2.01

Porosity and volume-specific surface area were calculated in Avizo; specific surface calculations were based on the marching cubes algorithm [190] with surface mesh smoothing and refinement. Mean pore size was calculated in ImageJ software using the continuous pore size distribution method [201]. Tortuosity was calculated geometrically with the aid of the fast marching algorithm [195] implemented in MATLAB.

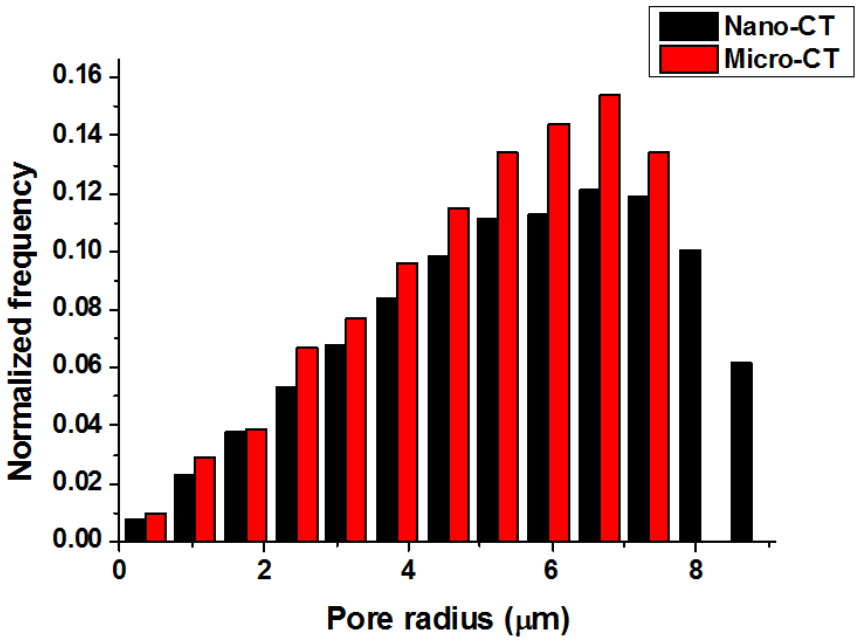

Figure 7.13. Pore size distribution extracted from the nano X-ray CT and micro X-ray CT image datasets.

The results show similar porosity, directional pore-phase tortuosity, and mean pore size values between the micron- and nano-scale datasets. The pores size distributions extracted from the nano-CT and micro-CT datasets (Figure 7.13) are in good agreement, which is a good validation of the similar porosity values obtained for both datasets. However, volume-specific surface area from the nano-scale scan was more than double that obtained from the micron-scale measurements. This is similar to observations made in a multi-length scale study of a lithium-manganese-oxide battery cathode material [24], reiterating the need for more stringent imaging resolution requirements for surface area measurement studies, which are sensitive to microscopic variations in surface roughness and cracks.

7.3.3 Conclusion

X-ray tomographic imaging enables non-invasive characterisation of the complex microstructures within lithium-ion battery electrodes. For low atomic number electrode materials, image segmentation of phase-contrast X-ray images may prove difficult due to insufficient attenuation contrast, which is usually present in absorption-contrast images. Here, for the first time, nano-scale X-ray absorption contrast and phase-contrast X-ray image data of a graphite electrode material for lithium-ion batteries are combined, allowing detailed complementary image information to be

gathered which enables straightforward image analysis that so far was extremely difficult to do. Using contrast enhancement and vertical tomography stitching algorithms, it was possible to generate 3D nano-scale reconstructions of a graphite electrode with an enhanced image with improved contrast and boundary edge information.

Multi-scale investigations of the electrode material were also performed using laboratory micro- and nano-scale XRM, and results from subsequent quantitative analysis showed that, depending on the electrode microstructural parameter under investigation, there is a variation in the imaging resolution and representative volume element requirements.

Chapter 8

Summary, Conclusions and Future Work

8.1 Summary and Conclusions

Understanding the influence of the electrode microstructure in lithium-ion batteries (LIBs) on their electrochemical performance is crucial, particularly towards the development of high capacity electrode materials (e.g. silicon, lithium) to meet more energy-demanding, large-scale applications such in electric vehicles and grid storage systems. By applying X-ray tomographic imaging techniques, this work presents both qualitative and quantitative investigations on the three-dimensional microstructure within various LIB electrode materials at multiple length and time scales.

8.1.1 Stereological *versus* direct 3D microstructural quantification

In the first phase of the research project, the suitability and reliability of direct 3D microstructural analysis for quantifying LIB electrodes was demonstrated by comparing it with stereological prediction methods. For this comparison, real microstructural data was obtained for three different commercial LIB electrodes using synchrotron X-ray tomographic imaging, and key electrode structural parameters, namely porosity, specific surface area, tortuosity and pore size, were extracted. Although stereological prediction of these parameters with 2D image sections introduces bias when applied to inhomogeneous 3D microstructures such as those examined, they could provide reasonable initial estimates for porosity values. However, direct 3D analysis is more suited for accurately quantifying parameters, such as tortuosity, which rely on the interconnectivity of phase networks in three-dimensions.

8.1.2 *In-situ* and *operando* 3D X-ray imaging of evolution within Si and Li electrodes

The next phase of the research project focused on using X-ray tomography to visualize and quantify microstructural and morphological evolution that occurs within

high capacity electrode materials, in particular Si and Li, as a result of battery operation.

The morphological evolution occurring at the surface of metallic Li electrodes was also investigated *in-operando* and *in-situ* using synchrotron and laboratory based X-ray sources, respectively. *Operando* synchrotron X-ray CT enabled the real-time 3D visualization of pit growth at the Li metal surface due to Li dissolution upon electrochemical stripping, and time-resolved *in-situ* laboratory X-ray CT imaging was used to track the growth of electrodeposited, moss-like lithium at the Li electrode surface. Although the high flux of the synchrotron pink beam provided sufficient resolution and contrast that enabled identification and tracking of surface morphology changes within the low attenuating Li metal, beam exposure to the sample led to performance degradation. Thus, the X-ray radiation dose to the cell samples must be carefully considered to prevent material degradation and cell performance losses in future X-ray experiments.

During the early stages of lithiation, laboratory X-ray micro-CT, coupled with DVC, enabled the visualization and quantification of volume changes, as well as 3D volume strain within bulk electrodes. Synchrotron X-ray micro-CT enabled real-time visualization of lithiation-induced phase transformation as well as fracture formation and propagation in individual silicon microparticles. The synchrotron X-ray CT results from this study highlight the severe nature of fracturing of crystalline Si microparticles during the first lithiation, which often leads to commonly observed irreversible capacity loss in Si electrodes after the first charge-discharge cycle. Although this fracturing in Si microparticles remains unavoidable, strategies to stabilize their performance and maintain their electrical conductivity are being developed, such as, for example, graphene encapsulation [301]. This study not only demonstrates that the dynamic morphological transformations that occur during the degradation and failure of Si microparticles can be non-invasively studied in real time using synchrotron X-ray imaging, but that the technique is useful in providing valuable information and insight to aid efficient design of micron-sized silicon particles for electrodes in next generation batteries.

8.1.3 X-ray nanotomographic characterisation of cycled Si electrodes

Cycling-induced microstructural degradation of a Si-based electrode was also examined using *ex-situ* X-ray nanotomography, in combination with SEM imaging. X-ray nanotomography enabled 3D visualization and quantification of the phase transformation occurring within the Si electrode with increasing cycle number. Electrode performance loss with repeated cycling was seen to be associated with loss of active Si. These results further highlight the capability of X-ray tomography to investigate the role of electrode microstructure in battery degradation and failure.

8.1.4 X-ray contrast enhancement for low-density electrode materials

A 3D X-ray image contrast enhancement approach for obtaining improved nano-scale image contrast on a laboratory X-ray microscope was demonstrated by combining information obtained from both absorption–contrast and Zernike phase-contrast X-ray CT images. The imaging approach also facilitated the first multi-length scale microstructural investigation of a weakly (X-ray) absorbing graphite electrode reported in the literature. This technique will significantly improve our understanding of the nano-scale structure of graphite electrodes for LIBs, and it is predicted to find widespread application in a diverse range of low-atomic number materials, which are characteristically challenging to image by absorption contrast alone.

8.2 Suggestions for Future Work

X-ray CT has been proven to be a powerful, non-invasive diagnostic tool for observing the evolution of LIB microstructures *in-situ* and *in-operando*, and the recent rapid proliferation of 3D X-ray CT techniques on both synchrotron and laboratory sources has greatly improved spatial and temporal imaging resolution that is achievable. In this work, X-ray CT has mostly been applied to conduct microstructural evolution investigations at the micrometre scale. However, this can effectively be extended to the nanometre scale with X-ray nanotomography to provide higher spatially and temporally–resolved 3D image information for a wide array of LIB investigations. Such dynamic investigations at this length scale can be challenging as they would require an appropriate X-ray transparent, *in-situ* electrochemical cell design that is well suited to the X-ray nanotomography system hardware being used. Efforts are currently being made at the Electrochemical Innovation Lab in UCL to

develop a new *in-situ* cell design suited for sub-micron and nano-scale studies. The proposed cell design, shown in Figure 8.1, is made from a cylindrical PEEK (polyetheretherketone) housing with an internal diameter of 800 µm, and stainless steel current collectors of the same diameter. The X-ray transparency and chemical durability of PEEK make it suitable for use in such electrochemical investigations, especially with different battery materials.

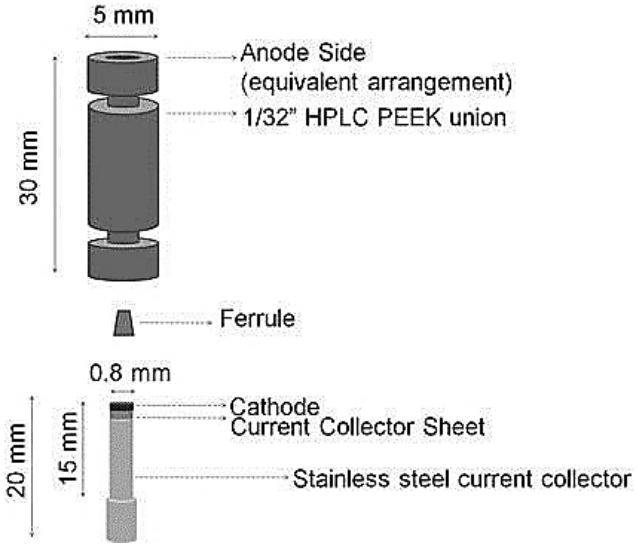

Figure 8.1. Proposed *in-situ* electrochemical cell design for nano-scale X-ray CT studies. Reproduced with permission from [302].

This promising miniature cell design will be applied in further electrode microstructural evolution studies using both laboratory and synchrotron sources.

Graphite electrode particles have been reported to suffer volume changes of up to 10% as a result of lithiation [11]. However, using convention absorption-contrast imaging, it is challenging to obtain sufficiently high contrast micro-CT images of such a low attenuating material that track this degree of volume expansion at the particle level. With *in-situ* nano-CT imaging capabilities, this can be tackled by applying the X-ray image contrast enhancement technique presented in Section 7.3, and could potentially enable more detailed qualitative and quantitative insights on graphite electrode 3D microstructure to be acquired.

As reported in the literature and also shown in Section 7.2, bulk Si electrodes fabricated from micron-sized Si particles show huge irreversible capacity loss as well as poor capacity retention. The use of nanostructured Si composite electrode materials, such as in Figure 8.2, has led to moderate success with reversible capacity retention and structural stability. It will be of interest to visualise how the 3D microstructure of

such nanocomposites evolves in relation to their relatively improved performance using *in-situ* and *in-operando* X-ray imaging techniques. This could also provide further insight on the critical diameter of Si nanoparticles above with fracturing occurs.

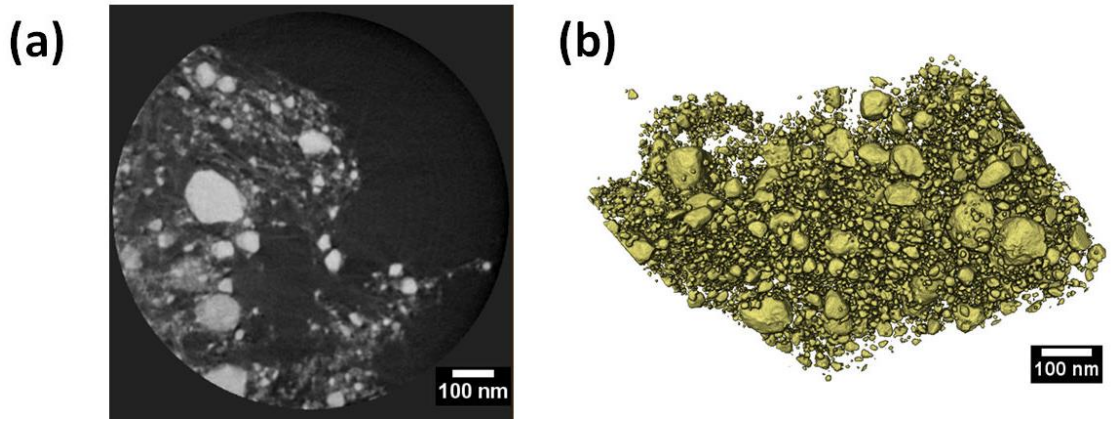

Figure 8.2. (a) X-ray tomogram cross-section of a pristine nanostructured Si-composite electrode. (c) 3D rendering of the Si nanoparticles.

In Chapter 5, the 3D morphological evolution of electrodeposited moss-like lithium structures was captured using X-ray micro-CT imaging. However, the nucleation and growth of dendritic lithium, which typically have feature sizes that begin in the nanometre range, has only been studied using 2D imaging techniques [243,303]. With the aid of high resolution phase-contrast 3D X-ray imaging techniques, it would be interesting to study the dynamic evolution of Li dendrite growth during battery operation, particularly to examine the influence of varying battery operating conditions (such as charging current density, electrolyte formulations, etc.) on the 3D morphology of dendrites at the nanometre length scale.

Dissemination and Outputs

Primary peer-reviewed publications

1. **O. O. Taiwo**, D. P. Finegan, D. S. Eastwood, J. L. Fife, L. D. Brown, J. A. Darr, P. D. Lee, D. J. L. Brett, and P. R. Shearing, "Comparison of three-dimensional analysis and stereological techniques for quantifying lithium-ion battery electrode microstructures", *Journal of Microscopy*, vol. 263, no. 3, pp. 280–292, 2016.
2. **O. O. Taiwo**, D. P. Finegan, J. Gelb. C. Holzner, D. J. L. Brett, and P. R. Shearing, "The use of contrast enhancement techniques in X-ray imaging of lithium–ion battery electrodes", *Chemical Engineering Science*, vol. 154, pp. 27–33, 2016.
3. **O. O. Taiwo**, D.S. Eastwood, P. D. Lee, J. M. Paz-García, S. A. Hall, D. J. L. Brett, and P. R. Shearing, "*In-Situ* Examination of Microstructural Changes within a Lithium-Ion Battery Electrode Using Synchrotron X-ray Microtomography", *ECS Transactions*, vol. 69, no.18, pp. 81-85, 2015.
4. **O. O. Taiwo**, J. M. Paz- García, S. A. Hall, T. M. M. Heenan, D. P. Finegan, R. Mokso, P. Villanueva-Pérez, A. Patera, D. J. L. Brett, and P. R. Shearing, "Microstructural degradation of silicon electrodes during lithiation observed via operando X-ray tomographic imaging", *Journal of Power Sources*, vol. 342, 904 – 912, 2017.
5. J. M. Paz- García, **O. O. Taiwo**, E. Tudisco, D. P. Finegan, P. R. Shearing, D. J. L. Brett, and S. A. Hall, "4D analysis of the microstructural evolution of Si-based electrodes during lithiation: Time-lapse X-ray imaging and digital volume correlation", *Journal of Power Sources*, vol. 320, 196 – 203, 2016.
6. **O. O. Taiwo**, D. P. Finegan, J. M. Paz- García, D. S. Eastwood, A. J. Bodey, C. Rau, S. A. Hall, D. J. L. Brett, P. D. Lee, and P. R. Shearing, "Quantification of the evolving microstructure of lithium metal electrodes in 3D using X-ray CT", *submitted*, 2016.

Other peer-reviewed publications

7. P. Trogadas, **O. O. Taiwo**, B. J. Tjaden, T. P. Neville, S. Yun, J. Parrondo, V. Ramani, M. Coppens, D. J. L. Brett, and P. R. Shearing, "X-ray micro-tomography as a diagnostic tool for the electrode degradation in vanadium redox flow batteries", *Electrochemistry Communications*, vol. 48, pp. 155 – 159, 2014.
8. D. S. Eastwood, R. S. Bradley, F. Tariq, S. J. Cooper, **O. O. Taiwo**, J. Gelb, A. Merkle, D. J. L. Brett, N. P. Brandon, P. J. Withers, P. D. Lee, and P. R. Shearing, "The application of phase contrast X-ray techniques for imaging Li-ion battery electrodes", *Nuclear Instruments and Methods in Physics Research Section B: Beam Interactions with Materials and Atoms*, vol. 324, pp. 118–123, 2014.
9. D. S. Eastwood, P. M. Bayley, H. J. Chang, **O. O. Taiwo**, J. Vila-Comamala, D. J. L. Brett, C. Rau, P. J. Withers, P. R. Shearing, C. P. Grey, and P. D. Lee, "Three-dimensional characterisation of electrodeposited lithium microstructures using synchrotron X-ray phase contrast imaging", *Chemical Communications*, vol. 51, no. 2, pp. 266 – 268, 2015.
10. D. P. Finegan, S. Cooper, B. Tjaden, **O. O. Taiwo**, J. Gelb, G. Hinds, D. J. L. Brett, and P. R. Shearing, "Characterising the structural properties of polymer separators for lithium-ion batteries in 3D using phase contrast X-ray microscopy", *Journal of Power Sources*, vol. 333, pp. 184–192, 2016.
11. J. B. Robinson, J. A. Darr, D. S. Eastwood, G. Hinds, P. D. Lee, P. R. Shearing, **O. O. Taiwo**, and D. J. L. Brett, "Non-uniform temperature distribution in Li-ion batteries during discharge–a combined thermal imaging, X-ray micro-tomography and electrochemical impedance approach", *Journal of Power Sources*, vol. 252, pp. 51–57, 2014.
12. J. B. Robinson, L. D. Brown, R. J. Jervis, **O. O. Taiwo**, J. Millichamp, T. J. Mason, T. P. Neville, D. S. Eastwood, C. Reinhard, P. D. Lee, D. J. L. Brett, and P. R. Shearing, "A novel high-temperature furnace for combined in situ synchrotron X-ray diffraction and infrared thermal imaging to investigate the effects of thermal gradients upon the structure of ceramic materials", *Journal of Synchrotron Radiation*, vol. 21, pp. 1134–1139, 2014.
13. J. B. Robinson, L. D. Brown, R. J. Jervis, **O. O. Taiwo**, T. M. M. Heenan, J. Millichamp, T. J. Mason T. P. Neville, R. Clague, D. S. Eastwood, C. Reinhard, P.

D. Lee, D. J. L. Brett, and P. R. Shearing, “Investigating the effect of thermal gradients on stress in solid oxide fuel cell anodes using combined synchrotron radiation and thermal imaging”, *Journal of Power Sources*, vol. 288, pp. 473–481. 2015.

14. D. P. Finegan, E. Tudisco, M. Scheel, J. B. Robinson, **O. O. Taiwo**, D. S. Eastwood, P. D. Lee, M. Di Michiel, B. Bay, S. A. Hall, G. Hinds, D. J. L. Brett, and P. R. Shearing, “Quantifying Bulk Electrode Strain and Material Displacement within Lithium Batteries via High-Speed Operando Tomography and Digital Volume Correlation”, *Advanced Science*, vol. 3. no. 3, pp. 1500332(1-11), 2015.
15. M. T. Dunstan, S. A. Maugeri, W. Liu, M. G. Tucker, **O. O. Taiwo**, B. Gonzalez, P. K. Allan, M. W. Gaultois, P. R. Shearing, D. A. Keen, A. E. Philips, M. T. Dove, S. A. Scott, J. S. Dennis, and C. P. Grey, “In situ studies of materials for high temperature CO_2 capture and storage”, *Faraday Discussions*, vol. 305, pp. 968–972, 2016.
16. Q. Meyer, S. Ashton, P. Boillat, M. Cochet, E. Engebretsen, D. P. Finegan, X. Lu, J. J. Bailey, N. Mansor, R. Abdulaziz, **O. O. Taiwo**, R. J. Jervis, S. Torija, P. Benson, S. Foster, P. Adcock, P. R. Shearing, and D. J. L. Brett, “Effect of gas diffusion layer properties on water distribution across air-cooled, open-cathode polymer electrolyte fuel cells: A combined ex-situ X-ray tomography and in-operando neutron imaging study”, *Electrochimica Acta*, vol. 211, pp. 478–487, 2016.
17. O. A. Obeisun, D. P. Finegan, E. Engebretsen, J. B. Robinson, **O. O. Taiwo**, G. Hinds, P. R. Shearing, and D. J. L. Brett, “Ex-situ characterisation of water droplet dynamics on the surface of a fuel cell gas diffusion layer through wettability analysis and thermal characterisation”, *International Journal of Hydrogen Energy*, In Press, 2017.

Talks and Conference Participation

10 oral and poster presentations in conferences, seminars, and workshops, including:

1. *Characterisation of 3D microstructural evolution within electrode materials during lithium-ion battery operation*, talk, 228th ECS Meeting, October 2015, Phoenix, USA.
2. *Characterisation of lithium-ion battery electrodes in-situ using X-ray tomography*, invited talk, Young Researchers Symposium, Energy Materials Network London, May 2015, London, UK.
3. *Observing microstructural evolution in Li-ion batteries using X-ray tomographic Imaging*, conference poster prize in the Imaging and Coherence Division, Diamond Synchrotron Radiation User Meeting, September 2014, Didcot, UK.
4. *Investigation of microstructural evolution in lithium ion battery electrodes using three-dimensional imaging,* talk, UCL Chemical Engineering PhD seminar series, April 2014, London, UK.

Honors and Awards

11/2013 – 11/2015 **UCL BEAMS Dean's Prize**

Research Scholarship award from the UCL Faculty of Engineering Sciences to support postgraduate studies.

08/2014 – 02/2015 **STFC Futures Early Career Award**

Travel grant to support collaborative research on 4D imaging of lithium ion batteries.

06/2015 – 12/2015 **STFC Futures Early Career Follow-On Award**

Travel grant to support dissemination of collaborative research.

05/2015 **UCL Provost's Public Engagement Award (shared)**

Research Team category award to 'UCell' recognising contribution towards public engagement in science and engineering.

References

[1] J.W. Fergus, Recent developments in cathode materials for lithium ion batteries, J. Power Sources. 195 (2010) 939–954.

[2] L. Ji, Z. Lin, M. Alcoutlabi, X. Zhang, Recent developments in nanostructured anode materials for rechargeable lithium-ion batteries, Energy Environ. Sci. 4 (2011) 2682 – 2699.

[3] B. Yan, C. Lim, L. Yin, L. Zhu, Three Dimensional Simulation of Galvanostatic Discharge of $LiCoO_2$ Cathode Based on X-ray Nano-CT Images, J. Electrochem. Soc. 159 (2012) A1604–A1614.

[4] M. Doyle, T.F. Fuller, J. Newman, Modeling of Galvanostatic Charge and Discharge of the Lithium/Polymer/Insertion Cell, J. Electrochem. Soc. 140 (1993) 1526 – 1533.

[5] J. Newman, Optimization of Porosity and Thickness of a Battery Electrode by Means of a Reaction-Zone Model, J. Electrochem. Soc. 142 (1995) 97–101.

[6] M. Doyle, J. Newman, A.S. Gozdz, C.N. Schmutz, J.-M. Tarascon, Comparison of Modeling Predictions with Experimental Data from Plastic Lithium Ion Cells, J. Electrochem. Soc. 143 (1996) 1890–1903.

[7] D. Kehrwald, P.R. Shearing, N.P. Brandon, P.K. Sinha, S.J. Harris, Local Tortuosity Inhomogeneities in a Lithium Battery Composite Electrode, J. Electrochem. Soc. 158 (2011) A1393–A1399.

[8] M. Ender, J. Joos, T. Carraro, E. Ivers-Tiffée, Three-dimensional reconstruction of a composite cathode for lithium-ion cells, Electrochem. Commun. 13 (2011) 166–168.

[9] Y.K. Chen-Wiegart, P. Shearing, Q. Yuan, A. Tkachuk, J. Wang, 3D morphological evolution of Li-ion battery negative electrode $LiVO_2$ during oxidation using X-ray nano-tomography, Electrochem. Commun. 21 (2012) 58–61.

[10] A.H. Wiedemann, G.M. Goldin, S.A. Barnett, H. Zhu, R.J. Kee, Effects of three-dimensional cathode microstructure on the performance of lithium-ion battery cathodes, Electrochim. Acta. 88 (2013) 580–588.

[11] Y. Qi, S.J. Harris, In Situ Observation of Strains during Lithiation of a Graphite Electrode, J. Electrochem. Soc. 157 (2010) A741–A747.

[12] L.Y. Beaulieu, K.W. Eberman, R.L. Turner, L.J. Krause, J.R. Dahn, Colossal

Reversible Volume Changes in Lithium Alloys, Electrochem. Solid-State Lett. 4 (2001) A137–A140.

[13] S.J. Harris, A. Timmons, D.R. Baker, C. Monroe, Direct in situ measurements of Li transport in Li-ion battery negative electrodes, Chem. Phys. Lett. 485 (2010) 265–274.

[14] A. Timmons, J.R. Dahn, In situ optical observations of particle motion in alloy negative electrodes for Li-Ion batteries, J. Electrochem. Soc. 153 (2006) A1206–A1210.

[15] F. Orsini, L. Dupont, B. Beaudoin, S. Grugeon, J.M. Tarascon, Scanning and transmission electron microscopy contributions to the improvement of electrode materials and interfaces in the design of better batteries, Int. J. Inorg. Mater. 2 (2000) 701–715.

[16] M. Dollé, S. Grugeon, B. Beaudoin, L. Dupont, J.-M. Tarascon, In situ TEM study of the interface carbon/electrolyte, J. Power Sources. 97-98 (2001) 104–106.

[17] D. Aurbach, The Application of Atomic Force Microscopy for the Study of Li Deposition Processes, J. Electrochem. Soc. 143 (1996) 3525–3532.

[18] M. Koltypin, Y.S. Cohen, B. Markovsky, Y. Cohen, D. Aurbach, The study of lithium insertion–deinsertion processes into composite graphite electrodes by in situ atomic force microscopy (AFM), Electrochem. Commun. 4 (2002) 17–23.

[19] R. Bhattacharyya, B. Key, H. Chen, A.S. Best, A.F. Hollenkamp, C.P. Grey, In situ NMR observation of the formation of metallic lithium microstructures in lithium batteries., Nat. Mater. 9 (2010) 504–510.

[20] E. Peled, D.B. Tow, A. Merson, L. Burstein, Microphase structure of SEI on HOPG, J. New Mater. Electrochem. Syst. 3 (2000) 321–328.

[21] P. Lu, S.J. Harris, Lithium transport within the solid electrolyte interphase, Electrochem. Commun. 13 (2011) 1035–1.37.

[22] T. Hutzenlaub, S. Thiele, R. Zengerle, C. Ziegler, Three-Dimensional Reconstruction of a $LiCoO_2$ Li-Ion Battery Cathode, Electrochem. Solid-State Lett. 15 (2012) A33–A36.

[23] J.R. Wilson, J.S. Cronin, S.A. Barnett, S.J. Harris, Measurement of three-dimensional microstructure in a $LiCoO_2$ positive electrode, J. Power Sources. 196 (2011) 3443–3447.

[24] P.R. Shearing, N.P. Brandon, J. Gelb, R. Bradley, P.J. Withers, A.J. Marquis, S. Cooper, S.J. Harris, Multi Length Scale Microstructural Investigations of a Commercially Available Li-Ion Battery Electrode, J. Electrochem. Soc. 159 (2012) A1023–A1027.

[25] S.J. Cooper, D.S. Eastwood, J. Gelb, G. Damblanc, D.J.L. Brett, R.S. Bradley, P.J. Withers, P.D. Lee, A.J. Marquis, N.P. Brandon, P.R. Shearing, Image based modelling of microstructural heterogeneity in $LiFePO_4$ electrodes for Li-ion batteries, J. Power Sources. 247 (2013) 1033–1039.

[26] P.R. Shearing, L.E. Howard, P.S. Jørgensen, N.P. Brandon, S.J. Harris, Characterization of the 3-dimensional microstructure of a graphite negative electrode from a Li-ion battery, Electrochem. Commun. 12 (2010) 374–377.

[27] F. Tariq, V. Yufit, M. Kishimoto, P.R. Shearing, S. Menkin, D. Golodnitsky, J. Gelb, E. Peled, N.P. Brandon, Three-dimensional high resolution X-ray imaging and quantification of lithium ion battery mesocarbon microbead anodes, J. Power Sources. 248 (2014) 1014–1020.

[28] V. Yufit, P. Shearing, R.W. Hamilton, P.D. Lee, M. Wu, N.P. Brandon, Investigation of lithium-ion polymer battery cell failure using X-ray computed tomography, Electrochem. Commun. 13 (2011) 608–610.

[29] M. Ebner, F. Geldmacher, F. Marone, M. Stampanoni, V. Wood, X-Ray Tomography of Porous, Transition Metal Oxide Based Lithium Ion Battery Electrodes, Adv. Energy Mater. 3 (2013) 845–850.

[30] S.A. Channagiri, S.C. Nagpure, S.S. Babu, G.J. Noble, R.T. Hart, Porosity and phase fraction evolution with aging in lithium iron phosphate battery cathodes, J. Power Sources. 243 (2013) 750–757.

[31] F. Meirer, J. Cabana, Y. Liu, A. Mehta, J.C. Andrews, P. Pianetta, Three-dimensional imaging of chemical phase transformations at the nanoscale with full-field transmission X-ray microscopy., J. Synchrotron Radiat. 18 (2011) 773–781.

[32] Y.K. Chen-Wiegart, Z. Liu, K.T. Faber, S.A. Barnett, J. Wang, 3D analysis of a $LiCoO_2$ – $Li(Ni_{1/3}Mn_{1/3}Co_{1/3})O_2$ Li-ion battery positive electrode using x-ray nano-tomography, Electrochem. Commun. 28 (2013) 127–130.

[33] Z. Liu, J. Scott Cronin, Y.K. Chen-Wiegart, J.R. Wilson, K.J. Yakal-Kremski, J. Wang,

K.T. Faber, S.A. Barnett, Three-dimensional morphological measurements of $LiCoO_2$ and $LiCoO_2/Li(Ni_{1/3}Mn_{1/3}Co_{1/3})O_2$ lithium-ion battery cathodes, J. Power Sources. 227 (2013) 267–274.

[34] P. Shearing, Y. Wu, S. Harris, N. Brandon, In Situ X-Ray Spectroscopy and Imaging of Battery Materials, ECS Interface. 20 (2011) 43–47.

[35] P.R. Shearing, D.S. Eastwood, R.S. Bradley, J. Gelb, S.J. Cooper, F. Tariq, D.J.L. Brett, N.P. Brandon, P.J. Withers, P.D. Lee, Exploring electrochemical devices using X-ray microscopy: 3D microstructure of batteries and fuel cells, Microsc. Anal. (2013) 19–22.

[36] T. Nagaura, K. Tozawa, Lithium ion rechargeable battery, Prog. Batter. Sol. Cells. 9 (1990) 209–212.

[37] S. Amjad, S. Neelakrishnan, R. Rudramoorthy, Review of design considerations and technological challenges for successful development and deployment of plug-in hybrid electric vehicles, Renew. Sustain. Energy Rev. 14 (2010) 1104–1110.

[38] B. Xu, D. Qian, Z. Wang, Y.S. Meng, Recent progress in cathode materials research for advanced lithium ion batteries, Mater. Sci. Eng. R Reports. 73 (2012) 51–65.

[39] T. Ohzuku, Y. Makimura, Layered lithium insertion material of $LiNi_{1/2}Mn_{1/2}O_2$: A possible alternative to $LiCoO_2$ for advanced lithium-ion batteries, Chem. Lett. 2 (2001) 744–745.

[40] X. Meng, S. Dou, W. Wang, High power and high capacity cathode material LiNi0.5Mn0.5O2 for advanced lithium-ion batteries, J. Power Sources. 184 (2008) 489–493.

[41] K. Kang, Y.S. Meng, J. Bréger, C.P. Grey, G. Ceder, Electrodes with high power and high capacity for rechargeable lithium batteries, Science. 311 (2006) 977–980.

[42] T. Ohzuku, Y. Makimura, Layered lithium insertion material of $LiCo_{1/3}Ni_{1/3}Mn_{1/3}O_2$ for lithium-ion batteries, Chem. Lett. 30 (2001) 642–643.

[43] N. Yabuuchi, T. Ohzuku, Novel lithium insertion material of $LiCo_{1/3}Ni_{1/3}Mn_{1/3}O_2$ for advanced lithium-ion batteries, J. Power Sources. 119-121 (2003) 171–174.

[44] N. Yabuuchi, T. Ohzuku, Electrochemical behaviors of $LiCo_{1/3}Ni_{1/3}Mn_{1/3}O_2$ in

lithium batteries at elevated temperatures, J. Power Sources. 146 (2005) 636–639.

[45] B.K.M. Shaju, P.G. Bruce, Macroporous $Li(Ni_{1/3}Co_{1/3}Mn_{1/3})O_2$: A High-Power and High-Energy Cathode for Rechargeable Lithium Batteries, Adv. Mater. 18 (2006) 2330–2334.

[46] Z. Li, N. a. Chernova, M. Roppolo, S. Upreti, C. Petersburg, F.M. Alamgir, M.S. Whittingham, Comparative Study of the Capacity and Rate Capability of $LiNi_yMn_yCo_{1-2y}O_2$ (y = 0.5, 0.45, 0.4, 0.33), J. Electrochem. Soc. 158 (2011) A516–A522.

[47] Z. Lu, L.Y. Beaulieu, R.A. Donaberger, C.L. Thomas, J.R. Dahn, Synthesis, Structure, and Electrochemical Behavior of $Li[Ni_xLi_{1/3-2x/3}\ Mn_{1/3-2x/3}]O_2$, J. Electrochem. Soc. 149 (2002) A778–A791.

[48] R.J. Gummow, M.M. Thackeray, Lithium-cobalt-nickel-oxide cathode materials prepared at 400°C for rechargeable lithium batteries, Solid State Ionics. 53-56 (1992) 681–687.

[49] E. Rossen, C.D.W. Jones, J.R. Dahn, Structure and electrochemistry of $Li_xMn_yNi_{1-y}O_2$, Solid State Ionics. 57 (1992) 311–318.

[50] M. Yoshio, H. Noguchi, J.-I. Itoh, M. Okada, T. Mouri, Preparation and properties of $LiCo_yMn_xNi_{1-x-y}O_2$ as a cathode for lithium ion batteries, J. Power Sources. 90 (2000) 176–181.

[51] L. Hernán, J. Morales, L. Sánchez, J. Santos, Use of Li-M-Mn-O [M=Co, Cr, Ti] spinels prepared by a sol-gel method as cathodes in high-voltage lithium batteries, Solid State Ionics. 118 (1999) 179–185.

[52] J.-H. Kim, S.-T. Myung, C.S. Yoon, S.G. Kang, Y.-K. Sun, Comparative Study of $LiNi_{0.5}Mn_{1.5}O_{4-\delta}$ and $LiNi_{0.5}Mn_{1.5}O_4$ Cathodes Having Two Crystallographic Structures: Fd3̄m and P4$LiNi_{0.5}Mn_{1.5}O_3$32, Chem. Mater. 16 (2004) 906–914.

[53] G. Li, H. Ikuta, T. Uchida, M. Wakihara, The spinel phases $LiM_yMn_{2-y}O_4$ (M = Co, Cr, Ni) as the cathode for rechargeable lithium batteries, J. Electrochem. Soc. 143 (1996) 178–182.

[54] J. Molenda, J. Marzec, K. Swierczek, W. Ojczyk, M. Ziemnicki, M. Molenda, M. Drozdek, R. Dziembaj, The effect of 3d substitutions in the manganese sublattice on the charge transport mechanism and electrochemical properties of

manganese spinel, Solid State Ionics. 171 (2004) 215–227.

[55] T. Ohzuku, S. Takeda, M. Iwanaga, Solid-state redox potentials for $Li[Me_{1/2}Mn_{3/2}]O_4$ (Me: 3d-transition metal) having spinel-framework structures: a series of 5 volt materials for advanced lithium-ion batteries, J. Power Sources. 81-82 (1999) 90–94.

[56] R. Singhal, S.R. Das, M.S. Tomar, O. Ovideo, S. Nieto, R.E. Melgarejo, R.S. Katiyar, Synthesis and characterization of Nd doped $LiMn_2O_4$ cathode for Li-ion rechargeable batteries, J. Power Sources. 164 (2007) 857–861.

[57] J. Tu, X.B. Zhao, D.G. Zhuang, G.S. Cao, T.J. Zhu, J.P. Tu, Studies of cycleability of $LiMn_2O_4$ and $LiLa_{0.01}Mn_{1.99}O_4$ as cathode materials for Li-ion battery, Phys. B Condens. Matter. 382 (2006) 129–134.

[58] N. Ravet, J.B. Goodenough, S. Besner, M. Simoneau, P. Hovington, M. Armand, Improved Iron based Cathode Material, Electrochem. Soc. Abstr. 99 (1999) 127–127.

[59] N. Ravet, S. Besner, M. Simoneau, A. Vallee, M. Armand, J.-F. Magnan, Materiaux d'e´lectrode pre´sentant une conductivite de surface e´leve´e., European Patent 1049182A2, 2000.

[60] H. Huang, S.C. Yin, L.F. Nazar, Approaching Theoretical Capacity of $LiFePO_4$ at Room Temperature at High Rates, Electrochem. Solid-State Lett. 4 (2001) A170–A172.

[61] S.-Y. Chung, J.T. Bloking, Y.-M. Chiang, Electronically conductive phospho-olivines as lithium storage electrodes., Nat. Mater. 1 (2002) 123–128.

[62] Y. Zhang, Q. Huo, P. Du, L. Wang, A. Zhang, Y. Song, Y. Lv, G. Li, Advances in new cathode material $LiFePO_4$ for lithium-ion batteries, Synth. Met. 162 (2012) 1315–1326.

[63] Y. Xing, Y.-B. He, B. Li, X. Chu, H. Chen, J. Ma, H. Du, F. Kang, $LiFePO_4$/C composite with 3D carbon conductive network for rechargeable lithium ion batteries, Electrochim. Acta. 109 (2013) 512–518.

[64] C. Chen, G.B. Liu, Y. Wang, J.L. Li, H. Liu, Preparation and electrochemical properties of $LiFePO_4$/C nanocomposite using $FePO_4 \cdot 2H_2O$ nanoparticles by introduction of $Fe_3(PO_4)_2 \cdot 8H_2O$ at low cost, Electrochim. Acta. 113 (2013) 464–469.

[65] X. Yang, Y. Xu, H. Zhang, Y. Huang, Q. Jiang, C. Zhao, Enhanced high rate and low-temperature performances of mesoporous $LiFePO_4$/Ketjen Black nanocomposite cathode material, Electrochim. Acta. 114 (2013) 259–264.

[66] D. Zhao, Y. Feng, Y. Wang, Y. Xia, Electrochemical performance comparison of $LiFePO_4$ supported by various carbon materials, Electrochim. Acta. 88 (2013) 632–638.

[67] M. Endo, C. Kim, K. Nishimura, T. Fujino, K. Miyahsita, Recent development of carbon materials for Li ion batteries, Carbon. 38 (2000) 183–197.

[68] K. Zaghib, X. Song, A. Guerfi, R. Rioux, K. Kinoshita, Purification process of natural graphite as anode for Li-ion batteries: chemical versus thermal, J. Power Sources. 119-121 (2003) 8–15.

[69] K. Ozawa, Lithium-ion rechargeable batteries with $LiCoO_2$ and carbon electrodes: the $LiCoO_2$/C system, Solid State Ionics. 69 (1994) 212–221.

[70] M. Yoshio, H. Wang, K. Fukuda, Y. Hara, Y. Adachi, Effect of Carbon Coating on Electrochemical Performance of Treated Natural Graphite as Lithium-Ion Battery Anode Material, J. Electrochem. Soc. 147 (2000) 1245–1250.

[71] D.W. Murphy, M. Greenbalt, S.M. Zahurak, R.J. Cava, J.V. Waszczak, G.W. Hull, R.S. Hutton, Lithium Insertion in Anatase: A New Route to the Spinel $LiTi_2O_4$, Rev. Chim. Miner. 19 (1982) 441–449.

[72] P.P. Prosini, R. Mancini, L. Petrucci, V. Contini, P. Villano, $Li_4Ti_5O_{12}$ as anode in all-solid-state, plastic, lithium-ion batteries for low-power applications, Solid State Ionics. 144 (2001) 185–192.

[73] K. Zaghib, M. Armand, M. Gauthier, Electrochemistry of anodes in solid-state Li-ion polymer batteries, J. Electrochem. Soc. 145 (1998) 3135–3140.

[74] K. Zaghib, M. Simoneau, M. Armand, M. Gauthier, J.T.S. Irvine, Electrochemical study of Li4Ti5O12 as negative electrode for Li-ion polymer rechargeable batteries, J. Power Sources. 81 (1999) 300–305.

[75] S. Scharner, W. Weppner, P. Schmid-Beurmann, Evidence of two-phase formation upon lithium insertion into the $Li_{1.33}Ti_{1.67}O_4$ spinel, J. Electrochem. Soc. 146 (1999) 857–861.

[76] K.M. Colbow, J.R. Dahn, R.R. Haering, Structure and electrochemistry of the spinel oxides $LiTi_2O_4$ and $Li_{4/3}Ti_{5/3}O_4$, J. Power Sources. 26 (1989) 397–402.

[77] J. Zhang, Y. Xia, Co-Sn Alloys as Negative Electrode Materials for Rechargeable Lithium Batteries, J. Electrochem. Soc. 153 (2006) A1466–A1471.

[78] C.J. Wen, B.A. Boukamp, R.A. Huggins, W. Weppner, Thermodynamic and Mass Transport Properties of "LiAl," J. Electrochem. Soc. 126 (1979) 2258–2266.

[79] C.J. Wen, R.A. Huggins, Chemical diffusion in intermediate phases in the lithium-silicon system, J. Solid State Chem. 37 (1981) 271–278.

[80] H. Morimoto, M. Nakai, M. Tatsumisago, T. Minami, Mechanochemical synthesis and anode properties of SnO-based amorphous materials, J. Electrochem. Soc. 146 (1999) 3970–3973.

[81] Y. Idota, T. Kubota, A. Matsufuji, Y. Maekawa, T. Miyasaka, Tin-Based Amorphous Oxide: A High-Capacity Lithium-Ion-Storage Material, Science. 276 (1997) 1395 – 1397.

[82] K. Wan, S. F.Y. Li, Z. Gao, K. Siong Siow, Tin-based oxide anode for lithium-ion batteries with low irreversible capacity, J. Power Sources. 75 (1998) 9–12.

[83] X. Li, M. Qu, Y. Huai, Z. Yu, Preparation and electrochemical performance of $Li_4Ti_5O_{12}$/carbon/carbon nano-tubes for lithium ion battery, Electrochim. Acta. 55 (2010) 2978–2982.

[84] C. Kim, M. Noh, M. Choi, J. Cho, B. Park, Critical size of a nano SnO_2 electrode for Li-secondary battery, Chem. Mater. 17 (2005) 3297–3301.

[85] J.O. Besenhard, J. Yang, M. Winter, Will advanced lithium-alloy anodes have a chance in lithium-ion batteries?, J. Power Sources. 68 (1997) 87–90.

[86] J. Yang, Small particle size multiphase Li-alloy anodes for lithium-ion batteries, Solid State Ionics. 90 (1996) 281–287.

[87] C.R. Becker, K.E. Strawhecker, Q.P. McAllister, C.A. Lundgren, In Situ Atomic Force Microscopy of Lithiation and Delithiation of Silicon Nanostructures for Lithium Ion Batteries., ACS Nano. 7 (2013) 9173–9182.

[88] S. Hossain, Handbook of Batteries, in: D. Linden (Ed.), 2nd ed., McGraw-Hill, New York, 1995: p. 36.1.

[89] L.A. Dominey, Lithium batteries: new materials, developments, and perspectives, in: G. Pistoia (Ed.), 2nd ed., Elsevier, Amsterdam, 1994: p. 137.

[90] K. Xu, Nonaqueous liquid electrolytes for lithium-based rechargeable batteries., Chem. Rev. 104 (2004) 4303–4417.

[91] I.A. Profatilova, S.-S. Kim, N.-S. Choi, Enhanced thermal properties of the solid electrolyte interphase formed on graphite in an electrolyte with fluoroethylene carbonate, Electrochim. Acta. 54 (2009) 4445–4450.

[92] H. Nakai, T. Kubota, A. Kita, A. Kawashima, Investigation of the Solid Electrolyte Interphase Formed by Fluoroethylene Carbonate on Si Electrodes, J. Electrochem. Soc. 158 (2011) A798–A801.

[93] V. Etacheri, O. Haik, Y. Goffer, G.A. Roberts, I.C. Stefan, R. Fasching, D. Aurbach, Effect of Fluoroethylene Carbonate (FEC) on the Performance and Surface Chemistry of Si-Nanowire Li-Ion Battery Anodes, Langmuir. 28 (2012) 965–976.

[94] L. Chen, K. Wang, X. Xie, J. Xie, Effect of vinylene carbonate (VC) as electrolyte additive on electrochemical performance of Si film anode for lithium ion batteries, J. Power Sources. 174 (2007) 538–543.

[95] S.S. Zhang, A review on electrolyte additives for lithium-ion batteries, J. Power Sources. 162 (2006) 1379–1394.

[96] W.C. Choi, Understanding the Capacity Fade Mechanisms of Spinel Manganese Oxide Cathodes and Improving their Performance in Lithium Ion Batteries, University of Austin at Texas, Ph.D. thesis, 2007.

[97] P. Arora, Z.J. Zhang, Battery separators., Chem. Rev. 104 (2004) 4419–62.

[98] M. Kirchhöfer, J. von Zamory, E. Paillard, S. Passerini, Separators for Li-ion and Li-metal battery including ionic liquid based electrolytes based on the TFSI- and FSI- anions., Int. J. Mol. Sci. 15 (2014) 14868–90.

[99] D. Carvalho, N. Loeffler, G.-T. Kim, S. Passerini, High Temperature Stable Separator for Lithium Batteries Based on SiO_2 and Hydroxypropyl Guar Gum, Membranes. 5 (2015) 632–645.

[100] C. Lin, A. Tang, H. Mu, W. Wang, C. Wang, Aging Mechanisms of Electrode Materials in Lithium-Ion Batteries for Electric Vehicles, J. Chem. (2015) 104673 (1–11).

[101] Y. Ko, Y.-G. Cho, H.-K. Song, Programming galvanostatic rates for fast-charging lithium ion batteries: a graphite case, RSC Adv. 4 (2014) 16545–16550.

[102] C. Sole, N.E. Drewett, L.J. Hardwick, In-situ Raman study of lithium-ion intercalation into microcrystalline graphite, Faraday Discuss. 172 (2014) 223–237.

[103] T. Ohzuku, Y. Iwakoshi, K. Sawai, Formation of Lithium-Graphite Intercalation Compounds in Nonaqueous Electrolytes and Their Application as a Negative Electrode for a Lithium Ion (Shuttlecock) Cell, J. Electrochem. Soc. 140 (1993) 2490–2498.

[104] E.M.C. Jones, Ö.Ö. Çapraz, S.R. White, N.R. Sottos, Reversible and Irreversible Deformation Mechanisms of Composite Graphite Electrodes in Lithium-Ion Batteries, J. Electrochem. Soc. 163 (2016) A1965–A1974.

[105] J. Kohanoff, G. Galli, M. Parrinello, Theoretical study of LiC_6, Le J. Phys. IV. 01 (1991) C5–351–C5–356.

[106] Y. Qi, H. Guo, L.G. Hector, A. Timmons, Threefold Increase in the Young's Modulus of Graphite Negative Electrode during Lithium Intercalation, J. Electrochem. Soc. 157 (2010) A558–A566.

[107] M. Winter, J.O. Besenhard, M.E. Spahr, P. Novák, Insertion Electrode Materials for Rechargeable Lithium Batteries, Adv. Mater. 10 (1998) 725–763.

[108] J. Vetter, P. Novák, M.R. Wagner, C. Veit, K.-C. Möller, J.O. Besenhard, M. Winter, M. Wohlfahrt-Mehrens, C. Vogler, A. Hammouche, Ageing mechanisms in lithium-ion batteries, J. Power Sources. 147 (2005) 269–281.

[109] D. Larcher, S. Beattie, M. Morcrette, K. Edström, J.-C. Jumas, J.-M. Tarascon, Recent findings and prospects in the field of pure metals as negative electrodes for Li-ion batteries, J. Mater. Chem. 17 (2007) 3759–3772.

[110] H. Jung, Amorphous silicon anode for lithium-ion rechargeable batteries, J. Power Sources. 115 (2003) 346–351.

[111] B.A. Boukamp, G.C. Lesh, R.A. Huggins, All-Solid Lithium Electrodes with Mixed-Conductor Matrix, J. Electrochem. Soc. 128 (1981) 725–729.

[112] P. Limthongkul, Y.-I. Jang, N.J. Dudney, Y.-M. Chiang, Electrochemically-driven solid-state amorphization in lithium-silicon alloys and implications for lithium storage, Acta Mater. 51 (2003) 1103–1113.

[113] M.N. Obrovac, L. Christensen, Structural Changes in Silicon Anodes during Lithium Insertion/Extraction, Electrochem. Solid-State Lett. 7 (2004) A93–A96.

[114] M.N. Obrovac, L.J. Krause, Reversible Cycling of Crystalline Silicon Powder, J. Electrochem. Soc. 154 (2007) A103–A108.

[115] J. Li, J.R. Dahn, An In Situ X-Ray Diffraction Study of the Reaction of Li with

Crystalline Si, J. Electrochem. Soc. 154 (2007) A156–A161.

[116] J. Graetz, C.C. Ahn, R. Yazami, B. Fultz, Highly Reversible Lithium Storage in Nanostructured Silicon, Electrochem. Solid-State Lett. 6 (2003) A194 – A197.

[117] C.K. Chan, H. Peng, G. Liu, K. McIlwrath, X.F. Zhang, R.A. Huggins, Y. Cui, High-performance lithium battery anodes using silicon nanowires., Nat. Nanotechnol. 3 (2008) 31–35.

[118] K. Peng, J. Jie, W. Zhang, S.-T. Lee, Silicon nanowires for rechargeable lithium-ion battery anodes, Appl. Phys. Lett. 93 (2008) 033105 (1–3).

[119] M. Ge, J. Rong, X. Fang, C. Zhou, Porous doped silicon nanowires for lithium ion battery anode with long cycle life., Nano Lett. 12 (2012) 2318–2323.

[120] L.-F. Cui, R. Ruffo, C.K. Chan, H. Peng, Y. Cui, Crystalline-amorphous core-shell silicon nanowires for high capacity and high current battery electrodes., Nano Lett. 9 (2009) 491–495.

[121] A. Magasinski, P. Dixon, B. Hertzberg, A. Kvit, J. Ayala, G. Yushin, High-performance lithium-ion anodes using a hierarchical bottom-up approach., Nat. Mater. 9 (2010) 353–358.

[122] I.H. Son, J. Hwan Park, S. Kwon, S. Park, M.H. Rümmeli, A. Bachmatiuk, H.J. Song, J. Ku, J.W. Choi, J.-M. Choi, S.-G. Doo, H. Chang, Silicon carbide-free graphene growth on silicon for lithium-ion battery with high volumetric energy density., Nat. Commun. 6 (2015) 7393 (1–8).

[123] J.-G. Ren, Q.-H. Wu, G. Hong, W.-J. Zhang, H. Wu, K. Amine, J. Yang, S.-T. Lee , Silicon-Graphene Composite Anodes for High-Energy Lithium Batteries, Energy Technol. 1 (2013) 77–84.

[124] L. Ji, H. Zheng, A. Ismach, Z. Tan, S. Xun, E. Lin, V. Battaglia, V. Srinivasan, Y. Zhang, Graphene/Si multilayer structure anodes for advanced half and full lithium-ion cells, Nano Energy. 1 (2012) 164–171.

[125] H. Wu, G. Yu, L. Pan, N. Liu, M.T. McDowell, Z. Bao, Y. Cui, Stable Li-ion battery anodes by in-situ polymerization of conducting hydrogel to conformally coat silicon nanoparticles., Nat. Commun. 4 (2013) 1943(1–6).

[126] C. Wang, H. Wu, Z. Chen, M.T. McDowell, Y. Cui, Z. Bao, Self-healing chemistry enables the stable operation of silicon microparticle anodes for high-energy lithium-ion batteries., Nat. Chem. 5 (2013) 1042–1048.

[127] W. Xu, J. Wang, F. Ding, X. Chen, E. Nasybulin, Y. Zhang, J.-G. Zhang, Lithium metal anodes for rechargeable batteries, Energy Environ. Sci. 7 (2014) 513–537.

[128] S. Chandrashekar, N.M. Trease, H.J. Chang, L.-S. Du, C.P. Grey, A. Jerschow, 7Li MRI of Li batteries reveals location of microstructural lithium., Nat. Mater. 11 (2012) 311–315.

[129] K.J. Harry, D.T. Hallinan, D.Y. Parkinson, A.A. MacDowell, N.P. Balsara, Detection of subsurface structures underneath dendrites formed on cycled lithium metal electrodes., Nat. Mater. 13 (2014) 69–73.

[130] Z. Stachurski, Rechargeable current-generating electrochemical system with wiper means, 3,440,098, 1969.

[131] B. Scrosati, Recent advances in lithium ion battery materials, Electrochim. Acta. 45 (2000) 2461–2466.

[132] X. Yu, A Stable Thin-Film Lithium Electrolyte: Lithium Phosphorus Oxynitride, J. Electrochem. Soc. 144 (1997) 524–532.

[133] G.M. Stone, S.A. Mullin, A.A. Teran, D.T. Hallinan, A.M. Minor, A. Hexemer, N.P. Balsara, Resolution of the Modulus versus Adhesion Dilemma in Solid Polymer Electrolytes for Rechargeable Lithium Metal Batteries, J. Electrochem. Soc. 159 (2012) A222–A227.

[134] S. Augustin, V. Hennige, G. Hörpel, C. Hying, Ceramic but flexible: new ceramic membrane foils for fuel cells and batteries, Desalin. 146 (2002) 23–28.

[135] O. Crowther, A.C. West, Effect of Electrolyte Composition on Lithium Dendrite Growth, J. Electrochem. Soc. 155 (2008) A806–A811.

[136] T. Hirai, Effect of Additives on Lithium Cycling Efficiency, J. Electrochem. Soc. 141 (1994) 2300–2305.

[137] F. Marchioni, K. Star, E. Menke, T. Buffeteau, L. Servant, B. Dunn, F. Wudl, Protection of lithium metal surfaces using chlorosilanes., Langmuir. 23 (2007) 11597–11602.

[138] I. Yoshimatsu, Lithium Electrode Morphology during Cycling in Lithium Cells, J. Electrochem. Soc. 135 (1988) 2422–2427.

[139] Z. Li, J. Huang, B. Yann Liaw, V. Metzler, J. Zhang, A review of lithium deposition in lithium-ion and lithium metal secondary batteries, J. Power Sources. 254 (2014) 168–182.

[140] F. Orsini, A. Du Pasquier, B. Beaudoin, J.. Tarascon, M. Trentin, N. Langenhuizen, E. De Beer, P. Notten, In situ Scanning Electron Microscopy (SEM) observation of interfaces within plastic lithium batteries, J. Power Sources. 76 (1998) 19–29.

[141] Yaron S. Cohen, A. Yair Cohen, D. Aurbach, Micromorphological Studies of Lithium Electrodes in Alkyl Carbonate Solutions Using in Situ Atomic Force Microscopy, J. Phys. Chem. B. 104 (2000) 12282–12291.

[142] D. Aurbach, E. Zinigrad, Y. Cohen, H. Teller, A short review of failure mechanisms of lithium metal and lithiated graphite anodes in liquid electrolyte solutions, Solid State Ionics. 148 (2002) 405–416.

[143] J. Yamaki, S. Tobishima, K. Hayashi, Y. Nemoto, M. Arakawa, A consideration of the morphology of electrochemically deposited lithium in an organic electrolyte, J. Power Sources. 74 (1998) 219–227.

[144] M. Arakawa, S. Tobishima, Y. Nemoto, M. Ichimura, J. Yamaki, Lithium electrode cycleability and morphology dependence on current density, J. Power Sources. 43 (1993) 27–35.

[145] T. Osaka, T. Homma, T. Momma, H. Yarimizu, In situ observation of lithium deposition processes in solid polymer and gel electrolytes, J. Electroanal. Chem. 421 (1997) 153–156.

[146] T. Tsuda, T. Kanetsuku, T. Sano, Y. Oshima, K. Ui, M. Yamagata, M. Ishikawa, S. Kuwabata, In situ SEM observation of the Si negative electrode reaction in an ionic-liquid-based lithium-ion secondary battery., Microscopy. 64 (2015) 159–68.

[147] D. Chen, S. Indris, M. Schulz, B. Gamer, R. Mönig, In situ scanning electron microscopy on lithium-ion battery electrodes using an ionic liquid, J. Power Sources. 196 (2011) 6382–6387.

[148] E. Strelcov, J. Cothren, D. Leonard, A.Y. Borisevich, A. Kolmakov, In situ SEM study of lithium intercalation in individual V_2O_5 nanowires, Nanoscale. 7 (2015) 3022–3027.

[149] C.-Y. Tang, S.J. Dillon, In Situ Scanning Electron Microscopy Characterization of the Mechanism for Li Dendrite Growth, J. Electrochem. Soc. 163 (2016) A1660–A1665.

[150] X.H. Liu, J.Y. Huang, In situ TEM electrochemistry of anode materials in lithium

ion batteries, Energy Environ. Sci. 4 (2011) 3844–3860.

[151] J.Y. Huang, L. Zhong, C.M. Wang, J.P. Sullivan, W. Xu, L.Q. Zhang, S.X. Mao, N.S. Hudak, X.H. Liu, A. Subramanian, H. Fan, L. Qi, A. Kushima, J. Li, In situ observation of the electrochemical lithiation of a single SnO_2 nanowire electrode., Science . 330 (2010) 1515–1520.

[152] A. Tokranov, B.W. Sheldon, C. Li, S. Minne, X. Xiao, In Situ Atomic Force Microscopy Study of Initial Solid Electrolyte Interphase Formation on Silicon Electrodes for Li-Ion Batteries, ACS Appl. Mater. Interfaces. 6 (2014) 6672–6686.

[153] K.A. Hirasawa, T. Sato, H. Asahina, S. Yamaguchi, S. Mori, In Situ Electrochemical Atomic Force Microscope Study on Graphite Electrodes, J. Electrochem. Soc. 144 (1997) L81–L84.

[154] B. Breitung, P. Baumann, H. Sommer, J. Janek, T. Brezesinski, In situ and operando atomic force microscopy of high-capacity nano-silicon based electrodes for lithium-ion batteries, Nanoscale. 47 (2016) 2930–2946.

[155] P.R. Shearing, N.P. Brandon, A Review of Microstructural Investigations in Li-Ion Battery Electrodes, 2010.

[156] A.C. Kak, M. Slaney, Principles of Computerized Tomographic Imaging, SIAM, 2001.

[157] M.D. Uchic, L. Holzer, B.J. Inkson, E.L. Principe, P. Munroe, Three-Dimensional Microstructural Characterization Using Focused Ion Beam Tomography, MRS Bull. 32 (2011) 408–416.

[158] S. Zaefferer, S.I. Wright, D. Raabe, Three-Dimensional Orientation Microscopy in a Focused Ion Beam–Scanning Electron Microscope: A New Dimension of Microstructure Characterization, Metall. Mater. Trans. A. 39 (2008) 374–389.

[159] G. Knott, S. Rosset, M. Cantoni, Focussed ion beam milling and scanning electron microscopy of brain tissue., J. Vis. Exp. (2011) e2588.

[160] B. Song, T. Sui, S. Ying, L. Li, L. Lu, A.M. Korsunsky, Nano-structural changes in Li-ion battery cathodes during cycling revealed by FIB-SEM serial sectioning tomography, J. Mater. Chem. A. 3 (2015) 18171–18179.

[161] L. Holzer, C. Marco, Review of FIB-tomography, in: I. Utke, S. Moshkalev, P. Russell (Eds.), Nanofabrication Using Focus. Ion Electron Beams Princ. Appl., Oxford University Press, 2012: pp. 410–435.

[162] J.L. Drummond, F. De Carlo, B.J. Super, Three-dimensional tomography of composite fracture surfaces., J. Biomed. Mater. Res. B. Appl. Biomater. 74 (2005) 669–675.

[163] S.R. Stock, X-ray microtomography of materials, Int. Mater. Rev. 44 (1999) 141–164.

[164] S.R. Stock, Recent advances in X-ray microtomography applied to materials, Int. Mater. Rev. 53 (2008) 129–181.

[165] E. Maire, P.J. Withers, Quantitative X-ray tomography, Int. Mater. Rev. 59 (2013) 1–43.

[166] L. Salvo, P. Cloetens, E. Maire, S. Zabler, J.. Blandin, J.. Buffière, W. Ludwig, E. Boller, D. Bellet, C. Josserond, X-ray micro-tomography an attractive characterisation technique in materials science, Nucl. Instruments Methods Phys. Res. Sect. B Beam Interact. with Mater. Atoms. 200 (2003) 273–286.

[167] H.T. and M.M. and S.K. and H.A. and S.S. and Y.T. and S.N. and N.K. and K.Y. and Y. Kagoshima, Development of real-time x-ray microtomography system, J. Phys. Conf. Ser. 463 (2013) 012025 (1–4).

[168] T.J. Davis, D. Gao, T.E. Gureyev, A.W. Stevenson, S.W. Wilkins, Phase-contrast imaging of weakly absorbing materials using hard X-rays, Nature. 373 (1995) 595–598.

[169] S.W. Wilkins, T.E. Gureyev, D. Gao, A. Pogany, A.W. Stevenson, Phase-contrast imaging using polychromatic hard X-rays, Nature. 384 (1996) 335–338.

[170] G. Schmahl, D. Rudolph, G. Schneider, P. Guttmann, B. Niemann, Phase-contrast X-ray Microscopy Studies, Optik. 97 (1994) 181–182.

[171] C. Holzner, M. Feser, S. Vogt, B. Hornberger, S.B. Baines, C. Jacobsen, Zernike phase contrast in scanning microscopy with X-rays, Nat. Phys. 6 (2010) 883–887.

[172] S. Irvine, R. Mokso, P. Modregger, Z. Wang, F. Marone, M. Stampanoni, Simple merging technique for improving resolution in qualitative single image phase contrast tomography., Opt. Express. 22 (2014) 27257–27269.

[173] M. Ebner, D.-W. Chung, R.E. García, V. Wood, Tortuosity Anisotropy in Lithium-Ion Battery Electrodes, Adv. Energy Mater. 4 (2013) 1301278(1–6).

[174] P.P.R.M.L. Harks, F.M. Mulder, P.H.L. Notten, In situ methods for Li-ion battery research: A review of recent developments, J. Power Sources. 288 (2015) 92–

105.

[175] D.S. Eastwood, V. Yufit, J. Gelb, A. Gu, R.S. Bradley, S.J. Harris, D.J.L. Brett, N.P. Brandon, P.D. Lee, P.J. Withers, P.R. Shearing, Lithiation-Induced Dilation Mapping in a Lithium-Ion Battery Electrode by 3D X-Ray Microscopy and Digital Volume Correlation, Adv. Energy Mater. 4 (2014) 1300506(1–7).

[176] M. Ebner, F. Marone, M. Stampanoni, V. Wood, Visualization and quantification of electrochemical and mechanical degradation in Li ion batteries., Science. 342 (2013) 716–720.

[177] J. Wang, Y.K. Chen-Wiegart, J. Wang, In Situ Three-Dimensional Synchrotron X-Ray Nanotomography of the (De)lithiation Processes in Tin Anodes, Angew. Chemie. 53 (2014) 4460–4464.

[178] J.N. Weker, N. Liu, S. Misra, J.C. Andrews, Y. Cui, M.F. Toney, In situ nanotomography and operando transmission X-ray microscopy of micron-sized Ge particles, Energy Environ. Sci. 7 (2014) 2771–2777.

[179] D.P. Finegan, M. Scheel, J.B. Robinson, B. Tjaden, I. Hunt, T.J. Mason, J. Millichamp, M. Di Michiel, G.J. Offer, G. Hinds, D.J.L. Brett, P.R. Shearing, In-operando high-speed tomography of lithium-ion batteries during thermal runaway., Nat. Commun. 6 (2015) 6924 (1–10).

[180] K.L. Kelly, B.K. Tanner, Factors affecting in-line phase-contrast imaging with a laboratory micro-focus x-ray source, Adv. X-Ray Anal. 49 (2007) 31–36.

[181] P. Cloetens, R. Barrett, J. Baruchel, J.-P. Guigay, M. Schlenker, Phase objects in synchrotron radiation hard x-ray imaging, J. Phys. D. Appl. Phys. 29 (1996) 133–146.

[182] F. Zernike, Diffraction theory of the knife-edge test and its improved form, the phase-contrast method, J. Micro/Nanolithography, MEMS, MOEMS. 1 (2002) 87–94.

[183] How Diamond Works - Education - Diamond Light Source, (2016).

[184] E.R. Pike, P.C. Sabatier, Scattering : scattering and inverse scattering in pure and applied science, Academic Press, 2002.

[185] R.A. Brooks, G. Di Chiro, Beam hardening in X-ray reconstructive tomography, Phys. Med. Biol. 21 (1976) 390–398.

[186] J. Banhart, Advanced Tomographic Methods in Material Research and

Engineering, Oxford, 2008.

[187] Y. Zhu, C. Huang, An Improved Median Filtering Algorithm for Image Noise Reduction, Phys. Procedia. 25 (2012) 609–616.

[188] A. Buades, B. Coll, J.-M. Morel, Neighborhood filters and PDE's, Numer. Math. 105 (2006) 1–34.

[189] R.D. Yapa, K. Harada, A connected component labelling algorithm for greyscale mammography image processing as a pre-processing tool, Mach. Graph. Vis. Int. J. 16 (2007) 305–327.

[190] W.E. Lorensen, H.E. Cline, Marching Cubes: A High Resolution 3D Surface Construction Algorithm, SIGGRAPH Comput. Graph. 21 (1987) 163–169.

[191] N. Epstein, On tortuosity and the tortuosity factor in flow and diffusion through porous media, Chem. Eng. Sci. 44 (1989) 777–779.

[192] L. Shen, Z. Chen, Critical review of the impact of tortuosity on diffusion, Chem. Eng. Sci. 62 (2007) 3748–3755.

[193] P.S. Jørgensen, K. V Hansen, R. Larsen, J.R. Bowen, Geometrical characterization of interconnected phase networks in three dimensions., J. Microsc. 244 (2011) 45–58.

[194] J.A. Sethian, Level Set Methods and Fast Marching Methods: Evolving Interfaces in Computational Geometry, Fluid Mechanics, Computer Vision, and Materials Science, Cambridge University Press, 1999.

[195] M.S. Hassouna, A.A. Farag, Multi-stencils fast marching methods: a highly accurate solution to the eikonal equation on cartesian domains., IEEE Trans. Pattern Anal. Mach. Intell. 29 (2007) 1563–1574.

[196] D.-J. Kroon, Accurate Fast Marching, MATLAB File Exch. (2009).

[197] C. Pudney, Distance-Ordered Homotopic Thinning: A Skeletonization Algorithm for 3D Digital Images, Comput. Vis. Image Underst. 72 (1998) 404–413.

[198] J.-F. Daïan, C.. Fernandes, P.. Philippi, J.. Bellini da Cunha Neto, 3D reconstitution of porous media from image processing data using a multiscale percolation system, J. Pet. Sci. Eng. 42 (2004) 15–28.

[199] P.M. Dupuy, P. Austin, G.W. Delaney, M.P. Schwarz, Pore scale definition and computation from tomography data, Comput. Phys. Commun. 182 (2011) 2249–2258.

[200] B. Yang, A. Wu, X. Miao, J. Liu, 3D characterization and analysis of pore structure of packed ore particle beds based on computed tomography images, Trans. Nonferrous Met. Soc. China. 24 (2014) 833–838.

[201] B. Münch, L. Holzer, Contradicting Geometrical Concepts in Pore Size Analysis Attained with Electron Microscopy and Mercury Intrusion, J. Am. Ceram. Soc. 91 (2008) 4059–4067.

[202] M.A. Sutton, J.-J. Orteu, H. Schreier, Image Correlation for Shape, Motion and Deformation Measurements, Springer US, Boston, MA, 2009.

[203] J. Quinta D A Fonseca, P.M. Mummery, P.J. Withers, Full-field strain mapping by optical correlation of micrographs acquired during deformation., J. Microsc. 218 (2005) 9–21.

[204] B.K. Bay, T.S. Smith, D.P. Fyhrie, M. Saad, Digital volume correlation: Three-dimensional strain mapping using X-ray tomography, Exp. Mech. 39 (1999) 217–226.

[205] D.P. Finegan, E. Tudisco, M. Scheel, J.B. Robinson, O.O. Taiwo, D.S. Eastwood, P.D. Lee, M. Di Michiel, B. Bay, S.A. Hall, G. Hinds, D.J.L. Brett, P.R. Shearing, Quantifying Bulk Electrode Strain and Material Displacement within Lithium Batteries via High-Speed Operando Tomography and Digital Volume Correlation, Adv. Sci. 3 (2015) 1500332(1–11).

[206] S.A. Hall, A methodology for 7D warping and deformation monitioring using time-lapse seismic data, Geophysics. 71 (2006) O21–O31.

[207] S.A. Hall, D. Muir Wood, E. Ibraim, G. Viggiani, Localised deformation patterning in 2D granular materials revealed by digital image correlation, Granul. Matter. 12 (2010) 1–14.

[208] H. S.A., M. Bornert, J. Desrues, Y. Pannier, N. Lenoir, G. Viggiani, P. Bésuelle, Discrete and continuum analysis of localised deformation in sand using X-ray μCT and volumetric digital image correlation, Géotechnique. 60 (2010) 315–322.

[209] B.K. Bay, Methods and applications of digital volume correlation, J. Strain Anal. Eng. Des. 43 (2008) 745–760.

[210] R. Zauel, Y.N. Yeni, B.K. Bay, X.N. Dong, D.P. Fyhrie, Comparison of the linear finite element prediction of deformation and strain of human cancellous bone to 3D digital volume correlation measurements., J. Biomech. Eng. 128 (2006) 1–

6.

[211] M.N. Richard, I. Koetschau, J.R. Dahn, A Cell for In Situ X-Ray Diffraction Based on Coin Cell Hardware and Bellcore Plastic Electrode Technology, J. Electrochem. Soc. 144 (1997) 554–557.

[212] I.A. Courtney, J.R. Dahn, Electrochemical and In Situ X-Ray Diffraction Studies of the Reaction of Lithium with Tin Oxide Composites, J. Electrochem. Soc. 144 (1997) 2045–2052.

[213] T.D. Hatchard, J.R. Dahn, In Situ XRD and Electrochemical Study of the Reaction of Lithium with Amorphous Silicon, J. Electrochem. Soc. 151 (2004) A838–A842.

[214] M. Giorgetti, S. Passerini, W.H. Smyrl, S. Mukerjee, X.Q. Yang, J. McBreen, In Situ X-Ray Absorption Spectroscopy Characterization of V_2O_5 Xerogel Cathodes upon Lithium Intercalation, J. Electrochem. Soc. 146 (1999) 2387–2392.

[215] J. Gao, M.A. Lowe, Y. Kiya, H.D. Abruña, Effects of Liquid Electrolytes on the Charge–Discharge Performance of Rechargeable Lithium/Sulfur Batteries: Electrochemical and in-Situ X-ray Absorption Spectroscopic Studies, J. Phys. Chem. C. 115 (2011) 25132–25137.

[216] M.A. Lowe, J. Gao, H.D. Abruña, Mechanistic Insights into Operational Lithium–Sulfur Batteries by In Situ X-ray Diffraction and Absorption Spectroscopy, RSC Adv. 4 (2014) 18347–18353.

[217] J. Wang, Y.K. Chen-Wiegart, J. Wang, In Operando Tracking Phase Transformation Evolution of Lithium Iron Phosphate with Hard X-ray Microscopy, Nat. Commun. 5 (2014) 4570 (1–10).

[218] S.-C. Chao, Y.-C. Yen, Y.-F. Song, Y.-M. Chen, H.-C. Wu, N.-L. Wu, A study on the interior microstructures of working Sn particle electrode of Li-ion batteries by in situ X-ray transmission microscopy, Electrochem. Commun. 12 (2010) 234–237.

[219] S.-C. Chao, Y.-C. Yen, Y.-F. Song, H.-S. Sheu, H.-C. Wu, N.-L. Wu, In Situ Transmission X-ray Microscopy Study on Working SnO Anode Particle of Li-Ion Batteries, J. Electrochem. Soc. 158 (2011) A1335–A1339.

[220] S. Titarenko, V. Titarenko, A. Kyrieleis, P.J. Withers, A ring artifact suppression algorithm based on a priori information, Appl. Phys. Lett. 95 (2009) 071113 (1–3).

[221] Y. Sun, J. Tao, H. Chen, C. Liu, An iterative algorithm for computed tomography

image reconstruction from limited-angle projections, J. Shanghai Jiaotong Univ. 20 (2015) 202–208.

[222] J. Guo, H. Qi, Y. Xu, Z. Chen, S. Li, L. Zhou, J. Guo, H. Qi, Y. Xu, Z. Chen, S. Li, L. Zhou, Iterative Image Reconstruction for Limited-Angle CT Using Optimized Initial Image, Comput. Math. Methods Med. 2016 (2016) 1–9.

[223] P. Pasierb, S. Komornicki, M. Rokita, M. Ręka s, Structural properties of Li2CO3–BaCO3 system derived from IR and Raman spectroscopy, J. Mol. Struct. 596 (2001) 151–156.

[224] L. Couture, J.E. Desnoyers, G. Perron, Some thermodynamic and transport properties of lithium salts in mixed aprotic solvents and the effect of water on such properties, Can. J. Chem. 74 (1996) 153–164.

[225] R.T. DeHoff, F.N. Rhines, Determination of number of particles per unit volume from measurements made on random plane sections: the general cylinder and the ellipsoid, Trans. AIME. 221 (1961) 975–982.

[226] R.T. DeHoff, F.N. Rhines, Quantitative microscopy, McGraw-Hill, 1968.

[227] E.E. Underwood, Quantitative stereology, Addison-Wesley Pub. Co., 1970.

[228] P.R. Mouton, Principles and Practices of Unbiased Stereology: An Introduction for Bioscientists, Johns Hopkins University Press, 2002.

[229] M. Stampanoni, A. Groso, A. Isenegger, G. Mikuljan, Q. Chen, A. Bertrand, S. Henein, R. Betemps, U. Frommherz, P. Böhler, D. Meister, M. Lange, R. Abela, Trends in synchrotron-based tomographic imaging: the SLS experience, in: U. Bonse (Ed.), Proc. SPIE, 2006: p. 63180M (1–14).

[230] F. Marone, M. Stampanoni, Regridding reconstruction algorithm for real-time tomographic imaging, J. Synchrotron Radiat. 19 (2012) 1029–1037.

[231] T. Kanit, S. Forest, I. Galliet, V. Mounoury, D. Jeulin, Determination of the size of the representative volume element for random composites: statistical and numerical approach, Int. J. Solids Struct. 40 (2003) 3647–3679.

[232] D. Bernard, D. Gendron, J.-M. Heintz, S. Bordère, J. Etourneau, First direct 3D visualisation of microstructural evolutions during sintering through X-ray computed microtomography, Acta Mater. 53 (2005) 121–128.

[233] M.S. Costanza-Robinson, B.D. Estabrook, D.F. Fouhey, Representative elementary volume estimation for porosity, moisture saturation, and air-water

interfacial areas in unsaturated porous media: Data quality implications, Water Resour. Res. 47 (2011) W07513 (1–12).

[234] D. Zhang, R. Zhang, S. Chen, W.E. Soll, Pore scale study of flow in porous media: Scale dependency, REV, and statistical REV, Geophys. Res. Lett. 27 (2000) 1195–1198.

[235] P. Baveye, H. Rogasik, O. Wendroth, I. Onasch, J.W. Crawford, Effect of sampling volume on the measurement of soil physical properties: simulation with x-ray tomography data, Meas. Sci. Technol. 13 (2002) 775–784.

[236] D. Onkaew, R. Turior, B. Uyyanonvara, N. Akinori, C. Sinthanayothin, Automatic retinal vessel tortuosity measurement using curvature of improved chain code, in: Int. Conf. Electr. Control Comput. Eng. 2011, IEEE, 2011: pp. 183–186.

[237] J.R. Wilson, W. Kobsiriphat, R. Mendoza, H.-Y. Chen, J.M. Hiller, D.J. Miller, K. Thornton, P.W. Voorhees, S.B. Adler, S.A. Barnett, Three-dimensional reconstruction of a solid-oxide fuel-cell anode., Nat. Mater. 5 (2006) 541–544.

[238] L. Safinia, A. Mantalaris, A. Bismarck, Nondestructive technique for the characterization of the pore size distribution of soft porous constructs for tissue engineering., Langmuir. 22 (2006) 3235–3242.

[239] J.R. Jones, G. Poologasundarampillai, R.C. Atwood, D. Bernard, P.D. Lee, Non-destructive quantitative 3D analysis for the optimisation of tissue scaffolds., Biomaterials. 28 (2007) 1404–1413.

[240] J.R. Izzo, A. Joshi, K. Grew, W. Chiu, A. Tkachuk, S. Wang, W. Yun, Nondestructive Reconstruction and Analysis of Solid Oxide Fuel Cell Anodes using X-ray Computed Tomography at sub-50 nm Resolution, in: ECS Trans., ECS, 2008: pp. 1–11.

[241] C.M. López, J.T. Vaughey, D.W. Dees, Morphological Transitions on Lithium Metal Anodes, J. Electrochem. Soc. 156 (2009) A726–A729.

[242] L. Gireaud, S. Grugeon, S. Laruelle, B. Yrieix, J.-M. Tarascon, Lithium metal stripping/plating mechanisms studies: A metallurgical approach, Electrochem. Commun. 8 (2006) 1639–1649.

[243] J. Steiger, D. Kramer, R. Mönig, Mechanisms of dendritic growth investigated by in situ light microscopy during electrodeposition and dissolution of lithium, J. Power Sources. 261 (2014) 112–119.

[244] J.A. Tang, S. Dugar, G. Zhong, N.S. Dalal, J.P. Zheng, Y. Yang, R. Fu, Non-destructive monitoring of charge-discharge cycles on lithium ion batteries using ^{7}Li stray-field imaging., Sci. Rep. 3 (2013) 2596 (1–6).

[245] M.M. Britton, P.M. Bayley, P.C. Howlett, A.J. Davenport, M. Forsyth, In Situ, Real-Time Visualization of Electrochemistry Using Magnetic Resonance Imaging., J. Phys. Chem. Lett. 4 (2013) 3019–3023.

[246] C. Monroe, J. Newman, Dendrite Growth in Lithium/Polymer Systems, J. Electrochem. Soc. 150 (2003) A1377–A1384.

[247] J.-N. Chazalviel, Electrochemical aspects of the generation of ramified metallic electrodeposits, Phys. Rev. A. 42 (1990) 7355–7367.

[248] D.R. Ely, R.E. Garcia, Heterogeneous Nucleation and Growth of Lithium Electrodeposits on Negative Electrodes, J. Electrochem. Soc. 160 (2013) A662–A668.

[249] D.S. Eastwood, P.M. Bayley, H.J. Chang, O.O. Taiwo, J. Vila-Comamala, D.J.L. Brett, C. Rau, P.J. Withers, P.R. Shearing, C.P. Grey, P.D. Lee, Three-dimensional characterization of electrodeposited lithium microstructures using synchrotron X-ray phase contrast imaging., Chem. Commun. . 51 (2014) 266–268.

[250] C. Rau, C.-P. Richter, Imaging cochlear soft tissue displacement with coherent x-rays, Phys. Scr. 90 (2015) 108006 (1–6).

[251] M. Basham, J. Filik, M.T. Wharmby, P.C.Y. Chang, B. El Kassaby, M. Gerring, J. Aishima, K. Levik, B.C.A. Pulford, I. Sikharulidze, D. Sneddon, M. Webber, S.S. Dhesi, F. Maccherozzi, O. Svensson, S. Brockhauser, G. Náray, A.W. Ashton, Data Analysis WorkbeNch (DAWN), J. Synchrotron Radiat. 22 (2015) 853–858.

[252] S. Titarenko, P.J. Withers, A. Yagola, An analytical formula for ring artefact suppression in X-ray tomography, Appl. Math. Lett. 23 (2010) 1489–1495.

[253] D. Aurbach, Y. Gofer, J. Langzam, The Correlation Between Surface Chemistry, Surface Morphology, and Cycling Efficiency of Lithium Electrodes in a Few Polar Aprotic Systems, J. Electrochem. Soc. 136 (1989) 3198–3205.

[254] E.E. Abd El Aal, Effect of Cl^- anions on zinc passivity in borate solution, Corros. Sci. 42 (2000) 1–16.

[255] A. Yalamanchili, Insights into the morphological changes undergone by the anode in the lithium sulphur battery system, Uppsala Universitet, Masters

thesis, 2014.

[256] K. Tamura, Y. Ohko, H. Kawamura, H. Yoshikawa, T. Tatsuma, A. Fujishima, J. Mizuki, X-ray induced photoelectrochemistry on TiO_2, Electrochim. Acta. 52 (2007) 6938–6942.

[257] A. Schneider, C. Wieser, J. Roth, L. Helfen, Impact of synchrotron radiation on fuel cell operation in imaging experiments, J. Power Sources. 195 (2010) 6349–6355.

[258] J. Roth, J. Eller, F.N. Buchi, Effects of Synchrotron Radiation on Fuel Cell Materials, J. Electrochem. Soc. 159 (2012) F449–F455.

[259] J. Eller, T. Rosén, F. Marone, M. Stampanoni, A. Wokaun, F.N. Büchi, Progress in In Situ X-Ray Tomographic Microscopy of Liquid Water in Gas Diffusion Layers of PEFC, J. Electrochem. Soc. 158 (2011) B963–B970.

[260] N. Ding, J. Zhu, Y.X. Yao, C.H. Chen, The effects of γ-radiation on $LiCoO_2$, Chem. Phys. Lett. 426 (2006) 324–328.

[261] N. Ding, J. Zhu, Y.X. Yao, C.H. Chen, The effects of gamma-radiation on lithium-ion cells, Electrochim. Acta. 51 (2006) 6320–6324.

[262] N. Ding, X. Fang, J. Xu, Y.X. Yao, J. Zhu, C.H. Chen, Performance of lithium-ion cells with a γ-ray radiated electrolyte, J. Appl. Electrochem. 39 (2008) 995–1001.

[263] D. He, Effect of radiation on the morphology of lithium-ion battery cathodes, Ohio State University, Masters thesis, 2014.

[264] C. Villevieille, M. Ebner, J.L. Gómez-Cámer, F. Marone, P. Novák, V. Wood, Influence of conversion material morphology on electrochemistry studied with operando X-ray tomography and diffraction., Adv. Mater. 27 (2015) 1676–1681.

[265] J. Wandt, C. Marino, H.A. Gasteiger, P. Jakes, R.-A. Eichel, J. Granwehr, Operando electron paramagnetic resonance spectroscopy – formation of mossy lithium on lithium anodes during charge–discharge cycling, Energy Environ. Sci. 8 (2015) 1358–1367.

[266] H. Wu, D. Zhuo, D. Kong, Y. Cui, Improving battery safety by early detection of internal shorting with a bifunctional separator., Nat. Commun. 5 (2014) 1–6.

[267] R. Younesi, G.M. Veith, P. Johansson, K. Edström, T. Vegge, Lithium salts for advanced lithium batteries: Li–metal, Li–O_2 , and Li–S, Energy Environ. Sci. 8 (2015) 1905–1922.

[268] O.O. Taiwo, D.P. Finegan, D.S. Eastwood, J.L. Fife, L.D. Brown, J.A. Darr, P.D. Lee, D.J.L. Brett, P.R. Shearing, Comparison of three-dimensional analysis and stereological techniques for quantifying lithium-ion battery electrode microstructures., J. Microsc. (2016) 1–13.

[269] M. Arakawa, S. Tobishima, Y. Nemoto, M. Ichimura, J. Yamaki, Lithium electrode cycleability and morphology dependence on current density, J. Power Sources. 43 (1993) 27–35.

[270] M.T. McDowell, I. Ryu, S.W. Lee, C. Wang, W.D. Nix, Y. Cui, Studying the kinetics of crystalline silicon nanoparticle lithiation with in situ transmission electron microscopy., Adv. Mater. 24 (2012) 6034–6041.

[271] M. Gu, Y. Li, X. Li, S. Hu, X. Zhang, W. Xu, S. Thevuthasan, D.R. Baer, J.-G. Zhang, J. Liu, C. Wang, In situ TEM study of lithiation behavior of silicon nanoparticles attached to and embedded in a carbon matrix., ACS Nano. 6 (2012) 8439–8447.

[272] M.T. McDowell, S.W. Lee, J.T. Harris, B.A. Korgel, C. Wang, W.D. Nix, Y. Cui, In Situ TEM of Two-Phase Lithiation of Amorphous Silicon Nanospheres, Nano Lett. 13 (2013) 758–764.

[273] X.H. Liu, F. Fan, H. Yang, S. Zhang, J.Y. Huang, T. Zhu, Self-limiting lithiation in silicon nanowires., ACS Nano. 7 (2013) 1495–1503.

[274] L.Y. Beaulieu, T.D. Hatchard, A. Bonakdarpour, M.D. Fleischauer, J.R. Dahn, Reaction of Li with Alloy Thin Films Studied by In Situ AFM, J. Electrochem. Soc. 150 (2003) A1457–A1464.

[275] J. Gonzalez, K. Sun, M. Huang, J. Lambros, S. Dillon, I. Chasiotis, Three dimensional studies of particle failure in silicon based composite electrodes for lithium ion batteries, J. Power Sources. 269 (2014) 334–343.

[276] F. Tariq, V. Yufit, D.S. Eastwood, Y. Merla, M. Biton, B. Wu, Z. Chen, K. Freedman, G. Offer, E. Peled, P.D. Lee, D. Golodnitsky, N. Brandon, In-Operando X-ray Tomography Study of Lithiation Induced Delamination of Si Based Anodes for Lithium-Ion Batteries, ECS Electrochem. Lett. 3 (2014) A76–A78.

[277] M.T. McDowell, S.W. Lee, W.D. Nix, Y. Cui, 25th Anniversary Article: Understanding the Lithiation of Silicon and Other Alloying Anodes for Lithium-Ion Batteries, Adv. Mater. 25 (2013) 4966–4985.

[278] D. Paganin, S.C. Mayo, T.E. Gureyev, P.R. Miller, S.W. Wilkins, Simultaneous

phase and amplitude extraction from a single defocused image of a homogeneous object, J. Microsc. 206 (2002) 33–40.

[279] B. Key, R. Bhattacharyya, M. Morcrette, V. Seznéc, J.-M. Tarascon, C.P. Grey, Real-time NMR investigations of structural changes in silicon electrodes for lithium-ion batteries., J. Am. Chem. Soc. 131 (2009) 9239–9249.

[280] M.J. Chon, V.A. Sethuraman, A. McCormick, V. Srinivasan, P.R. Guduru, Real-time measurement of stress and damage evolution during initial lithiation of crystalline silicon., Phys. Rev. Lett. 107 (2011) 045503(1–4).

[281] S.W. Lee, M.T. McDowell, J.W. Choi, Y. Cui, Anomalous shape changes of silicon nanopillars by electrochemical lithiation., Nano Lett. 11 (2011) 3034–3039.

[282] J.L. Goldman, B.R. Long, A.A. Gewirth, R.G. Nuzzo, Strain Anisotropies and Self-Limiting Capacities in Single-Crystalline 3D Silicon Microstructures: Models for High Energy Density Lithium-Ion Battery Anodes, Adv. Funct. Mater. 21 (2011) 2412–2422.

[283] X.H. Liu, J.W. Wang, S. Huang, F. Fan, X. Huang, Y. Liu, S. Krylyuk, J. Yoo, S.A. Dayeh, A. V Davydov, S.X. Mao, S.T. Picraux, S. Zhang, J. Li, T. Zhu, J.Y. Huang, In situ atomic-scale imaging of electrochemical lithiation in silicon., Nat. Nanotechnol. 7 (2012) 749–756.

[284] M. Pharr, K. Zhao, X. Wang, Z. Suo, J.J. Vlassak, Kinetics of initial lithiation of crystalline silicon electrodes of lithium-ion batteries., Nano Lett. 12 (2012) 5039–5047.

[285] A. Tremeau, N. Borel, A region growing and merging algorithm to color segmentation, Pattern Recognit. 30 (1997) 1191–1203.

[286] X.H. Liu, L. Zhong, S. Huang, S.X. Mao, T. Zhu, J.Y. Huang, Size-dependent fracture of silicon nanoparticles during lithiation., ACS Nano. 6 (2012) 1522–1531.

[287] S. Huang, F. Fan, J. Li, S. Zhang, T. Zhu, Stress generation during lithiation of high-capacity electrode particles in lithium ion batteries, Acta Mater. 61 (2013) 4354–4364.

[288] Y.S. Choi, M. Pharr, C.S. Kang, S.-B. Son, S.C. Kim, K.-B. Kim, H. Roh, S.-H. Lee, K.H. Oh, J.J. Vlassak, Microstructural evolution induced by micro-cracking during fast lithiation of single-crystalline silicon, J. Power Sources. 265 (2014) 160–165.

[289] I. Ryu, J.W. Choi, Y. Cui, W.D. Nix, Size-dependent fracture of Si nanowire battery anodes, J. Mech. Phys. Solids. 59 (2011) 1717–1730.

[290] E. Maire, J.Y. Buffière, L. Salvo, J.J. Blandin, W. Ludwig, J.M. Létang, On the Application of X-ray Microtomography in the Field of Materials Science, Adv. Eng. Mater. 3 (2001) 539–546.

[291] P.J. Withers, X-ray nanotomography, Mater. Today. 10 (2007) 26–34.

[292] S.D. Beattie, M.J. Loveridge, M.J. Lain, S. Ferrari, B.J. Polzin, R. Bhagat, R. Dashwood, Understanding capacity fade in silicon based electrodes for lithium-ion batteries using three electrode cells and upper cut-off voltage studies, J. Power Sources. 302 (2016) 426–430.

[293] R. Fathi, J.C. Burns, D.A. Stevens, H. Ye, C. Hu, G. Jain, E. Scott, C. Schmidt, J.R. Dahn, Ultra High-Precision Studies of Degradation Mechanisms in Aged $LiCoO_2$/Graphite Li-Ion Cells, J. Electrochem. Soc. 161 (2014) A1572–A1579.

[294] D.S. Eastwood, R.S. Bradley, F. Tariq, S.J. Cooper, O.O. Taiwo, J. Gelb, A. Merkle, D.J.L. Brett, N.P. Brandon, P.J. Withers, P.D. Lee, P.R. Shearing, The application of phase contrast X-ray techniques for imaging Li-ion battery electrodes, Nucl. Instruments Methods Phys. Res. Sect. B Beam Interact. with Mater. Atoms. 324 (2014) 118–123.

[295] S. Komini Babu, A.I. Mohamed, J.F. Whitacre, S. Litster, Multiple imaging mode X-ray computed tomography for distinguishing active and inactive phases in lithium-ion battery cathodes, J. Power Sources. 283 (2015) 314–319.

[296] T. Otaki, Artifact Halo Reduction in Phase Contrast Microscopy Using Apodization, Opt. Rev. 7 (2000) 119–122.

[297] A.S. Kumar, P. Mandal, Y. Zhang, S. Litster, Image segmentation of nanoscale Zernike phase contrast X-ray computed tomography images, J. Appl. Phys. 117 (2015) 183102 (1–10).

[298] Carl Zeiss X-ray Microscopy, Dual Scan Contrast Visualizer (DSCoVer), version 10.7.3245, (2014).

[299] T.A. Case, S. Candell, S. Seshadri, P. McGuinness, Multi energy X-ray microscope data acquisition and image reconstruction system and method, Patent US13768689, 2015.

[300] Y. Zhu, S.L. Manske, S.K. Boyd, Cartilage imaging of a rabbit knee using dual-

energy X-ray microscopy and 1.0 T and 9.4 T magnetic resonance imaging, J. Orthop. Transl. 3 (2015) 212–218.

[301] Y. Li, K. Yan, H.-W. Lee, Z. Lu, N. Liu, Y. Cui, Growth of conformal graphene cages on micrometre-sized silicon particles as stable battery anodes, Nat. Energy. 1 (2016) 15029(1–8).

[302] S. Randjbar Daemi, Advanced Characterization Techniques Applied to Battery Materials, University College London, M.Phil. thesis, 2016.

[303] R.L. Sacci, J.M. Black, N. Balke, N.J. Dudney, K.L. More, R.R. Unocic, Nanoscale Imaging of Fundamental Li Battery Chemistry: Solid-Electrolyte Interphase Formation and Preferential Growth of Lithium Metal Nanoclusters, Nano Lett. 15 (2015) 2011–2018.